Towards a Comprehensive Model for the Positive Electrode System of a Lead-Acid Traction Cell

A thesis presented
in partial fulfilment of the requirements
for the degree of
Doctor of Philosophy
in Production Technology at
Massey University

Ross Richard Nilson

1989

Massey University Library

Thesis Copyright Form

Title of thesis: Towards a Comprehensive Model for the Positive Electrode System of a Lead-Acid Traction Cell.

(1) (a) ✓ I give permission for my thesis to be made available to readers in the Massey University Library under conditions determined by the Librarian.

(~~b~~) I do not wish my thesis to be made available to readers without my written consent for _____ months.

(2) (a) ✓ I agree that my thesis, or a copy, may be sent to another institution under conditions determined by the Librarian.

(~~b~~) I do not wish my thesis, or a copy, to be sent to another institution without my written consent for _____ months.

(3) (a) ✓ I agree that my thesis may be copied for Library use.

(~~b~~) I do not wish my thesis to be copied for Library use for _____ months.

Signed R Nilson

Date 19/12/89

Cut here

The copyright of this thesis belongs to the author. Readers must sign their name in the space below to show that they recognise this. They are asked to add their permanent address.

NAME AND ADDRESS	DATE

Massey University Library

Thesis Copyright Form

Title of thesis: Towards a Comprehensive Model for the Positive Electrode System of a Lead-Acid Traction Cell.

(1) (a) ✓ I give permission for my thesis to be made available to readers in the Massey University Library under conditions determined by the Librarian.

(b) ~~✗~~ I do not wish my thesis to be made available to readers without my written consent for _____ months.

(2) (a) ✓ I agree that my thesis, or a copy, may be sent to another institution under conditions determined by the Librarian.

(b) ~~✗~~ I do not wish my thesis, or a copy, to be sent to another institution without my written consent for _____ months.

(3) (a) ✓ I agree that my thesis may be copied for Library use.

(b) ~~✗~~ I do not wish my thesis to be copied for Library use for _____ months.

Signed R Nilson

Date 19/12/89

Cut here

The copyright of this thesis belongs to the author. Readers must sign their name in the space below to show that they recognise this. They are asked to add their permanent address.

NAME AND ADDRESS	DATE

Abstract

This thesis develops a detailed model for the positive electrode system of an industrial lead-acid traction cell. This is referred to as the VIAM model since it relates the positive electrode voltage (V) and cell current (I) to internal distributions of current, potential, acid concentration and active mass (AM). The model can simulate both discharge and charge for a wide range of practical currents. The model takes account of microstructure, macrostructure and non-reactive structure in the positive active mass (AM). It also takes account of other cell components that affect the supply of acid to the positive electrode. The model has direct application to fundamental cell design (for example AM development) and cell systems design (for example cell charger design).

The model is based on established experimental studies, theories of electrochemical interface reactions and theories of ionic transport in electrolyte solution. From this base, three elemental models and an aggregate model are developed. The elemental models represent details of the microstructure of the positive electrode AM. The aggregate model represents the electrolyte mass (acid) and charge transport system within the positive electrode and other cell components. The combination of the elemental and aggregate models make up the VIAM model. The performance of the VIAM model (and underlying models) is assessed by comparing model results with findings from experimental studies in the literature. In addition, experiments undertaken as part of this work are used to test the model. The model and experimental results are in close agreement.

Acknowledgements

I would like to thank Dr R. I. Chaplin, Professor W. Monteith and Professor R. M. Hodgson for the encouragement and constructive criticism they have offered throughout the course of this work.

Neville Manson, Technical Manager of Chloride Batteries New Zealand Limited, kindly provided technical details for the cell used in experiments performed in this work.

My thanks also to my wife, Mary, who not only managed two very active children, Jonathan and Elissa, without help for many evenings during the preparation of this thesis, but also had enough energy left to proof-read the text.

Contents

List of Figures

Figure

Figure

Figure

Figure

List of Tables

Table

Units and Symbols

a) Units.

Normal SI units (Chiswell and Grigg (1971)) are used throughout this text with the following additions.

i) Hour(s) (abbreviated to hr(s)) is used as a measure of time (3600 s).

ii) Ampere hour(s) (abbreviated to Ahr(s)) is used as a measure of electrical charge (3600 A.s).

iii) Watt hour(s) (abbreviated to Whr(s)) is used as a measure of energy (3600 W.s).

iv) The gram (abbreviated to g) is used as a measure of mass ($1x10^{-3}$ kg).

These additions are consistent with common practices in the battery industry.

b) Symbols for units.

Normal SI unit symbols (Chiswell and Grigg (1971)) are used throughout this text with the following additions.

i) Hr(s) for hour(s).

ii) Ahr(s) for Ampere hour(s).

iii) Whr(s) for watt hour(s).

iv) g for the gram.

v) v for the volt.

c) Symbols for variables.

Symbols for variables are fully defined in the body of text where they are first used.

d) Symbols for experiment designations.

An example designation for the experiments performed in this work is AD100R20. This should be in interpreted as follows.

i) The first character (A) is the cell label that defines the cell involved (here cell A).

ii) The following four characters (D100) define the depth of discharge (here 100 Ahrs).

iii) The last three characters (R20) define the rate of discharge (here 20 A).

Chapter 1

Introduction

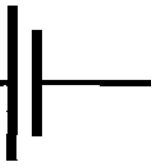

This thesis is concerned with the normal working cycle of a practical lead-acid cell. It sets out to link the important external parameters of cell voltage and current to the internal parameter distributions of current, potential, active mass (AM) and acid concentration using suitable models.

The internal parameters are defined throughout the larger cell components and the finely structured AM in the cell plates. Direct experimental measurements cannot be made within the small dimensions of the plate AM without disrupting the structure and the reaction processes. This dictates the use of indirect experimental methods and models to describe the operation of the plate.

As well as providing an alternative to direct experimental methods, an accurate cell model is a valuable research tool in its own right. It enables cell designs and systems to be evaluated by simulation, reducing the need for costly prototype tests. For example a cell model can be

used for the simulation of different discharge/charge cycles to provide a basis for the improvement of cell charging systems. An example of a more fundamental nature is the systematic improvement of cell design and performance using simulation methods to evaluate new cell components or materials.

The cell model is only of use in so far as it properly represents the required details of the system concerned. The model set out in this thesis represents the positive electrode system of the lead-acid traction cell. It is not a general model but gives a detailed representation of this electrode system. The model is referred to as the VIAM model since it connects voltage (V) current (I) and active mass (AM) distribution for the positive electrode system.

The VIAM model takes account of recent experimental studies which identify distinct functions for two levels of positive AM structure (Pavlov and Bashtavelova (1984,1986)). This is one important feature that distinguishes the VIAM model from other models used to represent the positive electrode in the literature. Other distinctive features of the VIAM model include the representation of the non-participating AM that develops over the life of the cell, the representation of structural changes based on experimental observations, the representation of acid transport effects for the complete cell, operation for both discharge and charge conditions and operation over the wide range of current involved in a practical work cycle.

The VIAM model is, in fact, a combination of four underlying models. Three of these describe the local structure of the AM. These are the elemental models. The fourth model describes the transport of charge and mass throughout the complete cell. This is the aggregate model. Figure 1.1 illustrates the relationship between the various models.

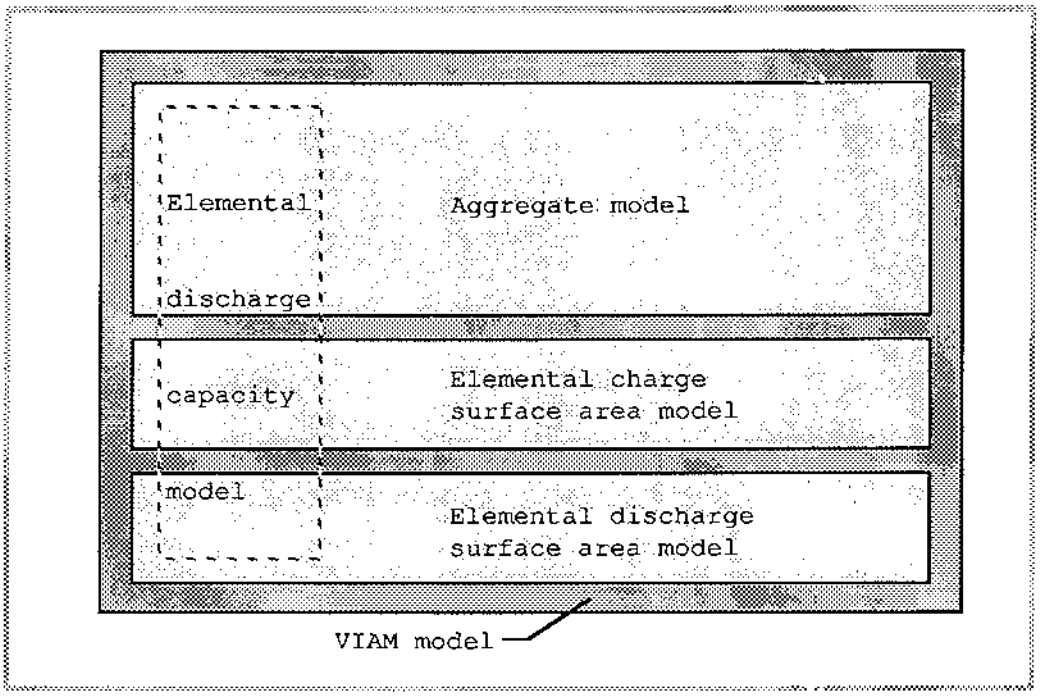

Figure 1.1: The VIAM Model and Underlying Models.

The elemental discharge surface area model, the elemental charge surface area model and the aggregate model are combined to give the comprehensive VIAM model. The elemental discharge capacity model is an implicit assumption on which the other models depend.

In the presentation that follows, chapter 2 introduces the lead-acid traction cell, reviews cell development and considers possible approaches to improving the performance of traction cell systems. This explains the background and motivation for the subsequent work.

Chapter 3 reviews the present understanding of the lead-acid cell as it relates to the concerns of the VIAM model. The work reviewed here provides the foundation for the development of the underlying models that make up the VIAM model.

The elemental models are set out in chapter 4. Here qualitative descriptions of structural changes in the positive AM are proposed based on the experimental work reviewed in chapter 3. These are then developed into the quantitative formulations that define the elemental discharge capacity model, the elemental discharge surface area model and the elemental charge surface area model.

The aggregate model is set out in chapter 5. This model represents all the cell components that influence the supply of acid to the positive electrode. This includes the separator region, the negative plates, the reservoir region and the positive plates themselves. The positive plates are further divided into macrostructure, microstructure and non-participating AM. Formulations are given to define the dimensions, electrical characteristics and mass transport of the system of components that makes up the aggregate model.

A series of experiments were performed on a commercial traction cell to provide data for testing the VIAM model. Chapter 6 describes the equipment, the cell and the procedure used for these experiments.

An extensive series of results is given in chapter 7. This includes results for each of the elemental models, the aggregate model, the VIAM model and the experimental work. The results are also discussed in this chapter.

Chapter 8 concludes the work presented in this thesis. The contribution of the work is considered and possible extensions are discussed in this chapter.

Chapter 2

Lead-Acid Traction Cells and Systems

This chapter gives the background and motivation for the positive electrode model set out in this thesis. The chapter begins with a brief introduction to lead-acid traction cells. It then shows that cell service life is an important factor in the economy of traction cell systems and summarises the processes that reduce cell life. Next, work aimed at improving cell life by improving cell design is reviewed. A complementary approach to improving cell life using cell charging systems that employ suitable models is then suggested. The development of a model for this purpose is given as an aim of this work. The model itself is set out in later chapters.

The chapter content is summarised below.

i) An introduction to lead-acid traction cells (section 2.1).

ii) Cell service life and life reducing processes (section 2.2).

iii) Cell centred approaches to improving cell life (section 2.3).

iv) A complementary approach for improving cell life (section 2.4).

v) A cell life prolonging charger (section 2.5).

vi) A positive electrode model (section 2.6).

2.1 LEAD-ACID TRACTION CELLS.

Lead-acid traction cells are designed to provide the motive power for electrical vehicles. These vehicles can be divided into three application groups.

i) Industrial vehicles such as mine locomotives, industrial trucks and fork-lift trucks.

ii) On-road vehicles such as electric cars and trucks.

iii) Limited-range lighter vehicles such as golf carts and invalid carriages.

Each of these groups require slightly different cell designs. For industrial vehicle cells, long life and large electrical capacity are important. This results in large, physically robust single cell designs. For on-road vehicle cells, low weight and cost are important. This results in cells with a minimum of electrochemical material, moderate electrical capacity and a single or multiple cell construction. The life of these cells is considerably less than that of industrial vehicle cells. Limited-range vehicle cells are similar to the on-road vehicle cells but have a small electrical capacity.

The internal cell construction is similar for all the application groups. The electrodes are shaped as relatively thin rectangular plates. These plates are assembled together as elements with the outer plates both negative and the inner plates alternatively positive and negative. The plates are held apart by porous insulating separators. Two positive plate types are common.

i) Flat pasted plates. These are rectangular conductive grid-like frames (grids) filled with a porous AM of lead dioxide.

ii) Tubular plates. These are a rectangular assembly of adjacent cylinders. The cylinders consist of a porous insulating tube (or tubes) enclosing porous lead dioxide packed around a central conducting spine.

The negative plates are flat pasted types filled with porous lead AM.

Table 2.1: Some Features of Traction and SLI Cells.

Feature	Traction Cell	SLI Cell
Cell type	Portable	Portable
Construction	Single cell	Multiple cell
Depth of discharge	Deep	Shallow
Positive plate	Flat pasted or tubular	Flat pasted
Negative plate	Flat pasted	Flat pasted
Specific energy ($Whrs.Kg^{-1}$)	30 to 32	34 to 40
Capacity measurement	Ahrs at 5 hr current rate	Ahrs at 20 hr current rate
Typical capacity (Ahrs)	100 to 1500	40 to 100
Typical life	1000 to 1500 cycles	3 to 6 years

Some features of traction cells are compared with those for normal automotive (starting-lighting-ignition or SLI) cells in table 2.1.

This text is particularly concerned with the industrial vehicle traction cells with flat pasted positive plates.

2.2 CELL SERVICE LIFE.

Cell service life is a major factor in the economy of traction cell systems. This point is illustrated when cell replacement cost is taken together with electrical energy cost as the true cost of "fuel" for an electric vehicle as shown in figure 2.1.

It is to be expected that traction cell life is a function of intrinsic cell properties. In practice, cell

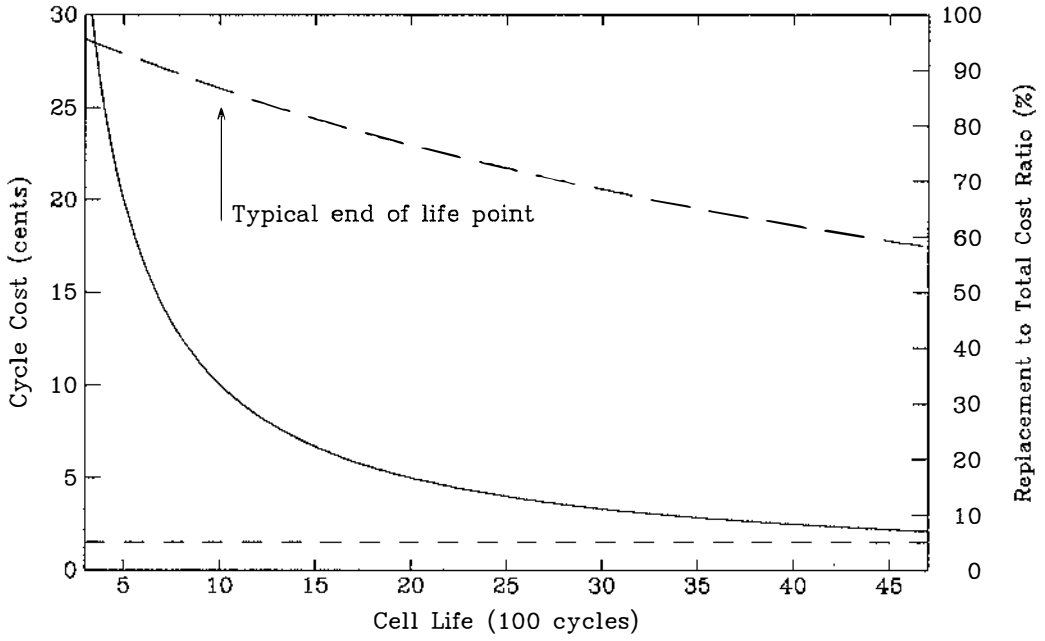

Solid: cycle replacement cost (cents) (cell replacement cost / cell life).
Small dash: cycle energy cost (cents) (80 Ahr at 2.3 volts, 0.72 efficiency).
Large dash: cycle replacement to total (replacement+energy) cost ratio (%).
Costs based on a 100 Ahr cell and 1988 New Zealand retail prices.

Figure 2.1: Cell Energy and Replacement Cost per Charge Cycle.

life is also determined by the operating conditions imposed by both the vehicle and the charger unit. Harsh conditions provoke or accelerate harmful processes in the cell leading to a drastically reduced service life.

2.2.1 The Influence of the Vehicle.

The vehicle influences cell life mainly through the depth of discharge it requires. Linden (1984) gives the data in figure 2.2 which shows a rapidly decreasing service life with increasing depth of discharge (note the logarithmic scale).

One process associated with over-discharge is the expansion of the AM. The molar volume of solid discharge product is considerably larger than that of the corresponding charge products (254% for the negative AM and 181% for the positive AM). This causes the AM to expand during discharge and contract during charge. The process is

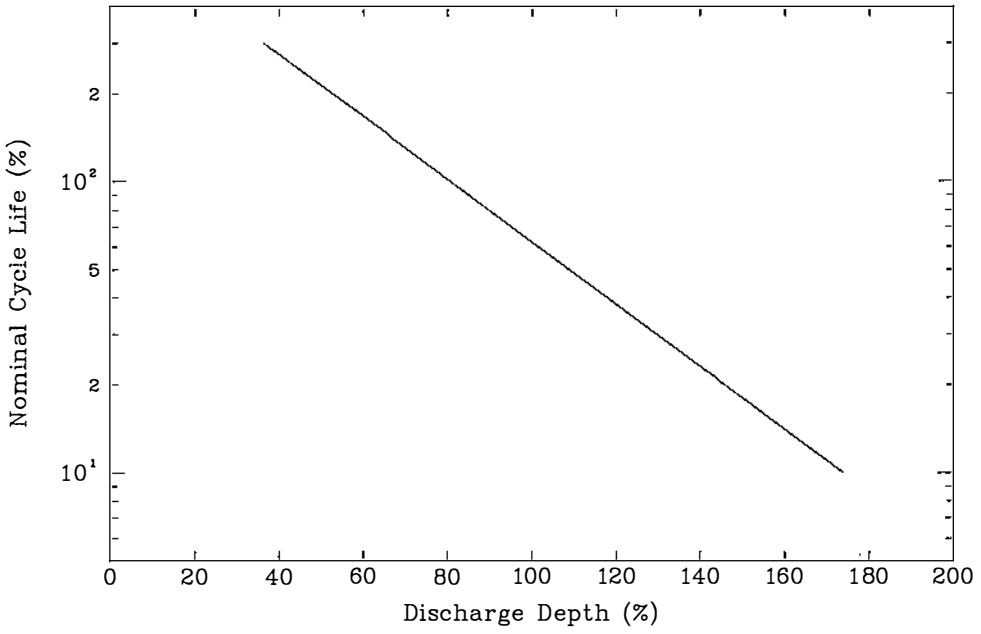

Redrawn from Linden (1984).
Discharge depth is percentage of 6 hour discharge capacity.
Cycle life is percentage of nominal for 80% discharge depth.

Figure 2.2: Traction Cell Cycle Life and Discharge Depth.

not perfectly reversible and a gradual net expansion throughout the cell life results. Evidence supporting the harmful effect of AM expansion is given by Takahashi *et al* (1983) and Alzieu *et al* (1987). Their experiments showed cell life improved dramatically when plate expansion was limited by the application of external mechanical pressure.

With over-discharge there is a consequent increase in the charge time needed to restore the AM to its fully charged state. This means harmful effects, which superficially appear to be a result of discharge depth, may in fact be the result of the increased charge time. These effects are discussed in relation to the charger unit below.

2.2.2 The Influence of the Charger Unit.

Cell service life is decreased by two undesirable charge conditions.

i) Over-charge where charge is continued beyond the fully charged state.

ii) Under-charge where the charge is prematurely terminated before the fully charged state is reached.

With over-charge, harmful processes include positive grid corrosion, positive AM shedding, non-participating positive AM, water loss, negative plate poisoning and temperature elevation. With under-charge the harmful processes include positive and negative plate sulphation. These processes are considered briefly below.

a) Positive plate corrosion.

On over-charge the positive plate grid is subjected to accelerated anodic corrosion. Corrosion directly reduces cell capacity by three mechanisms.

i) By isolating portions of AM from the grid with high resistance corrosion product (Pavlov (1984)).

ii) By reducing the cross-section of the grid and so increasing grid resistance (Pavlov (1984)).

iii) In extreme cases, by the destruction of the mechanical structure due to mechanical stresses and fractures (Vinal (1955)).

Correct charge rates and the elimination of over-charge are important in minimising corrosion.

b) Active mass shedding.

When undergoing repeated discharge/charge cycling the AM becomes loosely held in the grid structure. This can lead to the material being completely displaced from the plate and falling to the bottom of the cell to form a sludge. The material lost in this way is obviously not available for the cell reaction and as a result the cell capacity is reduced. Some causes for shedding have been proposed by Bode (1977) including dislodgment through vigorous gassing and loosening through changes in the structure of the AM during cycling. The latter effect is also dependent on the discharge depth as discussed above. Again correct charge rates and elimination of over-charge are important in minimising shedding.

c) Non-participating active mass.

Detailed studies of failed positive plates have revealed the existence of significant portions of AM that no longer participate in the discharge/charge reaction. This phenomenon is most likely associated with changes in AM structure during cycling (see Chang (1984)). Correct charging may well retard the development of non-participating AM.

d) Water loss.

Near the end of charge both electrodes are operating at potentials where gas evolution reactions proceed rapidly (oxygen at the positive electrode and hydrogen at the negative electrode). The net effect is a loss of water from the electrolyte. Water is also lost as water vapour, particularly at the elevated charge temperatures. Water loss can reduce cell life by two mechanisms.

i) By increasing acid concentration and further accelerating corrosion and chemical attack on other cell components.

ii) By reducing the electrolyte level and uncovering part of the electrodes. This prevents the associated AM from taking part in the cell reaction.

The problem of water loss can be overcome with regular maintenance (replacement of water).

e) Negative plate poisoning.

Negative plate poisoning is a side effect of positive grid corrosion. As the positive grid is corroded, alloy components (typically antimony) enter the electrolyte solution. These components then migrate and become deposited on the negative AM. As a result the hydrogen gas evolution potential is reduced leading to increased gassing, self-discharge and decreased charge efficiency of the negative. A recent study of this effect is given by Mahato *et al* (1985). Negative plate poisoning is reduced coincidentally when positive grid corrosion is reduced.

f) Temperature Elevation.

Any current flow in a cell causes heating due to the power dissipated in the cell conductors. As a result the cell temperature increases and cell reaction rates (worst

of all corrosion) increase. Unnecessary temperature elevation occurs in the case of over-charge. This can be minimised with the elimination of over-charge.

g) Sulphation.

Sulphation occurs when not all discharge product (lead sulphate) is converted to charge product during repeated charge cycles. The uncharged lead sulphate undergoes irreversible changes to become so called "hard" lead sulphate. This material cannot be made to take any further part in the cell reaction and is effectively a loss of AM that results in a reduction in cell capacity. What characterises the "hard" lead sulphate is not clearly understood. In a recent study Gibson and Peters (1982) consider particle size and solubility as possible factors. Sulphation can be avoided by eliminating under-charge.

2.2.3 Life Reducing Processes in Perspective.

In considering the processes above it should be pointed out that not all are of equal importance. Corrosion is cited as a major reason for cell failure (for example Simon (1967), Bode (1977), Rueschi (1977), Linden (1984), Bullock and Butler (1986)). Shedding is also given as a common reason for cell failure (for example Bode (1977) and Linden (1984)). Non-participating AM is a more recently observed phenomenon (see Simon and Caulder (1975), Pavlov and Bashtavelova (1986) and Chang (1984) for example). The presence of non-participating AM is difficult to detect without scientific examination. For this reason it is not mentioned in older failure data collected from the field. Improvements in separator technology and plate manufacturing processes have reduced the incidents of cell failure due to corrosion and shedding. As a consequence the significance of cell failure due to non-participating AM is increasing. The other major reason given for cell failure is sulphation (for example Bode (1977) and Linden (1984)).

The other life reducing conditions mentioned in section 2.2.2 are secondary or minor.

The major life reducing conditions of corrosion, shedding and non-participating AM are discussed further in the context of cell centred approaches to improving cell life below. Sulphation is not discussed in this context since it can be avoided by correct cell charging.

2.3 CELL CENTRED APPROACHES TO IMPROVING CELL LIFE.

Extensive research effort has been directed at understanding and improving the intrinsic properties of the cell. The general aim has been to improve cell service life. This work is summarised below under the headings of fundamental studies and technological improvements. The fundamental studies concern the mechanisms and materials in the cell. The technological improvements concern the construction and manufacturing of the cell. Comprehensive reviews covering both fundamental and technological concerns are given in the works of Bode (1977) and Pavlov (1984).

2.3.1 Fundamental Studies.

a) Corrosion

At potentials more positive than the lead dioxide electrode, the corrosion reaction proceeds through a layer of PbO_2. Experimental studies have shown this layer to consist of an inner part of dense material and an outer part of porous material (for example Simon (1967)). Pavlov and Rogachev (1978) and Pavlov and Dinev (1980) suggest that the corrosion rate is determined by the diffusion of oxygen species through the dense PbO_2 layer. Further these authors propose that this proceeds through ionic

defects transforming the lead to PbO and α-PbO_2 † in stages. This type of process is consistent with recent work (Bullock *et al* (1983,1986)).

Corrosion rate is strongly influenced by the grid composition. This is consistent with a process involving ionic defects in crystal structure as mentioned above. Lead/antimony (Pb/Sb) alloys are the most commonly used grid material. Many studies have been performed to find improved materials that exhibit low corrosion rates but retaining acceptable mechanical and electrical properties. Some recent examples include Bullock and Tiedemann (1980) comparing a lead/strontium/tin/aluminium alloy with alloys of lead/antimony and lead/calcium as well as pure lead, Papazov *et al* (1981) examining corrosion of pure lead and lead/antimony alloys of different composition, and Dacres *et al* (1983) examining several lead fibre composites and lead alloyed with calcium, calcium/tin, tin, and silver. All cases exhibited different corrosion characteristics.

The nature of the polarisation of the positive electrode has a marked effect on corrosion rate. Papazov *et al* (1981) showed that a long continuous charge on lead/antimony electrodes was considerably more harmful than interrupted charge and charge/discharge cycling (see figure 2.3a). Pavlov and Rogachev (1978) have shown that corrosion current is also dependent on potentials associated with cell charging (see figure 2.3b). This is one place where the charger can influence the positive grid corrosion.

† The two crystallographic forms of lead dioxide are orthorhombic α-PbO_2 and tetragonal β-PbO_2 (Bode (1977)).

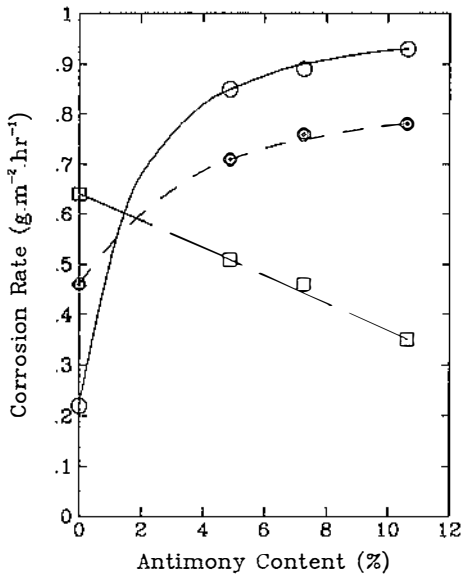

(a) Corrosion for different grid composition and charge cycles.

Redrawn from Papazov et al (1981).

Solid: continuous charge.
Small dash: discontinuous charge.
Large dash: charge/discharge cycling.

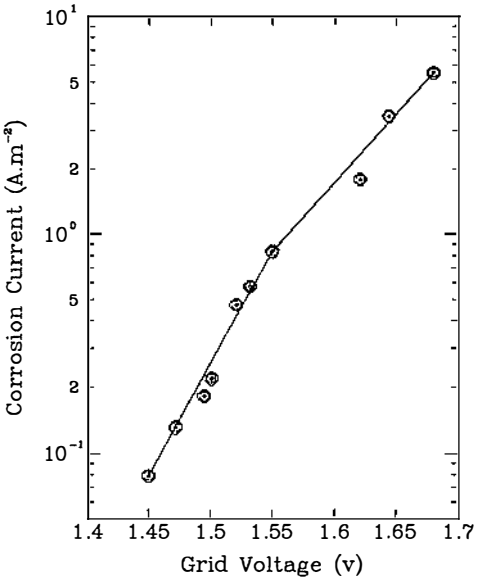

(b) Corrosion current and grid voltage.

Redrawn from Pavlov and Rogachev (1978).

Grid voltage measured relative to a Hg/Hg_2SO_4 electrode in $5.4x10^3$ $mol.m^{-3}$ H_2SO_4.

Figure 2.3: Positive Grid Corrosion and Polarisation Effects.

The PbO_2 corrosion film thickness influences the corrosion rate. The corrosion rate initially decreases with increasing film thickness and then settles to a steady value (see Valeriote and Gallop (1977) and Pohl and Schendler (1984)). This can be explained in terms of a limiting thickness of dense PbO_2, beyond which, it becomes cracked and porous because of increasing mechanical stresses due to volume changes. The thickness of the bulk AM covering the grid also has an effect on the corrosion rate. Papazov *et al* (1981) showed corrosion rate decreased with increasing AM thickness on tubular plates.

b) Shedding.

Explanations of shedding are rather tentative. This may be because individual influences are difficult to isolate or that shedding is a secondary effect caused by some other process. Some of the explanations offered in the literature are given below.

Bode (1977) cites vigorous gassing as promoting shedding. Chang (1984) suggests gassing may break off and carry out loosened particles.

Structural change in the AM during cycling is a likely cause of shedding. Deep discharge cycling in particular has been shown to cause shedding. Bode (1977) describes how AM does not return to its original structural form on consecutive discharge/charge cycles due to nucleation processes and different current densities. This, he suggests, leads to dendritic growths which may become detached from the conducting network and eventually be shed. Other authors (for example Takahashi *et al* (1983), Pavlov and Bashtavelova (1984)) have experimentally identified changes in the AM structure from a reticulate to a coralloid and finally to a uniform fine particle form. It is suggested that the final form decreases the cohesion of the AM particles and is a likely cause of shedding.

c) Non-participating AM.

Non-participating β-PbO_2 has been observed in cycled positive plates. Two explanations for this are given below.

Early work suggested non-participating β-PbO_2 may be due to the loss of hydrogen species in the PbO_2 crystal structure (Simon and Caulder (1975)). Some latter studies have shown this to be an unlikely reason as β-PbO_2 taken from new and failed plates show essentially the same crystal structure (Hill (1984)). Moseley (1983) has shown that hydrogen is most likely accommodated as water droplets within the pores or on the pore surface of the PbO_2 structure. On the other hand, study of the presence of hydrogen in the structure is continuing (for example Santoro *et al* (1983) and Hill and Madsen (1984)).

Changes in the high level mechanical structure are also given as reasons for the appearance of non-participating AM. These changes have already been mentioned

with regard to shedding. It has been suggested these changes cause non-participating AM in two ways (Pavlov and Bashtavelova (1986), Chang (1984)). A first effect is that the development of the uniform structure gives reduced mechanical rigidity and an accompanying increase in resistance between solid AM particles. A second effect is that the redistribution of pore geometry with cycling reduces the number of larger pores required to ensure mass transport with low polarisation in the electrolyte. The result is an increase in solution polarisation. Both these effects would cause the cell to reach its lowest allowed discharge voltage while considerable amounts of AM have not yet participated in the cell reaction.

2.3.2 Technological Improvements.

Many technological improvements in recent years have been aimed at reducing costs and increasing specific energy (reducing weight). Examples include the development of polyethylene containers and microporous polyethylene separator parts.

Improvements directly promoting longer life centre on the positive plate. These include the adoption of tubular plates and improvement in separator design for flat pasted plates.

a) Tubular plates.

Tubular plates have been shown to reduce both corrosion and shedding (Pavlov (1984)). Corrosion is reduced by having the spine or grid completely surrounded by AM. Shedding is reduced by having the AM completely enclosed in an inner sleeve of woven glass fibre tightly held in an outer sleeve of perforated PVC tubing (other arrangements are also used see Barak (1980)).

b) Separators on flat pasted plates.

Modern separators have enabled cell life to increase from 200 cycles to over 1500 cycles. The main advancement has been through the use of polymer-based microporous separators in place of wooden separators. These have virtually eliminated short circuits through the separator. A woven glass mat and a hard ribbed and perforated divider are two other components commonly used. The woven glass mat is placed against the positive plate to reduce shedding. The perforated divider is placed between the mat and microporous separator to increase the acid volume available to the positive plate (other arrangements are also used see Pavlov (1984)).

2.3.3 Expectations from Cell Centred Work.

Considerable gains in cell service life can be expected if fundamental improvements in intrinsic cell properties can be made, particularly properties affecting corrosion, shedding and non-participating AM. Fundamental studies over the past 35 years or so have greatly improved knowledge of processes in the cell but found limited application in practice. The most dramatic gains in battery life have come through technological improvements.

2.4 A COMPLEMENTARY APPROACH TO IMPROVING CELL LIFE.

While large gains from cell centred work are hoped for, they may be some time in coming. By comparison, the preceding discussion suggests that given cells of the present design, significant gains may well be possible through careful control of cell charging. This is a complementary approach to improving cell life which has received little attention.

It is difficult to estimate the gains to be made by this approach. One extreme might be set by the life observed in controlled laboratory conditions. This can be up to 50% higher than the average life obtained in practice (Pavlov (1984)). A study of cell life given different charging schemes would provide more objective data. Unfortunately these types of studies are few and inconclusive. For example Weininger and Siwek (1977) and Siwek (1977) studied the effect of various chargers on small cells and obtained large variations in cell life. However, these results could not be attributed to charge effects with any certainty because of the small sample size involved. Some data exists for fixed charging schemes where the charge time (over-charge) is adjusted. Pavlov (1984), referring to an earlier worker, gives the data for SLI batteries reproduced in table 2.2. A gain of 34% is obtained in the case of battery type 12H by reducing the charge time.

Table 2.2: Effect of Charge on SLI Cell Life.

	Charge factor*	Cell life†
Cell type 13HN	1.15	403
	1.35	366 ±35
	Charge factor	Cell life
Cell type 12H	1.15	670 ±100
	1.35	500 ±48

* Charge factor is the ratio of charge to discharge Ampere hours.

† Discharge/charge cycles to failure.

Data quoted in Pavlov (1984).

It can be concluded that significant gains in cell life are likely with improved cell charging. A process of defining and implementing a charging scheme that can achieve these gains is discussed in the following section.

2.5 DEVELOPING A CELL LIFE PROLONGING CHARGER.

The development of a cell life prolonging charger can be represented by the diagram in figure 2.4. A brief explanation of the components shown follows.

a) Operating conditions.

Normal concerns of the industrial work place need to be taken into account. These include such things as safety, construction standards, service connections and the like. These concerns will not be dwelt on here. Of primary interest for this discussion are operating conditions that

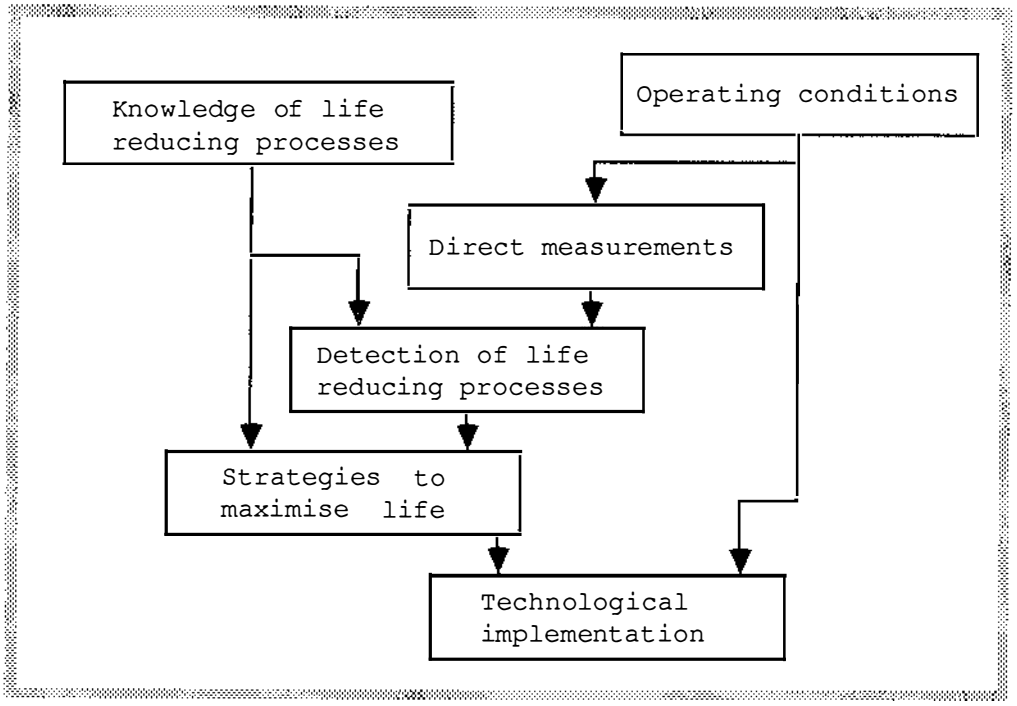

Figure 2.4: Development of a Life Prolonging Charger.

influence the information input and control responses of the charger.

The harsh environment of the industrial work place makes measurements that require specialised sensing devices and connections on the cell or battery unit undesirable. Ideally the charger should operate using only the normal charger connections (a heavy current carrying circuit and a light voltage sensing circuit). Information supplied by a human operator is also undesirable. This is because unattended operation, such as overnight charge, is often called for.

With the normal charger connections control responses are restricted to manipulating current or voltage.

b) Direct measurements.

The normal charger connections mentioned above limit direct measurements to current and voltage only. The charger is also likely to measure time.

c) Knowledge of life reducing processes.

A qualitative description of important life reducing processes has already been given. Ideally, what is required is a quantitative link between these processes and cell life. With this information, gains made by controlling particular conditions can be properly assessed. In the absence of such links, elimination of the three conditions that accelerate the life reducing processes has been identified as most important. The three conditions are over-discharge, over-charge and under-charge.

d) Detection of cell life reducing processes.

The underlying life reducing processes or the accelerating conditions must be detected if harmful effects are to be minimised. For the three accelerating conditions

mentioned above, the state of charge must be defined. The state of charge is fundamentally the amount of uncharged AM in the cell. A suitable model is required to define this quantity from the direct measurements.

e) Charging strategies to maximise cell life.

Charging strategies that reduce harmful effects and maximise cell life are required. Historically, these have been limited to schemes that can be implemented with simple discrete charger hardware. Modern microcomputer based systems employing power electronic devices provide the opportunity for improved charging strategies. In general this will also require a model.

f) Technological implementation.

To be used in practice the components above need to be incorporated into a suitable hardware device. Here again, cost and concerns of the industrial work place are important.

2.6 A MODEL FOR THE POSITIVE ELECTRODE SYSTEM.

This work recognises the important place of the charger in the economy of lead-acid traction cell systems. It is motivated by potential gains in cell life achieved through improved charging approaches. It has been shown above that there is a considerable amount of work to be done in a fairly broad range of areas before these gains can be fully realised.

The scope of this work is limited to a small portion of the possible work. Specifically, this work is concerned with the development of a model that connects the voltage, current and AM (the VIAM model) of the positive electrode for a practical traction cell during a normal discharge/

charge cycle.

This model has application in defining the quantity of charge state from voltage and current measurement. The determination of charge state is required for a charger unit that recognises the conditions of over-discharge, under-charge and over-charge. It also has application in determining such things as internal electrode potential distribution, internal acid concentration distribution and gassing rate. These quantities relate directly to the underlying life reducing processes discussed above.

It should also be pointed out that, while this work has been placed in the context of improving cell life, the model is of a fundamental nature and contributes to a general understanding of processes in the positive electrode of the lead-acid cell.

In chapter 3 existing work is reviewed to establish the foundation upon which the model is based. Chapters 4 and 5 give qualitative and quantitative descriptions of four underlying models that together make up the VIAM model.

Chapter 3

Foundations for a Positive Electrode Model

This chapter reviews the behaviour of the positive electrode of the lead-acid cell as it is understood at present. The purpose of the review is to establish a foundation for the development of a detailed electrode model (the VIAM model). This chapter makes use of relevant exemplary or recent work only. For a broad treatment the reviews of Pavlov (1984), Bode (1977), Carr and Hampson (1972) concerning the lead-acid cell and PbO_2 electrode, and Bockris and Reddy (1977), Vetter (1967) and Delahay (1965) concerning general electrochemical matters, can be consulted.

The mechanism for change in the AM is considered first to introduce important factors controlling the electrode behaviour. Each of these factors is then discussed in detail. Gas evolution that accompanies the charge is considered next. This is followed by a review of two common theoretical models for porous electrode systems. Data from experimental studies of voltage, current and AM for both discharge and charge are then presented. This data is used later (in chapter 7) to evaluate the VIAM model results. Finally, the development of the VIAM model is discussed.

The chapter content is summarised below.

i) The charge and discharge mechanism (section 3.1).

ii) The mechanical structure of the AM (section 3.2).

iii) The electrochemical reactions (section 3.3).

iv) Transport of mass and charge in solution (section 3.4).

v) Gas evolution effects (section 3.5).

vi) Common electrode models (section 3.6).

vii) Experimental studies of voltage, current and AM (section 3.7).

viii) The way ahead for the VIAM model (section 3.8).

3.1 THE CHARGE AND DISCHARGE MECHANISM.

3.1.1 A Description of the Charge and Discharge Mechanism.

The electrochemical reaction at the positive electrode (see Pavlov (1984) for example) can be written as

$$PbO_2(s) + 3H^+ + HSO_4^- + 2e^- = PbSO_4(s) + 2H_2O. \quad (3.1)$$

During charge (oxidation) the reaction proceeds towards the left and solid $PbSO_4$ is converted to solid PbO_2. The reverse process occurs during discharge (reduction).

The mechanism by which reaction 3.1 occurs is of primary importance in understanding the overall operation of the electrode. A solid-state or dissolution-

precipitation mechanism is possible. Work which identifies the mechanism is discussed below.

Hattori *et al* (1975) studied the same pin-point of positive electrode with a scanning electron microscope (SEM). They used a miniature (16.8 x 16.7 mm) electrode fitted into a small cell. The cell was discharged and charged in stages. The discharge and charge rates were 30 mA and 12 mA respectively which corresponds to a current density of about 107 and 43 $A.m^{-2}$.† At each stage the electrode was removed from the cell, washed and mounted in the microscope for examination. Crystals developed as three dimensional structures at preferred sites for both charge and discharge processes. This is convincing evidence in favour of a dissolution-precipitation mechanism. A uniform two dimensional covering would be expected for a solid-state mechanism.

Earlier, Simon *et al* (1970) studied samples taken from AM of commercial positive plates using x-ray analysis, differential thermal analysis and optical microscopy. The samples were taken at various stages of constant current

† In this text discharge and charge current will be defined in one of two ways. The preferred definition is as a current per unit area of electrode (or plate) surface ($A.m^{-2}$). That is, a current density. The plate surface area is used here since it is easily determined. The true interface surface, on the other hand, is often unknown. A current density in the order of 50 $A.m^{-2}$ is a moderate current for a lead-acid cell. The second definition is as a time to full discharge given the discharge capacity. For example the 5 hour rate for a 100 Ampere hour capacity defines the constant current required for a 100 Ampere hour discharge in 5 hours. That is, 100/5 or 20 Amperes. This is a common definition used in the battery industry. The 5 hour rate is a moderate current for a lead-acid cell.

discharge and charge. The discharge and charge rates were 3 and 1 Amperes respectively and the plate capacity to 1.8 volts was 17.1 Ampere hour. The discharge was therefore at approximately the 6 hour rate. They found that the x-ray analysis and differential thermal analysis showed no variation in crystal lattice structure. Some variation would be expected with a solid state mechanism. On the other hand, their optical observations were consistent with a dissolution-precipitation mechanism.

It should also be mentioned that there is some evidence for a solid-state mechanism. For example Dawson *et al* (1978) conducted experiments with both disc, wire and pasted plates using constant potential steps and other methods. They confirmed a dissolution-precipitation mechanism in the charge and discharge direction. In addition they took an increasing current transient (i vs t^2), observed at large discharge potential steps, as evidence of a two dimensional progressive nucleation and growth. This type of growth would be expected with solid-state electrocrystallisation of $PbSO_4$.

In general however, the few conditions for which the solid-state mechanism has been observed are not the same as those normally experienced in the lead-acid cell. In contrast, the dissolution-precipitation mechanism has been confirmed using a variety of techniques in situations similar to those for the lead-acid cell.

Pavlov (1984) summarised the dissolution-precipitation mechanism in the charge direction as follows.

Dissolution of a $PbSO_4$ crystal
with the formation of Pb^{2+} ions →
diffusion of Pb^{2+} ions (most often on
the surface of the $PbSO_4$ crystal) →
oxidation of Pb^{2+} upon the PbO_2 surface →
deposition of PbO_2.

A corresponding dissolution-precipitation sequence can also be written for the discharge direction.

3.1.2 Conclusions Regarding the Charge and Discharge Mechanism.

The dissolution-precipitation mechanism identified above suggests that at least three factors should be considered in a comprehensive description of the electrode. These are listed below.

i) The mechanical structure of the AM. This defines the system in which the Pb^{2+} ions and acid components move.

ii) The electrochemical reaction process. This (during charge) is the oxidation of Pb^{2+} at the PbO_2 surface (PbO_2/solution interface). It defines the current/ overpotential characteristic of the interface.

iii) The transport processes in solution. These determine the movement of charge (current) in the solution. In addition, they define the movement of mass and therefore the concentration of the solution species. These, in turn, affect such things as the solution resistance and the electrochemical reaction rate.

The sections 3.3 to 3.4 discuss these factors in detail.

3.2 THE MECHANICAL STRUCTURE OF THE AM.

3.2.1 A Description of the Mechanical Structure of the AM.

Some aspects of the mechanical structure have already been described in section 2.3.1. In particular, changes in structure with cycling were mentioned. The existence of a brain coral structure was associated with high cell capacity. The change of this structure into a uniform crystalline structure marked cell failure. It follows that short term (one-cycle) cell performance is largely dependent on the brain coral structure in which the discharge/charge reaction occurs. The uniform crystalline structure also plays a part since it constitutes a non-reactive porous barrier that restricts the transport of solution species. As this work focuses on the one-cycle cell performance, the brain coral structure is of primary concern.

The AM structure of fully charged and fully discharged SLI plates has recently been examined by Pavlov and Bashtavelova (1984,1986). Plates prepared from several different pastes were examined. Discharge was at the 20 hour rate. The authors performed pore surface area measurements, pore volume distribution measurements and SEM studies to characterise the structure. Surface area was determined using BET † gas adsorption techniques. Pore volume distribution was determined using mercury porosimetry equipment. Samples for SEM study were taken from the inner parts of the plates. Their results for pore volume and surface area distribution, for one plate, are given in figure 3.1. Other plates gave similar results.

† The BET method is named using the initials of the authors Brunauer, Emmett and Teller who developed the theory. The theory and application of this method is reviewed in Flood (1967)

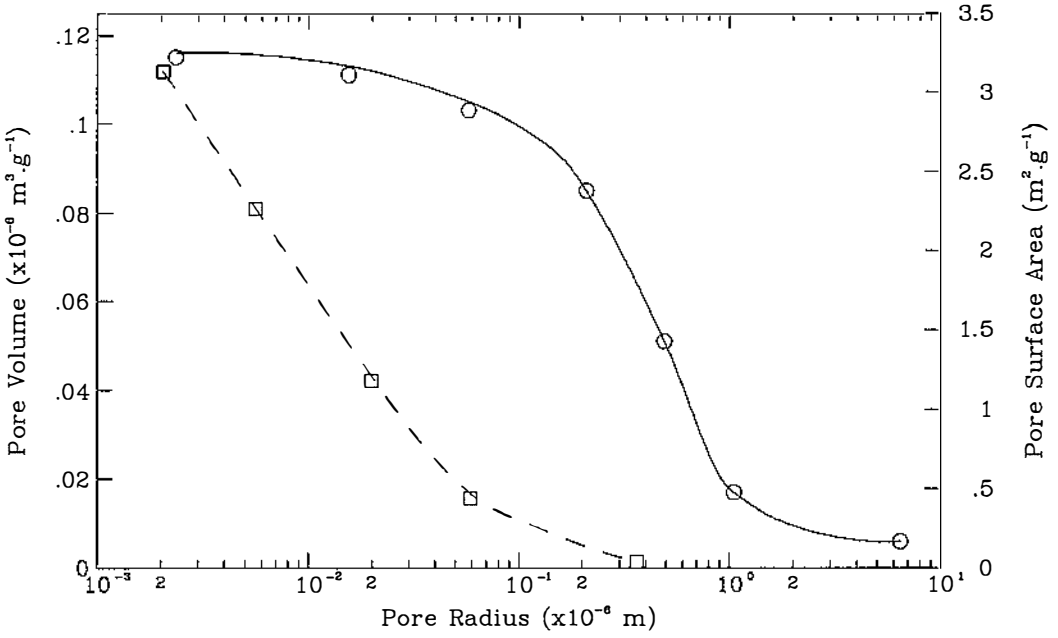

Solid: accumulative pore volume $x10^{-6}$ $m^3.g^{-1}$.
Dash: accumulative pore surface area $m^2.g^{-1}$.

Redrawn from Pavlov and Bashtavelova (1986).

Figure 3.1: Pore Volume and Surface Area Distribution.

It can be seen that the large pores (say greater than $0.2x10^{-6}$ m) account for a large proportion of the total pore volume, but only a small proportion of the total pore surface. Conversely, the small pores (less than $0.2x10^{-6}$ m) account for a small proportion of the total pore volume, but a large proportion of the total pore area. This led the authors to suggest two levels of structure: a microstructure with fine pores providing a large surface area and a macrostructure with larger pores providing electrolyte transport passages. They argue that both levels of structure are necessary for effective electrode operation. Chang (1984) in a similar study gives comparable results and also proposes a two level structure.

The volume changes between the charged and discharged conditions were found to be in good agreement with that calculated from the difference in molar volume of the PbO_2 and $PbSO_4$ and the amount of electricity passed.

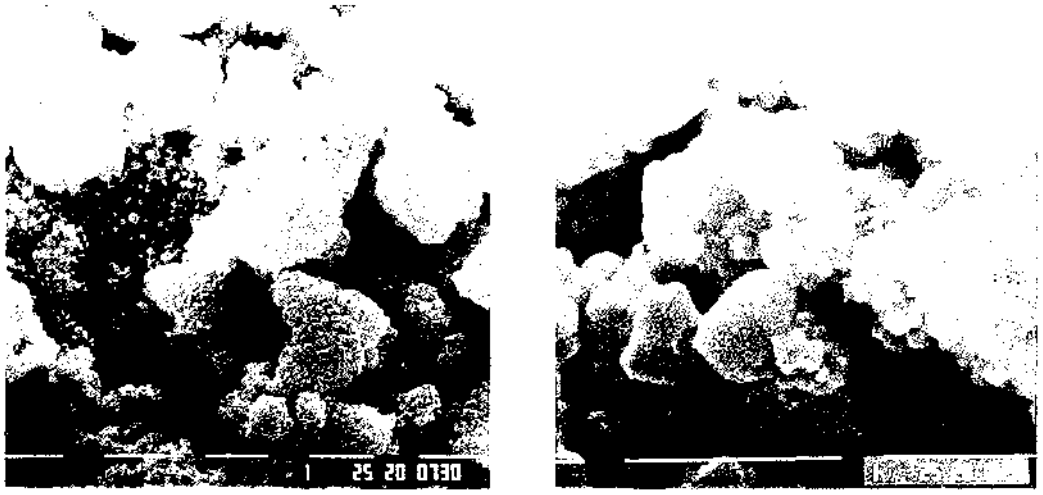

Macrostructure Microstructure

White lines $1x10^{-6}$ m. AM from tribasic lead sulphate paste.
Reproduced from Pavlov and Bashtavelova (1986).

Figure 3.2: Micrographs of Positive Active Mass.

The SEM studies show the physical arrangement of the structure. The micrographs for the same plate as used for figure 3.1 are given in figure 3.2. It can be seen that the AM is arranged as a skeleton of interconnected agglomerates surrounded by macropores. The agglomerates themselves are a microporous mass made up of small rock-like crystallites. The micrographs give a three dimensional picture of the brain coral structure mentioned earlier. Pavlov and Bashtavelova (1984,1986) describe this as an agglomerate structure.

Ekdunge and Simonsson (1985) have performed charge and discharge experiments on commercial positive electrodes and complete cells. The electrodes were cycled in a solution of excess 5000 $mol.m^{-3}$ H_2SO_4. The cells were made up with seven plates and both wide and standard separators. Various charge and discharge rates in the range 30 to 300 $A.m^{-2}$ were used. Ekdunge and Simonsson (1985) performed pore surface area measurements, pore volume distribution

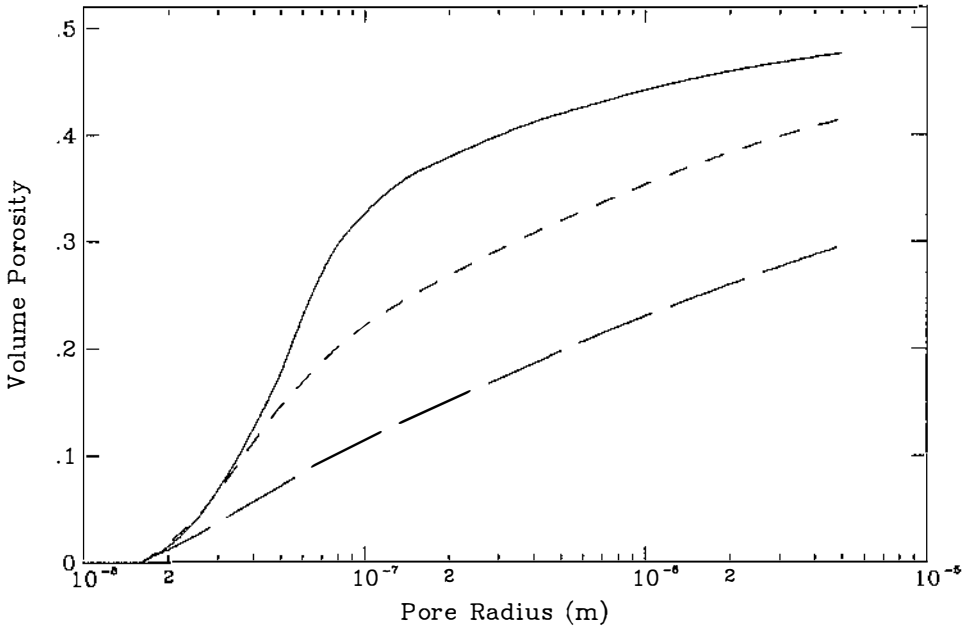

Solid: volume porosity at 100% charge.
Small dash: volume porosity at 50% charge.
Large dash: volume porosity at 0% charge.

Redrawn from Ekdunge and Simonsson (1985).

Figure 3.3: Pore Volume Distribution and Charge State.

measurements and made SEM observations in similar fashion to Pavlov and Bashtavelova (1984). They reported the pore volume distribution (as porosity) for 0, 50 and 100% of full charge and surface area for 0, 20, 50 and 100% of full charge. Their results for pore volume distribution are given in figure 3.3. It can be seen that the volume changes are mainly in the pores of small size (the micropores). Their results for surface area are given in figure 3.4. The surface area is not only for the PbO_2 surface but includes the surface of any $PbSO_4$ crystals present. It can be seen there is a rapid rise in surface area at the beginning of charge.

From SEM observations Ekdunge and Simonsson (1985) found larger (and consequently fewer) $PbSO_4$ crystals formed at low rates of discharge compared to those formed at high rates. This is consistent with earlier observations of

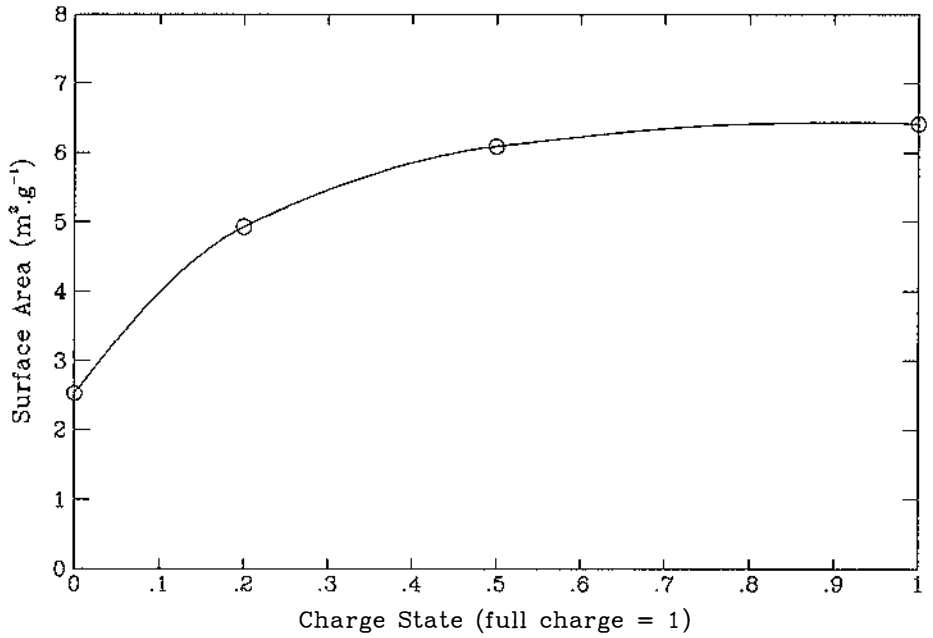

Experimental AM surface area ($PbSO_4$+PbO_2) $m^2.g^{-1}$.
Redrawn from Ekdunge and Simonsson (1985).

Figure 3.4: Experimental Surface Area and Charge State.

Wales and Simon (1981). They also found the size of the $PbSO_4$ crystals depended on the volume in which they formed. At the surface and in large voids, large closely packed crystals could be seen. In the microporous interior the $PbSO_4$ was randomly distributed as small crystallites.

The work outlined above has described the AM at various charge states. At this point the way in which the structure changes during charge and discharge will be considered.

It has already been pointed out that the discharge/charge reaction proceeds through a dissolution-precipitation mechanism. Further it was seen that crystals grow (at least initially) as three dimensional structures at various sites on the surface of the dissolving material.

In their optical studies Simon *et al* (1970) made several additional observations. During deep discharge,

$PbSO_4$ crystals were seen to merge and to completely encapsulate the PbO_2. Void areas were also present at all times in the structure. During the initial stage of charge they found PbO_2 lobes developed within the encapsulating $PbSO_4$. This was taken as evidence that the PbO_2 was part of an electrically conducting framework which was supplied with acid through the $PbSO_4$ layer. That is, the encapsulating $PbSO_4$ did not form an integral electrical or acid solution insulating layer on the PbO_2. As the charge continued PbO_2 appeared at the $PbSO_4$ surface and grew on it until the $PbSO_4$ was completely consumed. The density of the $PbSO_4$ layer was dependent on the state of charge. These observations were confirmed in later work employing a SEM (Simon *et al* (1975), Simon and Caulder (1975)).

Ekdunge and Simonsson (1985) also observed changes in the AM consistent with that described by Simon and co-workers. However, in many cases the growth of the PbO_2 during charge could not be related to the macrostructure of the underlying $PbSO_4$ with any certainty.

3.2.2 Conclusions Regarding the AM Mechanical Structure.

i) The AM involves different levels of structure. The microstructure provides a large reaction surface area while the macrostructure provides solution transport paths.

ii) During discharge, $PbSO_4$ forms primarily in the micropores of the AM.

iii) At all but the fully charged state, the PbO_2 surface area is not known with any certainty because of the additional $PbSO_4$ surface area. The total experimental surface area rapidly increases at the beginning of charge.

iv) The solid phase PbO_2 is at all times part of a conducting network. That is, the surrounding $PbSO_4$ does not electrically isolate the PbO_2.

v) The solid phase $PbSO_4$ forms a porous structure restricting the supply of acid to the PbO_2/solution interface, but not totally preventing such a supply. That is, the $PbSO_4$ does not form an impervious layer on the PbO_2 structure (in contrast to what would be expected from a solid state mechanism).

vi) The reaction proceeds where the supply of Pb^{2+} ions is controlled by a dissolution-precipitation equilibrium reaction of nearby $PbSO_4$. This is consistent with the size and number of $PbSO_4$ crystals that form for various discharge rates and the growth of PbO_2 on the surface of $PbSO_4$ during charge.

3.3 THE ELECTROCHEMICAL REACTION.

The electrochemical reaction occurs in an extremely thin region at the solid PbO_2/solution interface. This section is concerned with setting out an adequate description of the electrical characteristics of this region for the purpose of describing the overall electrode behaviour.

The PbO_2/solution interface forms a system at which two electrochemical reactions occur. The main reaction is the charge/discharge reaction involving PbO_2 and the Pb^{2+} ion. The second reaction is the oxygen evolution reaction where oxygen gas is produced from water in the electrolyte. The second reaction will not be dealt with here but is discussed further in the context of cell gassing in section 3.5.

3.3.1 The Equilibrium Potential.

The potential at the solid phase of the interface is the sum of the equilibrium potential and the current induced overpotential. That is,

$$E = E_e + E_\eta \qquad (3.2)$$

where

E (v) is the total potential at the solid phase,
E_e (v) is the interface equilibrium potential and
E_η (v) is the interface overpotential.

Both E and E_e are referred to some arbitrary electrode system (for example the standard hydrogen electrode).

The discharge/charge mechanism of the AM has already been given. It consisted of dissolution, diffusion, electrochemical reaction and precipitation steps. Writing the equation for the overall electrochemical reaction step gives

$$PbO_2(s) + 4H^+ + 2e^- = Pb^{2+} + 2H_2O. \qquad (3.3)$$

The Nernst equation for this reaction defines the equilibrium potential. The general Nernst equation (see Bockris and Reddy (1977) for example) is

$$E_e = E_0 + \frac{nF}{RT} \ln \frac{\text{activity of oxidised species}}{\text{activity of reduced species}} \qquad (3.4)$$

where

E_0 (v) is the standard electrode potential,
n is the number of electrons involved in the reaction,
F (A.s.mol^{-1}) is the Faraday constant,
R (v.A.s.K.mol^{-1}) is the gas constant and
T (K) is absolute temperature.

For the reaction of equation 3.3 this gives

$$E_e = 1.455 - 0.0128\ln[a_{Pb2+}] + 0.0514\ln[a_{H+}]. \qquad (3.5)$$

where

a_{Pb2+} is the activity of Pb^{2+},
a_{H+} is the activity of H^+ and
E_0 is taken as 1.455 volts (Pavlov (1984)).

The activity of water and solid PbO_2 are taken as unity.

A comparable equation could be written taking equation 3.1 as the electrode reaction. On evaluation of the activity of components this would give the same result as equation 3.5, provided the Pb^{2+} activity at the interface is determined by the dissolution-precipitation equilibrium reaction of $PbSO_4$. This will only be accurate where PbO_2 and $PbSO_4$ are close enough together to minimise the effects of Pb^{2+} concentration gradients.

3.3.2 The Current/Low Overpotential Characteristic.

Defining the current/overpotential characteristic of the interface is more difficult. It depends on the net effect of the processes occurring within the interface region. These can include electrochemical charge transfer reactions, chemical reactions, or some sequence of these. In addition the situation can be compounded by adsorption of species on the reacting surface and surface masking by components. All of these processes have been shown to occur to some extent at the PbO_2/solution interface (see Dasoyan and Aguf (1979) for example).

Hampson *et al* (1967,1968,1969) studied the PbO_2 electrode in perchlorate electrolytes. The perchlorate electrolyte was used in place of sulphuric acid to eliminate surface masking due to the formation of solid $PbSO_4$ and to allow the independent variation of H^+ and Pb^{2+} activities.

At low overpotentials (±10mv) Hampson *et al* (1967) found evidence of a single two electron charge transfer

step. The voltage/current relationship for this process is given by

$$i = i_0[\ e^{-\alpha nFE_\eta/RT} - e^{(1-\alpha)nFE_\eta/RT}\ ] \qquad (3.6)$$

where

i_0 ($A.m^{-2}$) is the exchange current density and

α is the charge transfer coefficient.

Equation 3.6 is the common form of the Butler-Volmer equation (Bockris and Reddy (1977)).

At low overpotentials the exponential terms in equation 3.6 can be approximated by the first two terms of the exponential series expansion. When differentiated this approximate form gives

$$dE_\eta/di = -RT/nFi_0. \qquad (3.7)$$

dE_η/di is the gradient of the overpotential/current curve at zero overpotential and can be obtained experimentally. This is one approach used to determine i_0. The right hand side of 3.7 is sometimes referred to as the charge transfer resistance since it has units of ohms and is approximately linear for small changes in overpotential.

In general the exchange current density is dependent on the activity of the species involved in the charge transfer step. This dependency can be written in analogous fashion to rate constants for chemical reactions. That is,

$$i_0 = nFk \prod a_i^{\gamma i} \qquad (3.8)$$

where

k is the homogeneous rate constant,

a_i is the activity of the species involved and

γ_i is the reaction order of these species.

In the case of electrochemical reactions, the reaction orders also relate to the charge transfer coefficient. The reaction orders can be estimated from the gradient of plots

of log i_0 against a_i. For reaction 3.1 Hampson *et al* (1967) has given the exchange current as

$$i_0 = nFk\ (c_{H+})^{4(1-\alpha)}\ (c_{Pb2+})^{\alpha} \qquad (3.9)$$

Here activities have been replaced by concentrations. Equation 3.9 shows that provided the homogeneous rate constant is known, the exchange current density can be calculated for any concentration of H^+ and Pb^{2+}.

Hampson *et al* (1967) evaluated i_0 using equation 3.7. Further, they evaluated the charge transfer coefficient by estimating the reaction orders for the exchange current density and applying equation 3.9. Both i_0 and α were also evaluated by directly fitting equation 3.6 to the experimental data. Their results indicate hydrogen adsorption at the interface surface. That is, the value of c_{H+} required in equation 3.9 needed to be considerably higher than the bulk value in the electrolyte solution to give the same results for α as obtained by directly fitting equation 3.6.

3.3.3 The Current/High Overpotential Characteristic.

At high overpotentials (up to ± 300 mv) Hampson *et al* (1968) found the reaction proceeded as two consecutive single electron charge transfer steps. This can be represented by

$$Ox + e = X \quad \text{(first step)} \qquad (3.10a)$$

and

$$X + e = Red \quad \text{(second step)} \qquad (3.10b)$$

where "Ox" is the oxidised species, "Red" is the reduced species and "X" is the intermediate species.

In the following formulations parameters associated with the first and second charge transfer steps will be denoted by subscripts 1 and 2 respectively. An equation of the form of equation 3.6 can be written for each of these steps. That is,

$$i/2 = i_{01} \left[e^{-\alpha_1 FE_\eta/RT} - (a_X/a_{X0}) e^{(1-\alpha_1)FE_\eta/RT} \right] \quad (3.11a)$$

and

$$i/2 = i_{02} \left[(a_X/a_{X0}) e^{-\alpha_2 FE_\eta/RT} - e^{(1-\alpha_2)FE_\eta/RT} \right]. \quad (3.11b)$$

Here each step is assumed to contribute half of the total current and only the activity of the transient intermediate species X is allowed to vary (from a_{X0}, for which the exchange currents are defined, to a_X).

The individual exchange current densities in this case can be defined as

$$i_{01} = nFk_1 (a_{Ox})^{1-\alpha_1} (a_{X0})^{\alpha_1} \quad (3.12a)$$

and

$$i_{02} = nFk_2 (a_{X0})^{1-\alpha_2} (a_{Red})^{\alpha_2} \quad (3.12b)$$

The characteristic of the combined steps is found by eliminating the term a_X/a_{X0} from 3.11. This gives

$$i = 2 \frac{e^{-(\alpha_1+\alpha_2)FE_\eta/RT} - e^{(2-\alpha_1-\alpha_2)FE_\eta/RT}}{(1/i_{02}) e^{(1-\alpha_1)FE_\eta/RT} + (1/i_{01}) e^{-\alpha_2 FE_\eta/RT}} \quad (3.13)$$

(Hurd (1962) and Vetter (1967) give a detailed treatment).

Equation 3.13 can be simplified if one of the individual steps has a comparatively slow homogeneous reaction rate (or small exchange current density) and therefore is the rate determining step (the slowest step that limits the overall rate of the complete sequence). In the case where the first charge transfer step (equation 3.10a) is assumed to be the rate determining step, this gives

$$i = 2i_{01} \left[e^{-\alpha_1 FE_\eta/RT} - e^{(2-\alpha_1)FE_\eta/RT} \right]. \quad (3.14a)$$

Similarly, in the case where the second charge transfer step (equation 3.10b) is assumed to be the rate determining step, this gives

$$i = 2i_{02} \left[e^{-(1+\alpha_2)FE_\eta/RT} - e^{(1-\alpha_2)FE_\eta/RT} \right]. \quad (3.14b)$$

Further simplifications can be made for high overpotentials since one or other of the exponential terms will be dominant. Equation 3.14a becomes

$$i = 2i_{01}\, e^{-\alpha_1 F E_\eta / RT} \qquad (3.15a)$$

and

$$i = -2i_{01}\, e^{(2-\alpha_1) F E_\eta / RT} \qquad (3.16a)$$

for high cathodic and anodic overpotential respectively. Equation 3.14b becomes

$$i = 2i_{02}\, e^{-(1+\alpha_2) F E_\eta / RT} \qquad (3.15b)$$

and

$$i = -2i_{02}\, e^{(1-\alpha_2) F E_\eta / RT} \qquad (3.16b)$$

for high cathodic and anodic overpotential respectively. These exponential current/overpotential relationships are often referred to as Tafel relationships.† The intercepts and gradients of plots of the logarithm of i versus E_η (Tafel plots) enable the exchange current density and charge transfer coefficient to be estimated.

Hampson *et al* (1968) found numerically different exchange current densities for the cathodic and anodic plots. This was taken as evidence of a different rate determining step for the cathodic and anodic reaction directions. Further, from the gradients of cathodic and anodic plots, they determined that the first charge transfer (equation 3.10a) was the rate determining step for the cathodic direction and the second charge transfer (equation 3.10b) was the rate determining step for the anodic direction. This means that equation 3.15a applies for high cathodic overpotentials and equation 3.16b applies for high anodic overpotentials.

Hampson *et al* (1968) went on to propose a particular reaction sequence and give numerical values for i_{01}, i_{02}, α_1 and α_2 for various H^+ and Pb^{2+} ion concentrations. They found the reaction order for Pb^{2+} was not constant but reduced with reducing Pb^{2+} concentration and the reaction order for H^+ was lower than expected, possibly due to hydrogen adsorption. The parameter values determined by Hampson *et al* (1968) are summarised in table 3.1.

† An empirical formulation of this form was first published by Tafel in 1905.

Table 3.1: Experimental Current/Overpotential Parameters.

Cathodic (discharge) case.	
Exchange current reaction order:	$2i_{01}=k_1 Fc_{H+}^{1.5}$
Charge transfer coefficient:	$\alpha_1=0.90$ *
Exchange current:	2.50 $A.m^{-2}$ * †
Anodic (charge) case.	
Exchange current reaction order:	$2i_{02}=k_2 Fc_{Pb2+}^{1} c_{H+}^{-0.4}$
Charge transfer coefficient:	$(1-\alpha_2)=0.88$ *
Exchange current:	2.50 $A.m^{-2}$ * †

From Hampson et al (1968).
* for $c_{H+}=3000$ $mol.m^{-2}$, $c_{Pb2+}=45$ $mol.m^{-2}$.
† for relative comparison only. Absolute value uncertain.

Later workers generally accept the ideas of Hampson *et al* (1967,1968) as giving a qualitative description of the electrochemical processes at the PbO_2/solution interface (for example Bode (1977), Ekdunge and Simonsson (1985)). Unfortunately, this work cannot be applied directly to give a quantitative description of the interface. Some reasons for this are listed below.

i) The uncertain surface area and therefore uncertain current density of the electrode.

ii) The uncertain reaction orders at the very low Pb^{2+} ion concentrations in the lead-acid cell. These are typically a factor 0.001 lower than those used in the work described above.

iii) The effect of the sulphate ion. Several workers have reported the presence of adsorbed sulphate species at the interface (for example Carr *et al*

(1970)). These species are likely to affect the exchange reaction.

Two other works which give complementary quantitative data for the forms indicated by Hampson *et al* (1967,1968) are considered below.

Simonsson (1973) performed experiments on electrodes formed by anodic oxidation of smooth lead sheet and electrodeposition of β-PbO_2 on polished platinum. These electrodes were discharged at several high overpotentials in 5000 $mol.m^{-3}$ H_2SO_4. The Tafel plots of the initial current/overpotential results gave the same slope (transfer coefficient) for both electrodes, but different zero overpotential intercepts (current exchange densities). The difference in exchange current density was due to a rough surface on the oxidised lead sheet. The cathodic exchange current density obtained for the electrodeposition electrode was about 0.1 $A.m^{-2}$. The Tafel plots involved in this case are given in figure 3.5.

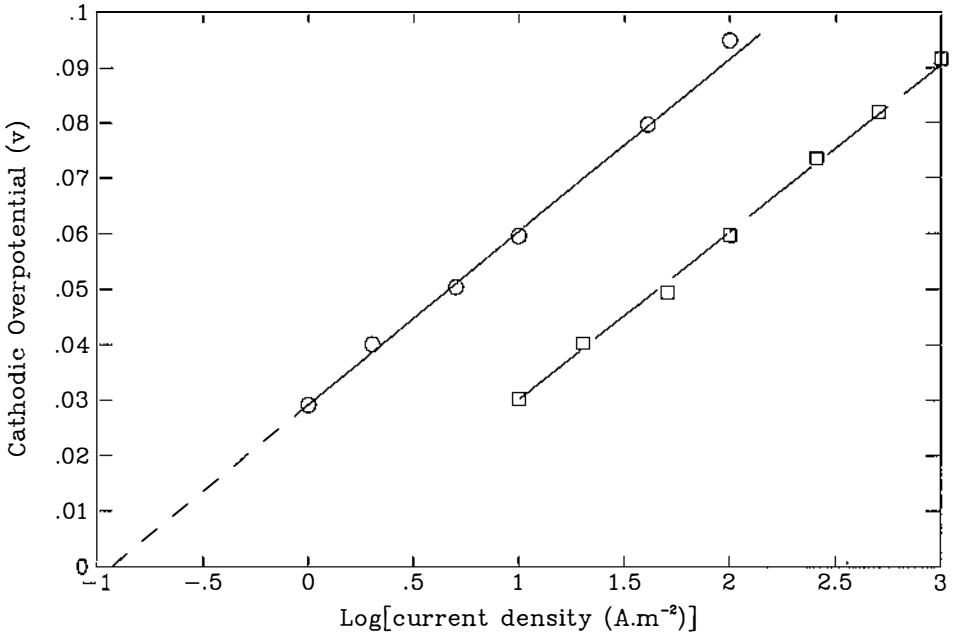

Solid: $\beta-PbO_2$ on polished platinum.
Small dash: extrapolation for exchange current density (at zero overpotential).
Large dash: oxidised lead sheet.

Redrawn from Simonsson (1973).

Figure 3.5: Cathodic Tafel Plots for Two Lead Dioxide Electrodes.

Ekdunge and Simonsson (1985) have made measurements on conventional and flow-through PbO_2 electrodes to determine the concentration dependence of the anodic interface reaction. The flow-through electrode was used to eliminate concentration gradients within the electrode interior. For 5000 $mol.m^{-3}$ H_2SO_4, an exchange current density of $47x10^{-3}$ $A.m^{-2}$ was obtained (calculated from the electrode surface current density assuming the ratio of true interface surface to electrode surface was 10^4).

3.3.4 Conclusions regarding the electrochemical reaction.

i) The equilibrium potential of the reaction is known. This can be written for Pb^{2+} and H^+ species based on the reaction given in equation 3.3.

ii) The general form and approximations for the current/overpotential characteristic are known.

iii) The low overpotential reaction involves a single two electron charge transfer step.

iv) At the medium to high overpotentials the reaction proceeds as two consecutive single electron charge transfer steps.

v) The rate determining steps for anodic and cathodic reactions are different. Consequently the exchange current densities for the anodic and cathodic reactions are different.

vi) Quantitative kinetic data (numeric values for α and i_0) are not known with any certainty.

3.4 TRANSPORT IN SOLUTION.

Matters concerning the transport of mass and charge are considered here. For simplicity the treatment will be limited to the one dimensional case (the x-dimension).

Two common assumptions used in analysing the lead-acid cell will be adopted at the outset.

Firstly, it will be assumed that the theory of dilute electrolyte (as presented by Bockris and Reddy (1977) for example) applies to the transport of mass in this case. Formulations based on this theory are used by many workers studying the lead-acid cell (for example Simonsson (1973), Turner and Moseley (1983), Kappus and Bohmann (1983) and Atlung and Fastrup (1984)). It must be noted however, that the theory of dilute electrolytes is an approximation and more general theories are available (for example Miller (1966), Micka (1968), Newman *et al* (1965), Newman and Tiedemann (1975)).

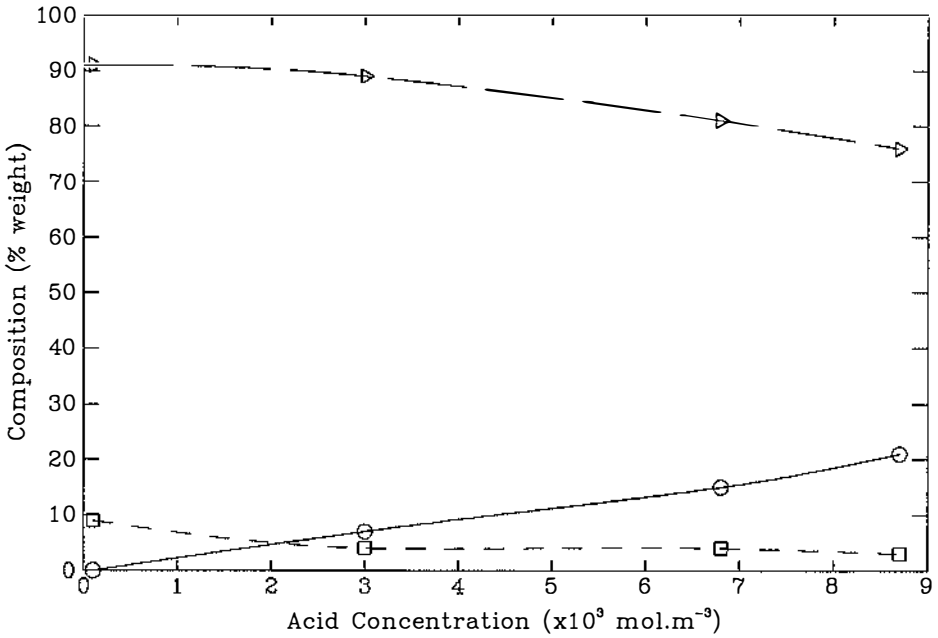

Solid: undissociated acid % weight.
Small dash: sulphate ion % weight.
Large dash: bisulphate ion % weight.
Typical concentration range in lead–acid cell 2 to 6 x10^3 mol.m^{-3}.
Based on data from Bode (1977).

Figure 3.6: Dissociation of Sulphuric Acid.

Secondly, it will be assumed that the water/sulphuric acid solution forms a binary electrolyte where the charge carrying species are H^+ and HSO_4^- ions. The validity of the binary electrolyte assumption can be judged from figure 3.6 which gives the dissociation of sulphuric acid according to Bode (1977).

Solution components that will be considered in detail in the following discussion are the H^+ ion, the HSO_4^- ion and the electrically neutral H^+/HSO_4^- ion pair representing a "molecule" of acid. Parameters associated with these components will be denoted by the subscripts +, - and ± respectively.

3.4.1 Mass Flux Density.

The independent mass flux density of species "i" in a dilute electrolyte can be written as

$$J_i = -D_i \frac{\partial c_i}{\partial x} - c_i l_i \frac{z_i}{|z_i|} \frac{\partial \phi}{\partial x} + c_i \upsilon \qquad (3.17)$$

where

J_i ($mol.m^{-2}.s^{-1}$) is the flux density of the species,
D_i ($m^2.s^{-1}$) is the diffusion coefficient of the species,
c_i ($mol.m^{-3}$) is the concentration of the species,
l_i ($m.s^{-1}.v^{-1}$) is the ionic mobility of the species,
z_i is the charge number of the species,
$\partial\phi/\partial x$ ($v.m^{-1}$) is the potential gradient surrounding the species and
υ ($m.s^{-1}$) is the solution velocity.

The three terms on the right hand side represent diffusion, conduction and convection processes. Writing equation 3.17 for each of the three species of interest here gives

$$J_+ = - D_+ \frac{\partial c_+}{\partial x} - c_+ l_+ \frac{\partial \phi}{\partial x} + c_+ \upsilon, \qquad (3.18a)$$

$$J_- = - D_- \frac{\partial c_-}{\partial x} + c_- l_- \frac{\partial \phi}{\partial x} + c_- \upsilon \qquad (3.18b)$$

and

$$J_\pm = - D_\pm \frac{\partial c_\pm}{\partial x} + c_\pm \upsilon. \qquad (3.18c)$$

The migration terms for the H^+ and HSO_4^- species have opposite signs because of their opposite ionic charge. The migration term for the acid does not appear since this species is regarded as electrically neutral.

3.4.2 Electroneutrality.

The species in the solution are also constrained by the requirement for electroneutrality. This dictates that the net charge in any incremental volume of solution must be zero. In this case, where the only charged species are the singularly charged H^+ and HSO_4^- ions, this amounts to

$$c_+ = c_- = c_\pm \qquad (3.19)$$

A second effect is that the two flux densities J_+ and J_- are not independent but coupled together to ensure the condition of electroneutrality is maintained. In the case where there is no solution current flow the two flux densities are the same and equal to the acid flux density. That is,

$$J_+ = J_- = J_\pm \text{ (when no solution current).} \qquad (3.20)$$

This identity allows the acid diffusion coefficient to be written in terms of the individual ion parameters (see Jordan (1979) for example). The procedure for this is given below.

With no solution current, the potential gradient affecting the two charged species is the driving force ensuring the coupling between these species. This potential

gradient can be found by combining equations 3.18a and 3.18b using equation 3.20 which gives

$$\frac{\partial \phi_c}{\partial x} = - \frac{D_+ - D_-}{c_\pm (l_+ + l_-)} \frac{\partial c_\pm}{\partial x} \qquad (3.21)$$

where $\partial \phi_c / \partial x$ ($v.m^{-1}$) is the coupling potential gradient.

Substituting equation 3.21 back into either equation 3.18a or 3.18b and again using equation 3.20 gives

$$J_\pm = - \frac{2D_+D_-}{D_+ + D_-} \frac{\partial c_\pm}{\partial x} + c_\pm v. \qquad (3.22)$$

Here use has been made of the Nernst-Einstein relationship to relate the ionic mobilities to the diffusion coefficients. This relationship states

$$D_i = \frac{RT}{|z_i| F} l_i. \qquad (3.23)$$

Equating the coefficient of $\partial c_\pm / \partial x$ in equation 3.18c with that in equation 3.22 gives the required expression for the acid diffusion coefficient. That is,

$$D_\pm = - \frac{2D_+D_-}{D_+ + D_-} \qquad (3.24)$$

which is commonly called the binary diffusion coefficient.

3.4.3 Charge Flux Density.

The charge flux density (current density) is defined by summing the mass fluxes taking into account their charge. That is,

$$i_2 = F \Sigma z_i J_i \qquad (3.25)$$

where i_2 ($A.m^{-2}$) is the current density in the solution.

Substituting equations 3.18a and 3.18b into equation 3.25 and using equation 3.19 gives

$$i_2 = Fc_{\pm}(l_+ + l_-) \frac{\partial \phi}{\partial x} - F(D_+ - D_-) \frac{\partial c_{\pm}}{\partial x} \qquad (3.26)$$

The first term on the right hand side represents the effect of the electrical potential gradient while the second term on the right hand side represents the effect of the chemical potential gradient. Equation 3.26 is often written in the equivalent form

$$i_2 = \kappa \frac{\partial \phi}{\partial x} - F(D_+ - D_-) \frac{\partial c_{\pm}}{\partial x} \qquad (3.27)$$

where $\kappa = Fc_{\pm}(l_+ + l_-)$ $(\Omega^{-1}.m^{-1})$ is the solution conductivity.

The potential gradient in equation 3.27 can be taken as the sum of the potential gradient due to the coupling of the charged species as given by equation 3.21 and the potential gradient due to current flowing in the solution. That is,

$$\frac{\partial \phi}{\partial x} = \frac{\partial \phi_c}{\partial x} + \frac{\partial \phi_s}{\partial x} \qquad (3.28)$$

where $\partial \phi_s / \partial x$ $(v.m^{-1})$ is the potential gradient due to current flowing in the solution.

Combining equations 3.21, 3.26 and 3.28 gives

$$i_2 = \kappa \frac{\partial \phi_s}{\partial x} \qquad (3.29)$$

which is the normal "ohms law" relationship for solution conductivity.

3.4.4 An Alternative Form for Mass Flux Equations.

Equation 3.26 can be used to eliminate the potential terms in equations 3.18a-b. This gives

$$J_+ = -\frac{t_+ i_2}{F} - D_\pm \frac{\partial c_\pm}{\partial x} + c_\pm \upsilon \qquad (3.30a)$$

and

$$J_- = \frac{t_- i_2}{F} - D_\pm \frac{\partial c_\pm}{\partial x} + c_\pm \upsilon \qquad (3.30b)$$

where

$t_+ = l_+(l_+ + l_-)$ is the transference number for H^+ and

$t_- = 1-t_+$ is the transference number for HSO_4^-.

Again the Nernst-Einstein relation (equation 3.23) has been used to relate the ionic mobilities to the diffusion coefficients.

3.4.5 Concentration Changes with Time.

The concentration changes of species "i" with time can be defined by writing the mass balance for an incremental volume. This is often taken as a volume of unit square area and width dx (see Cussler (1984) for examble). Here, however, the cross-sectional area of the incremental volume will be allowed to vary in time and space so that the structural features that were reported in section 3.2 can be explicitly represented in the transport equations. Under these circumstances the mass balance gives

$$\frac{\partial}{\partial t}\left(A\ c_i\right) = \frac{\partial}{\partial x}\left(A\ J_i\right) + P_i \qquad (3.31)$$

where

A (m^2) is the area of the incremental volume normal to the flux direction and

P_i ($mol.m^{-1}.s^{-1}$) is the rate of reaction (production or depletion) of species "i" per unit length normal to the flux direction.

From left to right the terms in equation 3.31 represent accumulation, divergence and the reaction of mass in the incremental volume respectively. Equation 3.31 can be

written for each of the three species of interest here by substituting the relevant expressions for mass flux density (equations 3.30a, 3.30b and 3.18c). Performing these substitutions and making use of equation 3.19 gives

$$\frac{\partial}{\partial t}\left(A\ c_{\pm}\right) = -\frac{\partial}{\partial x}\left(A\left(D_{\pm}\frac{\partial c_{\pm}}{\partial x} - \frac{t_{+}\ i_2}{F} + c_{\pm}v\right)\right) + P_{+}, \quad (3.32a)$$

$$\frac{\partial}{\partial t}\left(A\ c_{\pm}\right) = -\frac{\partial}{\partial x}\left(A\left(D_{\pm}\frac{\partial c_{\pm}}{\partial x} + \frac{t_{-}\ i_2}{F} + c_{\pm}v\right)\right) + P_{-} \quad (3.32b)$$

and

$$\frac{\partial}{\partial t}\left(A\ c_{\pm}\right) = -\frac{\partial}{\partial x}\left(A\left(D_{\pm}\frac{\partial c_{\pm}}{\partial x} + c_{\pm}v\right)\right) + P_{\pm}. \quad (3.32c)$$

Since the left hand side of equations 3.32a-c are equal, their right hand sides can be equated. This gives

$$P_{\pm} = \frac{\partial}{\partial x}\left(A\frac{t_{+}\ i_2}{F}\right) + P_{+} = -\frac{\partial}{\partial x}\left(A\frac{t_{-}\ i_2}{F}\right) + P_{-} \quad (3.33)$$

which is an identity that relates the reaction term of the acid to that for either of the individual ions.

3.4.6 Conclusions Regarding Transport in Solution.

i) The assumption of dilute solution theory and binary electrolyte allows a convenient simplification of the general formulations.

ii) Formulations for mass flux, charge flux and concentration change based on the theory of dilute electrolytes are known.

3.5 GAS EVOLUTION IN THE ELECTRODE AND CELL.

Oxygen gas is evolved at the positive electrode and hydrogen gas is evolved at the negative electrode of a

lead-acid cell. The equilibrium potential for the gassing reaction is closer to zero than that for the main reaction of the positive and negative electrodes (see Pavlov (1984) for example). This causes gas to be evolved and a gradual electrode self discharge during open circuit conditions. The gas evolution rates at open circuit potentials are low. However, at the high potentials near the end of charge, the evolution rates are high. In this discussion it is only the effects of gassing near the end of charge that are of interest. This is because traction cells are frequently charged and therefore subjected to considerable high rate gassing but little accumulative self discharge.

Gassing during charge has several effects including the diversion of current from the main reaction into the gassing reaction, the enhancement of electrolyte mass transport, the increase of electrolyte resistivity and interface surface masking. Each of these effects is discussed briefly below.

3.5.1 Current and the Gas Evolving Reaction.

Sides and Tobias (1980,1985) have performed experimental and theoretical studies of bubble formation on planar electrodes to define the mechanisms involved and the current/potential distributions around individual bubbles. They report considerable disruption of the current distribution and significant fluid motion at the gas evolving surface. Fundamental studies of this type have not been applied to the porous positive electrode of the lead-acid cell.

Experimental current/overpotential relationships for the gas evolution reaction at both the positive and negative electrode of the lead-acid cell are reviewed by Bode (1977) and Pavlov (1984). The net current/overpotential relationships are represented by exponential Tafel forms. However, the parameters involved are not

constant but vary with acid concentration and overpotential. The explanations given for these variations relate to changes in the interface surface structure. Uncertainties are also involved in estimating the surface area of the electrode on which gas is evolved.

Final charging rates for industrial cells show that the current diverted into the gassing reaction is significant. Typically, this is 25 to 50% of the 5 hour discharge rate (see Smith (1980)).

3.5.2 Electrolyte Mass Transport and Gas Evolution.

Mass transport parameters are affected by agitation due to gas bubble movement. Sides and Tobias (1985) and Dees and Tobias (1987) have recently studied this on a microscopic level. They found mass transfer effects at the interface surface were enhanced by bubble coalescence and, to a lesser extent, by bubble detachment. Mass transfer rates increased by more than an order of magnitude with the former effect. Again this type of effect has not been accounted for in the positive electrode of the lead-acid cell.

Apart from effects at the interface, mass transport in other cell parts that supply acid to positive electrode, would also be enhanced by gassing. Rapid changes in acid concentration with the onset of gassing (see Sunu and Burrows (1981)) suggest this effect is significant in the lead-acid cell.

3.5.3 Electrolyte Resistivity and Gas Evolution.

Electrolyte resistivity is increased by the inclusion of non-conducting gas bubbles. This effect has been studied by many authors (see Dukovic and Tobias (1987), Kreysa and Kulps (1981), Vogt (1981), Hine and Murakami (1980) and

Nagy (1976) for example). These studies are generally limited to the effect in the inter-electrode electrolyte of simple electrode systems. The effect of gas evolution on the resistivity of the electrolyte within the porous electrode of the lead-acid cell has not been determined.

3.5.4 Surface Masking and Gas Evolution.

Surface masking due to bubbles attached to the interface would be expected in the electrodes of the lead acid cell. The studies of Sides and Tobias (1980, 1985) and Dukovic and Tobias (1987) contribute to the understanding of the mechanisms involved. The effect of surface masking has not been quantified for the positive electrode in the lead-acid cell.

3.5.5 Conclusions Regarding Gas Evolution.

i) Cell gassing at the end of charge has a significant effect on the positive electrode behaviour by diverting current from the main reaction and enhancing mass transport. Other effects increasing electrolyte resistance and surface masking would also be expected.

ii) Tafel forms for the current/overpotential relationship for the gassing reactions can be used but the parameters are uncertain.

iii) Other gassing effects including mass transport enhancement, increased electrolyte resistivity and surface masking have not been quantified for the positive electrode of the lead-acid cell.

3.6 COMMON MODELS FOR POROUS ELECTRODES.

3.6.1 The Single Pore Model.

With the single pore model the AM is represented by a solid phase containing identical, solution-filled cylindrical pores arranged normal to the electrode surface. In this way it is supposed that the complete electrode can be characterised by analysing a single pore. De Levie (1967) gives a comprehensive review of the single pore model.

Electrically the pore can be represented by the equivalent circuit shown in figure 3.7. Writing the equation for this circuit gives

$$\partial\phi_s/\partial x + i_2 R_s = 0 \qquad (3.34)$$

and

$$\partial i_2/\partial x + \phi_s/Z_s = 0 \qquad (3.35)$$

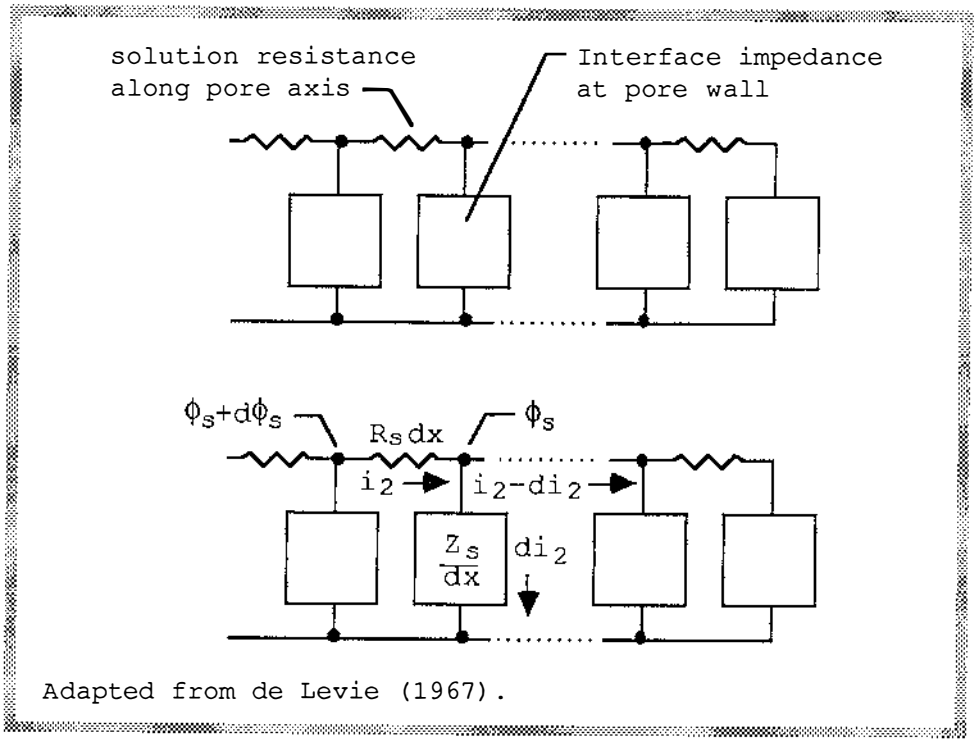

Figure 3.7. The Single Pore Model Equivalent Circuit.

where

ϕ_S (v) is the potential in the solution,

R_S ($\Omega.m^{-1}$) is the solution resistance per unit length and

Z_S ($\Omega.m^{-1}$) is the electrode interface impedance per unit length.

These equations can be combined to eliminate one variable or the other (i_2 or ϕ_S).

Much of the work with this model has been aimed at defining and solving an analytical equation of one variable for a particular form or function of R_S and Z_S.

The single pore model has been applied to the discharge of porous electrodes of storage cells (for example Winsel (1962), Lehning (1972) and Runge (1972)). These early workers, without the advantage of later developments, used simplified formulations in some parts of their models. The contributions of Winsel (1962) and Lehning (1972) will be mentioned below to represent the work.

Winsel (1962) incorporated time deperdent effects through the impedance Z_S which was instantaneously set to infinity when the local discharge reached a certain level. His result showed the discharge proceeded most rapidly near the pore mouth where the current is largest.

Lehning (1972) modelled the positive, negative and inter-electrode electrolyte of the lead-acid cell. He used differential equations for transport along the lines given above, to incorporate the time dependent effects. He calculated impedances on the basis of the concentrations these equations predicted. However, the interface potential was approximated by the equilibrium potential neglecting the interface overpotential. His results showed the acid concentration variations in the electrode for various constant current discharges. From this, cell

voltage and, therefore, capacity were predicted and compared with the known capacity dependence on current.

In recent years the single pore model has lost favour, with most workers preferring the macrohomogeneous model outlined below.

3.6.2 The Macrohomogeneous Model.

The macrohomogeneous model views the porous electrode on a coarse scale where electrode properties can be defined as homogeneous (average) composites of the true non-homogeneous properties. With this view, the structure is a superposition of solid and solution phases and is described by volume average quantities such as porosity and surface area. The volume average quantities disregard specific geometric features of the AM and allow the same set of equations to describe all points in the system. These attributes are seen as desirable and are a major factor in the popularity of the model. Newman and Tiedemann (1975) give a comprehensive review of the macrohomogeneous model.

The macrohomogeneous model has been used with some success to describe the high current discharge of the positive electrode of the lead acid battery (for example Micka and Rousar (1973,1976), Simonsson (1973,1974) and Turner and Moseley (1983)).

The approach of Simonsson will be given here to illustrate the model. Turner and Moseley (1983) followed a similar approach while Micka and Rousar (1973,1976) used more general transport equations but less general interface overpotential relationships.

Starting with transport equations 3.27 and 3.32a, equations for the current and concentration of acid can be written as

$$i_2 = \frac{\varepsilon\kappa}{\varepsilon_0}\left\{\frac{\partial E_e}{\partial c_\pm}\frac{\partial c_\pm}{\partial x} + \frac{\partial E_\eta}{\partial x}\right\} - \frac{\varepsilon F(D_+ - D_-)}{\varepsilon_0}\frac{\partial c_\pm}{\partial x} \qquad (3.36)$$

and

$$\frac{\partial c_\pm}{\partial t} = \frac{(3-2t_+)}{F\varepsilon}\frac{\partial i_2}{\partial x} + \frac{1}{\varepsilon}\frac{\partial}{\partial x}\left\{\frac{\varepsilon D_\pm}{\varepsilon_0}\frac{\partial c_\pm}{\partial x}\right\} + \frac{i_2(V_{mPbSO4} - V_{mPbO2})}{2F\varepsilon}\frac{\partial c_\pm}{\partial x}. \qquad (3.37)$$

In equation 3.36 the current density i_2 is defined for the current flowing through a unit square in a plane parallel to the electrode rather than the true interface area. Also, the diffusion coefficient and conductivity are effective values that take into account the proportion of solid in the elemental volume (by making use of the normalised porosity $\varepsilon/\varepsilon_0$). Lastly, the potential gradient has been replaced by the partial derivative of the local electrode potential (these are equivalent when there is no potential drop in the solid phase). This latter potential is $E=E_e+E_\eta$ which on differentiation gives the result shown.

In equation 3.37 account of the portion of the solid in the elemental volume has again been made (as seen by the appearance of the ε and ε_0 terms). Also, the local discharge rate per unit volume (defined as $\partial i_2/\partial x$) has been introduced. This allows the reaction term to be written as $P_{H+} = (3F/2)\,\partial i_2/\partial x$ in accordance with Faraday's law given the reaction of equation 3.1. In addition, the velocity term has been obtained from a consideration of the volume changes occurring for this reaction (hence the appearance of the molar volumes V_{mPbSO4} and V_{mPbO2} above).

The local discharge rate per unit volume is also given by the interface current/voltage characteristic using the approximation given in section 3.3. That is,

$$\partial i_2/\partial x = S i_0\, e^{-2FE_\eta/RT} \qquad (3.38)$$

where

E_η (v) is the overpotential and

S (m^{-1}) the local surface area per unit volume.

Simonsson (1973) defines two additional equations to embody the structural changes.

$$X = -\frac{1}{q_0}\int \frac{\partial i_2}{\partial x}\,dt \qquad (3.39)$$

and

$$S = S_0\,(1-X/X_{max}) \qquad (3.40)$$

where

X is the normalised local degree of discharge,
q_0 (A.s) is the initial discharge capacity,
S_0 (m^{-1}) is the initial local surface per unit volume
and
X_{max} the maximum material utilisation factor.

The following boundary conditions apply to this set of equations.

At $t=0$, $c_{\pm}=c_0$ and $X=0$ for all x,
at $x=0$, $i_2=0$ for all t and
at $x=L$, $c_{\pm}=c_0$, $i_2=I$ for all t

where

c_0 (mol.m^{-3}) is the initial acid concentration,
$x=0$ (m) defines the centre of the electrode,
$x=L$ (m) defines the outer face of the electrode and
I (A.m^{-2}) is the electrode current density.

Simonsson (1973) solved these equations at incremental time steps using numerical methods. I and t were given as independent variables and distributions for $c_{\pm}$, i_2, X, and E_{η} obtained at each time step. The discharge voltage predictions obtained by Simonsson (1973) are given in figure 3.8. The overpotential results show a reasonable agreement with experimental observations.

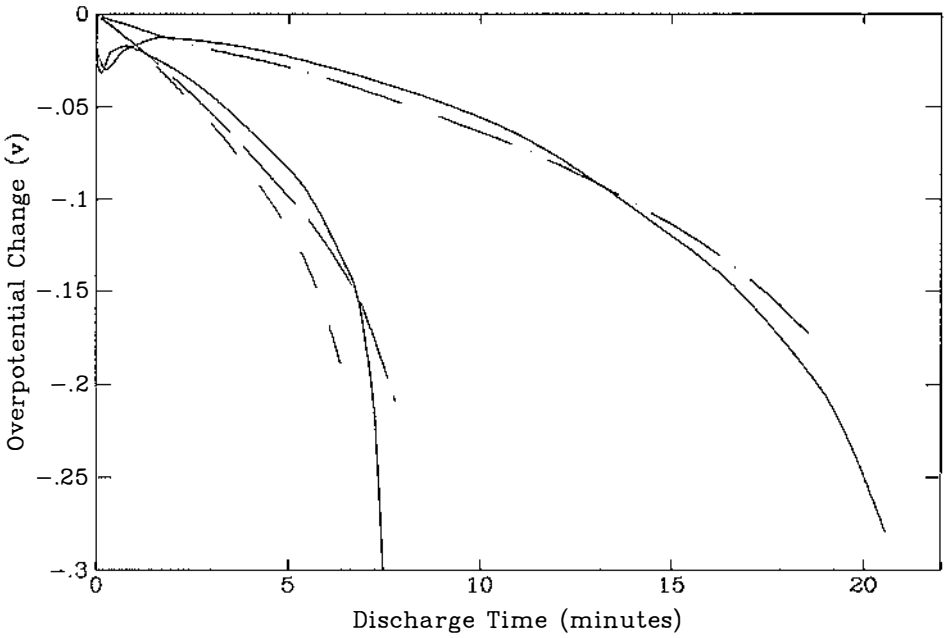

Left hand curves: 1000 A.m^{-2} discharge. Right hand curves: 500 A.m^{-2} discharge.

Solid: experimental results.
Small dash: model results, X_{max}=0.45. Dot dash: model results, X_{max}=0.60.
Large dash: model results, X_{max}=0.60.

Redrawn from Simonsson (1973).

Figure 3.8: Macrohomogeneous Model Discharge Voltage Predictions.

The macrohomogeneous model has been criticised for the somewhat arbitrary formulations for the structural effects (Asher *et al* 1980). In particular, results are sensitive to the factor X_{max}.

Whyatt and Hampson (1979) have found that the macrohomogeneous model does not predict a local discharge distribution consistent with that observed experimentally.

The macrohomogeneous model does not take into account the specific structure of the AM and in particular does not represent the different levels of structure recently said to be of major importance (section 3.2.1).

Finally, the application of the macrohomogeneous model to the charge cycle of the positive electrode does not appear to be reported in the literature.

3.6.3 Other Models of Interest.

a) A model for a general structure.

Kramer and Tomkiewicz (1984) have recently proposed a model which represents a general porous electrode structure by a matrix of solid and solution filled cubes. They give a numerical calculation procedure for solving the system when subjected to alternating current disturbances. This is a relatively simple situation, and takes no account of net changes in structure or redistribution of species in solution. As a consequence, the model in its present form, is not suited to simulating the working cycle of the positive electrode of the lead-acid cell. The model is of interest, however, because it attempts to account for structural variations and levels in porous electrodes. This is in contrast to the uniform structure assumed in the models reviewed above.

b) A model for two levels of structure in the positive electrode of the lead-acid cell.

Bjornbom (1987) has recently proposed a crude model for the positive electrode of the lead-acid cell that allows for the microstructure and macrostructure of the AM. This uses single pore model approximations to define charge current penetration and voltage relationships for the electrode. The model neither gives details of changes in acid and AM distribution within the electrode, nor applies to the practical working cycle. The main interest here is that a compound single pore arrangement has been proposed to represent the porous structure of the positive electrode of the lead-acid cell.

3.6.4 Conclusions Regarding Porous Electrode Models.

i) The single pore model showed promise in predicting electrode behaviour in early work.

ii) The single pore model has been left undeveloped in recent times and more work is required before it can used to accurately predict the discharge and charge behaviour of the positive electrode.

iii) The macrohomogeneous model has been used to predict the voltage behaviour of the positive electrode under constant current discharge. It did not predict such a rapid drop in voltage at the end of the discharge as found in practice.

iv) The macrohomogeneous model has simple approximations for representing the structural changes in the electrode.

v) The macrohomogeneous model has not been applied to the charge of the electrode.

vi) Considerable development remains to be done before the macrohomogeneous model can be used to accurately describe both the charge and discharge behaviour of the positive electrode.

vii) Compound single pore models have been proposed to represent complex porous electrode structures. Considerable development is required before models of this type can be used to accurately describe both the charge and discharge behaviour of the positive electrode.

3.7 VOLTAGE, CURRENT AND AM EXPERIMENTAL DATA.

Experimental work that gives the voltage and current characteristics and the state of the AM for various cell conditions is of interest here. The purpose is to expose

work against which the predictions from a VIAM model can be compared. This work is divided into two groups below.

i) Studies of voltage and current.

ii) Studies of the AM distribution.

Studies using constant current charge and discharge schemes have been selected to facilitate comparison. This is not a significant limitation as these are the most common type of studies in the literature.

3.7.1 Electrode Voltage and Current.

The general forms of the voltage and current characteristics of a lead-acid cell are well known (see Pavlov (1984) and Linden (1984) for example). What is of more interest for this work is the characteristics of the positive plate and the small changes in these characteristics for different conditions.

Sunu and Burrows (1981) have made measurements of potential and acid concentration at different points in a modified five plate electric vehicle cell. Their experiment made use of lead wires in the grid and Luggin capillary probes in the solution for measuring potential. Other tubes were fitted to extract small amounts of acid for concentration (density) measurements. Potential measurements at half plate height and at the cell terminals during constant current discharge and charge (two rates) are shown in figure 3.9. The currents correspond to approximately 107, 125 and 42 $A.m^{-2}$ for the discharge, initial and final charge rates respectively. The relative contribution of various cell components to the total cell polarisation is shown here.

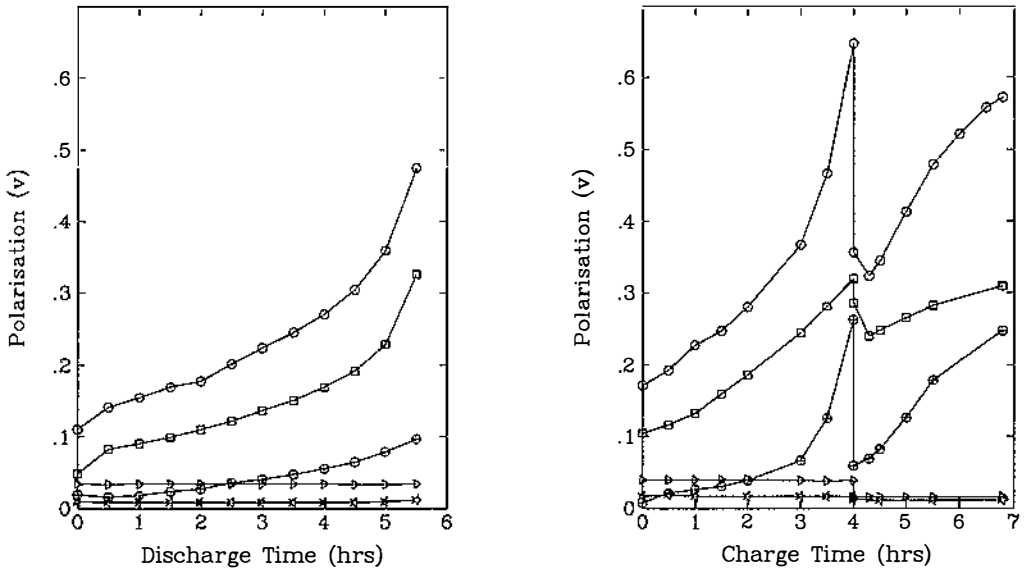

(a) Discharge Polarisation.
Current 107 $A.m^{-2}$ approx.

(b) Charge Polarisation.
Current 125/42 $A.m^{-2}$ approx.

Component key for (a) and (b).
□ : positive electrode.
▷ : terminal and grid.
○ : total.
⊕ : negative electrode.
✡ : separator.

Redrawn from Sunu and Burrows (1981).

Figure 3.9: Experimental Cell Polarisation Components.

It can be seen that during discharge and the initial portion of the charge the positive plate is responsible for most of the overpotential. However, in the final portion of charge, the polarisation of the negative plate rapidly increases as the plate becomes fully charged. These results show the important part the positive plates play in the overall cell characteristic. They also show that other components are significant, particularly the negative plate polarisation near the end of charge.

Ekdunge and Simonsson (1985) performed charge experiments on both commercial positive electrodes and complete cells. The commercial electrodes were of a thickness expected for SLI cells and were examined in a solution of excess 5000 $mol.m^{-3}$ electrolyte. The cells were made up with three positive and four negative plates using standard and wide separator systems.

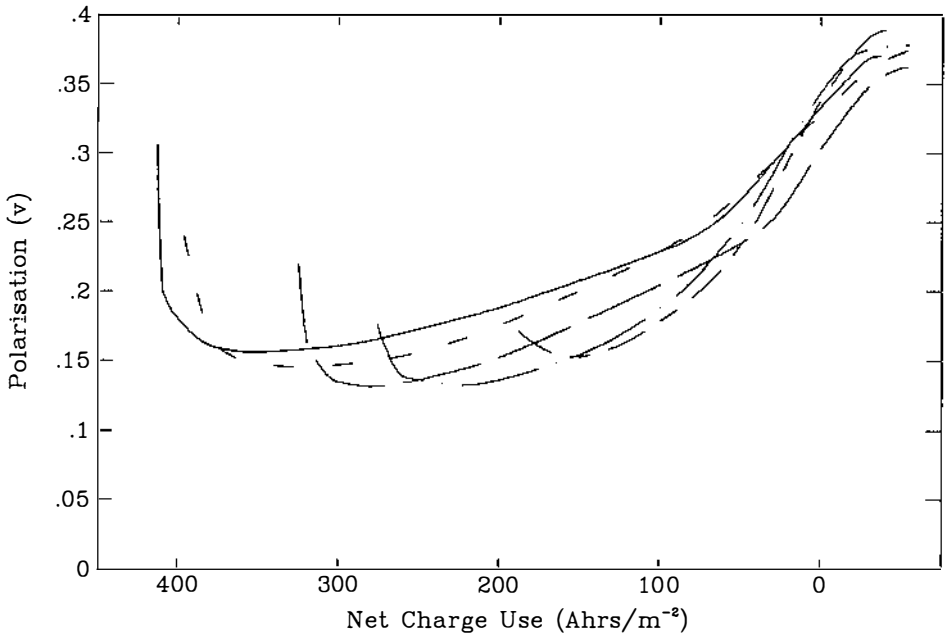

Solid: charge voltage at 200 $A.m^{-2}$ after 30 $A.m^{-2}$ full discharge.
Small dash: charge voltage at 200 $A.m^{-2}$ after 100 $A.m^{-2}$ full discharge.
Large dash: charge voltage at 200 $A.m^{-2}$ after 200 $A.m^{-2}$ full discharge.
Dot dash: charge voltage at 200 $A.m^{-2}$ after 500 $A.m^{-2}$ full discharge.
Mid and small dash: charge voltage at 200 $A.m^{-2}$ after 1000 $A.m^{-2}$ full discharge.
Redrawn from Ekdunge and Simonsson (1985).

Figure 3.10: Experimental Charge Voltage and Discharge Rate.

The positive electrodes were discharged at various rates (30-1000 $A.m^{-2}$) to a potential of 0.9 versus a Hg/Hg_2SO_4 reference electrode. The electrodes were then recharged at a rate of 200 $A.m^{-2}$. Results of these experiments are given in figure 3.10.

It should be pointed out that the discharge conditions were severe given the abundance of acid. They correspond to a potential drop of about 0.26 volts. By comparison a total potential drop of about 0.35 volts is the practical limit in a traction cell. This includes the potential drop due to a reduction in acid concentration (typically 0.1 volts), negative plate polarisation and resistive voltage drops.

The initial voltage peaks appear to relate strongly to the discharge conditions and therefore, presumably, the state of the AM. The authors ascribe the voltage peaks to nucleation and growth of lead dioxide. Transport restrictions at the surface of the discharged PbO_2 due to

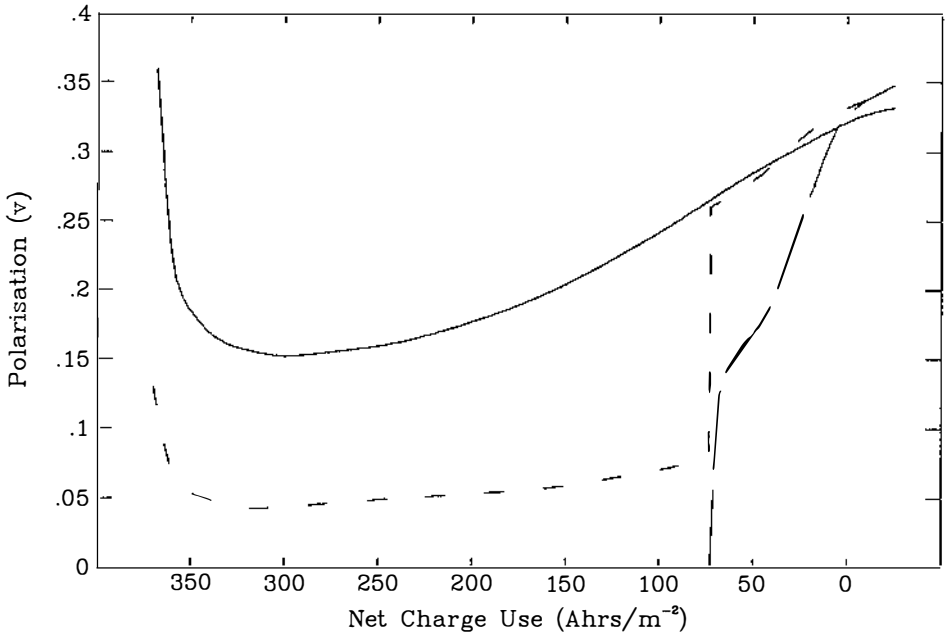

Solid: charge voltage at 200 $A.m^{-2}$ after 100% discharge.
Small dash: charge voltage at 20 then 200 $A.m^{-2}$ after 100% discharge.
Large dash: charge voltage at 200 $A.m^{-2}$ after 20% discharge.

Redrawn from Ekdunge and Simonsson (1985).

Figure 3.11: Experimental Charge Voltage and Discharge Depth.

the encapsulating $PbSO_4$ is a second likely explanation. The occurrence of these peaks in a practical situation may not be so marked since the discharge conditions would be less severe.

Ekdunge and Simonsson (1985) performed experiments on the electrodes discharged to 100% and 20% of full capacity at 200 $A.m^{-2}$. The charge was then performed at 20 and 200 $A.m^{-2}$. Results of these experiments are given in figure 3.11. The polarisation characteristic for the last 20% of the charge (from the 75 $Ahrs.m^{-2}$ point) has a significant dependence on the preceding discharge depth. The characteristic has little dependence on past charge rate given the same preceding discharge depth and the same present charge rate and charge state.

The complete cells were discharged (presumably to their rated capacity) and recharged at various rates (50-

150 $A.m^{-2}$). Total cell voltage readings were made during the charge. These are consistent with the well known data mentioned above. The application of this data to the positive electrode alone is limited. It has already been shown that the negative electrode contributes a large proportion of the overpotential in the latter stage of the charge. This is a likely explanation of the steeper rise in voltage for the cell compared to the electrode.

The work mentioned above gives only limited data for characterising the positive electrode in a practical cell during charge. More detailed data for this purpose is not available in the literature. The emphasis there is either technological, where total cell characteristics are measured, or fundamental, where practical cell components and conditions are absent.

3.7.2 Electrode AM Distribution.

Some aspects concerning the distribution of AM have already been presented in the context of discussing the mechanical structure of the electrode in section 3.2. These will not be repeated here where the focus is on changes in the distribution of AM with state of charge.

Using electron microprobes, Simonsson (1973) determined the distribution of $PbSO_4$ in discharged positive plates. Simonsson (1973) noted that the results obtained depended on the sample preparation procedure. This explained differences in his results compared to earlier results (Bode *et al* (1969)). He examined plates discharged at rates of 2.5 and 100 $A.m^{-2}$ to depths of 0, 25, 50, 75 and 100% discharge. The results obtained are given in figure 3.12a,b.

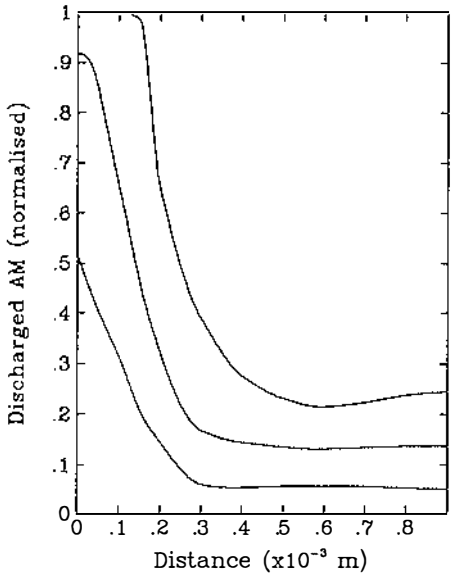

(a) Discharge Current 1000 A.m^{-2}.

Discharge depth for curves from top to bottom: 100, 50 and 25% full discharge.

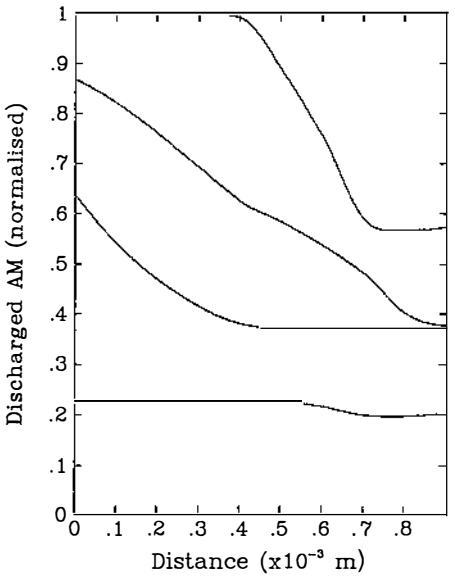

(b) Discharge Current 25 A.m^{-2}.

Discharge depth for curves from top to bottom: 100, 75, 50 and 25% full discharge.

Plate surface at 0.0, center at 0.9 x10^{-3} m.
Redrawn from Simonsson (1973).

Figure 3.12: Experimental AM Distribution in Positive Plate.

At the 100 A.m^{-2} rate the reaction was concentrated near the plate surface. At the 2.5 A.m^{-2} rate the reaction was initially fairly uniformly distributed within the plate but later became concentrated near the plate surface. The results show that the type of discharge (rate and depth) is encoded in the AM distribution.

Whyatt and Hampson (1979) performed discharge experiments on pellet shaped porous PbO_2 electrodes. The electrodes were constructed by punching holes in lead sheet and pasting conventional positive paste in these holes. The lead sheet was then masked and the AM cured and formed in preparation for the discharge experiments. Pellets of 1.0, 1.5 and 2.0 mm thickness and up to 8mm diameter were discharged at rates of 200, 800 and 2000 A.m^{-2}. The discharged pellets were removed, sectioned longitudinally and subjected to SEM examination. At the two highest discharge rates, discharged and charged AM was seen as stripes with abrupt boundaries in low magnification images.

More detailed examination showed no dispersion of this boundary for any current density. This was seen as evidence of an almost layer by layer discharge of AM for the high currents used here. The results are consistent with those of Simonsson (1973) sited above.

Chang (1984) has recently studied SLI positive plates during deep-discharge cycling using a SEM and by other means. The plates were discharged at rates corresponding to approximately 90 to 180 $A.m^{-2}$. He observed a preferential discharge at the outer regions as already seen. In addition he noticed that, for the initial discharge cycles, only the outer two thirds of AM thickness was discharged. As cycling proceeded this zone moved inwards as non-participating AM apparently formed in the outer regions. This gives an indication of a complicating effect due to non-participating AM as well as some expectation of the extent (physical depth) of discharged material that can occur during a single deep discharge of a practical electrode.

Results showing the change in AM distribution during the charge cycle appear to be absent in the literature.

3.7.3 Conclusions Regarding Experimental Data.

i) The general trends for voltage and current characteristics during discharge and charge are known.

ii) Limited data for the voltage and current characteristics of a positive electrode in a practical lead-acid cell are available in the literature.

iii) The AM distribution for electrodes discharged in excess electrolyte is known. This shows the discharge reaction occurs preferentially from the outer surface of the electrode at all but the lowest rates. At medium to high rates the boundary of discharged and charged AM is very abrupt.

iv) Data defining the AM distribution during charge given different initial discharge conditions are not available in the literature.

3.8 DEVELOPMENT AREAS FOR A POSITIVE ELECTRODE MODEL.

From the discussion above it can be seen that the overall charge/discharge mechanism is known with some certainty. Further, mathematical descriptions for the characteristics of the PbO_2/solution interface and for the solution transport processes are available. However, the numerical value of parameters in these descriptions is not known with certainty in all cases.

Three major areas require further work before quantitative descriptions required for a comprehensive positive electrode model can be formed.

The first area concerns the description of the structure and structural changes in the AM. This can be broken into three parts

i) a description of the microstructure including volume and surface area changes during discharge and charge,

ii) a description of the macrostructure (it has been shown above (section 3.2) that volume and surface area are small in this structure) and

iii) a description of the non-participating AM structure.

The second area concerns the gassing effects during charge. This should consider at least four effects. That is,

i) the current diverted from the main charge reaction into the gassing reaction,

ii) the enhancement of mass transport both within the positive electrode and other cell components that exchange acid with the positive electrode,

iii) the increase of electrolyte resistance in the positive electrode and

iv) the surface masking in the positive electrode.

The third area concerns the effect of other cell components on the positive electrode behavior. This includes all cell components that influence the acid supply to the positive electrode. These are,

i) the separator,

ii) the negative plate and

iii) the cell reservoir.

In the development of the VIAM model that follows the first and third major areas are dealt with. Chapter 4 develops quantitative descriptions for the structure and structural changes in the microstructure. Chapter 5 develops a quantitative description for acid transport in the positive electrode system. Chapter 5 also defines the electrical characteristics of the system. Chapter 6 describes experiments performed on standard traction cells to provide supplementary voltage/current data for that reviewed in section 3.7.1. All results are given in chapter 7.

Chapter 4

Three Elemental Models for the Positive Electrode

The single pore and macrohomogeneous models embody an implicit representation of the electrode structure. In the case of the single pore model a simple geometric cylinder is used (see section 3.6.1). In the case of the macrohomogeneous model a porous matrix characterised by average parameters is used (see section 3.6.2). In both cases the representation provides the framework into which factors such as interface polarisation and solution transport can be incorporated. The purpose is to accurately represent the overall electrode behaviour. The next two chapters set out a series of models that, taken together, represent the structure of the positive electrode system for this same purpose.

The components set out differ from the single pore and macrohomogeneous models as follows:

i) the structure and, in particular, changes in structure are defined by simple models based on the observed physical changes in the AM,

ii) the macro and micro levels in the AM organisation are taken into account,

iii) the non-participating AM is taken into account and

iv) other cell components that influence the behaviour of the positive electrode are taken into account.

Descriptions of the structure are developed on an elemental and aggregate level.

The elemental level concerns the structure of a small volume of participating AM. This structure varies from point to point in the AM and therefore is characterised by local parameters particular to the point in question. Elemental models defining the discharge capacity, discharge surface area and charge surface area are developed in this chapter.

The aggregate level concerns the structure of all the cell parts involved in acid transport. This includes the participating AM, the non-participating AM, the separator the negative plate and the cell reservoir regions. An aggregate model that represents the acid transport, current and potential in these parts is developed in chapter 5.

The content of the present chapter is summarised below.

i) The development of an elemental discharge capacity model (section 4.1).

ii) The development of an elemental discharge surface area model (section 4.2)

iii) The development of an elemental charge surface area model (section 4.3).

4.1 AN ELEMENTAL DISCHARGE CAPACITY MODEL.

The discharge capacity is taken here to mean the maximum quantity of electrical charge (Ampere hours) that can be obtained from an equivalent gram † of participating AM. A capacity limiting mechanism based on volume changes in the microstructure is proposed below. The discharge capacity is formulated from the volume identities involved. A dimensionless charge state factor is defined as simple extensions of the discharge capacity formulation.

4.1.1 The Microstructure: a Discharge Limiting Factor.

a) The role of the microstructure.

The maximum discharge capacity is obtained at low discharge rates where there are no limitations due to solution transport effects. Therefore the macrostructure, which provides solution transport passages (see section

† Note: an "equivalent gram" quantity is the quantity associated with, or derived from, a gram of dry PbO_2 in the fully charged AM structure.

3.2), is not a factor. Consequently, it can be assumed that the microstructure determines the local discharge capacity. Further, since the macrostructure volume consists of solution contained in transport passages, the microstructure volume can be said to contain all the PbO_2.

b) Volume limitations in the microstructure.

Given that solid $PbSO_4$ forms near the PbO_2 from which it is derived (see section 3.2), it can be assumed that the $PbSO_4$ that results from the discharge of the microstructure is contained within the volume of this structure. Further, given that the $PbSO_4$ does not form an integral insulating layer on the PbO_2 (see section 3.2), it can be assumed that the discharge will proceed until solid $PbSO_4$ and PbO_2 completely occupy the volume of the microstructure.

It should be pointed out that the assumptions above represent a simplification of the actual situation. Volume effects not accounted for are:

i) the presence of solution filled voids in the discharged structure (see section 3.2),

ii) the slight mechanical expansion of the discharged structure (see section 2.2.1) and

iii) the recrystallisation of $PbSO_4$ in the macrostructure at the end of the discharge (Pavlov and Bashtavelova (1986)).

4.1.2 Local Discharge Capacity Formulations.

By adopting the assumptions outlined above, the local discharge capacity can be determined from solid phase and solution volume relationships in the microstructure.

The total equivalent gram volume of the charged microstructure is the sum of the equivalent gram solution and solid PbO_2 volumes. The latter quantity is the inverse of the density of solid PbO_2. This gives

$$V_{\mu Tot} = V_{\mu} + 1/\rho_{PbO2} \tag{4.1}$$

where

$V_{\mu Tot}$ ($m^3.g^{-1}$) is the total equivalent gram volume of charged microstructure,

V_{μ} ($m^3.g^{-1}$) is the equivalent gram volume of solution in the charged microstructure and

ρ_{PbO2} ($g.m^{-3}$) is the density of solid PbO_2.

As the discharge proceeds the equivalent gram volume of PbO_2 and $PbSO_4$ solid phases are given by

$$V_{PbO2} = \frac{1}{\rho_{PbO2}} - \frac{V_{mPbO2}\, q}{2F} \tag{4.2}$$

and

$$V_{PbSO4} = \frac{V_{mPbSO4}\, q}{2F} \tag{4.3}$$

respectively, where

V_{PbO2} ($m^3.g^{-1}$) is the equivalent gram volume of solid PbO_2,

V_{PbSO4} ($m^3.g^{-1}$) is the equivalent gram volume of solid $PbSO_4$,

V_{mPbO2} ($m^3.mol^{-1}$) is the molar volume of PbO_2,

V_{mPbSO4} ($m^3.mol^{-1}$) is the molar volume of $PbSO_4$ and

q ($A.s.g^{-1}$) is the equivalent gram discharge.

The required discharge capacity is the value of $q(t)$ obtained when the total solid volume is equal to the total microstructure volume. Equating these volumes using equations 4.1 to 4.3 gives

$$q_d = \frac{2F\, V_{\mu}}{V_{mPbSO4} - V_{mPbO2}} \tag{4.4}$$

where q_d is the equivalent gram discharge capacity ($A.s.g^{-1}$).

Two other common discharge capacity measures will be defined in terms of the microstructure parameters before leaving this matter. Firstly, the theoretical discharge capacity can be defined as the value of q when all the solid PbO_2 in the microstructure has been consumed. That is, when V_{PbO2} is zero. Applying equation 4.2 gives

$$q_T = 2F/M_{mPbO2} \tag{4.5}$$

where

q_T ($A.s.g^{-1}$) is the theoretical discharge capacity and

M_{mPbO2} ($g.mol^{-1}$) is the molar mass of solid PbO_2 (density x molar volume).

Secondly, the PbO_2 utilisation factor at complete local discharge can be defined by the ratio of q_d/q_T which gives,

$$Q_d = \frac{V_\mu \, M_{mPbO2}}{V_{mPbSO4} - V_{mPbO2}} \tag{4.6}$$

where Q_d is the utilisation factor of PbO_2 at complete discharge.

4.1.3 Charge State Formulations.

The charge state can be conveniently written as a dimensionless quantity involving the discharge at a particular time and discharge capacity. That is,

$$X = 1 - q/q_d \tag{4.7}$$

where X is the charge state.

It can be seen that this quantity is unity at full charge and reduces to zero at complete discharge.

4.2 AN ELEMENTAL DISCHARGE SURFACE AREA MODEL.

The discharge surface area is taken to mean the surface area of PbO_2 in an equivalent gram of participating AM. This is an important parameter since it defines the interface area at which the electrochemical reaction takes place. The surface area is known for the fully charged state through BET surface area measurements. Unfortunately the BET surface measurement technique cannot distinguish between PbO_2 and $PbSO_4$ particles. This means the local surface area at other states (when $PbSO_4$ is present) is not known with any certainty.

The approach used to quantify the discharge surface area is given below.

i) The surface area changes are assumed to be determined by changes in the microstructure. This is consistent with the role of the microstructure outlined in section 4.1.

ii) A qualitative description of likely changes in the microstructure is developed. This is based on experimental observations outlined in section 3.2.

iii) The qualitative description is simplified to give an approximate formulation for the discharge surface area.

4.2.1 A qualitative description of the discharge.

The fully charged structure is made up of agglomerates containing a large number of individual PbO_2 crystallites. The crystallites are highly angular, rock-like forms ranging in size from about 0.05 to 1.0 μm (see figure 3.2).

When the discharge begins, PbO_2 dissolves and $PbSO_4$ nuclei form randomly on the PbO_2 surface indicating a

uniform surface process (see section 3.2). The fine PbO_2 structures, with a large surface area to volume ratio, would be expected to be rapidly converted to $PbSO_4$ with this process. As a consequence the PbO_2 would exhibit an initial rapid reduction in surface area. This would not be measured experimentally since the fine $PbSO_4$ particles that precipitate also have a high surface area to volume ratio.

As the discharge continues, more PbO_2 is converted to $PbSO_4$ causing small particles and the angular corners of larger particles to vanish. As a result the PbO_2 would be expected to take on the form of agglomerates of featureless particles of fairly uniform size (tending towards spheres). At the same time the $PbSO_4$ particles will enlarge and begin to intersect. The $PbSO_4$ particles make the direct experimental observation of the PbO_2 particle surface difficult (as noted by Hattori *et al* (1975) for example).

During the final stage of discharge, the featureless PbO_2 particles would be expected to reduce in volume and surface area in a similar way to true spheres (where the surface area is proportional to the volume raised to a fractional power). The $PbSO_4$ would continue to grow and form a dense structure that encloses the remaining PbO_2.

When completely discharged, the microstructure would consist of agglomerates of featureless PbO_2 particles fully enclosed in $PbSO_4$ (as described in section 3.2). There would be few voids in this structure. The total surface area of the structure would be made up of equal parts from the surface of the PbO_2 particles and the surface of the $PbSO_4$ which is pressing around these particles.

These changes in the microstructure during discharge are represented schematically in figure 4.1.

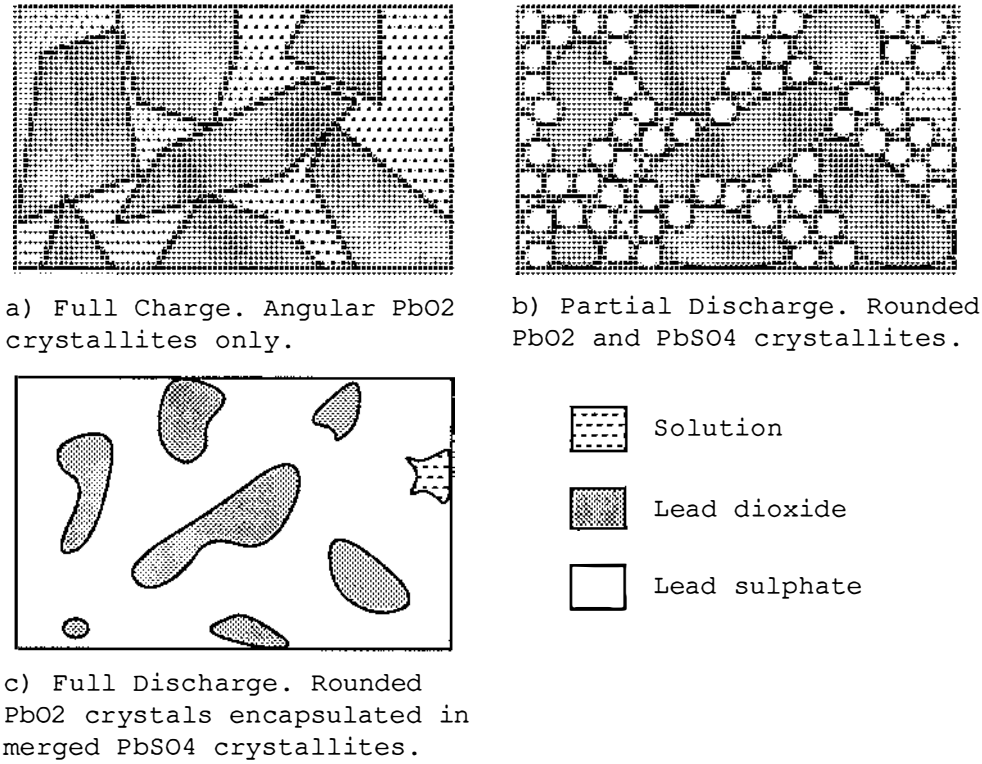

Figure 4.1: A Representation of the Discharge Process.

4.2.2 Discharge Surface Area Formulations.

The likely surface area variation with discharge suggested by the description above is represented in figure 4.2. The PbO_2 surface area at full charge is known from experimental measurements. The PbO_2 surface area at full discharge is half the total surface area at full discharge (the other half being the $PbSO_4$ surface area). This is likely to be greater than half the the full discharge area obtained from experimental measurements since some surfaces may be inaccessible because of encapsulating $PbSO_4$ (see Ekdunge and Simonsson (1985)). Further effort to quantify the area variation will not be made here. As a first approximation the discharge area will be taken as a linear function of charge state between the full charge and full discharge points. This is shown graphically in figure 4.2. The formulation involved is given below.

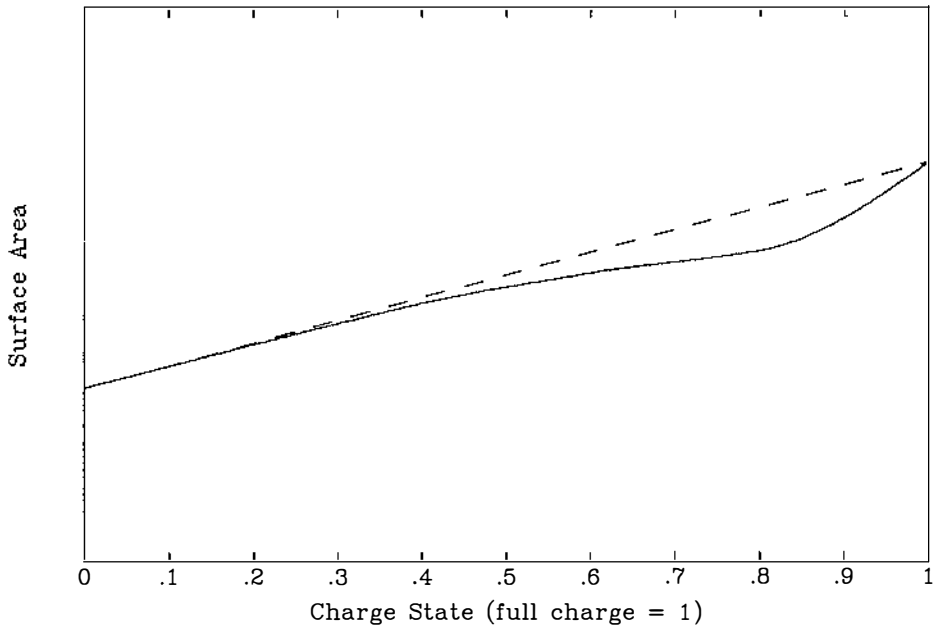

Solid: Actual surface area variation as suggested by qualitative discription.
Dash: Linear approximation to the actual area surface variation.

Figure 4.2: The Discharge Surface Area Model.

$$S_{PbO2} = X(t)(S_{cPbO2}-S_{dPbO2}) + S_{dPbO2} \qquad (4.8)$$

where,

S_{PbO2} ($m^2.g^{-1}$) is the equivalent gram elemental discharge surface area,

S_{dPbO2} ($m^2.g^{-1}$) is the equivalent gram surface area at full discharge and

S_{cPbO2} ($m^2.g^{-1}$) is the equivalent gram surface area at full charge.

4.3 AN ELEMENTAL CHARGE SURFACE AREA MODEL.

The charge surface area is again taken to mean the surface area quantity in an equivalent gram of participating AM. In the charge case however, more that one quantity is required. In particular, it is not only the

actual PbO_2 surface that is important but also the proportion of the actual surface where the electrochemical charge reaction is taking place. The latter quantity will be known as the effective PbO_2 surface area. The difference between the actual and effective quantities is clearly seen at the end of charge. Here the actual PbO_2 surface area reaches a maximum whereas the effective PbO_2 surface falls to zero. Surface area quantities are defined for the actual and effective PbO_2 charge surface area as well as for the $PbSO_4$ charge surface area in the work that follows.

The data obtained from experimental studies has already been discussed (see section 4.2). It is not sufficient for the determination of the individual surface area quantities required here. The approach used to determine these quantities is given below.

i) The surface area changes are assumed to be determined by changes in the microstructure. This is consistent with the role of the microstructure outlined in section 4.1.

ii) A qualitative description of likely changes in the microstructure is developed. The description is based on the experimental observations summarised in section 3.2.

iii) A charge model based on the qualitative description is formulated.

iv) The charge model is used to simulate the real system and determine the quantities required.

It can be seen that this is the same approach as used for the discharge case in section 4.2. In the charge case however, a comprehensive model is developed.

4.3.1 A Qualitative Description of the Charge.

The full discharge state will be assumed as the starting point for the charge. This means that the structure begins as shapeless agglomerates of PbO_2 particles enclosed in $PbSO_4$ (as described in section 4.2). The PbO_2 particles also have contact with other similar particles to maintain the electrical conductivity of the structure (see section 3.2).

As the charge proceeds, $PbSO_4$ near the PbO_2 particles will dissolve leaving a void which is filled by solution and growing PbO_2 crystallite lobes. Throughout the charge the PbO_2 surface would be expected to increase due to the growth of the additional lobe area. Initially the $PbSO_4$ surface area would show little change as it maintains the same shape and form but retreats fractionally from the PbO_2. Later in the charge the $PbSO_4$ surface would be expected to decrease as enclosed void volumes intersect and the dense $PbSO_4$ structure begins to break down.

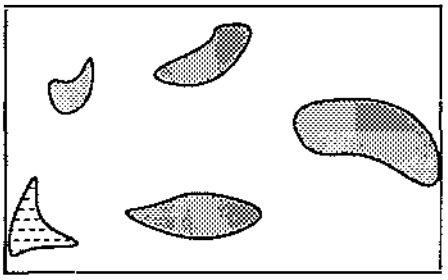

a) Full Discharge. Rounded PbO2 crystallites encapsulated in PbSO4.

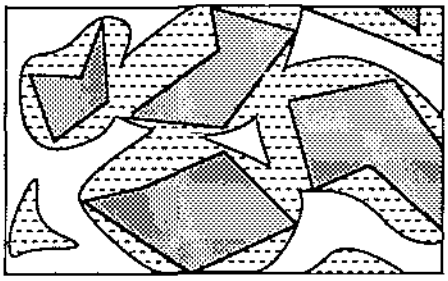

b) Partial Charge. Angular PbO2 crystallites surrounded by receding PbSO4.

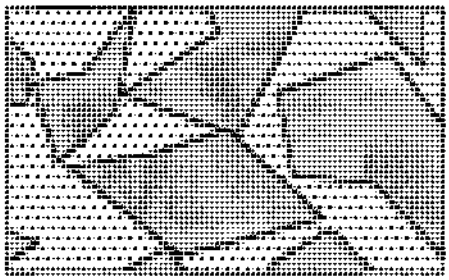

c) Full Charge. Angular PbO2 crystallites only.

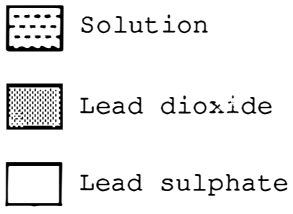

Figure 4.3: A Representation of the Charge Process.

At the end of charge the $PbSO_4$ would be completely consumed and the PbO_2 restored to its original form of agglomerates of rock-like crystallites.

These changes in the microstructure during charge are represented schematically in figure 4.3.

4.3.2 A Simple Geometric Model at Full Discharge.

Taking account of the description of the fully discharged AM above, the PbO_2 will be represented by spheres encapsulated in boxes of $PbSO_4$. Further, each PbO_2 sphere will touch four faces of the enclosing box to allow electrical contact with adjacent particles. This arrangement is illustrated in figure 4.4.

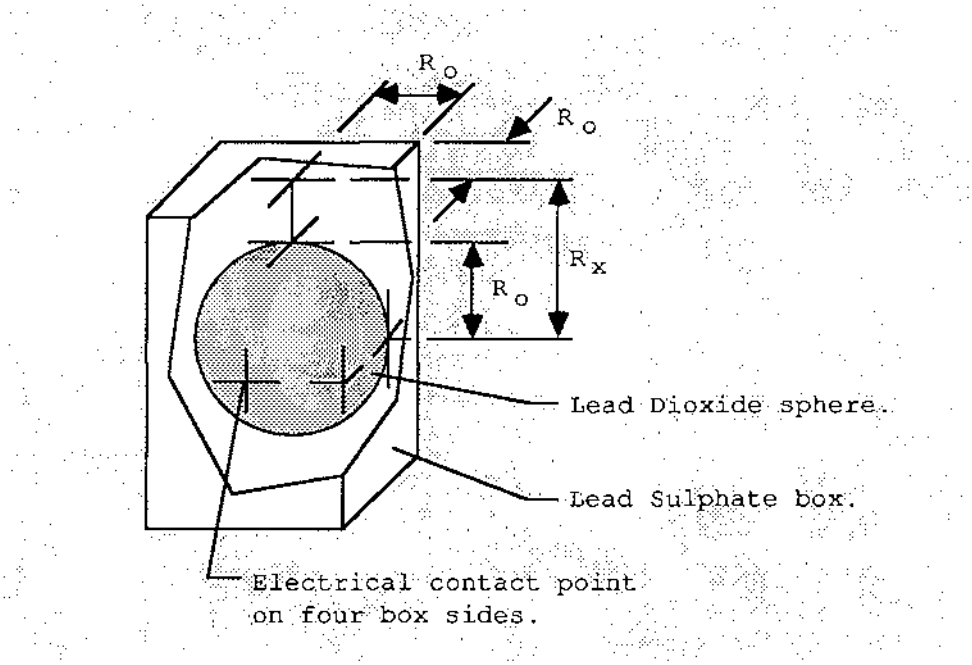

Figure 4.4: A Geometric Model of the Discharged AM.

Referring to figure 4.4

R_o (m) is the sphere radius and half the box width,
R_x (m) † is half the box height and
N_x (g^{-1}) is the number of identical boxes in a gram equivalent of AM.

The values of R_o, R_x and N_x can be determined from the volume and surface area of the discharged AM. Writing equations for the total volume, the PbO_2 volume and the PbO_2 surface area gives

$$V_{\mu Tot} = 8N_x R_o^2 R_x, \quad (4.9)$$

$$V_{dPbO2} = (4/3)\pi N_x R_o^3 \quad \text{and} \quad (4.10)$$

$$S_{dPbO2} = 4\pi f_o N_x R_o^2 \quad (4.11)$$

respectively, where

V_{dPbO2} ($m^3.g^{-1}$) is the equivalent gram volume of PbO_2 in the discharged AM.
S_{dPbO2} ($m^2.g^{-1}$) is the equivalent gram surface area of the encapsulated PbO_2 particles and
f_o is the ratio of the particle surface area to that of a perfect sphere (the sphere surface factor).

V_{dPbO2} is obtained by substituing q from equation 4.4 into equation 4.2. S_{dPbO2} is half the full discharge surface area as discussed above.

Manipulating equations 4.9 to 4.11 gives

$$R_o = 3f_o V_{dPbO2}/S_{dPbO2}, \quad (4.12)$$

$$N_x = 3V_{dPbO2}/(4\pi R_o^3) \quad \text{and} \quad (4.13)$$

$$R_x = V_{\mu Tot}/(8N_x R_o^2) \quad (4.14)$$

which specifies the box/sphere geometry.

† Note: the symbol " x " will be used to denote variables associated with the box/sphere geometry.

4.3.3 $PbSO_4$ Surface Area Formulations.

The volume of $PbSO_4$ is related to the local discharge by

$$q = 2F\, N_x\, V_{xPbSO4}/V_{mPbSO4} \qquad (4.15)$$

where

q ($A.s.g^{-1}$) is the local discharge and

V_{xPbSO4} (m^3) is the volume of $PbSO_4$ in a single box.

The volume V_{xPbSO4} can in turn be used to determine the $PbSO_4$ surface area within the box given that the surface maintains its spherical form and the fixed geometry of the box. The volume and surface area are most conveniently related by introducing the radius of the spherical surface as a common variable. This gives

$$V_{xPbSO4} = 8R_o^2R_x - ((4/3)\pi R^3 - F_v(R)) \qquad (4.16)$$

and

$$S_{xPbSO4} = f_o(4\pi R^2 - F_s(R)) \qquad (4.17)$$

where

R (m) is the radius of the $PbSO_4$ surface,

S_{xPbSO4} (m^2) is the surface area of $PbSO_4$ at radius R in a single box and

$F_v(R)$ (m^3) and F_s (m^2) account for the $PbSO_4$ volume and surface area loss, respectively, due to the portions of the sphere of radius R outside the boundaries of the box.†

† These are given by geometric identities for the spherical caps and segments that occur as the sphere of radius R intersects with the box boundaries. The spherical cap identities were taken from Bronshtein and Semendyayev (1973). The spherical segment identities were approximated by similar identities for cylindrical segments multiplied by a surface curvature correction factor. The cylindrical segment identities were taken from Bronshtein and Semendyayev (1973).

Finally the $PbSO_4$ surface area is given by

$$S_{PbSO4} = N_x \, S_{xPbSO4} \qquad (4.18)$$

where S_{PbSO4} ($m^2.g^{-1}$) is the equivalent gram surface area quantity.

4.3.4 Actual PbO_2 Surface Area Formulations.

PbO_2 will be precipitated at sites on existing PbO_2 according to the reaction given in equation 3.3. The supply of Pb^{2+} ions determines the precipitation volumes and therefore the structure of PbO_2 lobes grown on the initial PbO_2 sphere. The required surface area variation is in turn found from the structure of these lobes. The approach taken to quantify these effects is set out in two stages below. Firstly, the Pb^{2+} concentration (supply) within the box/sphere geometry is considered. This coincidentally defines the dimensions of the PbO_2 lobes. Secondly, the lobe dimensions are used to define the total PbO_2 surface area within a box and therefore the required actual PbO_2 surface.

a) The Pb^{2+} Concentration.

Let the volume which is supplied by Pb^{2+} ions be represented by the rectangular system shown in figure 4.5. This is a reasonable approximation to the spherical situation when the radial distance in which the reaction takes place is small compared to $PbSO_4$ surface supplying the Pb^{2+} ions. At the beginning of charge this is the case because of the small distance between the $PbSO_4$ and PbO_2 surfaces. At the end of charge this is also the case since the Pb^{2+} ion concentration will rapidly fall to zero away from the $PbSO_4$ surface due to the increased demand but reduced supply of Pb^{2+} ions.

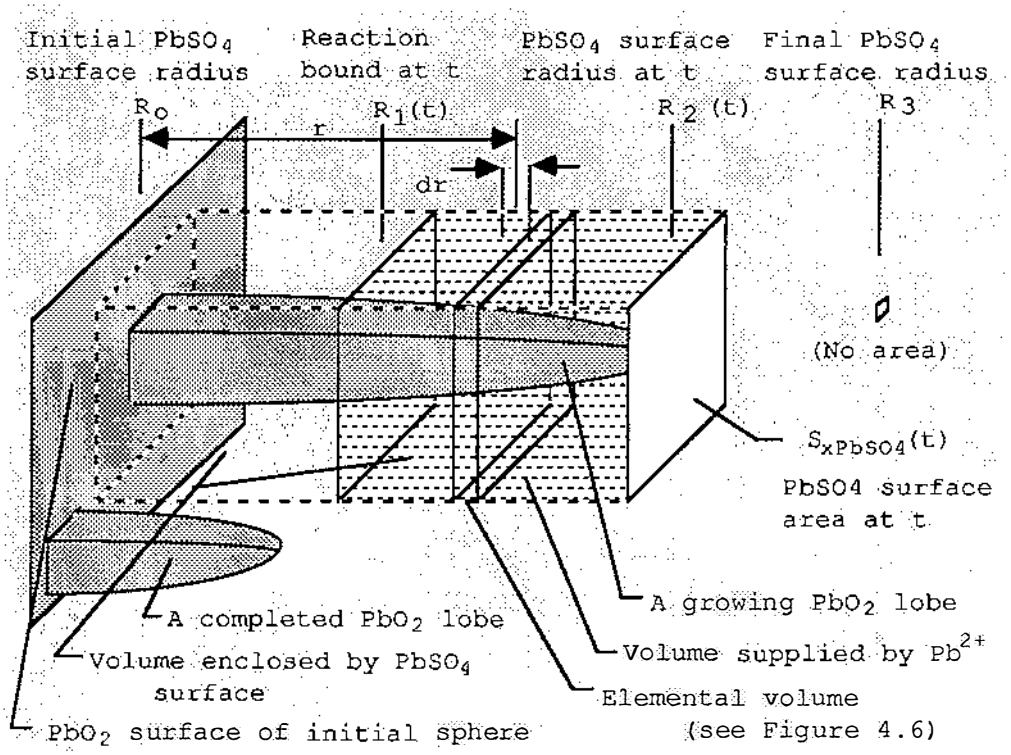

Figure 4.5: A Rectangular System for Lead Dioxide Growth.

Referring to figure 4.5

t (s) is the time from the start of charge,

r (m) is the distance from a fixed point (R_o) to an arbitrary point within the supplied volume,

dr (m) is the width of an elemental volume,

R_o (m) is the position of the $PbSO_4$ and PbO_2 surfaces at full discharge,

$R_1(t)$ (m) is the position at which the charge reaction becomes zero,

$R_2(t)$ (m) is the position of the moving $PbSO_4$ surface during charge,

R_3 (m) is the position of the $PbSO_4$ surface at the end of charge and

$S_{xPbSO4}(t)$ (m^2) is the $PbSO_4$ surface within the box during charge.

Consider next the details of the elemental volume shown in figure 4.5. These are given in figure 4.6.

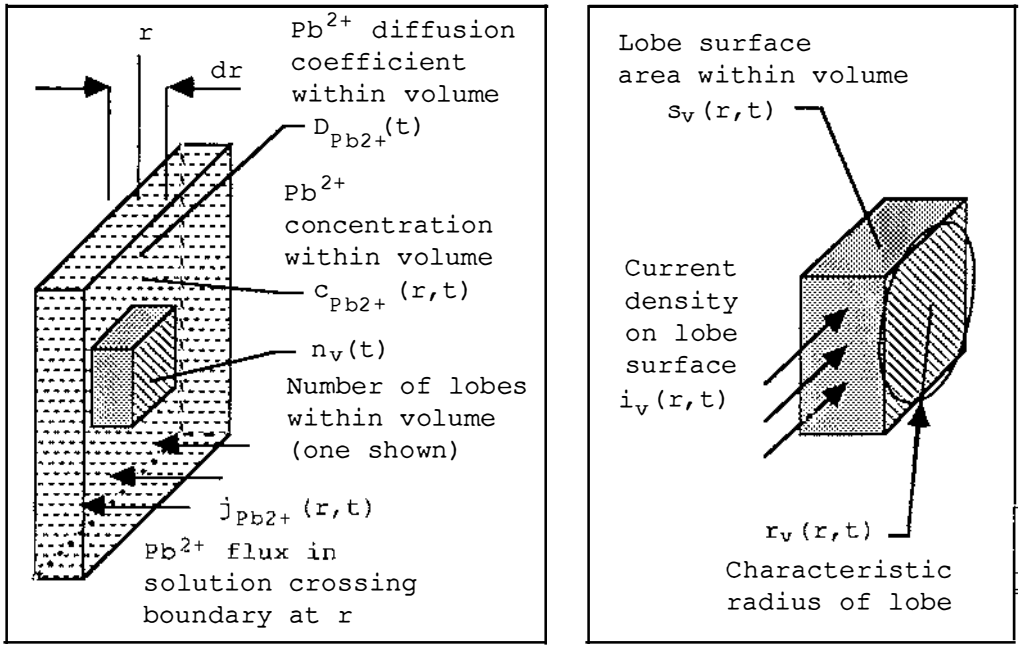

Figure 4.6: An Elemental Volume for the Pb^{2+} Mass Balance.

Referring to figure 4.6

$D_{Pb2+}(t)$ ($m^2.s^{-1}$) is the diffusion coefficient for the Pb^{2+} ion in sulphuric acid solution,

$j_{Pb2+}(r,t)$ ($mol.m^{-2}$) is the flux density of Pb^{2+} ions in solution,

$c_{Pb2+}(r,t)$ ($mol.m^{-3}$) is the Pb^{2+} ion concentration,

$n_v(t)$ † is the number of growing PbO_2 lobes within the supplied volume,

$r_v(r,t)$ (m) is the characteristic radius of a lobe,

$s_v(r,t)$ (m) is the lobe surface area per unit length and

$i_v(r,t)$ ($A.m^{-2}$) is the current density on the surface of a lobe.

† Note: the symbol " v " (visualised as a downward pointing lobe) will be used to denote variables associated with the PbO_2 lobe geometry.

Writing the mass balance for Pb^{2+} ions within the solution of the elemental volume gives

$$\frac{\partial}{\partial t}\left[\left[S_{xPbSO4}(t)-\pi n_v(t) r_v(r,t)^2\right] c_{Pb2+}(r,t)\right] =$$

$$+\frac{\partial}{\partial r}\left[\left[S_{xPbSO4}(t)-\pi n_v(t) r_v(r,t)^2\right] j_{Pb2+}(r,t)\right]$$

$$-\frac{n_v(t)\, s_v(r,t)\, i_v(r,t)}{2F}. \qquad (4.19)$$

Equation 4.19 assumes the Pb^{2+} concentration is controlled by diffusion with simultaneous reaction. From left to right the terms represent accumulation, diffusion and reaction of Pb^{2+} respectively. Migration effects are not included since potential gradients in the solution will be caused by the charge of the acid components and will not have a systematic effect on the Pb^{2+} movement. Similarly convection effects are not included since bulk solution movement will not have a systematic effect on the direction of Pb^{2+} movement.

A more useful form for equation 4.19 is found by using equivalent or likely identities for $j_{Pb2+}(r,t)$, $n_v(t)$, $s_v(r,t)$ and $i_v(r,t)$. These identities are set out below.

The flux of Pb^{2+} ions can be written in terms of the concentration gradient according to Fick's first law. This gives

$$j_{Pb2+}(r,t) = -D_{Pb2+}(t)\frac{\partial c_{Pb2+}(r,t)}{\partial r}. \qquad (4.20)$$

The number of lobes within the volume supplied by Pb^{2+} ions can be taken as being proportional to the area that encloses that volume. That is,

$$n_V(t) = \frac{n_{VO}}{S_{xPbSO4o}} S_{xPbSO4}(t) \qquad (4.21)$$

where

n_{VO} is the number of lobe sites at radius R_O and

$S_{xPbSO4o}$ (m^2) is the $PbSO_4$ surface at radius R_O.

The surface area of the lobe can be related to the characteristic radius of the lobe using the geometric model in figure 4.7. Adopting the geometric model shown gives

$$s_V(r,t) = 2\pi f_V \, r_V(r,t) - \pi \frac{\partial r_V(r,t)^2}{\partial r} \qquad (4.22)$$

where f_V is the surface factor for the lobe shape (the lobe surface factor, unity for a circular cross-section).

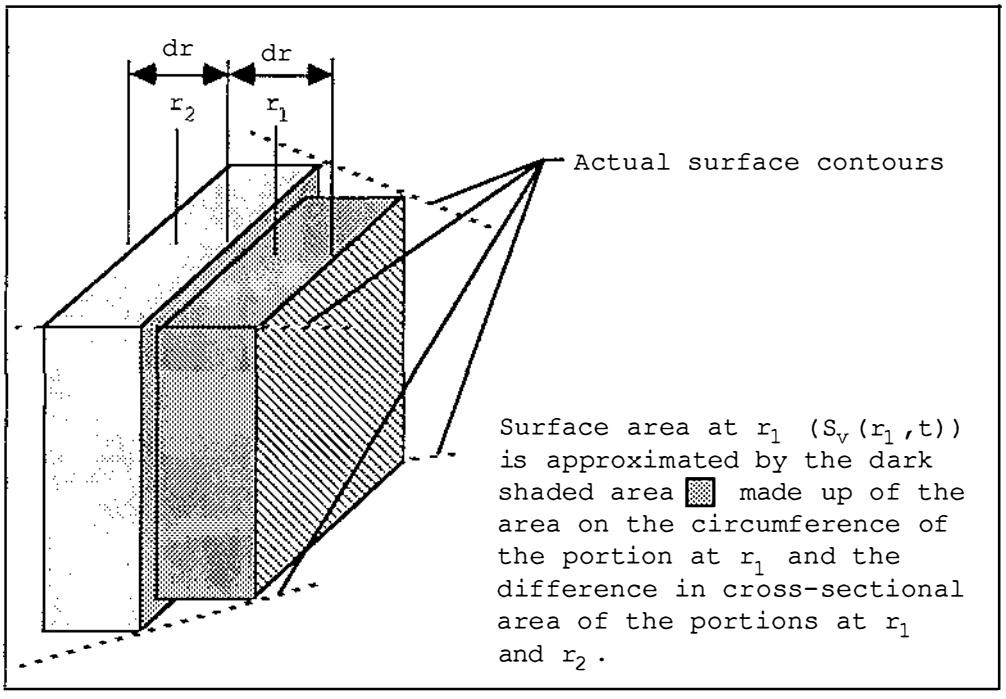

Figure 4.7: The Lead Dioxide Lobe Surface Area.

The current density can be represented by the product of a concentration dependent exchange current density and a potential dependent exponential term (see equations 3.8 and 3.6). Taking the exchange current reaction order for Pb^{2+} as unity (Hampson *et al* 1968) and combining other terms into a single potential dependent rate constant gives

$$i_v(r,t) = K_e(t)c_{Pb2+}(r,t) \tag{4.23}$$

where $K_e(t)$ $(A.m.mol^{-1})$ is the potential dependent rate constant.

Substituting the identities defined by equations 4.20 to 4.23 in equation 4.19 gives

$$\frac{\partial}{\partial t}\left[S_{xPbSO4}(t)\left[1 - \frac{\pi n_{vo}\, r_v(r,t)^2}{S_{xPbSO4o}}\right]c_{Pb2+}(r,t)\right] =$$

$$- D_{Pb2+}(t)\, S_{xPbSO4}(t)\, \frac{\partial}{\partial r}\left[\left[1 - \frac{\pi n_{vo}\, r_v(r,t)^2}{S_{xPbSO4o}}\right]\frac{\partial c_{Pb2+}(r,t)}{\partial r}\right]$$

$$- \frac{n_{vo}\, K_e(t)\, S_{xPbSO4}(t)}{2F\, S_{xPbSO4o}}\left[2\pi f_v r_v(r,t) - \pi \frac{\partial r_v(r,t)^2}{\partial r}\right]c_{Pb2+}(r,t). \tag{4.24}$$

Before equation 4.24 can be solved for c_{Pb2+}, boundary conditions and $r_v(r,t)$ must be known. These are set out below.

At the $PbSO_4$ boundary $(R_2(t))$ two conditions are known. Firstly, the concentration at this boundary is the equilibrium concentration of Pb^{2+} ions for $PbSO_4$ in sulphuric acid solution. That is,

$$c_{Pb2+}(R_2(t),t) = c_{ePb2+}(t) \tag{4.25}$$

where $c_{ePb2+}(t)$ $(mol.m^{-3})$ is the equilibrium concentration.

Secondly, the rate of dissolution of $PbSO_4$ is related to the concentration gradient at this boundary by Fick's first law. Assuming this in turn is controlled by the total current into the box gives

$$\frac{\partial c_{Pb2+}(R_2(t),t)}{\partial r} = \frac{I_x(t)}{2F\ D_{Pb2+}(t)\ S_{xPbSO4}(t)} \qquad (4.26)$$

where $I_x(t)$ is the total current into the box (A).

At the beginning of charge the concentration is also the equilibrium concentration. That is,

$$c_{Pb2+}(r,0) = c_{ePb2+}(0). \qquad (4.27)$$

Equations 4.25 to 4.27 are the required boundary conditions.

The radius at any arbitrary point (r_1,t_1 say) is determined by the volume of PbO_2 deposited at r_1. This, in turn, is given by the time integral of the current density and surface area product at r_1. Taking account of these relationships gives

$$r_v(r_1,t_1) = \left[\frac{V_{mPbO2}}{2\pi F}\int_0^{t1} i_v(r_1,t)s_v(r_1,t)dt\right]^{0.5}. \qquad (4.28)$$

Equation 4.28 needs to be qualified further by defining the maximum radius possible as determined by the volume in which the lobe is enclosed and the initial structure ($s_v(r,0)$ and $r_v(r,0)$).

The limiting condition for the maximum radius can be written by considering when an elemental volume is completely occupied by the lobes which it contains. This gives,

$$r_{vMax} = \left(\frac{b_v \, S_{xPbSO4o}}{\pi n_{vo}} \right)^{0.5} \qquad (4.29)$$

where

r_{vMax} (m) is the maximum radius and

b_v is the volume utilisation factor (approximately unity).

The initial structure is defined by

$$r_v(0,0) = r_{vMax}, \qquad (4.30a)$$

$$r_v(r,0) = 0 \quad \text{for } r \neq 0 \text{ and} \qquad (4.30b)$$

$$s_v(R_0,0) = 4\pi f_o \, R_o^2/(n_{vo} \, dr). \qquad (4.31)$$

The third equation accounts for the surface area of the initial sphere.

Solving the set of equations 4.24 to 4.31 gives the concentration distribution of Pb^{2+} ions. At the same time the structure of the PbO_2 lobes ($r_v(r,t)$ and $s_v(r,t)$) is also determined. This, in turn, means that the surface area development during charge can now be defined. Formulations for this surface area are given below.

b) The PbO_2 Surface Area.

The PbO_2 surface area is made up of following two components.

i) The surface area of lobes contained within the volume enclosed by the $PbSO_4$ surface and R_o (figure 4.5). This area is associated with the PbO_2 lobes that are still growing.

ii) The surface area of lobes that have passed outside the volume enclosed by the $PbSO_4$ surface and R_o as the $PbSO_4$ surface has diminished. This area is associated with PbO_2 lobes which are no longer growing (completed).

Formulations for these components at time t_1 are

$$s_{gPbO2}(t_1) = \int_{Ro}^{R2(t1)} s_v(r,t_1)\,dr \qquad (4.32)$$

and

$$s_{cPbO2}(t_1) = \int_0^{t1} \frac{1}{S_{xPbSO4}(t_1)} \frac{dS_{xPbSO4}(t)}{dt} s_{gPbO2}(t_1)\,dt \qquad (4.33)$$

where

$s_{gPbO2}(t)$ (m^2) is the surface area of growing lobes and

$s_{cPbO2}(t)$ (m^2) is the surface area of completed lobes.

The terms involving S_{xPbSO4} in equation 4.33 represent the proportion of the PbO_2 surface passing out of the growing volume in time dt.

The total PbO_2 surface area within a box is given by the sum of the growing and completed surfaces. That is,

$$S_{xPbO2}(t) = s_{gPbO2}(t) + s_{cPbO2}(t) \qquad (4.34)$$

where $S_{xPbO2}(t)$ (m^2) is the total PbO_2 surface area within a box.

Finally the actual PbO_2 surface area is given by

$$S_{PbO2}(t) = N_x\, S_{xPbO2}(t) \qquad (4.35)$$

where S_{PbO2} ($m^2.g^{-1}$) is the equivalent gram actual PbO_2 surface area quantity.

4.3.5 Effective PbO_2 Surface Area Formulations.

The effective charge surface area is the portion of the actual surface where the electrochemical reaction rates are nonzero. That is, the surface area where the Pb^{2+} ion concentration and current density is nonzero. The

formulations given in section 4.3.4 show that this information can be represented as a one-dimensional distribution of surface area and current density. While this representation is sufficient, it is not the most convenient representation to integrate with the aggregate model components that follows (in chapter 5). An equivalent representation which reduces the one-dimensional distribution to two parameters is given below.

Before continuing it should be noted that the concept of an effective surface area does not apply to the discharge case. This is because there is always a supply of Pb^{2+} ions to all the surface area due to the uniform covering of $PbSO_4$ nuclei (see section 3.2). As a result the reaction proceeds on the actual surface area during discharge.

a) Integrating the elemental and aggregate models.

The aggregate model concerns have been mentioned in the introduction this chapter. They relate to the transport of mass and charge in the cell components. The details of area/current distribution involving Pb^{2+} ions need not be known for this. It is sufficient for only the net current that controls the movement of mass and charge to be known. The net current can be represented by volume average parameters. In particular, the net current can be represented by an effective current density and an effective surface area. This effective surface area is formulated below by extending the actual surface area results of the preceding section.

b) The elemental effective surface area.

The effective surface area is defined to ensure the volume average and specific structural parameters give identical current and overpotential results for the same volume of AM (one equivalent gram).

Consider first the equivalent gram current. This can be written as

$$I(t) = S_E(t)\ I_E(t) \tag{4.36}$$

where

$I(t)$ $(A.g^{-1})$ is the equivalent gram or local current,
$S_E(t)$ $(m^2.g^{-1})$ is the effective surface area and
$I_E(t)$ $(A.m^2.g^{-1})$ is the effective current density.

This must be equal to the current predicted by the sphere/box model. That is,

$$I(t) = N_x\ I_x(t) \tag{4.37}$$

where I_x (A) is the current into a single box given by

$$I_x(t) = K_e(t)\int_{R1(t)}^{R2(t)} s_v(r,t)c_{Pb2+}(r,t)dr. \tag{4.38}$$

Equation 4.38 represents the summation of the current at the surface of growing dendrites within a single box.

Consider next the overpotential at the AM surface. The overpotential for the specific structure is represented by the term $K_e(t)$ in equation 4.38. To represent the same overpotential in the volume average quantities the effective current density can be written as

$$I_E(t) = K_e(t)c_{ePb2+}(t). \tag{4.39}$$

Combining equations 4.36 and 4.39 gives the required effective area. That is,

$$S_E(t) = I(t)/(K_e(t)c_{ePb2+}(t)). \tag{4.40}$$

4.3.6 The Elemental Charge Surface Area Model: A Practical Approach.

The actual and effective PbO_2 surface areas can, in

principle, be determined from the set of equations 4.24 to 4.35, 4.38 and 4.40. The independent variables are time, the equivalent gram current I(t), the lead ion equilibrium concentration $c_{ePb2+}(t)$ and the lead ion diffusion coefficient $D_{Pb2+}(t)$. The last three variables are determined by the aggregate model. In practice the set of equations does not lend itself to solution by analytical methods and numerical methods must be employed. The set of equations is reformed for solution by numerical methods and the solution algorithm is set out below.

a) Preliminary Simplifications.

Two simplifications for equation 4.24 based on the time dependence of variables are made at the outset.

Firstly, if changes in structure are slow then, over a small time interval, equation 4.24 can be considered as a partial differential equation for $c_{Pb2+}(r,t)$ with constant structural parameters. This is the case where time intervals in the order of seconds are used given the typical total charge time of eight hours.

Secondly, if changes in independent variables defined by the aggregate model are slow compared to the transport of Pb^{2+} then, over a small time interval, the transport system can be considered to be at steady state. This would be expected to be the case for a typical charging scheme where charge current reduces by about one order of magnitude and the acid concentration (which determines D_{Pb2+} and c_{ePb2+}) approximately doubles over the total charge time. The steady state simplification means the left hand side of equation 4.24 can be set to zero and the partial differential equation can be replaced by an ordinary differential equation with constant parameters. The ordinary differential equation represents the situation at one point in time. The time dependence can be dealt with by updating the equation parameters for each successive time step.

b) The Solution at One Point in Time.

Taking account of the simplifications above equation 4.24 becomes

$$\left[s_{vo} - \pi r_v^{k-1}(r)^2\right] \frac{d^2 c_{Pb2+}^{k}(r)}{dr^2}$$

$$+ \left[\frac{d}{dr}\left[s_{vo} - \pi r_v^{k-1}(r)^2\right]\right] \frac{dc_{Pb2+}^{k}(r)}{dr}$$

$$+ \frac{K_e^{k}}{2F\ D_{Pb2+}^{k}} \left[2\pi f_v r_v^{k-1}(r) - \pi \frac{dr_v^{k-1}(r)^2}{dr}\right] c_{Pb2+}^{k}(r)$$

$$= 0 \ \dagger \qquad (4.41)$$

where $s_{vo} = S_{xPbSO4o}/n_{vo}$ (m^2).

Equation 4.41 can now be solved in space using first order difference approximations for the concentration and concentration gradient. Rearranging the backwards difference approximation of the concentration space gradient gives

$$c_{Pb2+}^{n-1,k} = c_{Pb2+}^{n,k} - \Delta r\ c'^{n,k}_{Pb2+} \ \dagger\dagger \qquad (4.42)$$

where $c'^{n,k}_{Pb2+}$ represents the concentration space gradient.

† Note: the point in time for which the variables above are defined has been denoted by the superscripts involving " k ". These should be interpreted as $t = k\Delta t$ where Δt is the discrete time interval.

†† Note: the point in space for which the variables above are defined has been denoted by the superscripts involving " n ". These should be interpreted as $r = n\Delta r$ where Δr is the discrete space interval.

Rearranging the backwards difference approximation of the second space derivative of the concentration after equating this with the second order derivative defined by equation 4.41 gives

$$c'_{Pb2+}{}^{n-1,k} = c'_{Pb2+}{}^{n,k} + \Delta r(X^k\, c'_{Pb2+}{}^{n,k} + Y^k\, c_{Pb2+}{}^{n,k}) \qquad (4.43a)$$

where

$$X^k = \frac{\pi}{\Delta r}\,\frac{(r_v{}^{n-1,k-1})^2 - (r_v{}^{n,k-1})^2}{s_v 0 - \pi(r_v{}^{n,k-1})^2} \quad \text{and} \qquad (4.43b)$$

$$Y^k = \frac{2\pi f_v\, r_v{}^{n,k-1} + \pi\left((r_v{}^{n-1,k-1})^2 - (r_v{}^{n,k-1})^2\right)/\Delta r}{2F\, D_{Pb2+}{}^k\left(s_v 0 - \pi(r_v{}^{n,k-1})^2\right)}. \qquad (4.43c)$$

The boundary conditions (equations 4.25 and 4.26) can also be rewritten to account for the now discrete time and space intervals. These become

$$c_{Pb2+}{}^{R2(k),k} = c_{ePb2+}{}^k \quad \text{and} \qquad (4.44)$$

$$\frac{dc_{Pb2+}{}^{R2(k),k}}{dr} = \frac{I_x{}^k}{2F\, D_{Pb2+}{}^k\, S_{xPbSO4}{}^k}. \qquad (4.45)$$

Equations 4.42 to 4.45 are sufficient for the numerical solution of the concentration distribution at one point in time. The solution is obtained by first applying the boundary conditions at $R_2(k)$ to get concentration and the concentration gradient at this point and then working backwards to $R_1(k)$ using equations 4.42 and 4.43 to define the concentration and concentration gradient at each new point.

Unfortunately the solution cannot be found by applying the procedure suggested above once at each point. This is because the value of $K_e{}^k$ is not explicitly known but rather implied in the relationship defined by equation 4.38. The discrete form of this equation is

$$I_x^k = K_e^k \sum_{R1(k)}^{R2(k)} (s_v^{n,k}\, c_{Pb2+}^{n,k}\, \Delta r) \qquad (4.46)$$

Equation 4.46 allows K_e^k and therefore the required concentration to be found by an iterative scheme. The scheme used is summarised in the steps below.

i) Estimate the initial K_e^k

ii) Evaluate the concentration distribution using equations 4.42 to 4.45.

iii) Evaluate the box current using equation 4.46.

iv) Compare the current found at step ii) with the known current (from equation 4.37) and adjust K_e^k to give a more favorable comparison.

v) Repeat steps ii) to iv) until the currents agree to within acceptable limits.

c) Updating the Structural Parameters.

The concentration distribution obtained from the formulations above is related to the current density on the growing PbO_2 lobes by the discrete form of equation 4.23. That is,

$$i_v^{n,k} = K_e^k\, c_{Pb2+}^{n,k}. \qquad (4.47)$$

Assuming that this current is constant over the time interval Δt the change in structure ($r_v^{n,k}$) can be found using the discrete form of equation 4.28. This gives

$$r_v^{n,k} = \left(\frac{V_{mPbO2}}{2\pi F} \sum_{0}^{k(t1)} (i_v^{r1,k}\, s_v^{r1,k-1}\, \Delta t) \right)^{0.5}. \qquad (4.48)$$

The limiting value for $r_v^{n,k}$ is r_{vMax} as before. The initial structure is given by discrete representations that

correspond to equations 4.30 and 4.31. That is,

$$r_v^{0,0} = r_{vMax}, \tag{4.49a}$$

$$r_v^{n,0} = 0 \quad \text{for } n \neq 0 \text{ and} \tag{4.49b}$$

$$s_v^{0,0} = 4\pi f_o R_o^2/(n_{vo} \Delta r). \tag{4.50}$$

Finally, the surface area can be determined using the geometric identity defined by equation 4.22. The discrete representation of this equation gives

$$s_v^{n,k} = 2\pi f_v r_v^{n,k} + \pi((r_v^{n-1,k-1})^2 - (r_v^{n,k-1})^2)/\Delta r. \tag{4.51}$$

It should be pointed out that the structural parameters are updated for the points n = 1 to $n(R_2(k))$. The parameters at n = 0 although defined are invariant.

d) Computing the actual surface area.

The procedure given above defines the surface area of the PbO_2 lobes. Knowing this it is a simple matter to apply the discrete representation of equations 4.32 to 4.35 to get the true local surface area. The discrete representations are

$$s_{gPbO2}^{k} = \sum_{1}^{n(R2)} (s_v^{n,k} \Delta r), \tag{4.52}$$

$$s_{cPbO2}^{k} = \sum_{0}^{k1} \left(\frac{S_{xPbSO4}^{k} - S_{xPbSO4}^{k-1}}{S_{xPbSO4}^{k1}} s_{gPbO2}^{k1} \right), \tag{4.53}$$

$$S_{xPbO2}^{k} = s_{gPbO2}^{k} + s_{cPbO2}^{k} \text{ and} \tag{4.54}$$

$$S_{PbO2}^{k} = N_x S_{xPbO2}^{k} \tag{4.55}$$

for equations 4.32 to 4.35 respectively.

e) Computing the effective surface area.

Having evaluated K_e^k while calculating the concentration distribution the effective local surface area

is readily found by applying the discrete form of equation 4.40. That is,

$$S_e^k = I^k/(K_e^k\, c_{ePb2+}^{n,k}). \qquad (4.56)$$

f) Choosing the discrete time interval.

The order of magnitude for the discrete time interval has already been discussed. Here the particular value for the time interval will be considered. The obvious approach is to set a constant time interval. Unfortunately this will result in the moving boundary at R_2^k falling between the fixed space intervals on many occasions. This can be avoided using a small but variable time interval. That is, the time interval can be adjusted to ensure that the moving boundary falls on consecutive space intervals for consecutive (but not equally spaced) points in time. In practice the dependency can be reversed with R adjusted to fixed intervals in space and the time interval calculated from the $PbSO_4$ volume change (defined by equation 4.3) and the known current using Faraday's law. This gives,

$$\Delta t = \frac{2F}{V_{mPbSO4}}\, I^k\, \Delta V_{PbSO4}^k \qquad (4.57)$$

where ΔV_{PbSO4}^k can be evaluated using equation 4.16.

The approach of letting the time interval vary was used in the initial simulations of charging the AM.

g) The complete computational algorithm.

The computational method has been described in some detail above. This is summarised in the flow diagram given in figure 4.8. The system of equations represented here was converted to a Pascal computer program and solved using a MicroVAX II computer cluster. The program used is given in appendix 1.

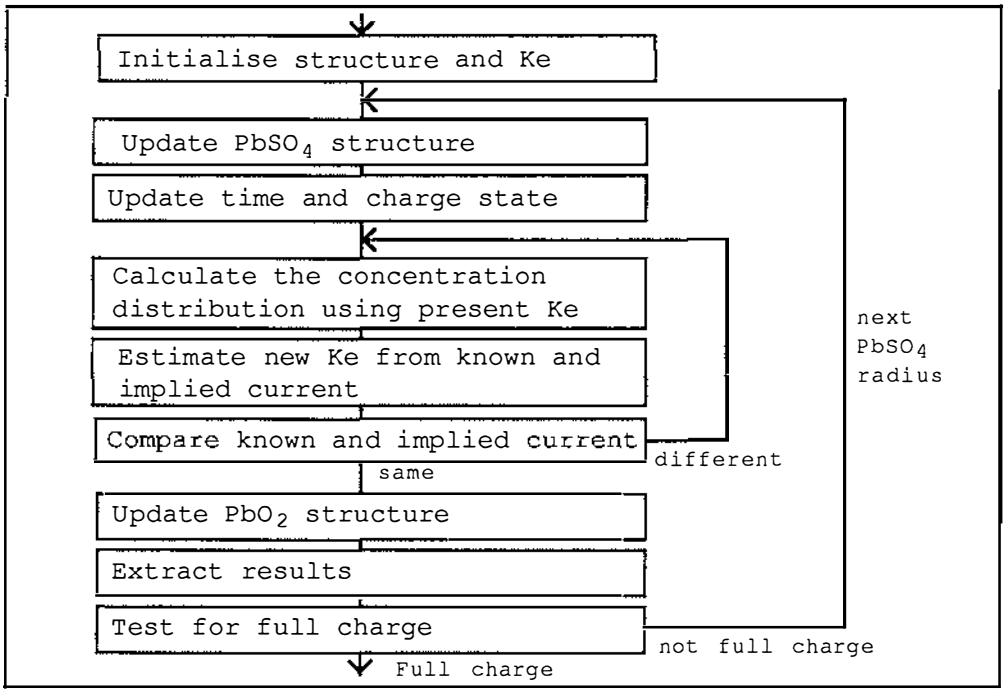

Figure 4.8: Calculation of Charge Surface Area.

The results for the elemental charge surface area model obtained in this way are given in chapter 7. Chapter 5 gives details of the aggregate model.

Chapter 5

An Aggregate Model for the Positive Electrode

The aggregate model represents all cell parts involved in the transportation of acid and charge to the PbO_2/ solution interface of the AM microstructure (the acid transport system). The model presupposes the elemental models of chapter 4. The aggregate model and the elemental models make up the needed components of the VIAM model. That is, together they connect the voltage, current and AM structure of the positive electrode system.

The aggregate model reduces the real cell parts of the acid transport system to a network of cylindrical components. The acid transport and electrical characteristics of the network are then taken to represent the behaviour of the real system. The approach results in a model that resembles a compound single pore model rather than a macrohomogeneous model (see section 3.6). The emphasis on structural form is consistent with recent descriptions of the organisation of the AM (reviewed in section 3.2).

The content of this chapter is summarised below.

i) A definition of the aggregate model based on the cell parts that make up the acid transport system (section 5.1).

ii) Formulations for the physical dimensions of the aggregate model components (section 5.2).

iii) Formulations for the electrical characteristics of the aggregate model components (section 5.3).

iv) Formulations for the acid transport characteristics of the aggregate model components (section 5.4).

v) The practical approach used to solve the formulations given for the aggregate model (section 5.5).

5.1 THE AGGREGATE MODEL.

The generalised acid transport system is a three dimensional network of solution volumes with a variety of structures, electrical characteristics and transport effects. The analysis of this system in total is difficult (if possible at all) because of the large number of points required to adequately represent it and the complex effects involved. For example a void volume in the microstructure is about 10^{-16} m^3. To represent all such volume within even the smallest traction cell would take in the order of 10^{14} points.

To make the system manageable three simplifying steps are performed.

i) The complexity of the problem is reduced by dividing the system into parts which have distinct structural features.

ii) The scale of the problem is reduced by taking a minimum set of these parts to represent the complete system.

iii) A model of connected cylindrical components is defined to represent the real system parts and facilitate analysis using particular one-dimensional system equations.

Each of these simplifying steps is discussed briefly below.

5.1.1 Transport System Parts.

Four transport system parts are readily identified from the cell construction. These are, the cell reservoir region, the cell separator region, the cell negative plate region and the cell positive plate region. The positive plate region, however, is known to contain AM in three structural forms, each of which plays an important role in determining the overall cell performance (see section 3.2.1). These forms are, the homogeneous non-participating AM, the participating AM macrostructure transport channels and the participating AM porous microstructure. A transport system part can be assigned to each of these structural forms. In total this gives six distinct transport system parts. These are illustrated in figure 5.1.

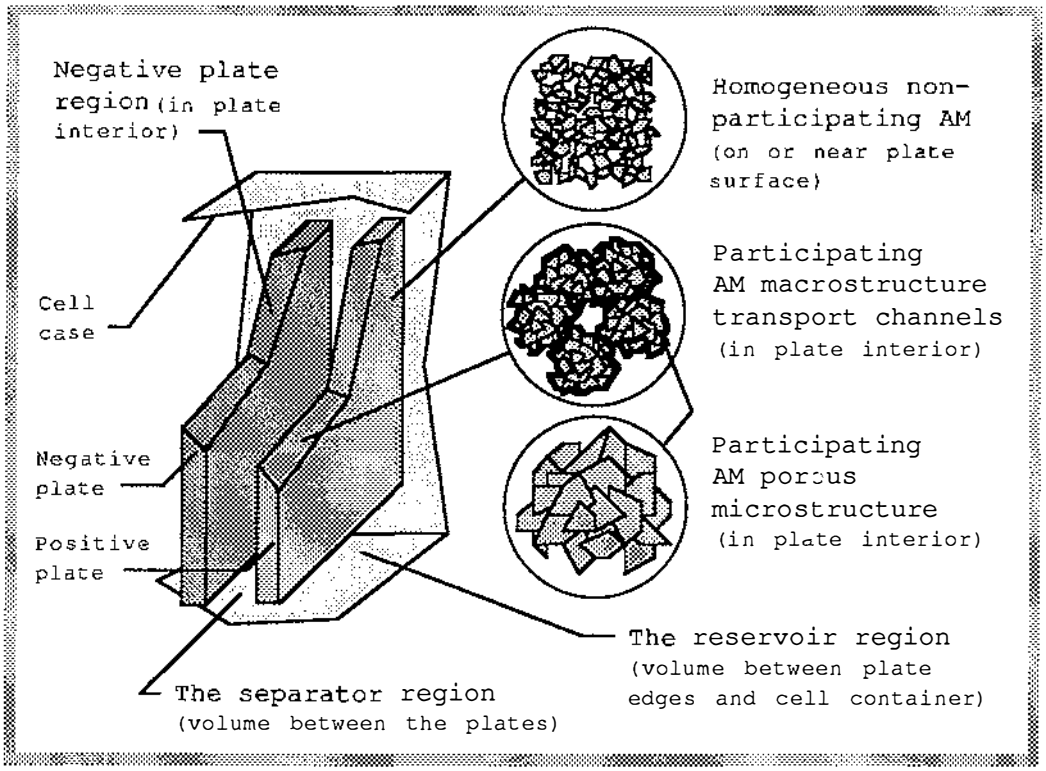

Figure 5.1: Components of the Acid Transport System.

Referring to figure 5.1 the six transport system parts are:

i) the participating AM porous microstructure,

ii) the participating AM macrostructure transport channels,

iii) the homogeneous non-participating AM,

iv) the separator region,

v) the negative plate region and

vi) the cell reservoir region.

5.1.2 A Minimum Representation of the Acid Transport System.

The acid transport system can be simplified if parameters vary mainly with plate thickness and show little dependence on plate height and width. This allows the complete plate behaviour to be determined by a single core sample taken anywhere within the plate area. By comparison, the general case must account for the combined effect of every such sample over the total plate area. The simplified situation is almost always assumed (as in all modelling work reported in section 3.2.3 for example) and will be adopted again here. It should be noted, however, that experimental and theoretical studies do show some dependence on cell height and width (see Sunu and Burrows (1981) and Shepherd (1965) for example). For the simplified situation the question arises as to how small the single core sample can be. The limit is reached at the point beyond which important structural features are lost. The size is therefore determined by the largest structural feature in the positive AM. This is the macrostructure transport channel with its surrounding porous microstructure. That is, the AM associated with one macrostructure transport channel is the minimum sample that can be used to represent the transport system in the plate. This idea can be extended beyond the region of the positive plate into the separator, negative plate and reservoir regions. Here representative portions of these parts which are likely to exchange acid with the parts in the single core sample can be included.

5.1.3 An Aggregate Model for the Acid Transport System.

The parts that make up the minimum representation of the complete acid transport system are formally specified as components of the aggregate model below.

i) A transport channel characterising the macrostructure transport channel contained within the single core sample (the m-channel). This channel has one open and one closed end. The closed end is defined by the plane of symmetry at the centre of the positive plate through which no mass passes. The open end is defined by the boundary between the participating and non-participating AM.

ii) Many smaller transport channels characterising the pores in the agglomerate microstructure of the participating AM contained within the single core sample (the μ-channels). These channels surround the m-channel and have one open and one closed end. The open ends are attached to the m-channel. The closed ends are defined by the points of symmetry within the microstructure through which no mass passes.

iii) A transport channel characterising the pores in the homogeneous structure of the non-participating AM contained within the single core sample (the h-channel). This channel has both ends open. One end is attached to the open end of the m-channel. The other end is defined by the boundary between the positive plate and the separator.

iv) A transport channel characterising the portion of the separator adjacent to the positive plate core sample and containing acid that affects the behaviour of the core sample (the s-channel). This channel has both ends open. One end is attached to the open end of the h-channel at the positive plate boundary. The other end is defined by the boundary between the negative plate and the separator.

v) A transport channel characterising the pores in the negative plate adjacent to the positive plate core sample and containing acid that affects the behaviour

of the core sample (the n-channel). This channel has one open and one closed end. The open end is attached to the open end of the s-channel at the negative plate boundary. The closed end is defined by the plane of symmetry at the centre of the negative plate through which no mass passes.

vi) A transport channel characterising the portion of the reservoir which contains acid that affects the behaviour of the positive plate core sample (the r-channel). This channel has one open and one closed end. The open end is attached midway along the length of the s-channel. The closed end is defined by the boundary at the cell case.

Together the components specified above make up the aggregate model illustrated in figure 5.2.

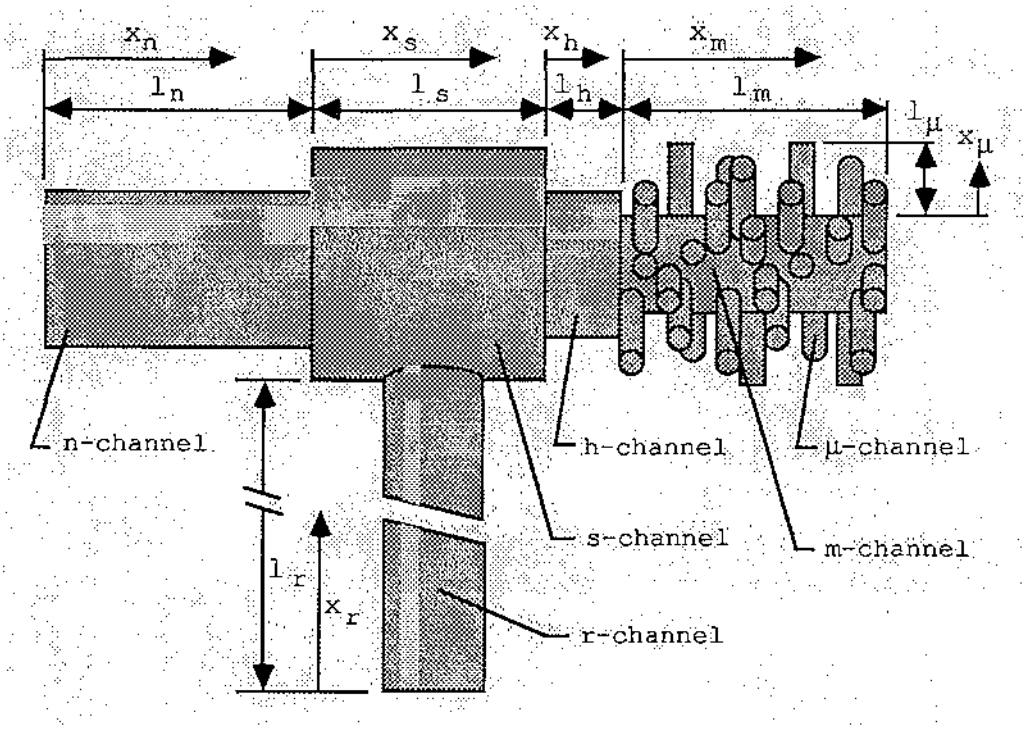

Figure 5.2: The Aggregate Model Components.

Detailed formulations for dimensions, electrical characteristics and acid transport for the model are given in the following sections.

5.2 PHYSICAL DIMENSIONS OF THE AGGREGATE MODEL.

5.2.1 The m-channel Dimensions.

The cross-sectional area of the m-channel can be defined from the equivalent gram volume and surface area values assuming a cylindrical form. The identities for these quantities are

$$V_m = N_m\, a_m\, l_m \quad \text{and} \tag{5.1}$$

$$S_m = N_m\, f_m\, 2(\pi\, a_m)^{0.5}\, l_m \tag{5.2}$$

where

V_m ($m^3.g^{-1}$) is the equivalent gram volume of m-channels,

N_m (g^{-1}) is the equivalent gram number of m-channels,

l_m (m) is the m-channel length,

a_m (m^2) is the m-channel cross-sectional area,

S_m ($m^2.g^{-1}$) is the equivalent gram surface area of m-channels and

f_m is the m-channel surface roughness factor.

Dividing equation 5.1 by equation 5.2 and rearranging gives

$$a_m = 4\pi(f_m\, V_m/S_m)^2 \tag{5.3}$$

The surface area of the m-channel is made up of the surface area of the surrounding agglomerates of microstructure crystallites (see figure 3.2a). This surface area is considerably greater than that of a cylinder of the same cross-sectional area and indicates that f_m is much greater than unity. The quantities V_m and S_m make up part of the experimental volume and surface area distribution data of

the type given in figure 3.1. That is, the part obtained after the boundary for the macro and microstructure has been set and an allowance has been made for the contribution of the non-participating AM.

The length of a m-channel can be written as

$$l_m = \theta_m \chi_m S_p \qquad (5.4)$$

where

θ_m is the m-channel tortuosity factor,

χ_m is the proportion of the positive plate thickness containing participating AM and

S_p (m) is half the positive plate thickness (thickness to the plane of symmetry).

The equivalent gram number of m-channels in the AM can be obtained by dividing the volume of a single m-channel into the equivalent gram volume of the macrostructure. This gives

$$N_m = V_m/(a_m l_m). \qquad (5.5)$$

Equations 5.3 to 5.5 define the dimensions of the m-channel from experimentally observable quantities.

5.2.2 The μ-channel Dimensions.

The cross-sectional area of the typical μ-channel in its fully charged state can be defined in a similar way to that for the m-channel. That is,

$$a_{\mu 0} = 4\pi(f_\mu V_\mu/S_\mu)^2 \qquad (5.6)$$

where

$a_{\mu 0}$ (m^2) is the full charge μ-channel cross-sectional area,

f_μ is the μ-channel surface roughness factor,

V_μ ($m^3.g^{-1}$) is the equivalent gram volume of μ-channels and

S_μ ($m^2.g^{-1}$) is the equivalent gram surface area of the μ-channels.

The symbol for the cross-sectional area has a "0" appended to indicate it is for the fully charged state. In general, the μ-channel cross-sectional area will be allowed to vary to represent the structural changes in the microstructure (these have already been discussed in section 4.1). The surface area of the μ-channel is made up of the surface area of the surrounding crystallites (see figure 3.2b). As with the m-channel, this surface area is considerably greater than that of a cylinder of the same cross-sectional area and indicates that f_μ is much greater than unity. The quantities V_μ and S_μ make up part of the experimental volume and surface area distribution data in the same way as did the corresponding quantities for the m-channel.

The μ-channel length can be defined in terms of the solution and total volumes of the microstructure associated with a single m-channel. These are given by

$$V_{m\mu} = V_\mu/N_m \text{ and} \tag{5.7}$$

$$V_{m\mu tot} = V_{\mu tot}/N_m \tag{5.8}$$

where

$V_{m\mu}$ (m^3) is the volume of solution phase microstructure associated with a m-channel and

$V_{m\mu tot}$ (m^3) is the total volume of the microstructure associated with a m-channel.

Two approximations are made concerning the arrangement of the microstructure volumes around the m-channel. Firstly, $V_{m\mu tot}$ is taken as being contained in a cylindrical sleeve around the m-channel. Secondly, within this sleeve, the μ-channels that make up the volume $V_{m\mu}$ are taken as radial cylinders that extend throughout the thickness of the sleeve. This situation is illustrated in figure 5.3.

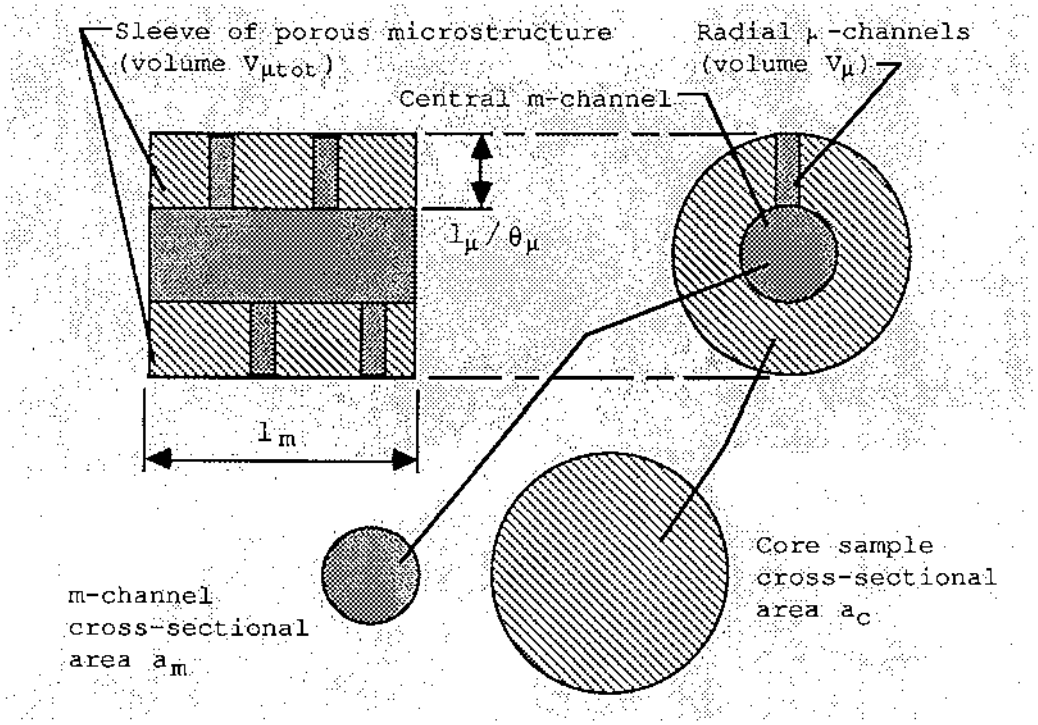

Figure 5.3: μ-channel Arrangement Around the m-channel.

The combined cross-sectional area of the m-channel and surrounding cylindrical sleeve is the cross-sectional area of the core sample for the minimum representation of the acid transport system discussed in section 5.1.2. This is given by

$$a_c = a_m + V_{m\mu tot}/l_m \qquad (5.9)$$

where a_c (m^2) is the core sample cross-sectional area.

The μ-channel length is obtained by manipulating geometric identities for the m-channel and core sample cross-sectional areas. This gives

$$l_\mu = \theta_\mu(\sqrt{a_c} - \sqrt{a_m})/\sqrt{\pi} \qquad (5.10)$$

where

l_μ (m) is the μ-channel length and

θ_μ is the μ-channel tortuosity factor.

The number of μ-channels associated with a single m-channel can be obtained by dividing the volume of one μ-channel into the solution volume of the microstructure associated with a single m-channel. That is,

$$N_{m\mu} = V_{m\mu}/(a_{\mu 0}\ l_{\mu}) \qquad (5.11)$$

where $N_{m\mu}$ is the number of μ-channels associated with a single m-channel.

The situation at full charge has now been defined. Consider next the situation at the general charge state X (X=1 for fully charged AM and X=0 for fully discharged AM). If the microstructure at some arbitrary position along a μ-channel is discharged to this state then solution volume at this position will be given by the fraction X of the fully charged volume (see the discussion on discharge capacity in section 4.1). Further, if the volume concerned is of a constant incremental length then the cross-sectional area will be this same fraction of the fully charged area. This gives

$$a_{\mu}(X) = a_{\mu 0}\ X. \qquad (5.12)$$

where $a_{\mu}(X)$ (m^2) is the μ-channel cross-sectional area at the general charge state X.

The general charge state is defined by the equivalent gram values in equation 4.7. For the purposes of this model it is necessary to relate this to the PbO_2/solution interface current in the μ-channel. This can be done by writing the equivalent gram capacity in terms of the time integral of the equivalent gram interface current. The equivalent gram interface current is given by product of the actual interface current and the ratio of the equivalent gram to actual interface surface area. Substituting expressions for these identities into equation 4.7 gives the charge state at time t_1 as

$$X(x_\mu, t_1) = 1 - \frac{N_m N_{m\mu} l_\mu}{q_0 \, dx_\mu} \int_{t=0}^{t_1} dI_\mu(x_\mu, t) \, dt \qquad (5.13)$$

where

dx_μ (m) is the increment of μ-channel length over which the charge state is defined and

dI_μ (A) is the current flowing through the solution/PbO_2 boundary within that increment.

Equations 5.6 and 5.10 to 5.13 define the dimensions of the μ-channel for the full charge and general charge state from experimentally observable quantities and the m-channel structure.

5.2.3 The h-channel Dimensions.

Assuming the transport channels through the thickness of the plate consist of an h-channel connected to a m-channel, the length of the h-channel can be written as

$$l_h = \theta_h (1 - \chi_m) S_p \qquad (5.14)$$

where

l_h (m) is the h-channel length and

θ_h is the h-channel tortuosity factor.

The volume of the solution in the non-participating AM associated with a single h-channel can be taken as the product of the average porosity of the positive AM, the cross-sectional area of the core sample and the proportion of the plate thickness occupied by non-participating AM. If this volume is equated with that of a single transport channel of length l_h then the cross-sectional area of this channel is given by

$$a_h = \rho_p \, a_c / \theta_h \qquad (5.15)$$

where

a_h (m^2) is the h-channel cross-sectional area,

ρ_p is the average positive AM porosity and

θ_h is the h-channel tortuosity factor.

Equations 5.14 and 5.15 define the structure of the h-channel in terms of known parameters.

5.2.4 The s-channel Dimensions.

The s-channel length is equal to the separator thickness and the s-channel cross-sectional area is equal to the core sample cross-sectional area when corrected for the area of the plate grid members. That is,

$$l_s = S_s \tag{5.16}$$

and

$$a_s = a_c \frac{H_p W_p}{(H_p - H_g)(W_p - W_g)} \tag{5.17}$$

where

l_s (m) is the s-channel length,
S_s (m) is the separator thickness,
a_s (m^2) is the s-channel cross-sectional area,
H_p (m) is the plate height,
W_p (m) is the plate width,
H_g (m) is the combined height of all horizontal grid members in the positive plate and
W_g (m) is the combined width of all vertical grid members in the positive plate.

The s-channel cross-sectional area also defines the number of m-channels per unit plate area. That is,

$$N_{ma} = 1/a_s \tag{5.18}$$

where N_{ma} (m^{-2}) is the number of m-channels per unit plate area.

Equations 5.16 and 5.17 define the s-channel dimensions in terms of other known parameters. They assume that the dimensions of the solid separator components are negligible compared to the dimensions of the solution in

the separator region .

5.2.5 The n-channel Dimensions.

The n-channel is defined to account for the acid present in the porous negative plate that affects the behavior of the adjacent components in the positive plate. It is not the intention here to give a detailed description of the negative plate system in its own right. With this in mind, the negative plate is treated as a porous structure of uniformly distributed crystallites and the n-channel dimensions are found in a similar way as those of the h-channel above. That is,

$$l_n = \theta_n S_n \tag{5.19}$$

and

$$a_{n0} = \rho_n a_c/\theta_n \tag{5.20}$$

where

l_n (m) is the n-channel length,
S_n (m) is half the negative plate thickness,
θ_n is the n-channel tortuosity factor,
a_{n0} (m^2) is the n-channel cross-sectional area at full charge and
ρ_n is the average negative AM porosity.

As before the "0" is appended to the n-channel cross-sectional area to indicate that it is defined for the fully charged state. In practice the area varies because of volume changes in the negative active mass. In this simple representation of the negative electrode this variation will be assumed to be uniform along the n-channel length. It can be calculated using Faraday's law, the known solid phase molar volumes and the current flowing into the n-channel. That is, the cross-sectional area at time t_1 is

$$a_n = a_{n0} - \frac{1}{l_n} \frac{V_{mPbSO4} - V_{mPb}}{2F} \int_{t=0}^{t_1} I_h(t)\,dt \tag{5.21}$$

where

a_n (m^2) is the n-channel cross-sectional area at the general charge state,

V_{mPbSO4} ($m^3.mol^{-1}$) is the molar volume of $PbSO_4$,

V_{mPb} ($m^3.mol^{-1}$) is the molar volume of Pb and

I_h (A) the current in the h-channel which is equal to the current flowing into the n-channel.

Equations 5.19 to 5.21 define the structure of the n-channel for the full charge and general charge state in terms of known parameters.

5.2.6 The r-channel Dimensions.

The r-channel is defined to account for acid in the reservoir region of the cell that affects the behaviour of components associated with a single core sample. Attention to the details of this channel reveals the major weakness in the assumption that transport parameters have little dependence on plate height and width. This assumption requires that all portions of the plate are affected to the same extent by the acid in the reservoir. In practice however, portions near the plate edge are affected to a greater extent than portions in the relatively inaccessible interior. The approach taken here attempts to define the r-channel in such a way that overall plate behaviour for the assumed case is equivalent to the case in practice. To this end the r-channel length is defined for an average position in the plate. In specifying this position it is convenient to represent the rectangular plate and surrounding rectangular cell case as circular components of the same cross-sectional area as the rectangular components. This gives,

$$R_p = (H_p\ W_p/\pi)^{0.5} \qquad (5.22)$$

and

$$R_c = (H_{c0}\ W_c/\pi)^{0.5} \qquad (5.23)$$

where

R_p (m) is the circular plate radius,

R_c (m) is the circular case radius,

H_{c0} (m) is the height from the case bottom to the solution level for the fully charged state and

W_c (m) is the case width.

The average position on the plate is at a circular radius of $R_p/\sqrt{2}$ which when subtracted from the circular cell radius gives

$$l_r = R_c - R_p/\sqrt{2} \tag{5.24}$$

where l_r (m) is the r-channel length.

The volume of solution in the r-channel at full charge can be found by dividing the total reservoir volume at full charge by the number of m-channels in the cell. This gives

$$V_{mr0} = \frac{H_{c0}\ W_c\ S_c - H_p\ W_p(N_p S_p + N_p S_s + (N_p+2) S_n)}{N_p\ H_p\ W_p\ N_{ma}} \tag{5.25}$$

where

V_{mr0} (m^3) is the volume of r-channel associated with an m-channel at full charge,

N_p is the number of positive half plates in the cell and

S_c (m) is the cell case thickness.

The cross-sectional area of the r-channel at full charge can now be given by

$$a_{r0} = V_{mr}/l_r \tag{5.26}$$

where a_{r0} (m^2) is the r-channel cross-sectional area for the full charge state.

Again it will be noted that several symbols above have a "0" appended to indicate they are defined for the fully charged state. In general, they will vary in response to the changes in solution volume in the reservoir. The

solution volume changes are due to the inflow of solution caused by volume changes in the positive and negative AM dimensions and, to a much lesser degree, to solution density changes caused by changes in acid concentration. Only the first effect will be taken into account in the formulations which follow. In the r-channel the volume variation is accounted for by allowing the r-channel radius to vary. As with the n-channel cross-sectional area this is readily calculated using Faraday's law, molar volumes for the positive and negative AM and the total current passing into the μ-channels and n-channel. That is the r-channel radius at time t_1 is

$$a_r = a_{r0} + \frac{1}{l_r} \frac{2V_{mPbSO4} - V_{mPbO2} - V_{mPb}}{2F} \int_{t=0}^{t_1} I_h(t)\,dt \qquad (5.27)$$

where

a_r (m^2) is the r-channel cross-sectional area in the general charge case and

V_{mPbO2} ($m^3.mol^{-1}$) is the molar volume of PbO_2.

Equations 5.24, 5.26 and 5.27 define the dimensions of the r-channel for the full charge and general charge state in terms of other known parameters.

This completes the specification of the physical structure of the aggregate model. Attention will now be given to electrical characteristics of the components through which current passes.

5.3 AGGREGATE MODEL ELECTRICAL FORMULATIONS.

The aggregate model can be used to determine the electrical characteristics that relate directly to the key parameters of the VIAM model of the positive electrode. These parameters are listed below.

i) The difference in potential between the solution at the s-channel/h-channel junction and the solid phase PbO_2 at the walls of the μ-channels which gives the potential across the positive electrode.

ii) The current passing in the h-channel which when multiplied by the number of such channels in the cell gives the total cell current.

iii) The local current distribution in the μ-channels which gives the structural changes in the AM.

The determination of these characteristics involves the calculation of the current and potential distribution throughout the h-channel, m-channel and all μ-channels.

The aggregate model can also be used to determine the potential across the separator and the potential across the negative electrode. These are not strictly characteristics of the positive electrode but are useful for providing data to compare with experimental studies. The potential across the negative electrode is based on a simplified representation of this part.

The electrical characteristics of the aggregate model can be found from the electrical characteristics of the channels passing cell current. All channels but the r-channel pass current. The time dependent nature of the electrical characteristics comes from changes in acid concentration determined by acid transport in all six channels and from the dimension changes in the μ-channel and n-channel with state of charge.

The electrical characteristics can be analysed using a distributed network of equivalent circuit components to represent the system (an approach more general than, but not unlike, that used for the single pore model described in section 3.6.1). The system involves the following situations and representative circuit componerts.

i) Current passing through electrolyte solution. Here potential difference is proportional to current (see equation 3.29) and the equivalent circuit component can be a simple resistance.

ii) Current passing through a PbO_2/solution interface. Here potential differences due to both the local interface equilibrium potential and the current induced overpotential are involved. These effects can be represented by an ideal cell and a nonlinear resistance respectively. The latter effect involves the surface area defined by the elemental models set out in chapter 4.

iii) Current passing through solid phase PbO_2. Here since the PbO_2 has a very high conductivity compared to sulphuric acid solution, the potential differences can be assumed to be negligible compared to those in other components containing acid solution (this is a common assumption, see Dasoyan and Aguf (1979) for example). A conductor (wire) of zero resistance can be used as the circuit component here.

In all but the last case the circuit components are time dependent due to the changes in acid concentration and dimensions mentioned above.

Details and formulations for the equivalent circuit components in the h-channel, m-channel μ-channels, s-channel and n-channel are given in the following sections. In these formulations current flowing from the solution towards the solid phase PbO_2 is taken as positive and the potential at the s-channel/h-channel junction is arbitrarily taken as zero.

5.3.1 The h-channel Equivalent Circuit.

In the h-channel current passes in electrolyte

solution only. Also, since there is no divergence of current into the AM surrounding the h-channel (it is inactive), the same current flows throughout the length of the h-channel. This means that the h-channel can be represented by a single equivalent resistance. The value of this resistance is obtained by dividing the h-channel into incremental segments and summing the resistance of each of these. Given that the segments have a length of dx_h and an area of a_h, the equivalent resistance is defined by

$$R_h(t) = \frac{1}{a_h} \int_{x_h=0}^{l_h} \rho_h(x_h,t)\ dx_h \qquad (5.28)$$

where

R_h (Ω) is the h-channel equivalent resistance and

ρ_h (Ω.m) is the solution resistivity (equal to $1/\kappa$ see equation 3.27).

The potential/current relationship for the h-channel can now be given by

$$U_h(t) = - I_h(t)\ R_h(t) \qquad (5.29)$$

where

U_h (v) is the potential at the h-channel/m-channel junction and

$I_h(t)$ (A) is the current in the h-channel.

The current in the h-channel is related to the total cell current by

$$I_h(t) = \frac{I_{cell}(t)}{N_p\ H_p\ W_p\ N_{ma}} \qquad (5.30)$$

where I_{cell} (A) is the total cell current and a uniform current distribution over the plate area is assumed.

5.3.2 The m-channel Equivalent Circuit.

Like the h-channel, in the m-channel current passes in electrolyte solution only. However, in this case, current diverges from the m-channel into the surrounding μ-channels. This means the m-channel cannot be represented by a single resistance but rather by a series of resistances with side branches at the μ-channel openings. The side branches allow for the current flow in the surrounding μ-channels. Assuming the μ-channels are equally spaced, the m-channel length naturally divides into $N_{m\mu}$ discrete segments of length $\Delta x_m = l_m / N_{m\mu}$. Division in this way gives rise to $N_{m\mu}$ series resistances and branches. This arrangement is illustrated in figure 5.4. The value of the series resistances is given by the resistance of the solution segments between each μ-channel. Given that these segments are of area a_m and taking the solution resistivity (concentration) to be constant over the small lengths involved the series resistances are defined by

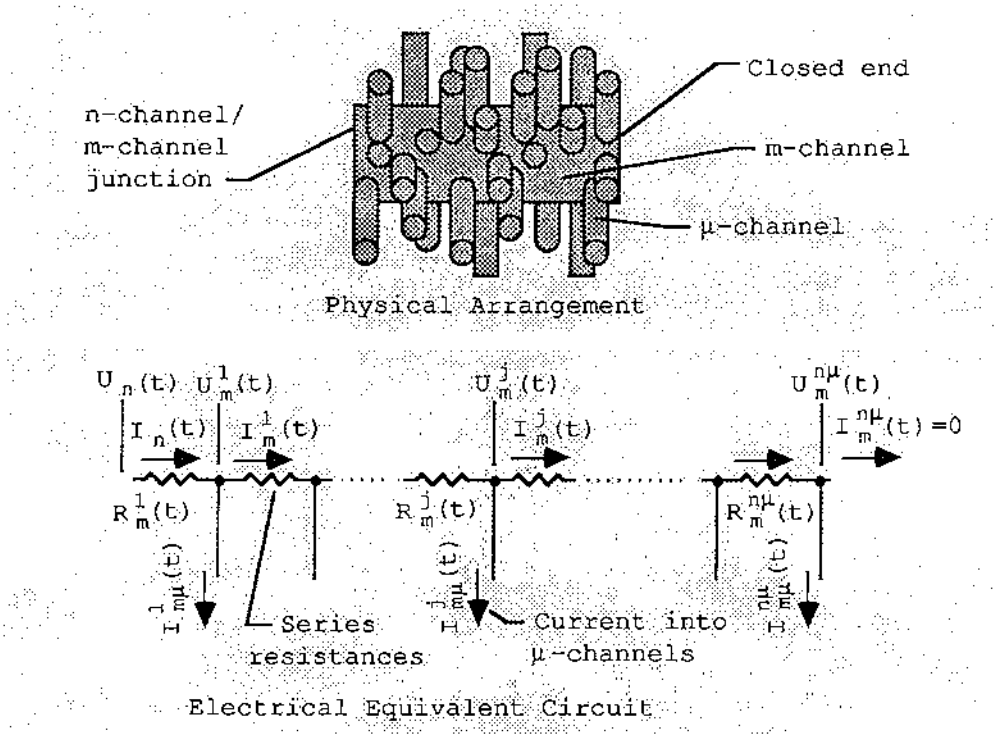

Figure 5.4: The m-channel Equivalent Circuit.

$$R_m^j(t) = \frac{l_m \rho_m^j(t)}{a_m N_{m\mu}} \qquad (5.31)$$

where

the superscript "j" defines the position on the m-channel (j=1 at the n-channel/m-channel junction and $j=N_{m\mu}$ at the closed end),

R_m (Ω) is the series resistance and

ρ_m (Ω.m) is the solution resistivity.

The potential at position j_1 on the m-channel is given by

$$U_m^{j1}(t) = U_h(t) - \sum_{j=1}^{j1} R_m^j(t)\, I_m^j(t) \qquad (5.32)$$

where

U_m (v) is the m-channel potential and

I_m^j (A) is the m-channel current flowing between the j^{th} and $j+1^{th}$ μ-channel.

The current along the m-channel axis is itself given by the current into the m-channel at the h-channel/m-channel junction less the current passing into the surrounding μ-channels. That is,

$$I_m^{j1}(t) = I_h(t) - \sum_{j=1}^{j1} I_{m\mu}^j(t) \qquad (5.33)$$

where $I_{m\mu}^j$ (A) is the current into the j^{th} μ-channel.

5.3.3 The μ-channel Equivalent Circuit.

Current passes in solution along the axis of the μ-channel and through the PbO_2/solution interface at the surface of the μ-channel where the electrochemical reaction occurs. This is a distributed process that does not have the naturally occurring discrete division seen in the m-channel case. If, however, the μ-channel is divided into

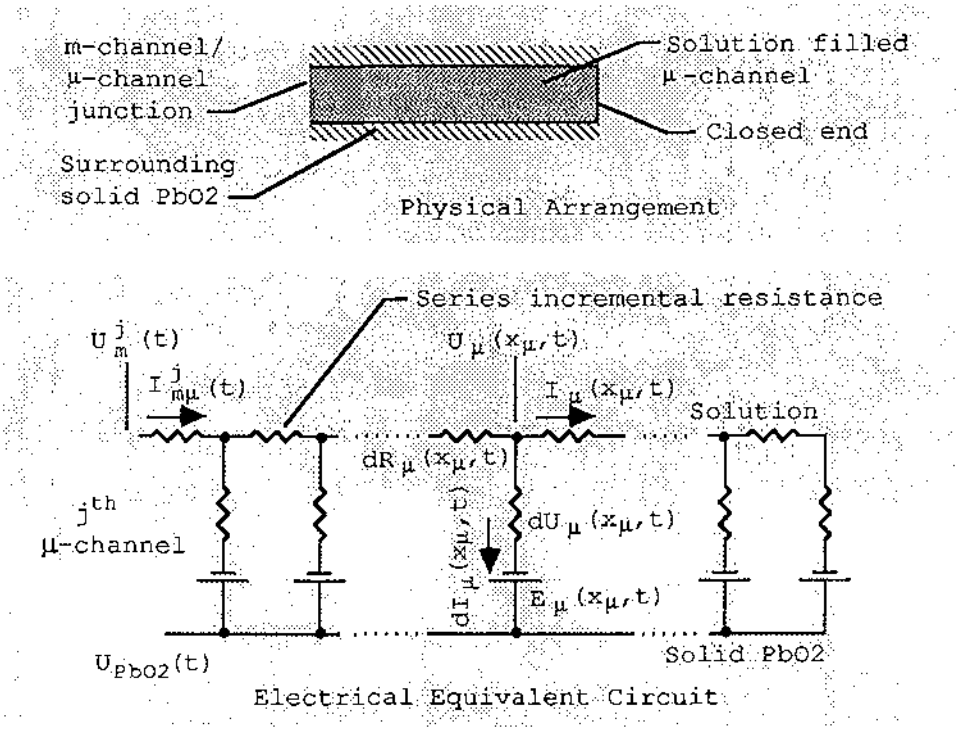

Figure 5.5: The μ-channel Equivalent Circuit.

incremental segments of length dx_μ, it can be treated in a similar manner to the m-channel. That is, as a series of incremental resistances with side branches allowing for current passing into incremental areas of PbO_2/solution interface. This arrangement is illustrated in figure 5.5.

The value of each of the series incremental resistances is given by the resistance of each incremental volume of solution involved. Given that these volumes are of length dx_μ and area $a_{\mu 0}$ X the series incremental resistances are defined by

$$dR_\mu(x_\mu,t) = \frac{dx_\mu \ \rho_\mu(x_\mu,t)}{a_{\mu 0} \ X(x_\mu,t)} \qquad (5.34)$$

where

x_μ (m) defines the position of the series incremental resistance on the μ-channel,

dR_μ (Ω) is the series incremental resistance and
ρ_μ ($\Omega.m$) is the solution resistivity in the μ-channel.

Two circuit components can also be assigned to the branches. Conceptually these components connect points in the solution of the μ-channel to the solid phase PbO_2 of the plate. The components are an ideal cell, representing the local equilibrium potential of the solution/PbO_2 interface, and a nonlinear resistance, representing the current/overpotential characteristic of the interface.

The ideal cell potential is given by equation 3.5 where the acid concentration is for the local point concerned and the lead ion concentration is given by the $PbSO_4$ dissolution-precipitation equilibrium reaction in the acid at this point.

Equations 3.15a and 3.16b can be written in terms of the current through the PbO_2/solution interface of an μ-channel segment of length dx_μ. The resulting equations define the current/overpotential relationship of the nonlinear resistance. The surface area involved is the fraction $dx_\mu/(N_m\ N_{m\mu}\ l_\mu)$ of the equivalent gram quantity. These identities give

$$dI_\mu(x_\mu,t) = \frac{2i_{01}\ dx_\mu\ S_{PbO2}}{N_m\ N_{m\mu}\ l_\mu}\ e^{(\alpha_1 F\ dU_\mu(x_\mu,t)/RT)} \quad (5.35)$$

and

$$dI_\mu(x_\mu,t) = -\frac{2i_{02}\ dx_\mu\ S_E}{N_m\ N_{m\mu}\ l_\mu}\ e^{((1-\alpha_2)F\ dU_\mu(x_\mu,t)/RT)} \quad (5.36)$$

for the discharge and charge respectively, where

dU_μ (v) is the overpotential at the PbO_2/solution interface in the segment and
dI_μ (A) is the current through the PbO_2/solution interface area within the segment.

An explicit form for the nonlinear resistance is not required.

The surface area S_{PbO2} in equation 5.35 is a simple function of charge state given by equation 4.8. As a result the calculation of dI_μ is relatively straight forward for the discharge case. In contrast, the effective surface area S_E in equation 5.36 is a complex function of past discharge/charge conditions, present charge state and present charge current. It is determined by operating the elemental charge surface area model set out in chapter 4. As a result considerable effort is required to calculate dI_μ in the charge case. Further, it should be realised that this effort is multiplied many times to find dI_μ at enough points to adequately define the complete system. In chapter 7 however, it will be seen that S_E is not greatly dependent on the past discharge/charge conditions. This is a fortuitous result that means S_E can be treated as a function of present charge state and present charge current only. The elemental charge surface model can be used to give tabulated data for this function thereby greatly reducing the effort required to define S_E.

The current/potential relationship at some point $x_{\mu 1}$ on the μ-channel axis is given by summing the potential drops across the series incremental resistances. This gives

$$U_\mu(x_{\mu 1},t) = U_m{}^j(t) - \int_{x_\mu=0}^{x_{\mu 1}} dR_\mu(x_\mu,t)\ I_\mu(x_\mu,t) \qquad (5.37)$$

where

U_μ (v) is the μ-channel potential and

I_μ (A) is the μ-channel axial current.

The μ-channel axial current is itself given by the current passing into the opening of the μ-channel less the current passing through the PbO_2/solution interface. That is,

$$I_\mu(x_{\mu 1},t) = I_{m\mu}{}^j(t) - \int_{x_\mu=0}^{x_{\mu 1}} dI_\mu(x_\mu,t). \qquad (5.38)$$

The potential/current relationship along a branch in the μ-channel axis is given by the potential difference across each branch circuit component. That is,

$$U_{PbO2}(t) = U_{\mu}(x_{\mu},t) - dU_{\mu}(x_{\mu},t) + E_{\mu}(x_{\mu},t) \qquad (5.39)$$

where

U_{PbO2} (v) is the potential at the PbO_2 solid phase and

E_{μ} (v) is the potential across the ideal cell.

U_{PbO2} in equation 5.39 is independent of position since the potential differences in the highly conductive solid phase are assumed to be negligible in comparison to those in the solution phase. In addition, since the potential at the h-channel mouth on the plate surface has arbitrarily been defined as zero, U_{PbO2} is equal to the potential difference across the positive electrode.

5.3.4 The Complete Equivalent Circuit.

The complete equivalent circuit is illustrated in figure 5.6. It is formed by combining the individual circuit components defined above. In principle this circuit can be solved by writing voltage loop and current node circuit equations and evaluating these simultaneously. The independent variable is the cell current. The solution gives the current in all the equivalent circuit components and the potential at all component junctions in the system. These results enable the evaluation of the state of charge using equation 5.13 and the acid transport formulations given in the following section. These, in turn, control the time dependence of the circuit components and ultimately time dependent behaviour of the complete electrode system.

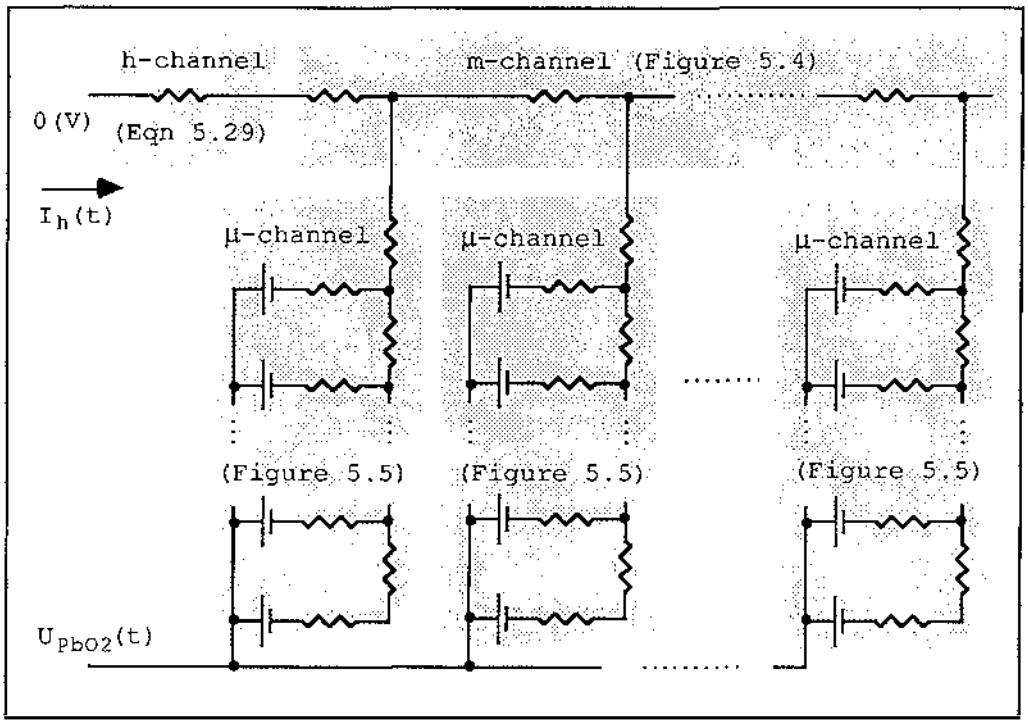

Figure 5.6: The Aggregate Model Equivalent Circuit.

5.3.5 Supplementary Formulations for the s-channel and n-channel.

Although the electrical characteristics of the s-channel and n-channel are not required to describe the positive electrode, they are given below as supplementary formulations that can be used where an estimation of the total voltage of a lead-acid cell is required.

The s-channel can be represented by a single resistance in the same way as the h-channel above. This gives

$$R_s(t) = \frac{1}{a_s} \int_{x_s=0}^{l_s} \rho_s(x_s,t)\, dx_s \qquad (5.40)$$

and

$$U_s(t) = I_h(t)\, R_s(t) \qquad (5.41)$$

where

R_s (Ω) is s-channel equivalent resistance,

ρ_s (Ω.m) is the solution resistivity and

U_s (v) is the potential at the s-channel/n-channel junction.

The n-channel can be represented as a distributed network of components similar to that for the μ-channels above. However, this representation requires an unjustifiable effort to gain a secondary result. As a simple alternative, the n-channel is represented by a single resistance and single ideal cell. The resistance is defined for the channel segment from the s-channel/n-channel junction to the midpoint of the n-channel. The ideal cell is defined at the midpoint of the n-channel. This gives

$$R_n(t) = \frac{1}{a_n(t)} \int_{x_n=l_n/2}^{l_n} \rho_n(x_n,t)\, dx_n \qquad (5.42)$$

and

$$U_{Pb}(t) = U_s(t) + I_h(t)\, R_n(t) - E_n(t) \qquad (5.43)$$

where

R_n (Ω) is the n-channel equivalent resistance,

ρ_n (Ω.m) is the solution resistivity,

U_{Pb} (v) is the potential of the solid phase Pb of the negative plate and

E_n (v) is the equilibrium potential for the negative electrode reaction at the midpoint of the n-channel.

It can be seen that the n-channel formulations neglect the overpotential of the negative electrode. This is a reasonable approximation except near the end of charge (see Sunu and Burrows (1981)).

5.4 AGGREGATE MODEL ACID TRANSPORT FORMULATIONS.

Transport of acid in the aggregate model is defined by general equation 3.31. This equation can be made particular to each of the model components by taking into account the individual component characteristics. This allows the equation to be simplified where the dependency of the cross-sectional area, bulk solution velocity or acid reaction rate is less general than in the original formulation. It also enables explicit formulations for these parameters to be given. The resulting equations can in principle be solved to give the acid distribution in space and time for the particular component concerned, provided a suitable initial condition and two boundary conditions are known.

The general transport, general boundary condition and general initial condition equations are given below. These are followed by the particular forms that apply to each of the six model components. The equations are developed assuming the structural details given by the formulations in section 5.2 and the solution currents found from the formulations in section 5.3. In the notation employed "i" and "i̱" are used as subscripts to indicate the general case and the channel prefix is used as a subscript to indicate a particular case. When the m-channel is under consideration it is assumed to be divided into $N_{m\mu}$ discrete segments of length Δx_m as in section 5.3.2.

5.4.1 The General Transport, Boundary Condition and Initial Condition Equations.

a) The general transport equation.

An expanded form of equation 3.32 compatible with the formulations that are to follow is

$$\frac{\partial c_i(x_i,t)}{\partial t} = L_i(x_i,t)\frac{\partial^2 c_i(x_i,t)}{\partial x_i^2} + M_i(x_i,t)\frac{\partial c_i(x_i,t)}{\partial x_i} + N_i(x_i,t)c_i(x_i,t) + O_i(x_i,t) \quad (5.44a)$$

where

$$L_i(x_i,t) = D_i(x_i,t), \quad (5.44b)$$

$$M_i(x_i,t) = \left[\frac{1}{a_i(x_i,t)} \frac{\partial a_i(x_i,t)D_i(x_i,t)}{\partial x_i} - v_i(x_i,t) \right], \quad (5.44c)$$

$$N_i(x_i,t) = \left[\frac{-1}{a_i(x_i,t)} \left[\frac{\partial a_i(x_i,t)v_i(x_i,t)}{\partial x_i} + \frac{\partial a_i(x_i,t)}{\partial t} \right] \right] \quad (5.44d)$$

and

$$O_i(x_i,t) = \frac{P_i(x_i,t)}{a_i(x_i,t)}. \quad (5.44e)$$

b) The general boundary condition equation.

The boundary condition equation assumes conservation of acid flux. That is,

$$\left[J_i(x_i,t)\right]_{x_i=l_i} = \left[J_{\dot{i}}(x_{\dot{i}},t)\right]_{x_{\dot{i}}=0} \quad (5.45)$$

where

J_i (mol.s^{-1}) is the acid flux on left hand side of the i-channel/$\dot{i}$-channel junction and

$J_{\dot{i}}$ (mol.s^{-1}) is the acid flux on right hand side of the i-channel/$\dot{i}$-channel junction.

Using Fick's first law and known cross-sectional areas equation 5.45 can be written as

$$\left[- a_i(x_i,t)D(x_i,t)\frac{\partial c_i(x_i,t)}{\partial x_i} \right]_{x_i=l_i} =$$

$$\left[- a(x_{\dot{i}},t)D_{\dot{i}}(x_{\dot{i}},t)\frac{\partial c_{\dot{i}}(x_{\dot{i}},t)}{\partial x_{\dot{i}}} \right]_{x_{\dot{i}}=0}. \quad (5.46)$$

c) The initial condition equation.

At the beginning of discharge the concentration of acid throughout the acid transport system will be assumed to have reached a constant equilibrium value. This gives the initial condition equation

$$c_i(x_i,0) = c_0 \text{ (for all } x_i) \qquad (5.47)$$

where

c_i (mol.m^{-3}) is the acid concentration in any channel,
x_i (m) is the space variable in any channel and
c_0 (mol.m^{-3}) is the concentration of acid in the fully charged cell after rest.

When applying equation 5.44 and 5.46 to the m-channel, finite difference approximations replace the continuous space derivatives. The initial condition equation applies unchanged to all channels of the aggregate model.

5.4.2 Acid Transport in the μ-channels.

The electrochemical reaction (equation 3.1) occurs throughout the μ-channels. This reaction causes the movement of acid components by three mechanisms. Firstly, the reaction consumes or produces acid components. This sets up concentration gradients in the solution which cause component movement by diffusion. Secondly, the reaction involves the passing of an electrical current in the solution. This sets up potential gradients in the solution which cause component movement by migration. Thirdly, the reaction results in solid phase volume changes which are reflected as changes in the cross-sectional area of the μ-channels. These changes cause the inflow or outflow of bulk solution inducing a nonzero solution velocity and component movement by convection.

From the description given above it can be seen that cross-sectional area, bulk solution velocity and reaction

rate terms vary in the general way indicated by equation 5.44. However, some simplification of the equation is possible. By inspection it can be seen that the term in the inner bracket of equation 5.44d is indicative of conservation of volume within a segment boundary. In the μ-channel case volume is conserved (that is, the net volume flow out of a segment is equal to its rate of change in volume). As a consequence this term and therefore the whole equation is identically zero.

The μ-channel cross-sectional area has already been shown to depend on state of charge in section 5.2.2. and is given by equation 5.12.

The μ-channel bulk solution velocity at some arbitrary position $x_{\mu 1}$ is given by the rate of change of volume between $x_{\mu 1}$ and the closed end of the μ-channel divided by the cross-sectional area at $x_{\mu 1}$. The rate of change of volume involved can be calculated using Faraday's law, molar volumes for the positive AM and the current passing into the solution/PbO_2 interface between x_μ and the closed end of the μ-channel. The resulting velocity equation is

$$v_\mu(x_{\mu 1},t) = -\frac{V_{mPbSO4} - V_{mPbO2}}{2F\ a_\mu(x_{\mu 1},t)} \int_{x_\mu=l_\mu}^{x_{\mu 1}} dI_\mu(x_\mu,t). \qquad (5.48)$$

The acid reaction rate term can be found from either of the ionic reaction terms according to equation 3.33. The ionic reaction terms can be determined by taking the change of current in the solution as being equal to the current passed in reaction 3.1 (conservation of charge) and applying Faraday's law to define the mass this produces or consumes. In the case of the H^+ ion this gives

$$P_+(x_\mu,t) = \frac{3}{2F} \frac{\partial i_\mu(x_\mu,t)}{\partial x_\mu}. \qquad (5.49a)$$

Applying equation 3.33 gives

$$P_\mu(x_\mu,t) = \frac{\partial}{\partial x_\mu}\left[\frac{3-2t_+(x_\mu,t)}{2F}\, i_\mu(x_\mu,t)\right]. \qquad (5.49b)$$

Assuming the transportation number is constant over the acid concentration range found in a practical lead-acid cell (as per Simonsson (1973) for example) equation 5.47 simplifies to

$$P_\mu(x_\mu,t) = \frac{3-2t_+}{2F}\,\frac{\partial i_\mu(x_\mu,t)}{\partial x_\mu}. \qquad (5.50)$$

The boundary condition equation for the closed end of the μ-channel can be formed by setting the right hand side of equation 5.46 to zero (since zero flux can flow on this side of the boundary). This gives

$$\frac{\partial c_\mu(l_\mu,t)}{\partial x_\mu} = 0. \qquad (5.51)$$

The boundary condition equation for the open end of the μ-channel is given by the general equation 5.46 where parameters on the right hand side of the equation refer to the μ-channel at $x_\mu=0$ and parameters on the left hand side refer to the m-channel segment into which the μ-channel opens. In the latter case the area parameter involved is not the m-channel cross-sectional area but rather the m-channel area at segment circumference through which flux flowing radially into the attached μ-channel passes. That is the area given by

$$a_{m\mu} = 2\sqrt{(\pi a_m(j,t))}\; l_m/N_{m\mu} \qquad (5.52)$$

where

$a_{m\mu}$ (m^2) is the segment circumference area and
j locates the position on the m-channel where the μ-channel is attached.

5.4.3 Acid Transport in the m-channel.

In the m-channels diffusion, migration and bulk solution movement effects occur as charge and mass are supplied to the microstructure. The cross-sectional area is constant (given by equation 5.3) in this case. The bulk solution moving in and out of the μ-channels cause a varying solution velocity in the m-channel. There is no reaction as such in the m-channel. The acid components moving in and out of the μ-channels can, however, be treated using a reaction rate term. In this respect the m-channels can be considered to have mass transport and simultaneous reaction effects in a similar way to the μ-channels above.

From the description above it can be seen that equation 5.44 can be simplified only with regard to the constancy of the cross-section area. Volume is not conserved in this case since it can be supplied via attached μ-channels.

The m-channel bulk solution velocity at some arbitrary position j_1 can be found in a similar way to that for the μ-channel. Here it is given by the rate of change in volume of all attached μ-channel between j_1 and the closed end of the m-channel divided by the m-channel cross-sectional area. The rate of change of volume here can be calculated using Faraday's law, molar volumes for the positive AM and the total current passing into the solution/PbO_2 interface of all the μ-channels involved. This total current is equal to the current through the m-channel at the position concerned. The resulting velocity equation is

$$v_m{}^{j1}(t) = -\frac{V_{mPbSO4} - V_{mPbO2}}{2F\ a_m} I_m{}^{j1}(t). \qquad (5.53)$$

The m-channel acid reaction term is determined by the amount of acid flowing in or out of the attached μ-channel.

The quantity per segment is given by the acid flux through the μ-channel opening as defined by the boundary condition equation for the open end of the μ-channel. The required quantity per unit length is obtained by dividing by the m-channel segment length. This gives,

$$P_m{}^j(t) = \frac{N_{m\mu}}{l_m} \left[-a_\mu(x_\mu,t) D_\mu(x_\mu,t) \frac{\partial c_\mu(x_\mu,t)}{\partial x_\mu} \right]^j_{x_\mu=0.} \qquad (5.54)$$

The boundary equation for the closed end of the m-channel is essentially the same as that for the closed end of the μ-channel. That is,

$$\frac{\partial c_m(l_m,t)}{\partial x_m} = 0. \qquad (5.55)$$

The boundary condition equation for the h-channel/m-channel junction is the general equation 5.46 where parameters on the right hand side of the equation refer to the m-channel at $x_m=0$ and parameters on the left hand side refer to the h-channel at $x_h=l_h$.

In the two boundary condition equations that apply in this case, finite difference approximations can replace the continuous space derivatives with respect to x_m.

5.4.4 Acid Transport in the h-channel.

In the h-channels diffusion, migration and bulk solution movement effects are again present as mass and charge is supplied to the m-channels. The cross-sectional area is constant in this channel (given by equation 5.15). In addition, the reaction rate term is zero since the adjacent mass is inactive, the bulk solution velocity is dependent on time only since the cross-section is constant and there is no supply of solution volume through attached side channels.

From the description above it can be seen that the

general transport equation 5.44 simplifies through the reaction rate term 5.44e and the volume conservation term 5.44d both being zero, the constant cross-sectional area and the bulk solution dependence on time only.

The h-channel bulk solution velocity is given by the product of the velocity of solution leaving the m-channel and the ratio of the m-channel to h-channel cross-sectional areas. That is,

$$v_h(t) = v_m^1(t)\ a_m/a_h \qquad (5.56)$$

where v_m^1 ($m.s^{-1}$) is the velocity in the m-channel segment attached to the h-channel (position 1).

The boundary condition equation for the h-channel/m-channel junction has already been discussed in section 5.4.3.

The boundary condition equation for the s-channel/h-channel junction is the general equation 5.46 where parameters on the right hand side of the equation refer to the h-channel at $x_h=0$ and parameters on the left hand side refer to the s-channel at $x_s=l_s$.

5.4.5 Acid Transport in the r-channel.

In the r-channel transport is by diffusion and convection only. The r-channel cross-sectional area depends on time only (given by equation 5.27) to account for the effect of volume changes in the positive and negative AM with time. There is no reaction and volume is conserved in the r-channel.

From the description above it can be seen that the general transport equation 5.44 simplifies through the reaction rate term 5.44e and the volume conservation term 5.44d both being zero and the dependence of the cross-sectional area on time only.

The bulk solution velocity is zero at the closed end of the r-channel. At the open end of the r-channel it is defined by the rate of change of volume in the positive and negative AM divided by the r-channel cross-sectional area. Between the two ends the velocity distribution is linear. Faraday's law and the positive and negative AM molar volumes give the rate of change of volume required. The resulting velocity is

$$v_r(x_r,t) = -\frac{x_r}{a_r(t)l_r}\frac{2V_{mPbSO4} - V_{mPbO2} - V_{mPb}}{2F} I_h(t). \tag{5.57}$$

The boundary condition equations for the r-channel are comparable to those for the μ-channels. The equation for the closed end of the r-channel is

$$\frac{\partial c_r(l_r,t)}{\partial x_r} = 0. \tag{5.58}$$

The equation for the open end of the r-channel is given by the general equation 5.46, where parameters on the left hand side of the equation refer to the r-channel at $x_r=l_r$ and parameters on the right hand side refer to the s-channel parameters that control the flow of flux from the r-channel opening. The r-channel opening does not span a small segment of the s-channel but rather spans the complete channel length. With this in mind, s-channel parameters for the concentration and diffusion coefficient are defined midway along the s-channel length. Single parameters at this position are assumed to represent the effect of the distributed parameters along the s-channel length. The s-channel area through which radial flux from the r-channel passes is the complete s-channel circumference area. This area is

$$a_{sr} = 2\sqrt{(\pi a_s)}\, l_s \tag{5.59}$$

where a_{sr} (m^2) is the s-channel circumference area.

5.4.6 Acid Transport in the n-channel.

In the n-channel diffusion, migration and bulk solution movement effects are again present as mass and charge is supplied to the reacting surface of the negative AM. In this simplified representation of the negative electrode, the reaction rate is assumed to be constant along the n-channel length. This gives a cross-sectional area (given by equation 5.21) and reaction rate term that are dependent on time only. In the n-channel volume is conserved since there are no attached channels representing fine features of the negative AM.

From the description above it can be seen that the general transport equation 5.44 simplifies through the volume conservation term 5.44d being zero and the dependence of the cross-sectional area and reaction rate on time only.

The bulk solution velocity for the n-channel is found in a similar way as that for the r-channel above. At the closed end of the n-channel it is zero. At the open end of the n-channel it is defined by rate of change of volume in the negative AM divided by the n-channel cross-sectional area. The velocity distribution between the two ends is linear. Again Faraday's law and the negative AM molar volume give the rate of change of volume required. The resulting velocity is

$$v_n(x_n,t) = \frac{x_n}{a_n l_n} \frac{V_{mPbSO4} - V_{mPb}}{2F} I_h(t). \qquad (5.60)$$

The total acid reaction rate in the n-channel can be found from the total reaction rate for the overall lead-acid cell less the total reaction rate in the μ-channels. Applying Faraday's law to the overall cell shows the overall acid reaction rate to be the fraction 1/F of the current. In the μ-channels the reaction rate is the fraction $(3-2t_+)/(2F)$ of the current (see equation 5.50).

The resulting total reaction rate in the n-channel is

$$P_n(t)l_n = \frac{-1 + 2t_+}{2F} I_h(t) \qquad (5.61)$$

Dividing through by the n-channel length gives the required reaction rate per unit length.

The boundary condition equations for the n-channel are comparable to those for the m-channels. The equation for the closed end of the n-channel is

$$\frac{\partial c_n(l_n,t)}{\partial x_n} = 0. \qquad (5.62)$$

The boundary condition equation for the n-channel/s-channel junction is the general equation 5.46 where parameters on the right hand side of the equation refer to the s-channel at $x_s=0$ and parameters on the left hand side refer to the n-channel at $x_n=l_n$.

5.4.7 Acid Transport in the s-channel.

The s-channel is in many ways similar to the h-channel. Again diffusion, migration and bulk solution movement effects are present as mass and charge is supplied to both the h-channel and the n-channel. Also, the s-channel cross-sectional area is constant (given by equation 5.17). The significant difference between the s-channel and h-channel is a result of the attached r-channel. For the sake of simplifying the s-channel formulations and to be consistent with the boundary condition for the open end of the r-channel discussed above, the r-channel is assumed to be attached at a position midway along the s-channel length. Here solution volume and acid flux are exchanged with the attached r-channel. The latter effect can be treated as a reaction rate term (as in the corresponding case where μ-channels were attached to the m-channel above). The bulk solution velocity is zero at this

position as solution moves radially to or from the r-channel. Elsewhere along the s-channel length the reaction rate term is zero and volume is conserved. The bulk solution velocity has a space independent value each side of the position of r-channel attachment, since the cross-sectional area is constant. The value of this velocity is on one side determined by volume changes in the positive AM and on the other side determined by volume changes in the negative AM.

From the description above it can be seen that for most of the s-channel length the general transport equation 5.44 simplifies through the reaction rate term 5.44e and the volume conservation term 5.44d both being zero and the constant cross-sectional area. However, at the position where the r-channel is attached the reaction rate term and volume conservation term are both non-zero.

The bulk solution velocity on the h-channel side of the position of r-channel attachment is given by the product of the velocity of solution leaving the h-channel and the ratio of the h-channel to s-channel cross-sectional areas. That is,

$$v_{sh}(t) = v_h(t)\ a_h/a_s. \qquad (5.63)$$

where v_{sh} ($m.s^{-1}$) is the s-channel velocity between the h-channel and the position of r-channel attachment.

The bulk solution velocity on the n-channel side of the position of r-channel attachment is given by the product of the velocity of solution leaving the n-channel and the ratio of the n-channel to s-channel cross-sectional areas. That is,

$$v_{sn}(t) = v_n(l_n,t)\ a_h/a_s. \qquad (5.64)$$

where v_{sn} ($m.s^{-1}$) is the s-channel velocity between the n-channel and the position of r-channel attachment.

The total acid reaction term for the s-channel is given by the flux defined by the boundary condition equation for the open end of the r-channel. If the r-channel attachment position covers an s-channel segment of length Δx_s then the required reaction term per unit length is given by dividing the total term by Δx_s. That is,

$$P_s(t) = \frac{1}{\Delta x_s} \left[-a_r(t) D_r(x_r,t) \frac{\partial c_r(x_r,t)}{\partial x_r} \right]_{x_r=l_r}. \qquad (5.65)$$

The boundary condition equations for the n-channel/s-channel and s-channel/h-channel junctions have already been described above for the n-channel and h-channel respectively.

This completes the acid transport formulations for the aggregate model. The solution of these and those defining the electrical characteristics given in section 5.3 is dealt with in the following section.

5.5 OPERATING THE AGGREGATE MODEL: A PRACTICAL APPROACH.

Operating the aggregate model amounts to solving a set of simultaneous algebraic and partial differential equations. These equations are those given for the structure, electrical and transport characteristics in sections 5.2, 5.3 and 5.4 respectively. The solution determines the electrical and physical behaviour of the complete aggregate model in both space and time. The equations do not lend themselves to solution by analytical methods due to the number of equations and the complexity of functions involved. The solution is obtained through numerical methods where discrete approximations for the space and time intervals are used. Other approximations regarding the grouping of μ-channels and the decoupling of the equations are made to reduce the computational effort to a realistic level. Details of approximations, discrete

equation forms and solution procedures are given below.

5.5.1 Discrete Representations for Time and Space.

In the discrete equations that follow the time interval will be represented by $k\Delta t$ where k is an integer equal to 1 at the start of discharge. Similarly, the space interval will be represented by $j\Delta x$ in the general case, and by $j_\mu \Delta x_\mu$, $j_m \Delta x_m$, $j_h \Delta x_h$, $j_s \Delta x_s$, $j_n \Delta x_n$ and $j_r \Delta x_r$ for the specific case of the μ-channel, m-channel, h-channel, s-channel, n-channel and r-channel respectively †. Here j_i is an integer equal to 1 at the position closest to $x_i=0$ and equal to j_{li} at the position closest to $x_i=l_i$. The notation used to define space (position) and time for parameters appearing in the discrete equations will be the two superscripts "j_i,k" (space followed by time). If the parameter concerned is independent of either space or time the corresponding superscript will be absent.

5.5.2 A Practical Equation Set and Solution Procedure.

Even though the aggregate model is based on a minimum representation of the acid transport system, the number of equations involved is still enormous. For example there are in the order of 10^6 μ-channels opening on to a single m-channel (see table 7.3) each of which requires a complex set of equations to define the electrical and transport properties. The computing effort required to solve all of these equations is prohibitive. The key problems are the number of equations involved and the simultaneous nature of

† In fact the space interval for the m-channel has already been treated in this way in sections 5.3.2 and 5.4.3 where Δx_m was set to $l_m/N_{m\mu}$. The size of Δx_m will, however, be adjusted in the formulations that follow.

these equations. The first problem is relieved by assuming that the condition of all μ-channels over a small length of m-channel is identical. This allows a single set of equations to be used to describe the behaviour of a group of μ-channels. The number of equations involved in the system can be reduced from hundreds of thousands to perhaps a few hundred by this approach. The final number of equations is determined by the number required to adequately represent the distributed arrangement of μ-channels along the m-channel length. The second problem is relieved by decoupling some of the equations. To this end electrical algebraic equations are solved using structural and transport parameter values from the previous time step. Also, the partial differential and algebraic equations for acid transport are solved using structural and some transport parameter values from the previous time step. The decoupling does not introduce significant errors provided the time step is small compared to the time taken for significant changes in the parameter values held over from the previous time step. These values relate to the structure and transport characteristics of the aggregate model. The magnitude of the time step for this type of situation has already been discussed with regard to the elemental model in section 4.3.6. The decoupling described above allows the reduced set of equations to be solved in three stages for each time step.

i) The electrical equations are solved as a set of simultaneous algebraic equations using previous time step parameter values.

ii) The transport equations are solved as simultaneous algebraic and partial differential equations using previous time step structural parameter values, some previous time step transport parameter values and present time step electrical and electrically derived transport parameter values.

iii) The structural algebraic equations are updated

using present time step electrical parameter values.

Further details of the calculation procedures and discrete equation forms for each of the three stages above are given in the sections that follow.

5.5.3 Discrete Electrical Equations.

The discrete form of equations for the electrical characteristics can be written directly from the continuous forms given in section 5.3 using the definitions for the discrete time and space intervals given above.

The discrete form of equations for the h-channel are

$$R_h^k = (\Delta x_h / a_h) \sum_{j_h=1}^{j_{1h}} \rho_h^{j_h,k}, \tag{5.66}$$

$$U_h^k = - I_h^k \, R_h^k \tag{5.67}$$

and

$$I_h^k = I_{cell}^k / (N_p \, H_p \, W_p \, N_{ma}) \tag{5.68}$$

which are derived from equations 5.28 to 5.30 respectively.

Equations that relate to the m-channel need to take into account the μ-channel groups discussed above. If there are $N_{\mu g}$ μ-channels in each group then the m-channel space is divided into $N_{m\mu}/N_{\mu g}$ segments rather than $N_{m\mu}$ as before. As a result the discrete form of equations 5.31 to 5.33 can be written as

$$R_m^{j_m,k} = N_{\mu g} \, l_m \, \rho_m^{j_m,k} / (a_m \, N_\mu), \tag{5.69}$$

$$U_m^{j_{m1},k} = U_h^k - \sum_{j_m=1}^{j_{m1}} R_m^{j_m,t} \, I_m^{j_m,k} \tag{5.70}$$

and

$$I_m^{j_{m1},k} = I_h^k - N_{\mu g} \sum_{j_m=1}^{j_{m1}} I_{m\mu}^{j_m,k} \tag{5.71}$$

respectively.

The discrete form of the equations for the μ-channel are

$$\Delta R_\mu^{j_\mu,k} = \frac{\Delta x_\mu \ \rho_\mu^{j_\mu,k}}{a_{\mu 0} \ X^{j_\mu,k}}, \tag{5.72}$$

$$\Delta I_\mu^{j_\mu,k} = \frac{2 i_{01} \ \Delta x_\mu \ S_{PbO2}}{N_m \ N_{m\mu} \ l_\mu} \ e^{(\alpha_1 F \ \Delta U_\mu^{j_\mu,k})/RT} \tag{5.73}$$

$$\Delta I_\mu^{j_\mu,k} = -\frac{2 i_{02} \ \Delta x_\mu \ S_E}{N_m \ N_{m\mu} \ l_\mu} \ e^{((1-\alpha_2) F \ \Delta U_\mu^{j_\mu,k})/RT} \tag{5.74}$$

$$U_\mu^{j_\mu 1,k} = U_m^{j_m,k} - \sum_{j_\mu=1}^{j_\mu 1} \Delta R_\mu^{j_\mu,k} \ I_\mu^{j_\mu,k} \tag{5.75}$$

$$I_\mu^{j_\mu 1,k} = I_{m\mu}^{j_m,k} - \sum_{j_\mu=1}^{j_\mu 1} \Delta I_\mu^{j_\mu,k} \tag{5.76}$$

and

$$U_{PbO2}^{k} = U_\mu^{j_\mu,k} - \Delta U_\mu^{j_\mu,k} + E_\mu^{j_\mu,k} \tag{5.77}$$

which are derived from equations 5.34 to 5.39 respectively.

The equations that correspond to the supplementary equations 5.40 to 5.43 are

$$R_s^k = (\Delta x_s / a_s) \sum_{j_n=1}^{j_{1s}} \rho_s^{j_s,k}, \tag{5.78}$$

$$U_s^k = R_s^k \ I_h^k \tag{5.79}$$

$$R_n^k = (\Delta x_n / a_n^k) \sum_{j_n=j_{1n}}^{0.5 j_{1n}} \rho_n^{j_n,k}, \tag{5.80}$$

and

$$U_n^k = U_s^k + R_n^k \ I_h^k - E_n^k \tag{5.81}$$

respectively.

5.5.4 Computing the Electrical Parameter Values.

a) Overall electrical calculation procedure.

The iterative calculation procedure using I_{cell} as the independent variable is summarised below.

i) Initial estimation of U_{PbO2} based on the open circuit potential at the first μ-channel group.

ii) Calculation of the potential at the h-channel/m-channel junction from the potential drop in the h-channel. Equations 5.66 to 5.68 define this. Equation 5.68 also defines the m-channel current at this position.

iii) Calculation of the potential at the given position in the m-channel from the potential at the previous position and the potential drop in the given segment of m-channel. Equations 5.69 and 5.70 are relevant here.

iv) Calculation of the current into the surrounding μ-channels. Equations 5.72 to 5.77 are relevant here. This step is dealt with in more detail below.

v) Calculation of the current at the next m-channel position by combining the results of step iv) with the known current at the given m-channel position. Equation 5.71 is relevant here.

vi) Repetition of steps iii) to v) until parameters have be calculated for the last m-channel segment.

vii) Update of U_{PbO2} to using a bisection algorithm to minimise the current calculated for the last m-channel segment by step v).

viii) Repetition of Steps ii) to vii) until the current calculated at the last m-channel segment by step v) is less than some predefined maximum value.

ix) Adoption of parameter values as the solution and the termination of the overall electrical calculation procedure.

This procedure determines the current and potential parameters for the h-channel, m-channel and all μ-channels.

b) Calculation procedure for μ-channel parameters.

The calculation of the current flowing into the surrounding μ-channels (step iv) above) employs a second iterative procedure using U_m calculated at step iii) above as the independent variable. This procedure is summarised below.

i) Initial estimation of the current at the open end of the μ-channel ($I_\mu^{1,k}$) assuming the solution potential drop in the μ channel is negligible.

ii) Calculation of the potential at the given position in the μ-channel from the potential at the previous position and the potential drop in the given segment of μ-channel. Equation 5.77 is relevant here.

iii) Calculation of the current into the PbO_2/solution interface within the given μ-channel segment using the potential calculated at step ii). Equations 5.73 and 5.74 are relevant here.

iv) Calculation of the current at the next μ-channel position by combining the results of step iii) with the known current at the given μ-channel position. Equation 5.76 is relevant here.

v) Repetition of steps ii) to iv) until parameters have be calculated for the last μ-channel segment.

vi) Update of $I_{\mu}^{1,k}$ initially using a bisection algorithm and finally using a Newton-Rapson algorithm to minimise the current calculated for the last μ-channel segment by step v).

vii) Repetition of Steps ii) to vii) until the current calculated at the last μ-channel segment by step iv) is less than some predefined maximum value.

viii) Adoption of parameter values as the solution and the termination of the μ-channel calculation procedure.

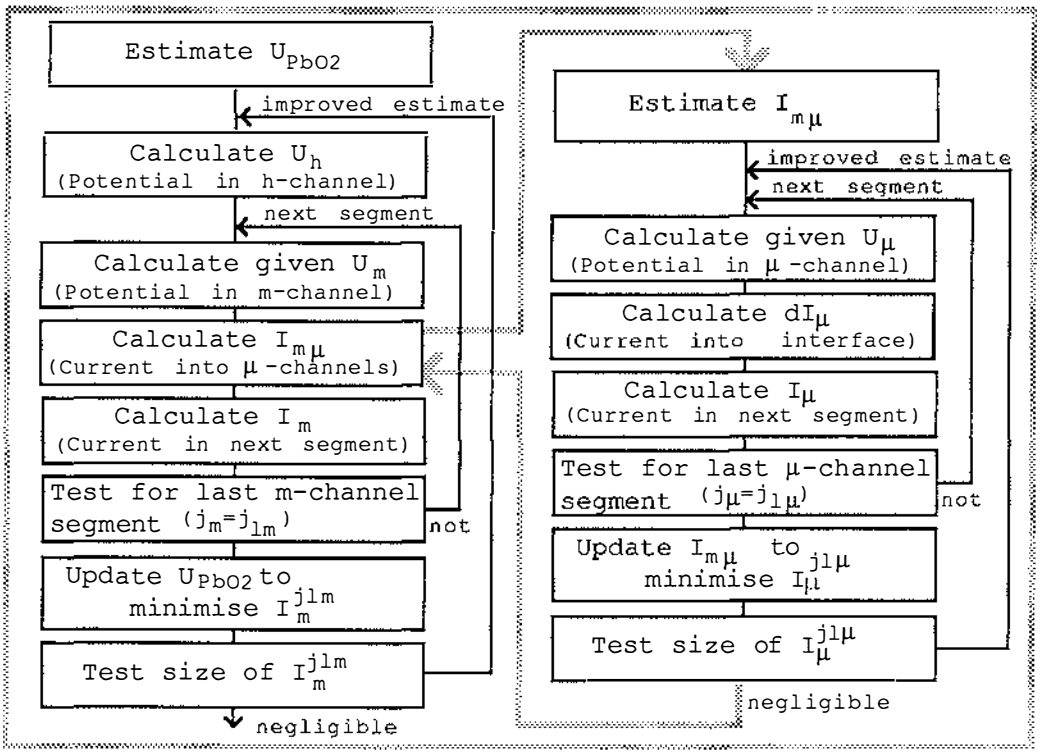

Figure 5.7: Calculation of Electrical Parameters.

c) The over-all calculation scheme.

The over-all calculation scheme for finding the electrical parameter values is the combined arrangement of the procedures described above. A flow diagram of the over-all scheme is given in figure 5.7.

d) The supplementary parameters.

The supplementary parameter values are found by the direct application of equations 5.78 to 5.81 if required.

5.5.5 Discrete Acid Transport Equations.

a) The general transport, general boundary condition and general initial condition equations.

The discrete form of the general transport equation 5.44 is obtained by replacing the left hand side by the backward difference time approximation and the right hand side by the average of the finite difference space approximations at the present and previous time steps. This is the Crank-Nicolson implicit method (see Smith (1969) and Twizell (1984) for example). Further, to effect the decoupling of the equations discussed above, parameter values other than the current derived reaction rate and bulk solution velocity terms are delayed by one time step. This gives

$$\left(-L_i^{j,k} + M_i^{j,k}\right) c_i^{j-1,k+1} + \left(1 + 2L_i^{j,k} - N_i^{j,k}\right) c_i^{j,k+1}$$

$$+ \left(-L_i^{j,k} - M_i^{j,k}\right) c_i^{j+1,k+1} =$$

$$\left(L_i^{j,k-1} - M_i^{j,k-1}\right) c_i^{j-1,k} + \left(1 - 2L_i^{j,k-1} + N_i^{j,k-1}\right) c_i^{j,k}$$

$$+ \left(L_i^{j,k-1} + M_i^{j,k-1}\right) c_i^{j+1,k} + \left(O_i^{j,k+1} + O_i^{j,k}\right) \tag{5.82a}$$

where

$$L_i^{j,x} = (\Delta t / 2\Delta x_i^2)\, D_i^{j_i,k}, \tag{5.82b}$$

$$M_i^{j,k} = \frac{\Delta t}{4\Delta x_i}\left[\frac{a_i^{j_i+1,k}\, D_i^{j_i+1,k} - a_i^{j_i-1,k}\, D_i^{j_i-1,k}}{2\Delta x_i\, a_i^{j_i,k}} + v_i^{j_i,k}\right], \tag{5.82c}$$

$$N_i^{j,k} = \frac{-\Delta t}{2}\left[\frac{a_i^{j_i+1,k}\, v_i^{j_i+1,k} - a_i^{j_i-1,k}\, v_i^{j_i-1,k}}{2\Delta x_i\, a_i^{j_i,k}} + \frac{a_i^{j_i,k} - a_i^{j_i,k-1}}{\Delta t\, a_i^{j_i,k}}\right] \tag{5.82d}$$

and

$$O_i^{j,k} = \frac{\Delta t}{2a_i^{ji,k}}\, P_i^{j_i,k}. \tag{5.82e}$$

An equation of this form can be written for every non-boundary segment of the six channels of the aggregate model. The equation involves three unknown concentration terms on the left hand side (see 5.82a).

A discrete form of the general boundary equation can be found by replacing the continuous space derivatives on the left and right hand side of equation 5.46 with backward and forward finite difference approximations respectively. However, this form is undesirable for two reasons.

i) The form involves four unknown concentrations in the general case. An alternative form involving only

three unknown concentrations is preferable to give equations of the same form as the general transport equation above. This allows an efficient solution algorithm to be used to solve the set of simultaneous equations.

ii) The form is unnecessarily inaccurate. The discrete form involves finite length segments which in general contain acid consumption or production reaction processes. This reaction is not accounted for.

To overcome these undesirable features different approaches were used for the open end and closed end boundary cases.

For the closed end boundary case the general boundary condition equation has already been seen to reduce to a single partial derivative equal to zero (see equation 5.51 for example). In the discrete representation a dummy segment is added next to the true boundary segment. The continuous space derivative is then replaced by a finite difference scheme involving the true and dummy boundary segments. This ensures that the correct boundary condition is maintained between the true and dummy segments, but allows the general transport equation to be applied to the true boundary segment. The general transport equation accounts for any reaction rate term. The boundary condition equation using this approach is

$$c_i^b - c_i^a = 0 \qquad (5.83)$$

where

c_i^b is the concentration at the true boundary segment and

c_i^a is the concentration at the dummy boundary segment adjoining the true boundary segment.

For the open end boundary condition the discrete situation is represented as in figure 5.8.

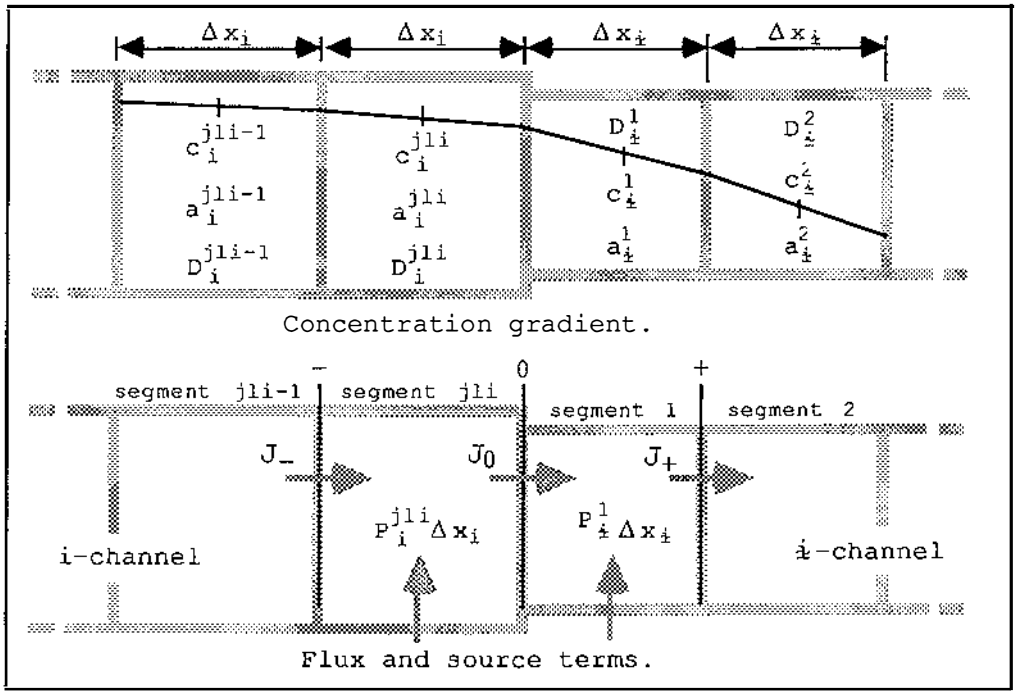

Figure 5.8: Boundary between Channels on Same Axis.

Referring to figure 5.8, the true boundary is denoted by the subscript "0" and the boundary of the segments to the left and right of the true boundary are denoted by the subscripts "-" and "+" respectively. Conservation of flux in the segment to the left and segment to the right of the true boundary requires that

$$J_- + P_i^{jli,k}\,\Delta x_i = J_0 \qquad (5.84)$$

and

$$J_0 + P_{\bar{i}}^{1,k}\,\Delta x_{\bar{i}} = J_+ \qquad (5.85)$$

respectively.

Consider now the flux J_-. Applying Fick's first law with finite difference representations for the continuous partial derivatives gives

$$J_- = -g_i^{jli-1,k}(c_- - c_i^{jli-1,k}) \quad (5.86a)$$

or

$$J_- = -g_i^{jli,k}(c_i^{jli,k} - c_-) \quad (5.86b)$$

where

$$g_i^{j,k} = 2a_i^{j,k}D_i^{j,k}/\Delta x_i \quad (5.87)$$

and is a measure of the ease with which flux can flow in response to a difference in concentration (analogous to electrical conductivity). Combining equations 5.86a and 5.86b to eliminate the c_- term gives

$$J_- = -\frac{g_i^{jli-1,k}\, g_i^{jli,k}}{g_i^{jli-1,k} + g_i^{jli,k}}(c_i^{jli,k} - c_i^{jli-1,k}) \quad (5.88)$$

which is an expression for the flux which involves only the parameter values normally defined for the channel segments (the additional values at the segment boundaries have been eliminated). Similar expressions can be found for the remaining fluxes J_0 and J_+. Substituting these expressions into equations 5.84 and 5.85 gives

$$\left[\frac{g_i^{jli-1,k}\, g_i^{jli,k}}{g_i^{jli-1,k} + g_i^{jli,k}}\right] c_i^{jli-1,k} +$$

$$\left[-\frac{g_i^{jli-1,k}\, g_i^{jli,k}}{g_i^{jli-1,k} + g_i^{jli,k}} - \frac{g_i^{jli,k}\, g_{i\pm}^{1,k}}{g_i^{jli,k} + g_{i\pm}^{1,k}}\right] c_i^{jli,k} +$$

$$\left[\frac{g_i^{jli,k}\, g_{i\pm}^{1,k}}{g_i^{jli,k} + g_{i\pm}^{1,k}}\right] c_{i\pm}^{1,k} = -P_i^{jli,k}\,\Delta x_i \quad (5.89)$$

and

$$\left[\frac{g_i^{jli,k}\, g_{i\pm}^{1,k}}{g_i^{jli,k} + g_{i\pm}^{1,k}}\right] c_i^{jli,k} +$$

$$\left[-\frac{g_i^{jli,k}\, g_{i\pm}^{1,k}}{g_i^{jli,k} + g_{i\pm}^{1,k}} - \frac{g_{i\pm}^{1,k}\, g_{i\pm}^{2,k}}{g_{i\pm}^{1,k} + g_{i\pm}^{2,k}}\right] c_{i\pm}^{1,k} +$$

$$\left[\frac{g_{i\pm}^{1,k}\, g_{i\pm}^{2,k}}{g_{i\pm}^{1,k} + g_{i\pm}^{2,k}}\right] c_{i\pm}^{2,k} = -P_{i\pm}^{1,k}\,\Delta x_{i\pm} \quad (5.90)$$

respectively. These are the desired boundary condition equations. It can be seen they involve only three unknown concentrations and take account of any reaction terms.

The initial condition equation corresponds directly to the continuous equation 5.47. That is,

$$c_i^{j,1} = c_0 \quad \text{(for all values of j)}. \tag{5.91}$$

The simplifications given for the equations for each of the six channels of the aggregate model in section 5.4 apply in the discrete case and will not be discussed again here. The discrete form of the equations that apply specifically to each of the six channels are given below.

b) Formulations for particular channels.

The equations that define the cross-sectional area, bulk solution velocity and reaction rate term for the μ-channel are

$$a_\mu^{j_\mu,k} = a_{\mu 0}\, X^{j_\mu,k}, \tag{5.92}$$

$$v_\mu^{j_\mu 1,k} = -\frac{V_{mPbSO4} - V_{mPbO2}}{2F\, a_\mu^{j_\mu 1,k}} \sum_{j_\mu=j_{1\mu}}^{j_\mu 1} dI_\mu^{j_\mu,k} \tag{5.93}$$

and

$$P_\mu^{j_\mu,k} = \frac{3-2t_+}{2F}\, \frac{\Delta I_\mu^{j_\mu,k}}{\Delta x_\mu}, \tag{5.94}$$

respectively. The corresponding continuous equations are 5.12, 5.48 and 5.50.

The boundary condition equation for closed end of the μ-channel is given by equation 5.83.

The boundary condition equation at the open end of the μ-channel is given by equation 5.90. In this case the subscript "i" should be replaced by "μ" and the subscript "i" replaced by "mμ". The subscript "mμ" is used to indicate properties of the m-channel segment that control

the flux flowing radially into the attached μ-channel. The m-channel properties involved are brought together in equation 5.87 which in this case becomes

$$g_{m\mu}^{jm,k} = 2a_{m\mu} D_m^{jm,k}/\Delta x_{m\mu} \qquad (5.95)$$

where jm defines the position of the μ-channel attachment.

The terms $a_{m\mu}$ and $\Delta x_{m\mu}$ define the ease with which flux will flow radially in response to the difference in concentration in the m-channel proper and the mouth of the attached μ-channel. They characterise the surface area that the flux flows through and the radial length it travels. The arrangement used to determine these quantities is illustrated in figure 5.9. The radial concentration distribution is assumed to place the characteristic m-channel concentration at the volume average position. This is defined by the radius that encloses half the m-channel volume. This radius (the half volume radius) is the

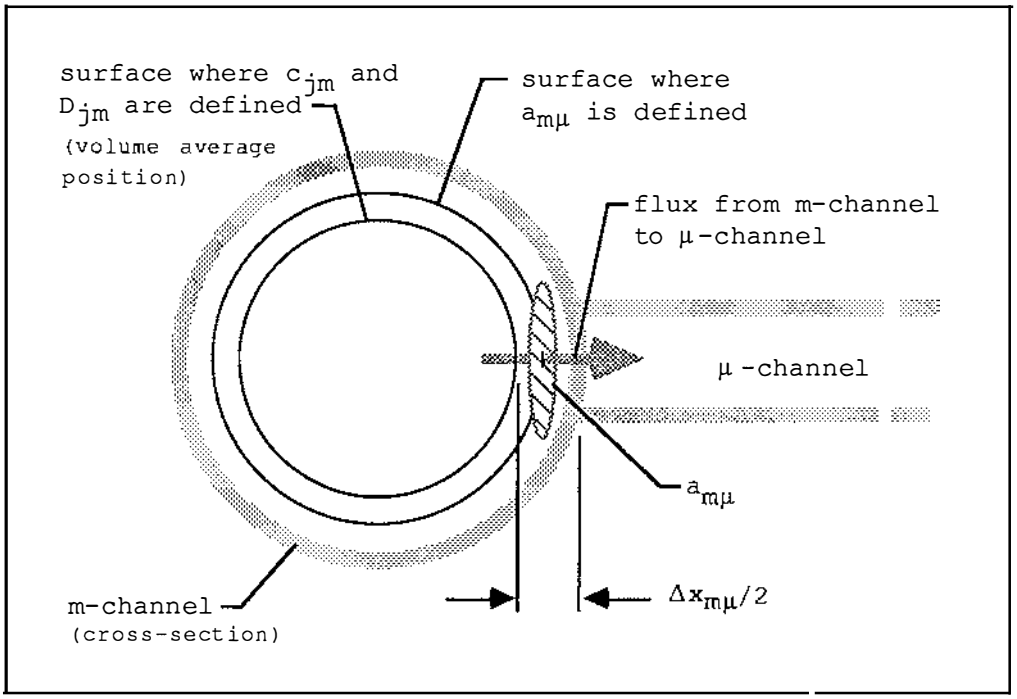

Figure 5.9: The m-channel/μ-channel Boundary.

fraction $1/\sqrt{2}$ of the full m-channel radius. This gives the radial distance for flux flow required above. That is,

$$\Delta x_{m\mu}/2 = (1 - 1/\sqrt{2})\ \sqrt{(a_m/\pi)}. \qquad (5.96)$$

The area through which the radial flux flows is defined at the cylindrical surface half way between the full volume and half volume radius. It is given by dividing the area of this surface by the number of μ-channels adjacent to it. That is,

$$a_{m\mu} = \sqrt{(\pi a_m)}\, l_m (1 + 1/\sqrt{2})/N_{m\mu} \qquad (5.97)$$

The equations that define the bulk solution velocity and reaction rate term for the m-channel are

$$v_m{}^{jm1,k} = -\frac{V_{mPbSO4} - V_{mPbO2}}{2F\ a_m}\ I_m{}^{jm1,k} \qquad (5.98)$$

and

$$P_m{}^{jm,k} = \frac{N_{\mu g}}{\Delta x_m}\ \frac{g_{m\mu}{}^{jm,k}\ g_\mu{}^{1,k}}{g_{m\mu}{}^{jm,k} + g_\mu{}^{1,k}} \left(\left(c_\mu{}^{1,k-1} \right)^{jm} - c_m{}^{jm,k-1} \right) \qquad (5.99)$$

respectively. The corresponding continuous equations are 5.53 and 5.54. In equation 5.99 the grouping of the μ-channels has been taken into account by the inclusion of the $N_{\mu g}$ term.

The boundary condition equation for the closed end of the m-channel is given by equation 5.83.

The boundary condition equation for the open end of the m-channel is given by equation 5.90. In this case the subscript "i" should be replaced by "m" and the subscript "i" replaced by "h".

The equation that defines the bulk solution velocity in the h-channel is

$$v_h{}^k = (a_m/a_h)\ v_m{}^{1,k}. \qquad (5.100)$$

The corresponding continuous equation is 5.56.

The boundary condition equation for the h-channel/m-channel end of the h-channel is given by equation 5.89. In this case the subscript "i" should be replaced by "m" and the subscript "i" replaced by "h".

The boundary condition equation for the s-channel/h-channel end of the h-channel is given by equation 5.90. In this case the subscript "i" should be replaced by "h" and the subscript "i" replaced by "s".

The bulk solution velocity in the r-channel is given by

$$v_r^{jr,k} = -\frac{j_r}{a_r^k\, j_{lr}} \frac{2V_{mPbSO4} - V_{mPbO2} - V_{mPb}}{2F} I_h^k. \quad (5.101)$$

which is derived from the continuous equation 5.57.

The boundary conditions for the closed end of the r-channel is given by equation 5.83.

The boundary condition equation for the open end of the r-channel is given by equation 5.89. In this case the subscript "i" should be replaced by "r" and the subscript "i" replaced by "sr". The subscript "sr" is used to indicate properties of the s-channel that control the flux flowing radially from the attached r-channel. This situation is directly comparable to that for the boundary condition equation for the open end of the μ-channel. The explanations used in that case apply again here and will not be repeated. The formulations comparable to equations 5.95 to 5.97 are

$$g_{sr}^{jsr,k} = 2a_{sr}\, D_s^{jsr,k}/\Delta x_{sr}, \quad (5.102)$$

$$\Delta x_{sr}/2 = (1 - 1/\sqrt{2})\, \sqrt{(a_s/\pi)} \quad (5.103)$$

and

$$a_{sr} = \sqrt{(\pi a_s)}\, l_s (1 + 1/\sqrt{2}) \quad (5.104)$$

respectively, where jsr defines the position of the r-channel attachment.

The equations that define the bulk solution velocity and reaction rate terms for the n-channel are

$$v_r^{jr,k} = \frac{x_r}{a_n^k \, l_r} \frac{V_{mPbSO4} - V_{mPb}}{2F} I_h^k \qquad (5.105)$$

and

$$P_n^k = \frac{1}{l_n} \frac{-1 + 2t_+}{2F} I_h^k. \qquad (5.106)$$

These are derived from the continuous equations 5.60 and 5.61.

The boundary condition equation for the closed end of the r-channel is given by equation 5.83.

The boundary condition equation for the open end of the r-channel is given by equation 5.89. In this case the subscript "i" should be replaced by "n" and the subscript "i" replaced by "s".

The bulk solution velocity equations for the s-channel are

$$v_{sh}^k = v_h^k \, a_h/a_s \qquad (5.107)$$

and

$$v_{sn}^k = v_n^{jln,k} \, a_h/a_s. \qquad (5.108)$$

These are derived from the continuous equations 5.63 and 5.64.

The acid reaction term equation for the s-channel at the position where the r-channel is attached is

$$P_s^k = - \frac{1}{\Delta x_s} \frac{g_r^{jlr,k} \, g_{sr}^{jsr,k}}{g_r^{jlr,k} + g_{sr}^{jsr,k}} \left[c_s^{jsr,k} - \left[c_r^{jlr,k} \right]^{jsr} \right] \qquad (5.109)$$

which is derived from the continuous equation 5.65.

The boundary condition for the s-channel/h-channel end of the s-channel is given by equation 5.89. In this case the subscript "i" should be replaced by "h" and the subscript "i" replaced by "s".

The boundary condition for the n-channel/s-channel end of the s-channel is given by equation 5.90. In this case the subscript "i" should be replaced by "s" and the subscript "i" replaced by "n".

5.5.6 Computing the Concentration Values from the Transport Equations.

A μ-channel has one equation written for each segment. These include an open end and closed end boundary condition equation and a general transport equation for each intermediate channel segment. This results in an equation set with $j_{l\mu}+1$ equations in all (since there are $j_{l\mu}$ segments proper and one dummy segment). This equation set involves unknown concentration terms for the $j_{l\mu}+1$ μ-channel segments and an additional unknown concentration term for the m-channel at the position where the μ-channel is attached. The additional term is introduced by the boundary equation for the m-channel/μ-channel junction. In all, this gives $j_{l\mu}+2$ unknown concentration terms. In the complete transport system representation there are j_{lm} equation sets of this type.

The r-channel case is comparable with the μ-channel case above. It results in $j_{lr}+1$ equations and $j_{lr}+2$ unknown concentration terms. The concentration terms in this case include those for the r-channel segments and an additional term for the s-channel segment where the r-channel is attached.

The remaining channels in the transport system can be taken together. As before one equation is written for each segment in remaining channels. These include two closed end

boundary condition equations, six open end boundary condition equations and a general transport equation for the intermediate channel positions. This results in $j_{ln}+j_{ls}+j_{lh}+j_{lm}+2$ equations in all (since there are $j_{ln}+j_{ls}+j_{lh}+j_{lm}$ segments proper and two dummy segments). These equations involve unknown concentration terms for the segments of the remaining channels as well as additional concentration terms for the segments that have a μ-channel or r-channel attached. The additional concentration terms are introduced by the source terms that account for flux from attached channels. In all, this gives $j_{ln}+j_{ls}+j_{lh}+j_{lm}+2$ plus $j_{lm}+1$ unknown concentration terms.

Taken together the three equation sets described above result in $j_{lm}(j_{l\mu}+1)$ plus $j_{lr}+1$ plus $j_{ln}+j_{ls}+j_{lh}+j_{lm}+2$ equations involving the same number of unknown concentration terms. The number of unknown concentration terms is equal to the number of equations since the additional concentration terms in the μ-channel and r-channel equation sets coincide with segment concentration terms in the equation set for the remaining channels and vice versa. The concentrations can be found at each time step by solving the combined set of simultaneous equations above. In the solution procedure used, each of the three equation sets were dealt with in a sequential fashion that enabled them to be solved as tri-diagonal systems by Gauss elimination (see Smith (1969) for details of Gauss elimination of tri-diagonal systems). The solution procedure is summarised in the steps below.

i) A forward elimination was performed on each of the μ-channel tri-diagonal equation sets to define single equations that gave the concentration in the segment at the open end of the μ-channel in terms of the concentration at the attachment position in the m-channel.

ii) A forward elimination was performed on the r-channel tri-diagonal equation set to define a single equation that gave the concentration in the segment at the open end of the r-channel in terms of the concentration at the attachment position in the s-channel.

iii) A substitution in the source terms of the remaining channels using the equations defined in steps i) and ii) was made. This eliminated additional unknowns in this set giving it a tri-diagonal form.

iv) A forward elimination and backward substitution was performed on the tri-diagonal equation set for the remaining channels to get the solution for the concentrations of the segments in this set.

v) A substitution of the solutions found in step iv) into the equations defined in steps i) and ii) was made to give the starting point for backward substitution of the μ-channel sets and r-channel set.

vi) A backward substitution was performed on partially solved μ-channel equation sets to get the solution for the concentration of all the segments in the μ-channel sets.

vii) A backward substitution was performed on the partially solved r-channel equation set to get the solution for the concentration of all the segments in the r-channel.

Details of the particular equations involved in the the solution procedure are given in section 5.5.5. A flow diagram of the procedure is given in figure 5.10.

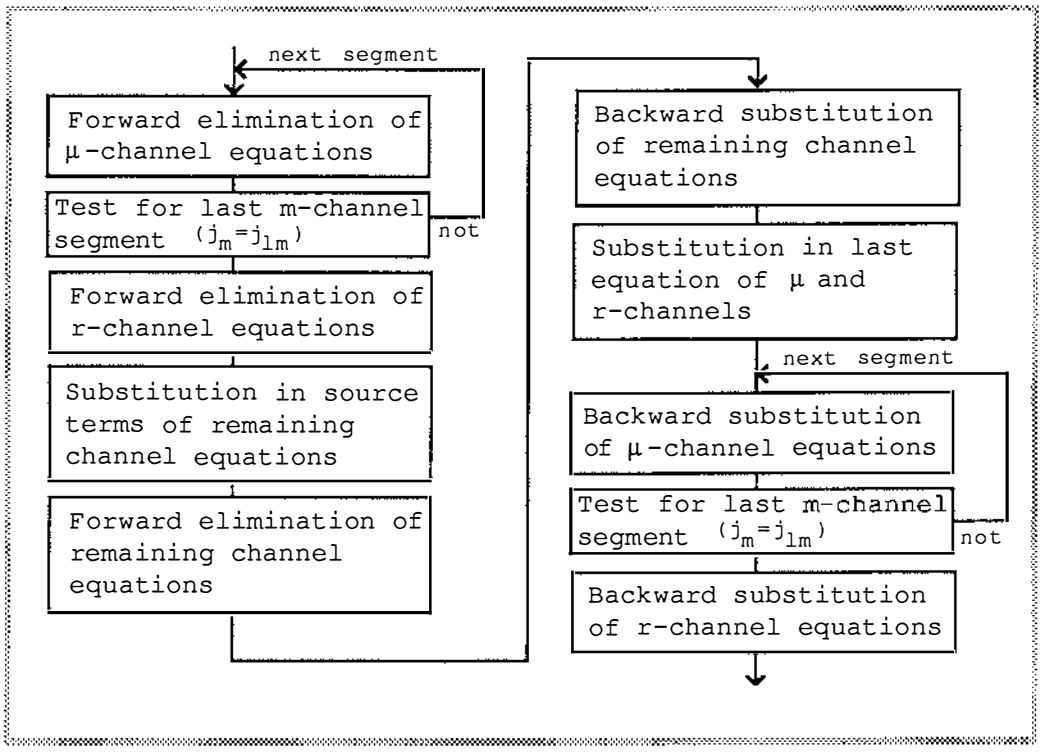

Figure 5.10: Calculation of Transport Parameters.

5.5.7 Discrete Equations for Structural Change.

Changes in structure with charge and discharge occur in the μ-channel, n-channel and r-channel only. In all cases this is represented by changes in cross-sectional area.

The μ-channel cross-sectional area is dependent on state of charge (see equation 5.12). The state of charge is given by

$$X^{j_\mu,k1} = 1 - \frac{N_m\, N_{m\mu}\, l_\mu\, \Delta t}{q_0\, \Delta x_\mu} \sum_{k=1}^{k1} \Delta I_\mu^{j_\mu,k} \qquad (5.110)$$

which corresponds to the continuous equation 5.13.

The n-channel and r-channel cross-sectional areas are given by

$$a_n = a_{n0} - \frac{1}{l_n} \frac{V_{mPbSO4} - V_{mPb}}{2F} \Delta t \sum_{k=1}^{k1} I_h{}^k \qquad (5.111)$$

and

$$a_r = a_{r0} + \frac{1}{l_r} \frac{2V_{mPbSO4} - V_{mPbO2} - V_{mPb}}{2F} \Delta t \sum_{k=1}^{k1} I_h{}^k \qquad (5.112)$$

respectively. These equations correspond to the continuous equations 5.21 and 5.27.

5.5.8 Computing the Structural Parameter Values.

Computing the structural parameter values amounts to applying equations 5.110 to 5.112 every time step. Equation 5.110 is applied to every segment in the μ-channels.

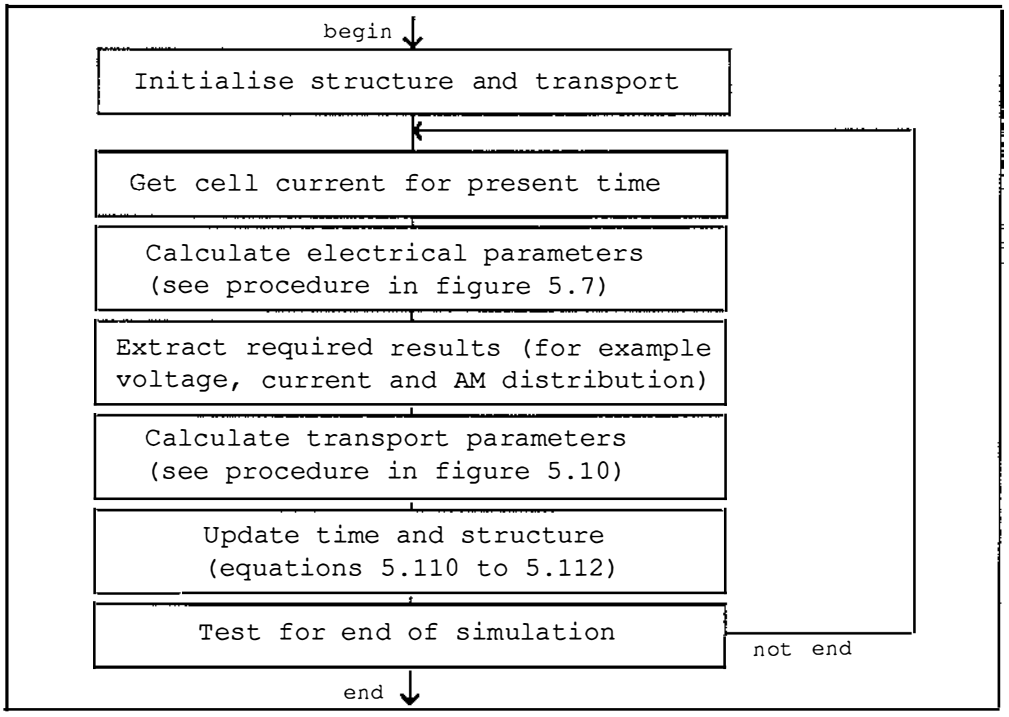

Figure 5.11: Over-all Calculation Procedure.

5.5.9 The Over-all Computational Procedure.

The over-all computational procedure for operating the aggregate model consists of applying the procedure for calculating the electrical parameters, the procedure for calculating the concentration parameters and the procedure for calculating structural parameters in sequence for each time step. A flow diagram for the over-all calculation procedure is given in figure 5.11. The system description represented here was converted to a Pascal computer program and solved on a MicroVax II cluster. The program used is given in appendix 2.

The results obtained for the aggregate model are given in chapter 7. Chapter 6 describes experiments that were performed to collect data to test these results.

Chapter 6

Industrial Traction Cell Experiments

This chapter gives details of the equipment, cell and procedure used in experiments performed on a single, 100 Ampere hour (5 hour rate), industrial traction cell. The primary objective of the experiments was to obtain the data for the operation and evaluation of the VIAM model. The cell was subjected to a discharge/charge cycle consisting of

i) a selected constant current discharge to a selected discharge depth,

ii) a zero current rest time of 0.5 hours and

iii) a 20 Ampere constant current, 2.600 volt upper voltage limit, charge.

The charge was terminated 5 hours after the cell voltage attained 2.400 volts.

Four constant current discharge rates of 40, 20, 10 and 5 Amperes were used. Three discharge depths of 100, 50 and 10 Ampere hours were used. Conditioning charge cycles were also performed to ensure the cell was fully charged when needed. The constant current discharge/charge scheme was used to maintain compatibility with the majority of studies in the literature. Measurements taken during the discharge/charge cycles were the cell discharge current, the cell charge current, the cell voltage, the cell gas evolution rate, the electrolyte specific gravity and the voltage difference between the positive plate post and a PbO_2 reference electrode post (the post voltage). The cell temperature was kept at 25 ±0.25°C using a temperature controlled water jacket.

The chapter content is summarised below.

i) A description of the experimental equipment (section 6.1)

ii) A description of the cell under test (section 6.2)

iii) A description of the experimental procedure (section 6.3)

The experimental results are given together with results for the elemental models, aggregate model and VIAM model in chapter 7.

6.1 THE EXPERIMENTAL EQUIPMENT.

6.1.1 Equipment Overview.

A block diagram of the experimental equipment is given in figure 6.1.

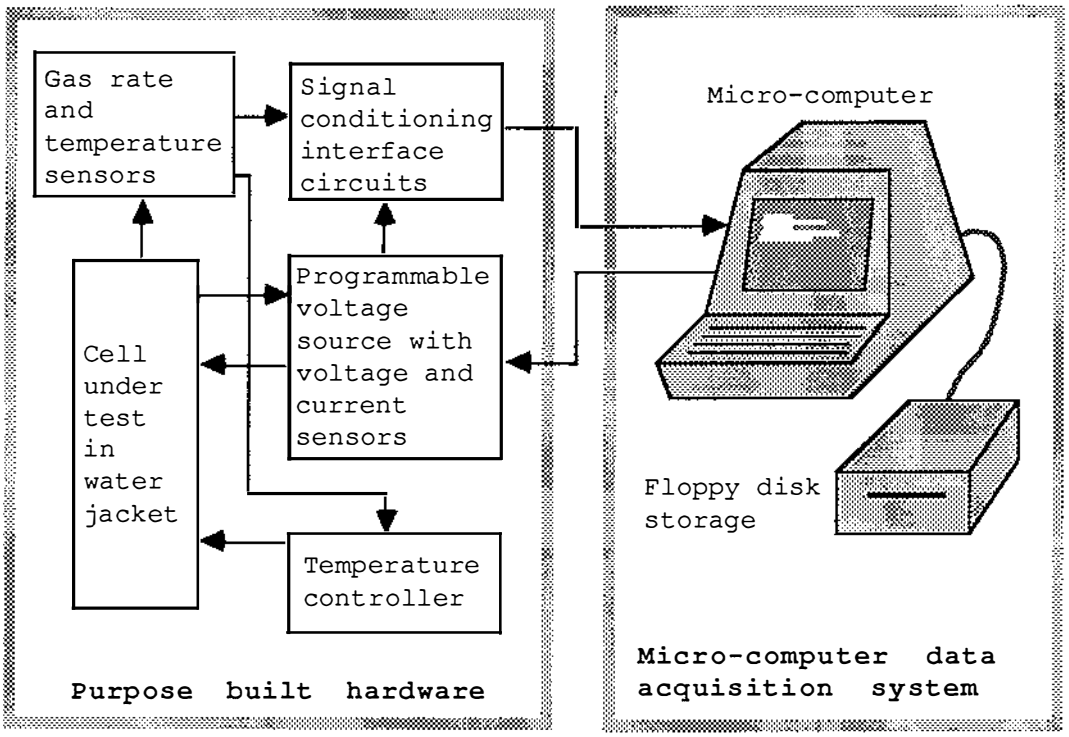

Figure 6.1: Block Diagram of Experimental Equipment.

The data acquisition system consisted of a general purpose micro-computer fitted with specialised input/output cards. The general purpose micro-computer allowed the discharge/charge algorithm to be written in a standard high-level programming language. It also provided a floppy disk facility for the storage of data obtained during the charge/discharge cycle. The specialised input/output cards provided digital to analog, analog to digital and pulse accumulator interface circuits for sending and receiving signals to and from the purpose built hardware.

The main component of the purpose built hardware was a high current programmable voltage source. This was used to both discharge and charge the cell under test. In addition the purpose built hardware included interface circuits to condition the signals sent to the data acquisition system and a temperature controller to hold the cell temperature constant.

6.1.2 The Data Acquisition System.

The data acquisition system used was the Laboratory Instrumentation System (or "LIS") produced by the Department of Production Technology at Massey University. The "LIS" software runs under the CP/M operating system. The "LIS" hardware has an extended input/output bus which caters for a variety of input/output cards. The software algorithm and hardware configuration that was used in this application are described below.

a) The discharge/charge algorithm.

The discharge/charge algorithm was written in the Turbo Pascal programming language. A simplified flow diagram of the algorithm is given in figure 6.2. A brief description of the most important functions in figure 6.2 follows.

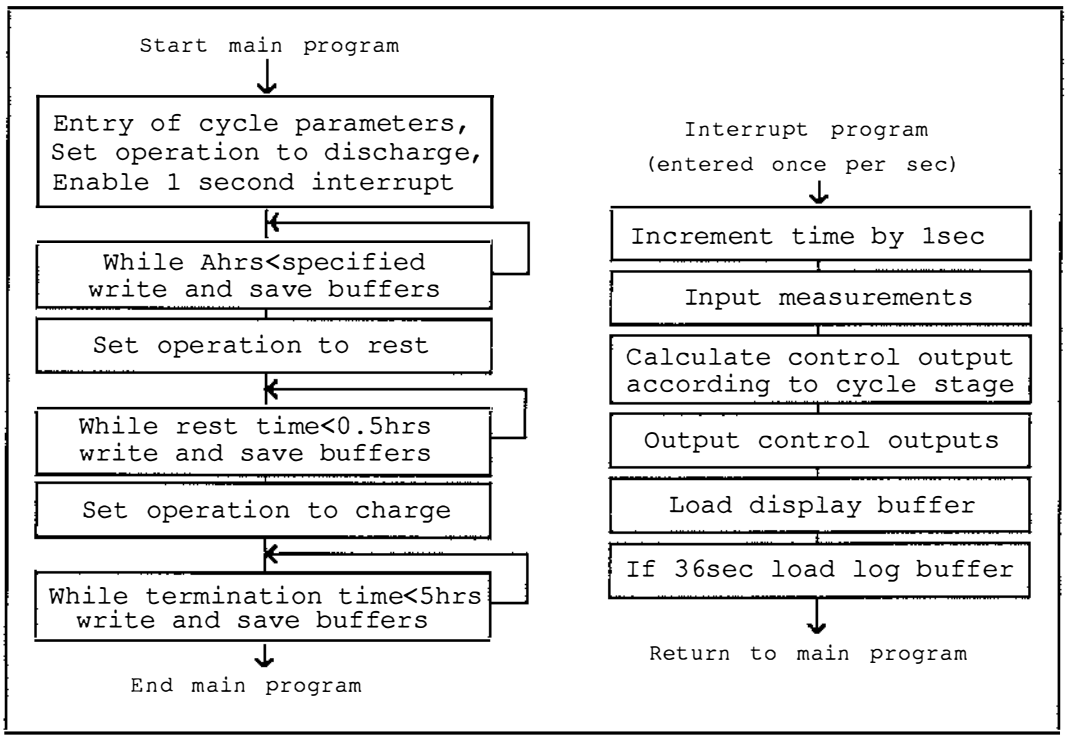

Figure 6.2: Discharge/Charge Cycle Algorithm.

All discharge/charge cycle parameters were entered via the computer keyboard in response to prompts on the computer display. The parameters included selected discharge current, selected discharge depth, rest time, charge current, charge voltage limit and charge termination time. In addition maximum total cycle time and maximum gassing rate were also entered to ensure safe cycling of the cell.

The measurement signals input from the purpose built hardware were cell discharge current, cell charge current, cell voltage, the post voltage and cell gassing rate. Time and cell Ampere hours were calculated by the computer. The specific gravity of the cell electrolyte was recorded manually.

The control calculations depended on the stage of the cycle. For the constant current discharge stage the control calculations changed the control voltage at a rate of 0.002 $v.s^{-1}$ to bring the discharge current into a 0.2 Ampere dead-zone centred on the selected value. For the rest stage the control calculations set the voltage enable control inactive. For the constant current part of the charge stage, the control calculations operated in much the same way as for the constant current discharge. The difference in this case was that the dead-zone was centred on the charge rather than the discharge current value. In addition a 5 hour termination time-out was started when the cell voltage reached 2.400 volts during this stage. For the constant voltage part of the charge stage, the control calculations changed the control voltage at a rate of 0.002 $v.s^{-1}$ to bring the cell voltage into a 0.002 volt dead-zone centred on the constant voltage charge value.

Three control signals were output to the purpose built hardware. Two of the signals were derived from the calculated control voltage and set the output voltage on the programmable voltage source. These were the voltage and

offset controls. The third signal was derived from the voltage enable control. When inactive this signal set the programmable voltage source into a high impedance state, effectively disconnecting the cell.

The computer display was updated each time the display buffer was loaded by the interrupt program. This occurred once per second. The display update gave the present value for cell voltage, post voltage, cell current, cell gassing rate and time. Both the computer display and floppy disk were updated when the log buffer was loaded by the interrupt program. This occurred once every 36 seconds (or 0.01 hours). The values logged were the average (over the previous 36 seconds) cell voltage, reference electrode voltage, cell current, cell gassing rate, and the current cell Ampere hours and cycle time.

b) The hardware configuration.

The "LIS" system is based on a 4 MHz Z80 CPU with a 256K byte dynamic RAM memory and an 800K byte 5.25 inch floppy disk drive.

Analog to digital and digital to analog cards were used to input and output the cell current, voltage and control signals once per second. These were 8-channel/8-bit units having an analog range of 0.00 to 5.10 volts. Taking account of the signal conditioning performed by the purpose built hardware this corresponded to a range of 1.700 to 2.710 volts for the cell voltage signals, a range of 0.0 to 51.0 Amperes for the cell current signals and a range of 0.000 to 0.510 volts for the reference voltage signal. The single bit resolution was 0.002 volts and 0.2 Amperes for the voltage and current signals respectively.

A pulse accumulator card was used to input the cell gassing rate. This counted up to 255 pulses and was read every 36 seconds. Taking into account the stroke of the gas metering pump used for the gas rate measurement, this

corresponded to a gas rate range of 0 to 2.361×10^{-6} $m^3.s^{-1}$ in increments of 9.259×10^{-9} $m^3.s^{-1}$.

6.1.3 The Purpose Built Hardware.

The programmable voltage source, measurement interface circuits and temperature controller parts of the purpose built hardware are discussed in turn below.

a) The programmable voltage source.

Figure 6.3 gives a schematic diagram for the programmable voltage source. The programmable voltage source was a negative feedback, high current, voltage amplifier. The amplifier input was the required cell voltage. This was determined by the voltage and offset controls output from the data acquisition system using the divide by ten, offset source and unity gain offset differential amplifier circuits. The feedback signal was

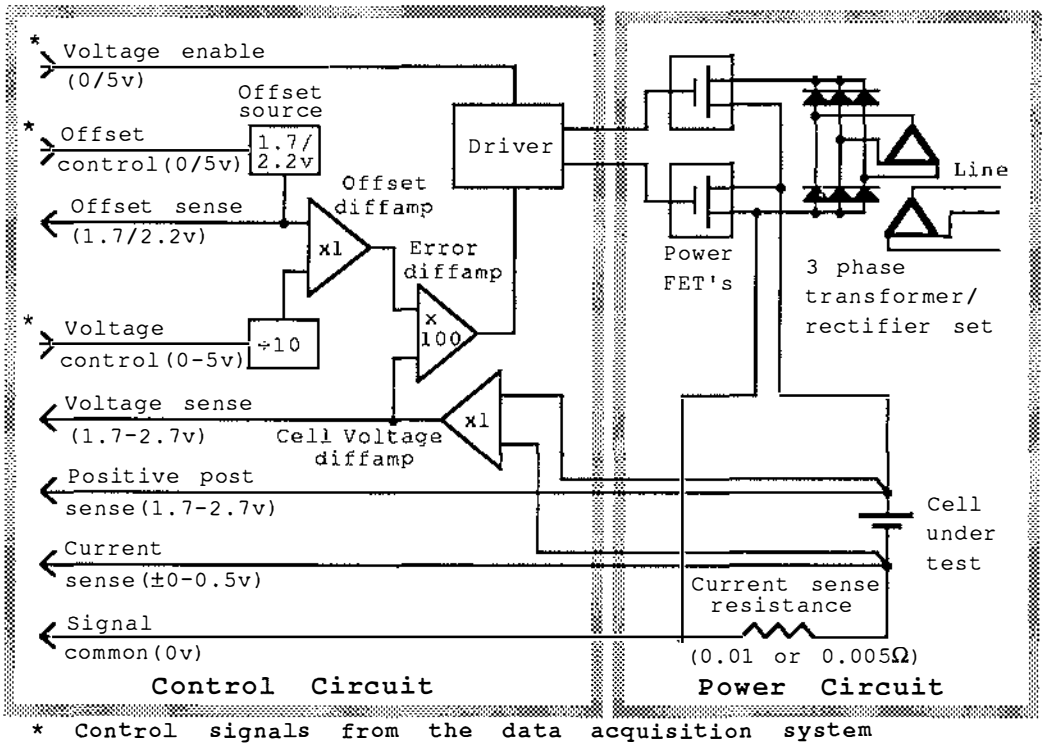

Figure 6.3: Programmable Voltage Source Schematic.

the actual cell voltage determined by the unity gain cell voltage differential amplifier. This amplifier was required to eliminate any voltage drop across the 0.01Ω current sensing resistor. The actual and required voltages were compared in the high gain error differential amplifier. Any error was sensed by the driver circuit which adjusted the actual voltage to null out the error. The net effect of the negative feedback operation ensured that the actual cell voltage was equal to the required cell voltage. The power supply for the amplifier was a 100 ampere (average), 7.3 volt (average) three phase transformer/bridge rectifier set. The amplifier output used three 35 Ampere power field effect transistors (FET's) in parallel for both the upper and lower half of the circuit. The amplifier output could be placed in a high impedance state when the voltage enable control output from the data acquisition system was inactive. The programmable voltage source also provided current sense, voltage sense, offset sense, positive post sense and signal common connections to the measurement interface circuits.

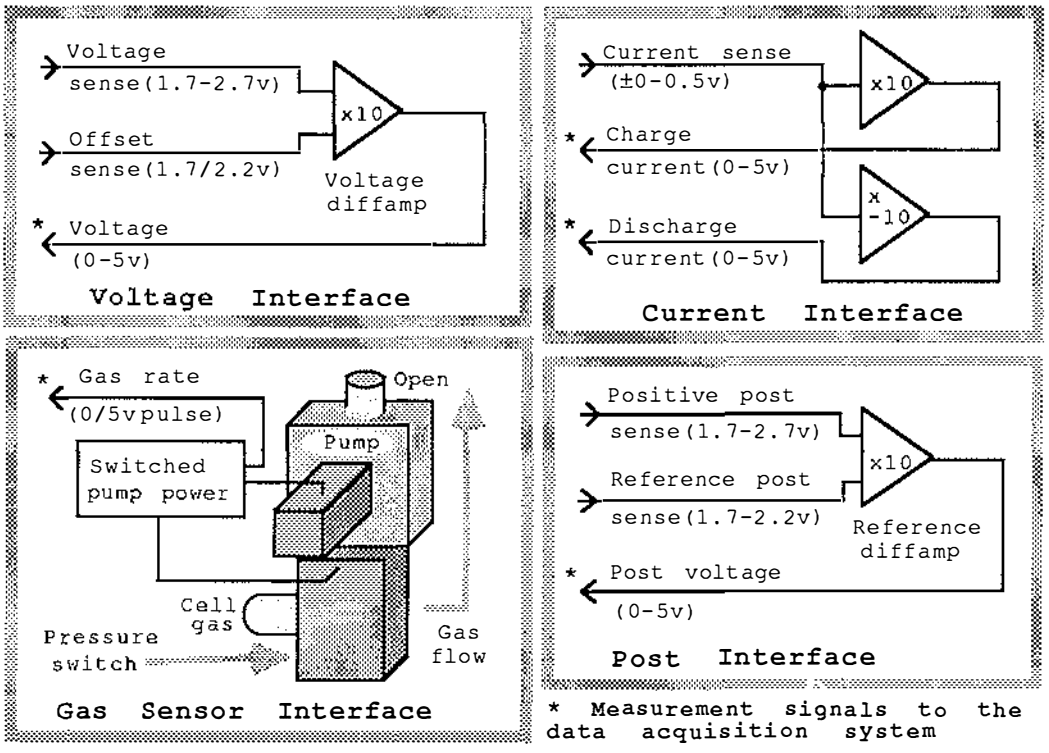

Figure 6.4: Measurement Interface Circuits.

b) The measurment interface circuits.

Schematic diagrams for the measurement interface circuits are given in figure 6.4. The voltage interface circuit subtracted the offset sense from the voltage sense signal and multiplied the result by ten using the voltage differential amplifier. The current interface circuit multiplied the sense current by ten and minus ten to give the charge and discharge current respectively. In both cases simple single input amplifiers were used. The post voltage interface circuit subtracted the reference electrode post sense from the positive post sense and multiplied the result by ten using the post differential amplifier. The reference PbO_2 electrode itself was formed by charging a small grid segment. It was immersed in the electrolyte solution at the top of the cell and electrical connection was made through the cell plug. The gas measuring components produced a pulse frequency proportional to the gas evolution rate of the cell at atmospheric pressure. The pulses were derived from the filtered output of a differential pressure switch. This switch consisted of an optical sensor arranged to detect very small changes in the fluid level of a small U-tube manometer. The metering pump pulses also activated the positive displacement metering pump itself via a switched power supply.

c) The temperature controller.

A schematic diagram for the temperature controller is given in figure 6.5. The controller had a feedback signal obtained using the cell temperature feedback sensor. The controller also had a feed forward signal derived from the charge or discharge current using the current square/sum circuit. The feed forward signal accounted for the heating effect of the cell current. The input to the controller was the temperature set point. The temperature set point was compared with the feedback signal to give a temperature error using the error differential amplifier. The error and

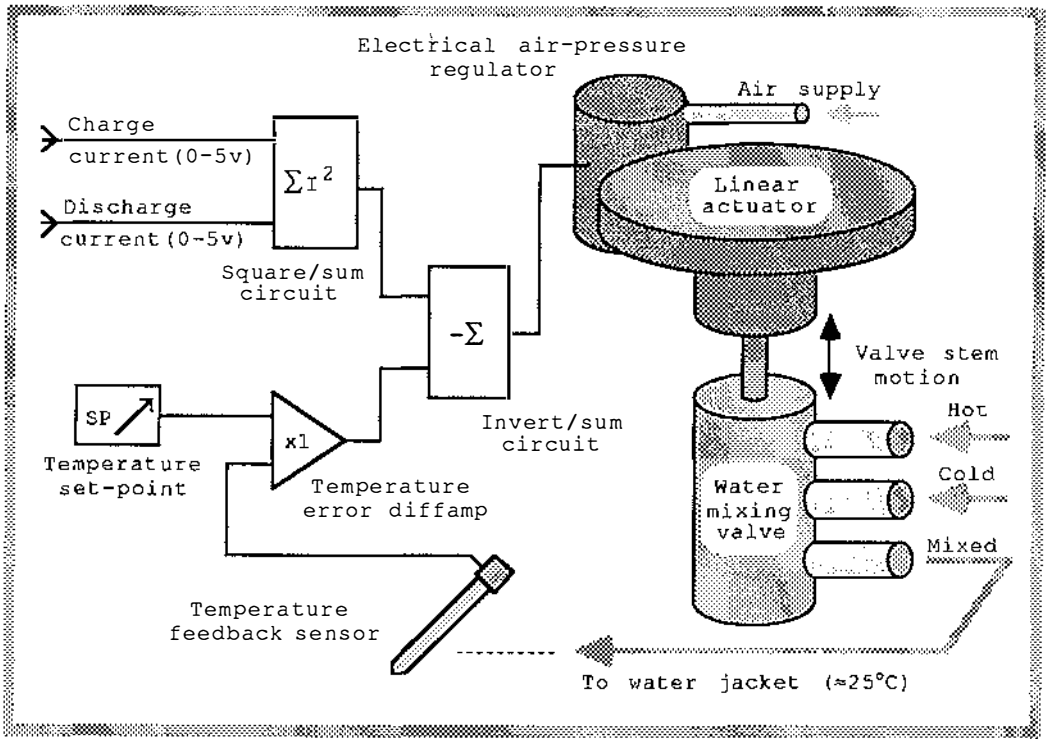

Figure 6.5: Temperature Controller Schematic.

the feed forward signals were combined by the invert/sum circuit and used to operate a pneumatic powered linear actuator. The linear actuator, in turn, operated a hot and cold water mixing valve which supplied the cell water jacket. The feedback control loop was completed by the heating effect of the water jacket which determined the temperature of the cell electrolyte and therefore the temperature of the feedback sensor. The gains of the invert/sum circuit and the feedback sensor position were selected by trial and error to restrict temperature variations to ±0.25°C of the set point under conditions when the cell current was stepped from 0 to 100 Amperes. The temperature variations were measured using a thermometer inserted through the cell plug into the electrolyte solution at the top centre of the cell. The feedback temperature sensor was placed in a glass tube filled with thermally conductive grease. The glass tube was inserted diagonally through the cell plug into electrolyte solution at the top of the cell.

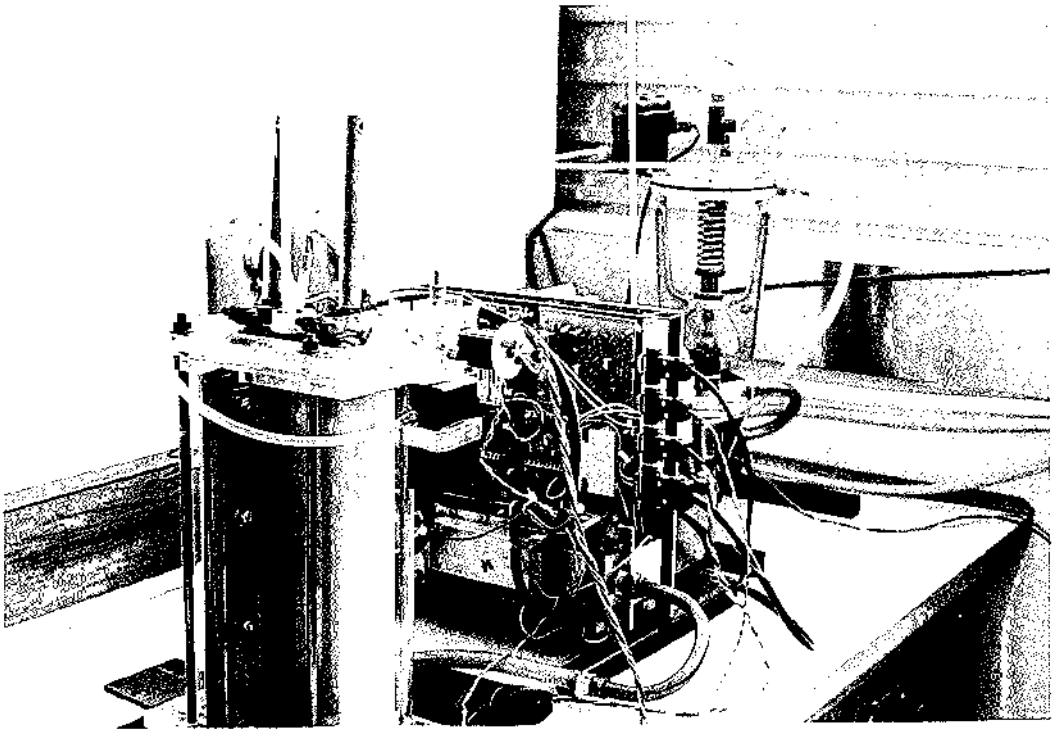

Figure 6.6: The Purpose Built Hardware.

A photograph of the purpose built hardware is given in figure 6.6. The main equipment frame is seen in the centre of the photograph. The three phase transformer set used for the programmable voltage source is on the back of this frame. The rectifiers and FET's used for the voltage source are mounted on the water cooled heat sink at the bottom of this frame. The electronic circuits associated with the voltage source, the measurement interface and the temperature controller are mounted on the upper portion of the main equipment frame. The cell under test is seen in the left hand foreground of the photograph. It is enclosed in the temperature controlled water jacket. Mounted on the front of the water jacket top plate is the gas metering pump and pressure switch assembly. On top of the cell is the cell plug assembly containing the reference electrode, feedback temperature sensor, thermometer and gas metering pump feed line. The linear actuator and mixing valve used for the temperature controller are seen in the right hand background of the photograph.

6.2 THE CELL UNDER TEST.

6.2.1 General Specification.

The general specification of the cell under test is given below.

Manufacturer: Chloride Batteries New Zealand Limited.
Cell Designation: N7.
Nominal capacity: 100 Ahrs (5 hour rate).
Number of plates: 3 positive and 4 negative.
Approximate overall dimensions ($x10^{-3}m$): 359x160x63
(height x width x thickness).
Approximate weight ($x10^{3}g$): 11.0 (wet).

6.2.2 Physical Construction Details.

The cell was of the conventional flat plate type (see chapter 2). The cell element was made up of alternate negative and positive plates held apart by separator assemblies. Both the outside plates were negative. The plates were constructed using pasted lead antimony grids. The separator assemblies included a glass fibre mat, a ridged microporous polyethylene separator and a flat microporous polyethylene veneer. The glass mat rested against the positive plate, the ridged separator was placed next and the flat veneer rested against the negative plate. The ridged separators on each side of a positive plate were welded together and formed an envelope around the plate to reduce shorting. The element was held together by negative and positive busbars welded to the top the plates. The busbars include the cell terminal posts. The element was fitted into a polyethylene case. This was made up of a case tank, an element footing and a case top. The case top was fitted with terminal post seals and a vent plug.

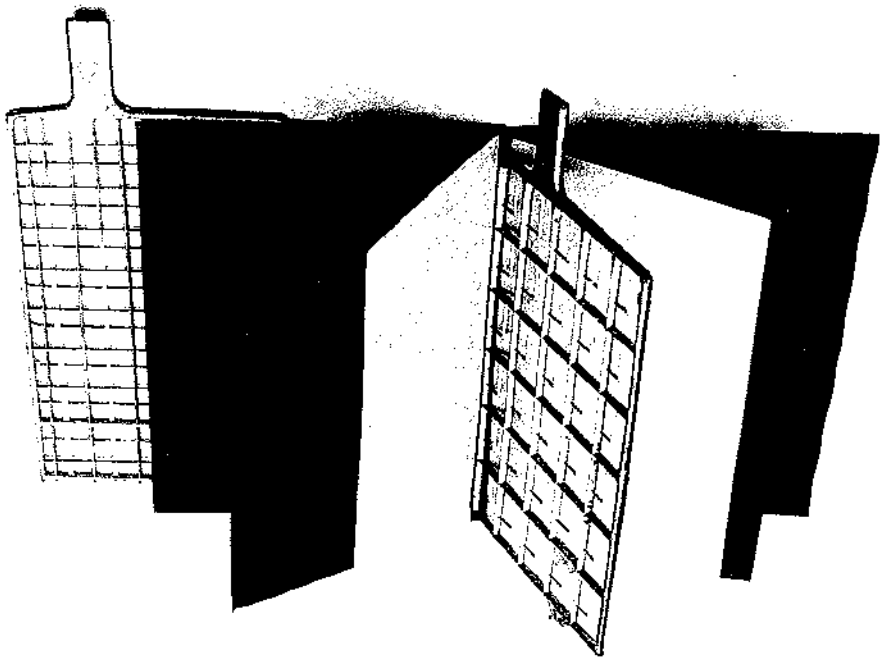

Figure 6.7: Cell Grid and Separator Components.

A photograph of the assembled cell is given on the cover page of this work. A photograph showing the unpasted plates (bare grids) and separator assembly parts is given in figure 6.7. The plate on the right is the positive. The ridged separator envelope weld in the foreground has been opened to give an improved view. The positive grid is a rectangular framework of both heavy and light members. The negative grid is a rectangular framework of medium weight members.

Dimensions of the components described above are given in table 6.1.

Table 6.1: Cell Dimensions.

Dimension description	Value($x10^{-3}$m)
Plate height:	218
Plate width:	136
Positive plate thickness:	5.1
Combined positive grid height:	21
Combined positive grid width:	17
Negative plate thickness:	4.1
Separator glass mat thickness:	1.5
Ribbed separator thickness:	1.7
Separator flat veneer thickness:	0.4
Average case thickness:	66
Average case width:	156
Cell container wall thickness:	2.0
Electrolyte solution height:	300

6.2.3 Grid and Paste Composition Details.

The details given below are based on data kindly supplied by the cell manufacturer. Some details have been intentionally omitted to protect commercial interests.

The positive and negative grids were made from a lead-antimony alloy. The alloy also contained small amounts of other elements. The alloy composition is given below.

94.4 to 94.9% lead
4.8 to 5.2% antimony
0.15 to 0.20% arsenic
0.10 to 0.14% tin
0.02 to 0.05% copper

The leady oxide used for the positive and negative AM paste was produced by a Barton Pot process. The plant gave 70 to 80% tetragonal lead oxide particles. The remaining particles were lead.

For the production of positive AM paste sulphuric acid and leady oxide were mixed in the ratio of 5% H_2SO_4/PbO (by weight) with measured quantities of water. The mixing temperature started at about 18°C (room temperature) and rose to a peak of 55°C. The resulting paste contained mainly tri-basic lead sulphate with some (about 15%) residual lead. The paste had a density of 4.35×10^6 $g.m^{-3}$. After pasting into the grids the density increased to 4.55×10^6 $g.m^{-3}$.

The positive plates were cured in a 40°C, 80 to 100% relative humidity (RH) atmosphere for 24 hours. The plates were then dried in a 45°C atmosphere of recirculating free air for a further 24 hours. The residual lead content in the AM after curing was typically 2 to 3%.

The cured plates were formed in sulphuric acid solution (specific gravity 1.190 at 25°C). The forming process involved constant current charge and discharge cycles at moderate rates. Every few discharge cycles the cell capacity was measured at the designed 5 hour rate. The cycles were continue until the cell reached its designed capacity.

Unfortunately the AM structure of the formed plates is not investigated by the manufacturer. To estimate the structural details required for the models set out in chapters 4 and 5 measurements for similar AM published in the literature were used.

Pavlov and Bashtavelova (1984 and 1986) performed porosity and surface area distribution measurements on positive AM made from many different pastes. They showed that the paste composition and manufacturing process

Table 6.2: Comparison of AM Production Processes.

Production Process Parameter	AM produced by Pavlov and Bashtavelova*	AM produced for the cell under test
PbO/total ratio in leady oxide:	63%	70-80%
H_2SO_4/PbO ratio in mixing:	6%	5%
Mixing temperature:	30°C	18-55°C
Paste density ($x10^6 g.m^{-3}$):	4.40	4.35
Phase composition:	Tri-basic lead sulphate	Tri-basic lead sulphate
Curing conditions:	30°C,100% RH, 48 hrs.	40°C,80-100% RH 24 hrs.
Drying conditions:	40°C, 60% RH, 24 hrs.	45°C, free air, 24 hrs.

* Pavlov and Bashtavelova (1986)

controlled the characteristics of the formed AM. For one AM in particular, the paste composition and manufacturing process was very similar to that used for the cell under test. The similarity can be seen from the summary data given in table 6.2. Details of the positive AM formed from this paste were adopted as a first estimate of the details of the positive AM of the cell under test. Measurements recorded by Pavlov and Bashtavelova (1986) are given in figure 3.1. A SEM micrograph of the positive AM concerned is given in figure 3.2.

Micka and Svata (1979) performed porosity and tortuosity measurements on plates from SLI cells. The negative porosity and positive and negative tortuosity results they reported are adopted for the AM of the cell under test.

6.3 EXPERIMENTAL PROCEDURE AND SCHEDULE.

6.3.1 Discharge/Charge Cycle Procedures.

a) Calibration.

Before starting the discharge/charge cycle the gas metering pump and temperature controller calibration were checked. In the case of the gas metering pump this was done by opening the pump feed line to the air, tilting the manometer to start the pump and counting the number of strokes required to displace 400×10^{-6} m^3 of water from an inverted graduated cylinder. The pump was adjusted to displace 0.333×10^{-6} m^3 per stroke when necessary. In the case of the temperature controller the actual cell temperature was checked using the cell plug thermometer and the temperature controller set-point adjusted to bring this to 25°C when necessary.

b) The discharge/charge cycle.

At regular intervals throughout the discharge/charge cycle the gas metering pump feed line was removed from the cell plug to allow access to a float type hydrometer. The hydrometer was used to withdraw and measure the specific gravity of a small amount of cell electrolyte. Upon completion of the measurement the electrolyte was returned to the cell and the metering pump feed line refitted. Measurements of this type were performed every 0.25 to 0.5 hours. All other measurements were made automatically using the purpose built hardware and data acquisition system described above.

c) The conditioning charge.

The cell was occasionally subjected to an additional conditioning charge to ensure it was in a fully charged state. This was performed at a constant 2.600 volts.

Table 6.3: Experimental Schedule.

Experiment Designation	Depth/Rate (Ahrs/A)	Experiment Order	Time between Cycles (days)
AD010R40	10/40	4	1
AD010R20	10/20	1	4
AD010R10	10/10	2	1
AD010R05	10/5	3	1
AD050R40	50/40	5	1
AD050R20 **	50/20	6	15
AD050R10 *	50/10	7	2
AD050R05 *	50/5	8	1
AD100R20 *	100/20	9	1
AD100R10	100/10	10	1

Interpretation of the experiment designation: AD100R20

Cell label

Discharge depth (Ahrs)

Discharge rate (A)

* Succeeding conditioning charge

** Preceding conditioning charge

6.3.2 The Experimental Schedule.

The experimental schedule is summarised in table 6.3. This gives the experiment designation, the discharge depth and rate, the order in which the experiments were performed and the time between the listed experiment and the previous experiment. Three other cells were also subjected to a similar schedule and gave comparable results.

Chapter 7 presents the results for the elemental and aggregate models based on parameters for the cell under test. In addition the experimental results obtained from the schedule above are compared with the VIAM model results in chapter 7.

Chapter 7

Results and Discussion

A series of results are reported in this chapter. Firstly, the partial results obtained from the stand-alone application of the three elemental models are given. These are followed by the partial results for the stand-alone application of the aggregate model. Both sets of partial results are discussed in the light of known data where possible. Next, the more general results for the VIAM model are given and discussed. The VIAM model is formed by the simultaneous application of the three elemental models and the aggregate model. Results from the cell tested experimentally are then given. Finally, the VIAM model results and the experimental results are compared and discussed.

The parameters used for all the models are based on the actual or adopted data for the cell tested experimentally (see section 6.2).

The chapter content is summarised below.

i) Results for the elemental models (section 7.1).

ii) Results for the aggregate model (section 7.2).

iii) Results for the VIAM model (section 7.3).

iv) Experimental results (section 7.4).

v) A comparison of the VIAM model and the experimental results (section 7.5).

7.1 THE ELEMENTAL MODELS.

7.1.1 The Discharge Capacity Model Results.

The discharge capacity model is set out in section 4.1. The results for this model are obtained by solving equations 4.4 to 4.6. These equations require the equivalent gram solution volume in the AM microstructure to be known.

a) Solution volume in the microstructure.

The solution volume in the microstructure is equated to the total volume changes in the AM for a full discharge of the adopted AM (see section 6.2). This is an average value taken over the total plate thickness. The average value may be quite different from the required local full discharge value since, under normal discharge conditions,

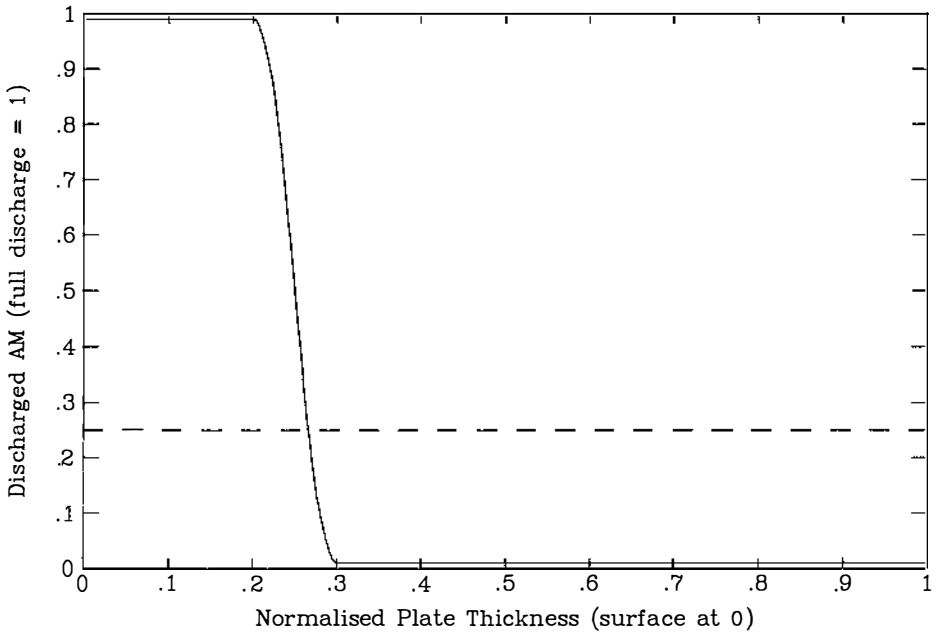

Solid: Actual discharged AM distribution.
Dash: Average discharged AM level.

(Average value)=(Full discharge value)x(Plate proportion discharged).

Figure 7.1: Possible Distribution of Discharged AM in Plate.

the AM near the plate surface is subjected to a full discharge, while AM in the centre of the plate is subjected to a small discharge only (see section 3.7.2). This is illustrated in figure 7.1. It can be seen that the full discharge value is approximated by the product of the average value and the proportion of the plate thickness that is fully discharged.

The discharge volume change for the adopted AM was 0.044×10^{-6} $m^3.g^{-1}$ (Pavlov and Bashtavelova (1986)). The discharge was terminated when the positive electrode potential reached 0.6 volts versus a Hg/Hg_2SO_4 reference electrode. This corresponds to a voltage drop during discharge of some 0.7 volts (compared to 0.3 volts for a normal discharge) and indicates a deep discharge. The AM utilisation factor for the discharge was about 0.52 which is high (0.2 to 0.5 are typical see Smith (1980)) and also indicates a deep discharge. Given the deep discharge conditions and the relatively thin plates of the SLI cell

tested, it will be assumed that the plate was fully discharged over its entire thickness. That is, the average and full discharge volume changes in this case are equal.

The full discharge volume change for the adopted AM is the volume change per gram of discharged AM (AM that contains both PbO_2 and $PbSO_4$). The value required to define the equivalent gram solution volume in the microstructure is the volume change per gram of original PbO_2. The equivalent gram value is obtained by correcting the change in mass using Faraday's law and the molar mass of $PbSO_4$. This gives

$$V_\mu = 0.050 \times 10^{-6} \ m^3.g^{-1}. \qquad (7.1)$$

b) The discharge capacity results.

The results for the elemental discharge capacity model using the value of V_μ given above are,

$$q_d = 418 \ A.s.g^{-1}, \qquad (7.2a)$$

$$q_T = 807 \ A.s.g^{-1} \qquad (7.2b)$$

and

$$Q_d = 0.52. \qquad (7.2c)$$

7.1.2 The Discharge Capacity Model: a Discussion.

One way the discharge capacity model can be tested is to use the results determined above to estimate the proportion of the plate involved in the rated capacity discharge of the cell under test. Some confidence can be placed in the model if this is close to typical values found experimentally.

It is possible to calculate the average AM utilisation factor for the cell under test assuming the rated 100 Ampere hour capacity. This is given by the mass of PbO_2 consumed in a 100 Ampere hour discharge divided by the total mass of PbO_2 in the plates of the cell. The former

quantity is obtained directly from the theoretical discharge capacity and is equal to 446.3 g. The latter quantity is obtained by dividing the total plate volume by the sum of the equivalent gram PbO_2 solid and total pore volumes. This gives a total mass of 1645 g. The average AM utilisation factor for the cell under test is therefore 0.271. Using the AM utilisation factor as determined by the discharge capacity model above, the proportion of the plate fully discharged in the cell under test is 0.521.

Chang (1984) performed experimental studies where AM utilisation was determined by observing the different appearance of discharged and charged AM within the plate thickness. The proportion of the plate fully discharged was in the range 0.75 to 0.66. This is somewhat larger than the proportion calculated using the discharge capacity model. The difference is not unexpected and can be accounted for as follows. Firstly, the cell under test was found to be conservatively rated. In the experiments performed the actual capacity was found to be about 110 Ampere hours. Calculations based on this experimental capacity show the proportion of plate thickness fully discharged to be 0.573. Secondly, the plates Chang (1984) tested were discharged in an excess of electrolyte and were considerably thinner than those of the cell under test ($3x10^{-3}$ m compared to $5.1x10^{-3}$ m). A high AM utilisation is expected in this case since the occurrence of the normal end of charge overpotential is delayed due to low solution resistance and short transport paths. Taken together these factors indicate that the discharge capacity model results and the experimental results reported by Chang (1984) are comparable.

The discharge capacity model can be tested further when it is combined with other model components and used for the VIAM model. The discharge capacity model is validated if there is a satisfactory agreement between the VIAM model results and the experimental results.

7.1.3 The Discharge Surface Area Model Results.

The discharge surface area model is set out in section 4.2. The results for this model are given by the application of equation 4.8. This equation represents a simple linear approximation to the variation of surface area with charge state. The equation requires the PbO_2 surface area values for the fully charged and fully discharged conditions to be known.

a) The full charge surface area.

The full charge surface area can be obtained directly from the adopted data (Pavlov and Bashtavelova (1986)). This gives

$$S_{\mu c} = 3.60\ m^2.g^{-1}. \qquad (7.3)$$

b) The full discharge surface area.

The full discharge surface area can be derived from the adopted data by correcting the value given to the equivalent gram value (as was done for the discharge volume change in section 7.1.1). The required PbO_2 surface area can then be found by assuming the corrected value is made up of equal parts of PbO_2 and $PbSO_4$ surface (see section 4.2). The value given for the discharge surface is 2.75 $m^2.g^{-1}$. When corrected this gives 3.13 $m^2.g^{-1}$. The required PbO_2 surface area is half the corrected value. That is,

$$S_{\mu d} = 1.57\ m^2.g^{-1}. \qquad (7.4)$$

c) The discharge surface area results.

The discharge surface area results obtained by substituting full charge and full discharge values into equation 4.8 is shown in figure 7.2.

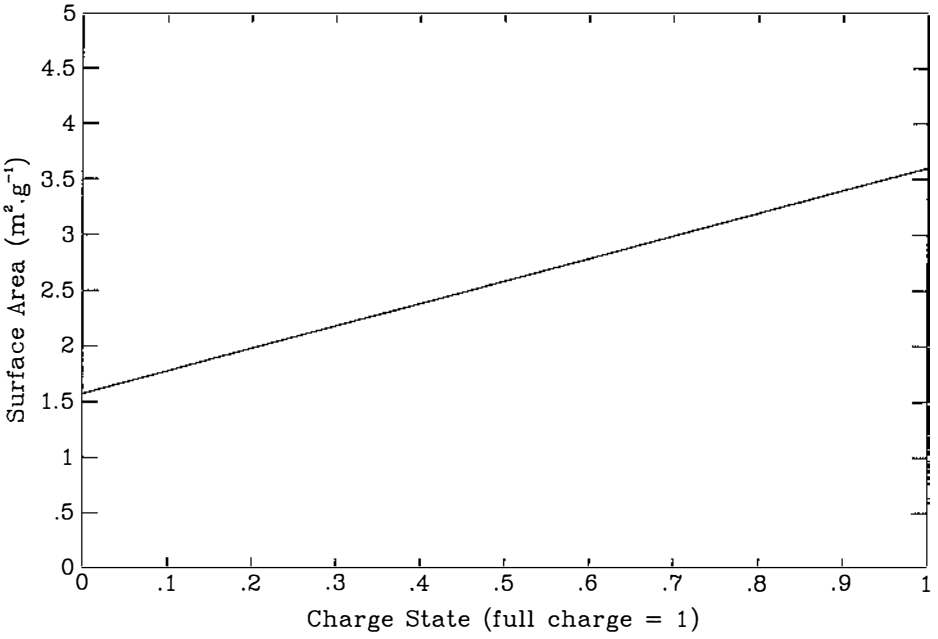

The discharge surface is defined by the approximation $X(S_{\mu c}-S_{\mu d}) + S_{\mu d}$ where: X is the charge state, $S_{\mu c}$ is the surface at full charge (3.60 $m^2.g^{-1}$) and $S_{\mu d}$ is the surface at full discharge (1.57 $m^2.g^{-1}$).

Figure 7.2: The Discharge Surface Area Model Approximation.

7.1.4 The Discharge Surface Model: a Discussion.

The discharge surface area model can be expected to give only a first approximation to the actual surface area change with discharge. This is because the formulation used is, itself, a simple approximation of the complex changes in structure described in section 4.2.1. It is difficult to directly assess the accuracy of the model because, at all but the fully charged state, two solid phase species (PbO_2 and $PbSO_4$) contribute to experimental surface area measurements. The model can only be tested indirectly when it is combined with other model components and used for the VIAM model. Here, as before, the agreement of the VIAM model and the experimental results would go some way in validating the discharge surface area model in its simplified form.

7.1.5 The Charge Surface Area Model Results.

The charge surface area model is set out in section 4.3. The surface area results are obtained by operating the model according to the procedure given in section 4.3.6. This amounts to solving the set of simultaneous equations (equations 4.42 to 4.56) that represent the structural changes described in section 4.3.1. The results give several quantities including the actual and effective PbO_2 surface area development with charge. The former quantity represents the total PbO_2 surface and the latter quantity represents only the PbO_2 surface area where the charge reaction is occurring. Obviously these two quantities differ greatly towards the end of charge where the actual PbO_2 surface reaches a maximum, but the effective PbO_2 surface tends towards zero. The effective PbO_2 surface area is a key quantity required by the VIAM model.

a) Model parameters.

Lead ion transport parameters including concentration and diffusion coefficent are required for the charge surface area model. These depend on acid concentration and are taken from the data given in Danel and Plichon (1982).

Structural parameters including equivalent gram quantities and geometric constants are also required for the charge surface area model. The required equivalent gram quantities are the solution microstructure volume and discharge total surface area. These are defined by the adopted AM and have already been determined for the previous elemental models above (see equations 7.1 and 7.4). The required geometric constants are the sphere surface factor, lobe surface factor and lobe number per sphere. These were determined as follows.

i) The surface area factors were fixed. The sphere surface factor was kept within the range 1.2 to 1.5 of a normal spherical surface. This is consistent with

the discharge model description which suggests high surface area features are largely removed by the discharge process (see section 4.2). The lobe surface factor was kept within the range 1.2 to 2 of a normal cylindrical surface. This acknowledges that the lobe structures grow in irregular high surface area forms.

ii) The number of lobes per sphere was selected by trial and error to give a result for the equivalent gram surface area at full charge that was equal to the value for the adopted AM. This surface area value has already been determined for the elemental models above (see equation 7.3). In the standard case, used for most of the results that follow, the sphere surface factor was 1.2 and the lobe surface factor was 2.

b) Typical model results.

Typical results for the charge surface area model that show the surface area development during constant current charge are given in figure 7.3. The vertical axis gives the equivalent gram surface area for the four area quantities ($PbSO_4$, actual PbO_2, $PbSO_4$+PbO_2 and effective PbO_2) defined by the model. The horizontal axis gives the charge state from fully discharged to fully charged (0 to 1 respectively).

It can be seen that the $PbSO_4$ surface area slowly reduces throughout most of the charge and then falls rapidly towards the end of charge. The slow reduction is consistent with the gradual consumption of solid $PbSO_4$. Towards the end of charge this will leave relatively low volume high surface area particles. The rapid reduction in surface area at the end of charge is consistent with the consumption of particles of this type. The PbO_2 surface increases throughout the charge. The increase is slightly more marked towards the end of charge. This is consistent

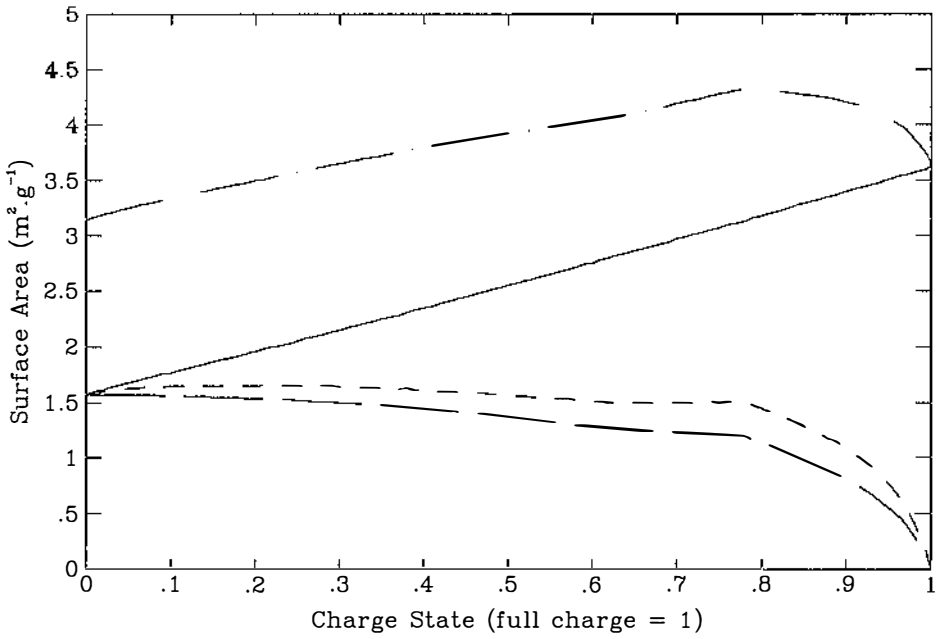

Solid: PbO_2 surface.
Small dash: Effective PbO_2 surface.
Large dash: $PbSO_4$ surface.
Dot dash: PbO_2+$PbSO_4$ surface.

Charge current: 62.5×10^{-3} $A.g^{-1}$ (approximately the 1 hr rate).
Acid concentration: 5.0×10^{3} $mol.m^{-3}$.

Figure 7.3: Charge Surface Area Development.

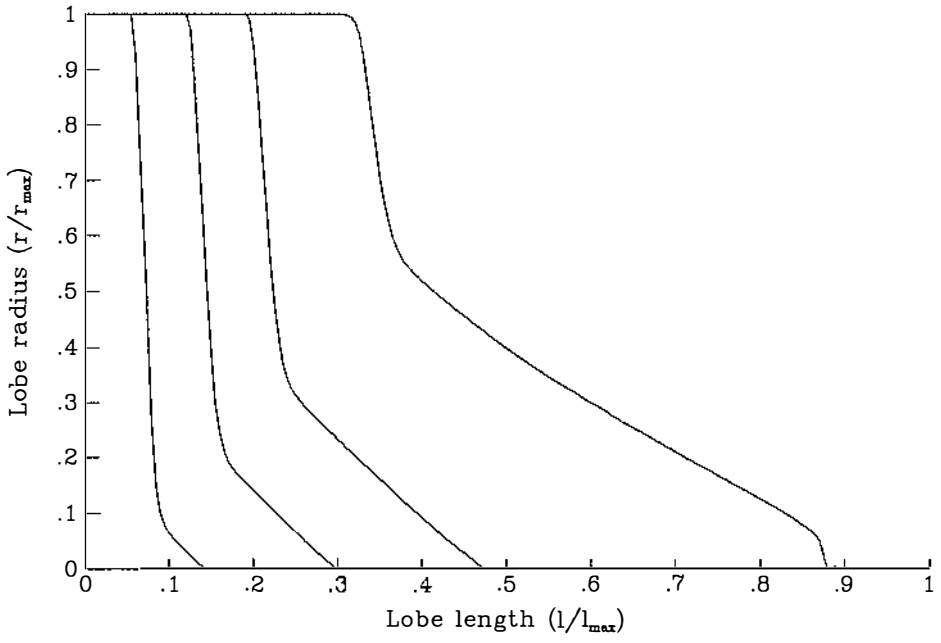

Charge state for profiles from left to right: 0.25, 0.5, 0.75 and 0.99.

Charge current: 62.5×10^{-3} $A.g^{-1}$ (approximately the 1 hr rate).
Acid concentration: 5.0×10^{3} $mol.m^{-3}$.

Figure 7.4: Lobe Profiles at Various Charge States.

with the development of lobes which grow more rapidly in length as the surrounding $PbSO_4$ retreats more rapidly into the corners of the sphere/box geometry towards the end of charge. The effective PbO_2 surface follows above the $PbSO_4$ surface throughout most of the charge. This is consistent with the controlling effect of the supply of ions from the $PbSO_4$ surface to the adjacent PbO_2 surface. The effective PbO_2 surface falls to zero at the end of charge as the reducing $PbSO_4$ surface and associated ion supply vanishes. The total ($PbSO_4$+PbO_2) solid phase surface area increases for most of the charge but decreases towards the end of charge.

The profiles of lobes at various stages of the surface area development are given in figure 7.4. The vertical axis gives the normalised lobe radius obtained by dividing the actual radius by the maximum possible radius. The horizontal axis gives the normalised lobe length obtained by dividing the actual length by the maximum possible length. The latter quantity is the radial distance from the sphere surface to the box corner within the sphere/box geometry. The horizontal axis is an axis of symmetry through the centre of the lobe. That is, the lobe itself can be visualised by rotating a given profile around this axis.

It can be seen that the lobes in figure 7.4 have grown as pointed tent-like shapes. As the charge proceeds the shapes get proportionately longer. This indicates that lobe growth is favoured near the retreating $PbSO_4$ surface (near the lobe point) as the charge proceeds. This is consistent with an increasing gradient in Pb^{2+} ion concentration caused by the increasing current density throughout the charge. The overall effect is that lobes that continue to grow until the end of charge have a larger surface area than those fully formed at an earlier stage. It must be remembered when examining the lobe profiles that the vast majority of lobes in the fully charged AM will be those formed during the early part of the charge. Only a few

lobes would be accompanied by adjacent $PbSO_4$ and therefore able to continue to grow during the latter stages of the charge. Because of this, the surface area of lobes at charge states approaching unity have only a minor effect on the overall PbO_2 surface area.

Figures 7.3 and 7.4 give the results for the charge surface area model in one particular case. That is, the case of a low current charge in an acid concentration typical for a partially charged cell and with a particular set of geometric constants. Questions arise as to how these results will vary for different charge currents, different acid concentrations and different geometric constants. Results for the charge area model where these factors are varied are given below.

c) Model results for various charge currents.

Figures 7.5 and 7.6 give the results of the charge surface area model where the charge current is varied. From figure 7.5 it can be seen that at all but very high currents, the actual PbO_2 surface area is almost the same as the low current case. That is, it is virtually independent of current. At very high currents the surface area at the end of charge rapidly exceeds that of the low current case. The reason for the increase in surface area at high currents can be seen in figure 7.6. At moderate and high currents the lobes develop a radial shelf of large surface area near the retreating $PbSO_4$ surface. At moderate currents this shelf is only a minor feature on the few lobes growing at the very end of charge. At high currents it is more extensive, on more lobes and forms earlier than at moderate currents. No growth of this type is evident until the charge is more than 75% complete. The development of rapidly growing finely structured lobes as seen here is typical of the dendritic growth that occurs when precipitation reactions are concentrated onto a small area (see Bockris and Reddy (1977)). It is expected here as the Pb^{2+} ion concentration gradient increases with increasing

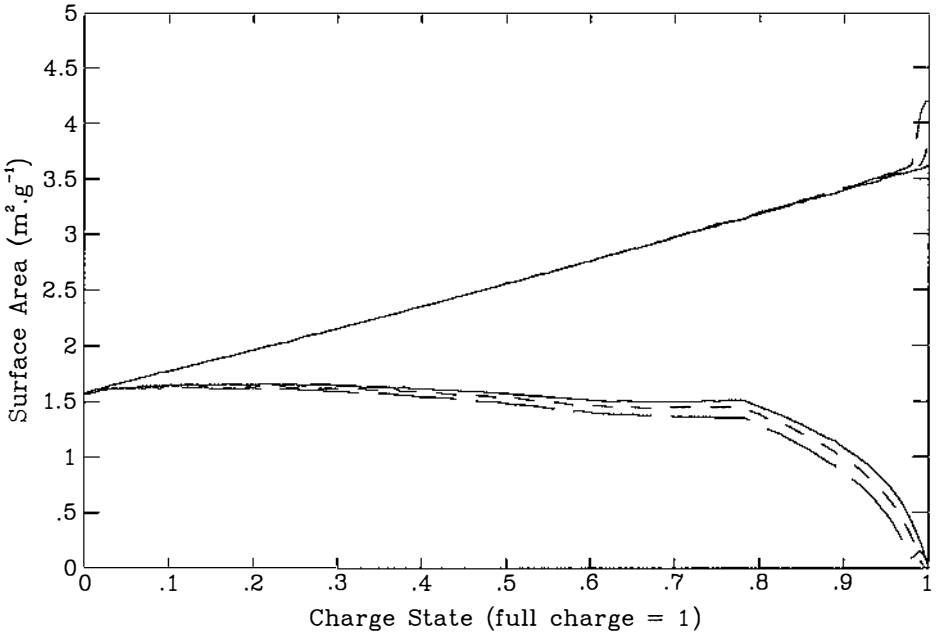

Top curves: actual PbO_2 surface.
Solid: current $62.5x10^{-3}$ $A.g^{-1}$ or less.
Large dash: current $625.0x10^{-3}$ $A.g^{-1}$.

Bottom curves: effective PbO_2 surface.
Small dash: current $312.5x10^{-3}$ $A.g^{-1}$.

$62.5x10^{-3}$ $A.g^{-1}$ is approximately the 1 hr rate.
Acid concentration in all cases: $5.0x10^{3}$ $mol.m^{-3}$.

Figure 7.5: Charge Surface Area for Various Currents.

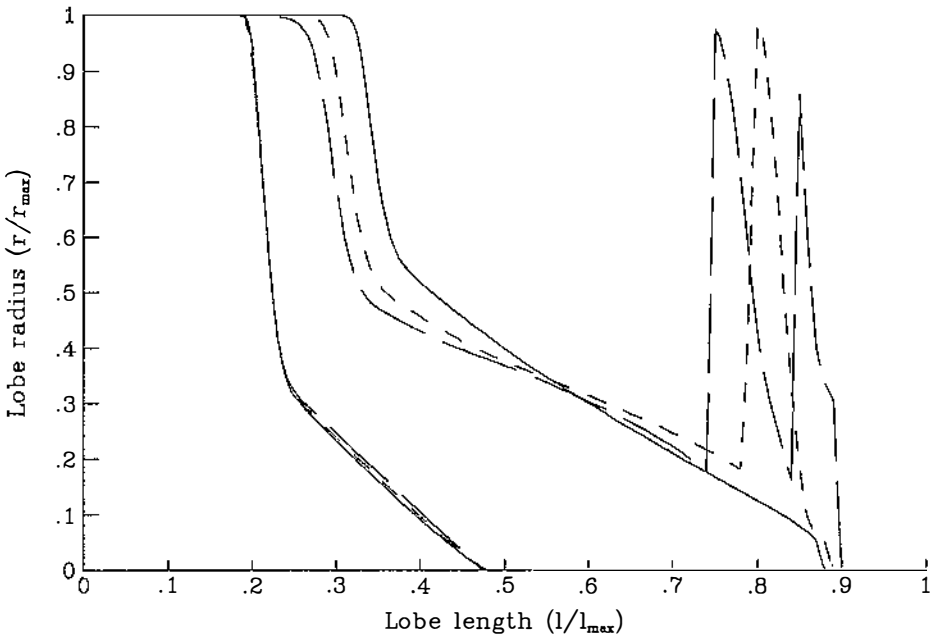

Charge state of profiles on left: 0.75.
Solid: current $62.5x10^{-3}$ $A.g^{-1}$.
Large dash: current $625.0x10^{-3}$ $A.g^{-1}$.

Charge state of profiles on right: 0.99.
small dash: current $312.5x10^{-3}$ $A.g^{-1}$.

$62.5x10^{-3}$ $A.g^{-1}$ is approximately the 1 hr rate.
Acid concentration in all cases: $5.0x10^{3}$ $mol.m^{-3}$.

Figure 7.6: Lobe Profiles for Various Currents.

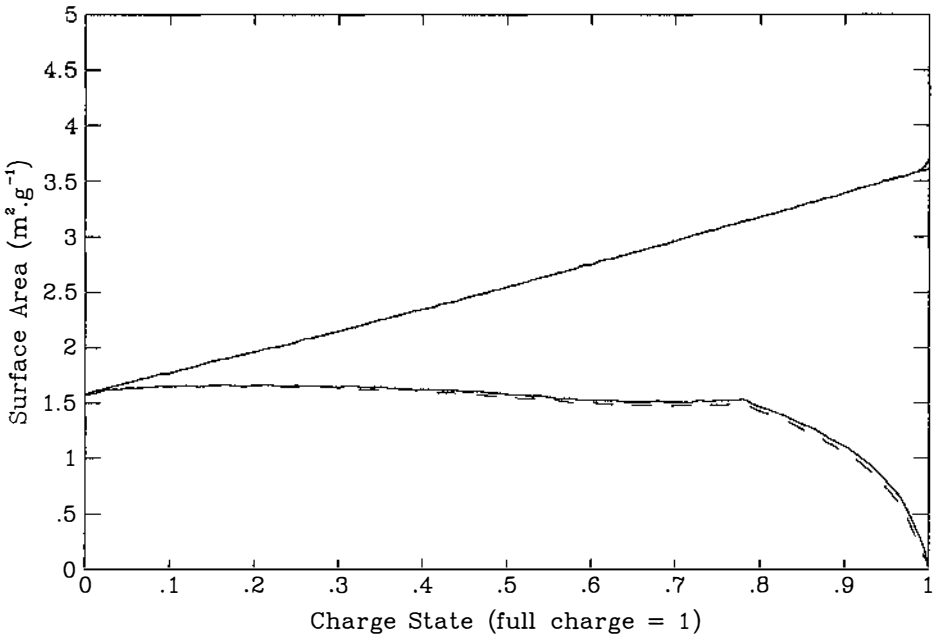

Top curves: actual PbO_2 surface. Bottom curves: effective PbO_2 surface.
Solid: concentration 1000 $mol.m^{-3}$ or less.
Small dash: concentration 10000 $mol.m^{-3}$.
Current in all cases: $62.5x10^{-3}$ $A.g^{-1}$ (approximately the 1 hr rate).

Figure 7.7: Charge Surface Area for Various Acid Concentrations.

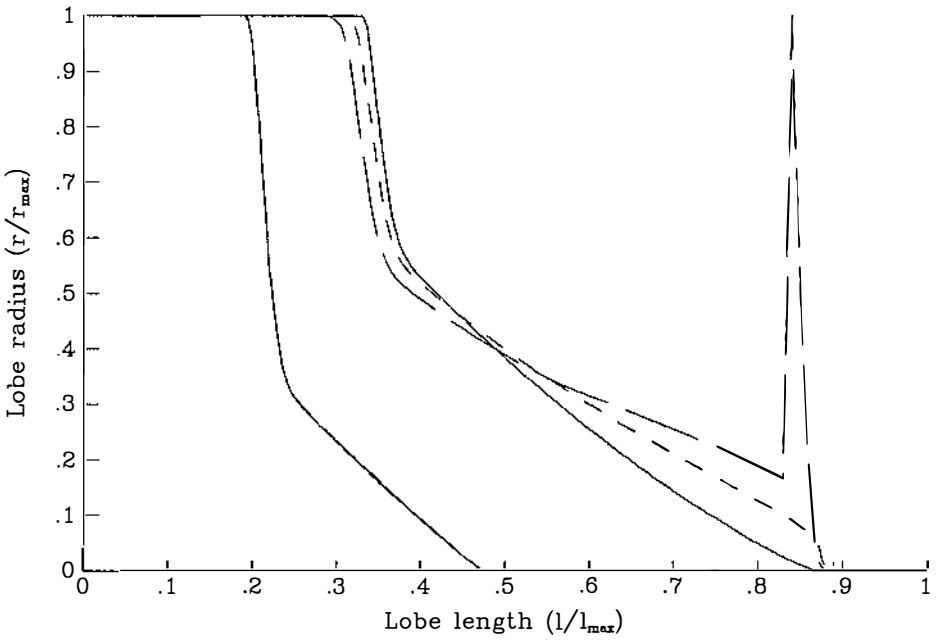

Charge state of profiles on left: 0.75. Charge state of profiles on right: 0.99.
Solid: concentration 1000 $mol.m^{-3}$ or less. Small dash: concentration 5000 $mol.m^{-3}$.
Large dash: concentration 10000 $mol.m^{-3}$.
Current in all cases: $62.5x10^{-3}$ $A.g^{-1}$ (approximately the 1 hr rate).

Figure 7.8: Lobe Profiles for Various Acid Concentrations.

current density and ions are only available very near the retreating $PbSO_4$ surface. The effective PbO_2 surface area seen in figure 7.5 reduces as the current increases to medium and high values. This effect is also expected as the Pb^{2+} ion concentration gradient increases with increasing current density, restricting the supply of ions to the lower regions of the growing lobes. The effect is, however, counteracted to some extent by the growth of "shelves" of large surface area near the retreating $PbSO_4$ as already discussed. The overall result is that the reduction in the effective surface area with increasing current is not particularly great.

d) Model results for various acid concentrations.

Figures 7.7 and 7.8 give the results for the charge surface area model where the acid concentration is varied. Figure 7.7 shows that both the actual and effective PbO_2 surface areas are only slightly effected by acid concentration. Even then the largest effect is associated with a very concentrated acid solution which is unlikely to be found in a practical cell. Figure 7.8 shows the lobe profiles for various acid concentrations. The appearance of radial shelves can be seen at high acid concentrations. Here these shelves are always minor features on the few growing lobes at the end of charge. The lobes are again expected as the Pb^{2+} ion concentration gradient increases with increasing acid concentration. This is because the Pb^{2+} ion diffusion coefficient falls as the acid concentration increases.

e) Model results for various geometric constants.

Figure 7.9 and 7.10 give the results of the charge surface area model where the geometric constants are varied. The actual and effective surface area development shown in figure 7.9 is virtually independent of the particular values chosen. This is a surprising result in the light of the lobe profiles shown in figure 7.10. Here

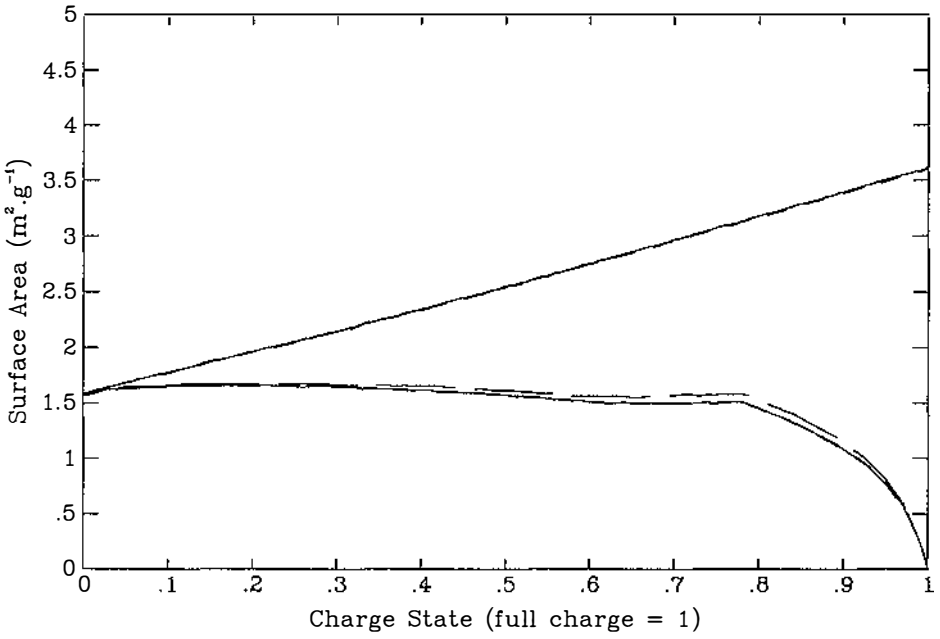

Top curves: actual PbO_2 surface. Bottom curves: effective PbO_2 surface.
Solid: f_o=1.2, f_v=2, n_v=4. Large dash: f_o=1.5, f_v=2, n_v=7.
Small dash: f_o=1.2, f_v=1.2, n_v=11.

where f_o and f_v are the sphere and lobe surface factors respectively and n_v is the number of lobes. Current in all cases: 62.5×10^{-3} $A.g^{-1}$.

Figure 7.9: Charge Surface Area for Various Geometric Constants.

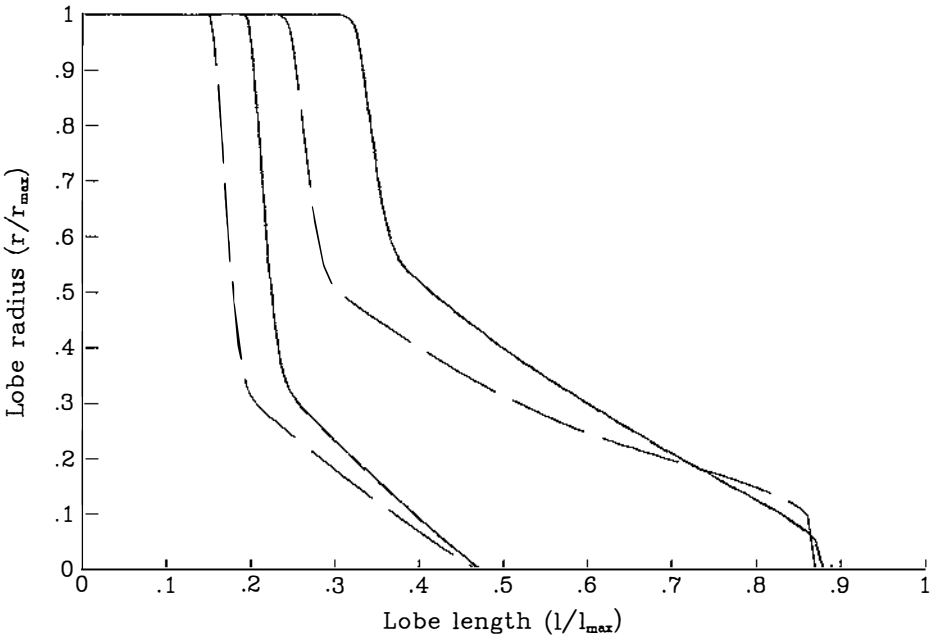

Charge state of profiles on left: 0.75. Charge state of profiles on right: 0.99.
Solid: f_o=1.2, f_v=2, n_v=4. Large dash: f_o=1.5, f_v=2, n_v=7.
Small dash: f_o=1.2, f_v=1.2, n_v=11.

where f_o and f_v are the sphere and lobe surface factors respectively and n_v is the number of lobes. Current in all cases: 62.5×10^{-3} $A.g^{-1}$.

Figure 7.10: Lobe Profiles for Various Geometric Constants.

it can be seen that the lobe surface factor has little effect on the lobe profiles. The lobe profiles are, however, strongly dependent on the sphere surface factor. This is a consequence of a change in the proportions of the sphere/box geometry dictated by this constant (see equations 4.12 to 4.14). The surprising point is that the different lobe shape and the change in sphere/box proportions work together to give an equivalent gram area that remains virtually independent of the sphere surface factor. For the purpose of defining the effective surface area distribution results (as for the VIAM model) the minor dependence seen above eliminates the need for precise estimates of the geometric constants. This is fortunate since these constants cannot be easily defined from experimental studies.

f) The effective surface area and the VIAM model.

The incorporation of the charge surface area model into the VIAM model will now be considered. Here it is only the effective PbO_2 surface area that is required. The results above show that this is virtually independent of acid concentration and geometric constants. This means the determination of the effective PbO_2 surface area can be simplified. That is, it can be taken as a function of charge state and instantaneous current only, without recourse to the general charge surface area model.

To implement this simplification, the effective PbO_2 results for low and high currents were fitted to polynomial forms of charge state. The required effective surface area was then defined by fixing the charge state and performing a linear interpolation between the two curves based on the instantaneous current. The close agreement of the results obtained by this procedure and actual model results can be seen in figure 7.11. The procedure was adopted for the VIAM model to reduce the required computational effort. The polynomials used are given in appendix 3.

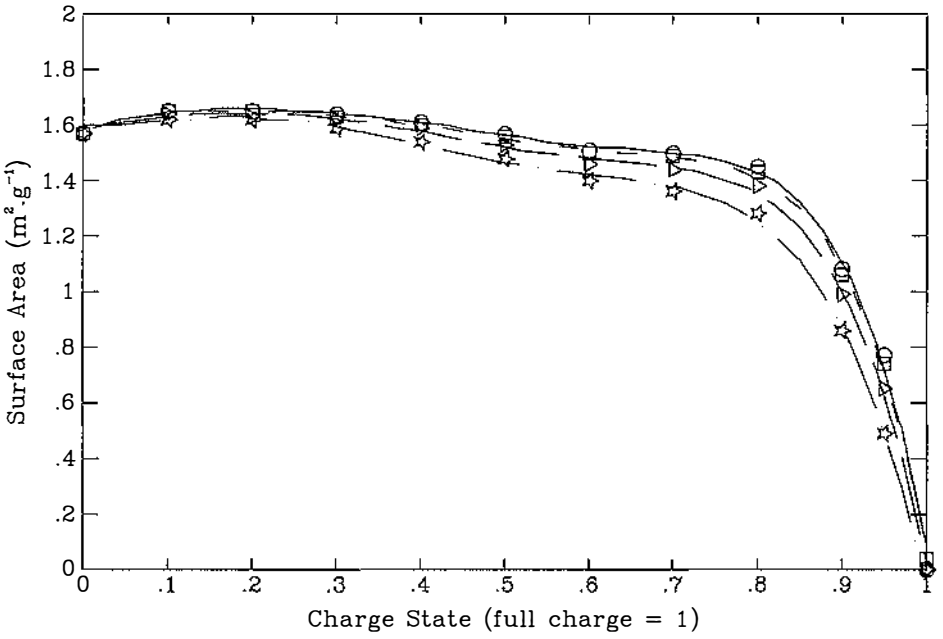

Symbols: model results. Lines: fitted polynomial results.
○/solid: current $62.5x10^{-3}$ $A.g^{-1}$ or less. □/Small dash: current $125.0x10^{-3}$ $A.g^{-1}$.
▷/Large dash: current $312.5x10^{-3}$ $A.g^{-1}$. ☆/Dot dash: current $625.0x10^{-3}$ $A.g^{-1}$.
$62.5x10^{-3}$ $A.g^{-1}$ is approximately the 1 hr rate.
Acid concentration in all cases: $5.0x10^{3}$ $mol.m^{-3}$.

Figure 7.11: Model and Fitted Effective PbO_2 Charge Surface Area.

7.1.6 The Charge Surface Area Model: a Discussion.

The charge surface area model has already been discussed in the context of particular results above. Quantitative model results have been shown to be consistent with the qualitative descriptions upon which the model is based. At this point attention will be given to comparing the model results to the limited data available from experimental studies.

a) The dimensions of structural features.

The model represents the dimensions and structure of a typical PbO_2 crystallite within the microstructure of the AM. At full charge, the overall dimensions are those of the sphere/box arrangement (see figure 4.4). Within these dimensions the crystallite has many lobes (edges and

spires) surrounding a solid base structure slightly larger than the sphere of the sphere/box arrangement. This representation can be compared with experimental observations of AM microstructure. The model dimension and structure for the results shown in figure 7.3 are characterised by

$$R_o = 0.119 \times 10^{-6} \text{ m} \qquad (7.5a)$$

and

$$R_x = 0.190 \times 10^{-6} \text{ m}. \qquad (7.5b)$$

where R_o is the sphere radius and half the box width and R_x is half the box height. A SEM micrograph of fully charged AM similar to the adopted AM is given in figure 3.2. It can be seen that there is a wide range of crystallites within the structure varying in radius from about 0.25 to 0.03 $\times 10^{-6}$ m. These dimensions compare well with the dimensions of the model given above.

b) Trends in total surface area variation.

The charge surface area model results give the total ($PbSO_4$+PbO_2) surface area variation with charge state. Ekdunge and Simonsson (1985) performed experimental measurements of this area at four points in a charge cycle. Their results are given in figure 3.4. Unfortunately the AM involved in these experiments is quite different from the adopted AM for which the charge surface area model results are given. The difference can be seen in the numerical values for the surface areas in each case †. This invalidates a direct comparison of the model and experimental results. None-the-less, discounting numerical values, some similarities would be expected. Both results show a significant increase in surface area in the first

† In the experiments of Ekdunge and Simonsson (1985) these were 6.40 and 1.25 $m^2.g^{-1}$ and in the adopted AM 3.60 and 2.75 $m^2.g^{-1}$ for the full charge and full discharge areas respectively.

half of the charge cycle and little overall increase in surface area thereafter. Two main differences are also seen. Firstly, the initial experimental surface area increase is very rapid compared to that for the model. Ekdunge and Simonsson (1985) account for this by suggesting that $PbSO_4$ encapsulation of PbO_2 depresses the surface area measurement value at full discharge. This means that the true experimental surface area value at full discharge should be adjusted upwards toward the model value. Secondly, the final experimental surface area shows no change compared to a declining value for the model. In fact Ekdunge and Simonsson (1985) assume the form they report and have no additional measurements in this region. The assumed form is reasonable given the original data but if the value of the area at full discharge is adjusted as discussed above a form approaching the model results is likely.

c) A direct comparison of total surface area variation.

An alternative approach can be used to give a more direct comparison between the model results and the experimental results of Ekdunge and Simonsson (1985). This involves defining new model parameters for the particular AM used by Ekdunge and Simonsson (1985) and using these to obtain new model results. To this end a new equivalent gram solution volume of the microstructure was found from the reported volume changes. In addition, the reported surface area results were corrected to equivalent gram values on the basis of the change of mass required to fill this volume during discharge. The charge surface area model was operated with the new microstructure solution volume (0.037×10^{-6} $m^3.g^{-1}$), a sphere and lobe surface factor of 1.2 and 2 respectively and estimates for the PbO_2 surface area at full discharge and the number of lobes per sphere. The estimated parameters were changed by trial and error until the model area results agreed with the corrected full and half charge experimental values. The experimental values at less than half charge were not taken into

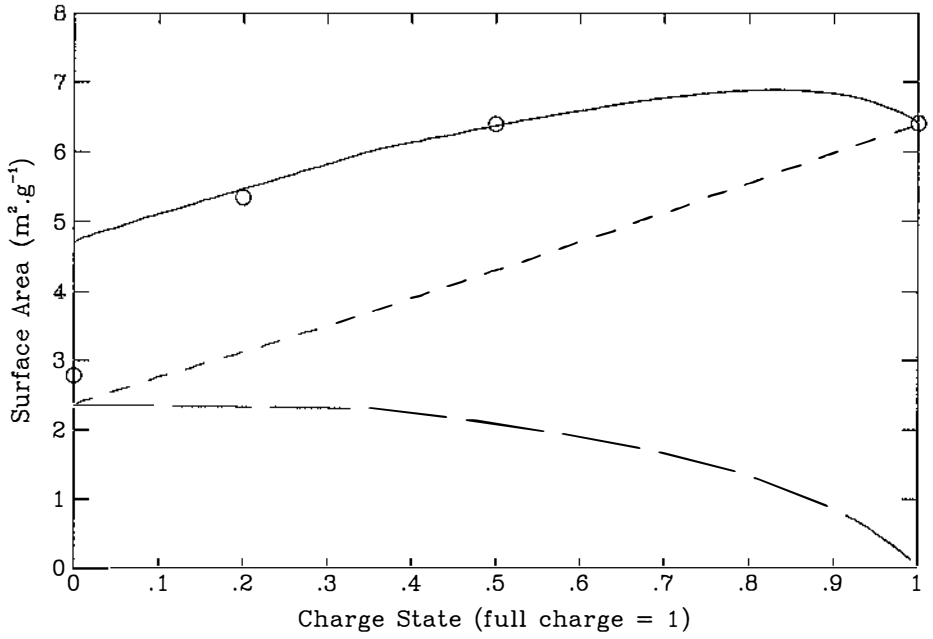

Solid: Model $PbSO_4$+PbO_2 surface. Small dash: Model PbO_2 surface.
Large dash: Model $PbSO_4$ surface. O: Experimental $PbSO_4$+PbO_2 surface #.

Ekdunge and Simonsson (1985) corrected for weight change.
Model charge current: $31.2x10^{-3}$ $A.g^{-1}$ (approximately the 2 hr rate).
Model acid concentration: $5.0x10^{3}$ $mol.m^{-3}$.

Figure 7.12: Model and Experimental Charge Surface Area.

account because of the undetermined amount of encapsulated surface involved. The model results obtained in this way are given together with the corrected experimental results in figure 7.12. It can be seen that a considerable upward adjustment of the experimental values in the initial part of the charge is still required to align the two results. Without further experimental work it cannot be determined whether or not the argument of encapsulated PbO_2 justifies this adjustment.

d) The effective PbO_2 surface area.

The effective PbO_2 surface area cannot be determined from published experimental data.

Some measure of the validity of the model in general, and the effective area quantity in particular, can be made by comparing the VIAM model (which incorporates the charge surface area model) with the experimental results.

7.2 THE AGGREGATE MODEL.

The Aggregate model is set out in chapter 5.

7.2.1 Aggregate Model Dimensions.

The model dimensions at full charge are found by solving equations 5.1 to 5.12, 5.14 to 5.20, and 5.22 to 5.26. These equations can be solved by substitution of the appropriate aggregate model parameters.

A number of aggregate model parameters relate directly to the dimensions of the cell under test as given in table 6.1. These parameters are given in table 7.1.

The remaining aggregate model parameters relate to details of the AM structure. Most of these are defined by adopted data for the positive AM (see section 6.2). The model parameters were derived from this data as follows.

Table 7.1: Some Aggregate Model Parameters.

Parameter description (symbol)	Value
Number of positive half plates (N_p):	6

Parameter description (symbol)	Value ($\times 10^{-3}$ m)
Plate height (H_p):	218
Plate width (W_p):	136
Half positive plate thickness (S_p):	2.55
Combined positive grid height (H_g):	21
Combined positive grid width (W_g):	17
Separator assembly thickness (S_s):	3.6
Half negative plate thickness (S_n):	2.05
Cell case width (inside) (W_c):	152
Cell case thickness (inside) (S_c):	62
Electrolyte solution height (H_{c0}):	300

The equivalent gram μ-channel volume was taken as the equivalent gram microstructure pore volume, which has been defined for the discharge capacity elemental model in section 7.1. Subtracting this volume from the total pore volume on the adopted accumulative pore volume curve (figure 3.1), defined the equivalent gram m-channel volume. This assumed the volume of the h-channel was negligible which is consistent with the low cycle life of the AM. The division of microstructure and macrostructure volumes by this approach occurred at a radius of 0.35×10^{-6} m. Transferring this radius onto the adopted accumulated pore surface curve (figure 3.1), defined the equivalent gram μ-channel and m-channel surface areas. The average positive AM porosity was calculated from the adopted total pore volume and solid volume for a gram of fully charged AM.

The few remaining parameters that relate to the structure of both the positive and negative AM are taken from the adopted data of Micka and Svata (1979). Specifically, the h-channel tortuosity factor was taken as the value reported and the μ-channel and m-channel tortuosity factors were taken as an intermediate value between unity and the value reported. The intermediate value was used since the m-channel/μ-channel trunk/branch structure inherently models a highly tortuous system where the individual components themselves need not have a large tortuosity factor. In addition to the positive AM parameters, the n-channel tortuosity and average porosity are taken as the values reported for the negative AM.

The aggregate model parameters described above are summarised in table 7.2. When these are substituted into the equations that define the aggregate model dimensions, the results summarised in table 7.3 are obtained.

Table 7.2: Remaining Aggregate Model Parameters.

Parameter description (symbol)	Value
Average positive AM porosity (ρ_p):	0.518 *
Positive macrostructure	
Equivalent gram volume ($x10^{-6} m^3.g^{-1}$) (V_m):	0.066 *
Equivalent gram surface ($m^2.g^{-1}$) (S_m):	0.08 *
Surface roughness (f_m):	1.2 **
Tortuosity (θ_m):	1.3 ††
Positive microstructure	
Equivalent gram volume ($x10^{-6} m^3.g^{-1}$) (V_μ):	0.050 *
Equivalent gram surface ($m^2.g^{-1}$) (S_μ):	3.52 *
Surface roughness (f_μ):	2.0 **
Tortuosity (θ_μ):	1.3 ††
Non-participating positive AM tortuosity (θ_h):	2.19 †
Average negative AM porosity (ρ_n):	0.548 †
Negative AM tortuosity (θ_n):	1.18 †

* Pavlov and Bashtavelova (1986)
** Estimate from micrographs Pavlov and Bashtavelova (1986).
† Micka and Svata (1979)
†† Discounted value from Micka and Svata (1979).

Table 7.3: Aggregate Model Dimensions.

Model Component	Length (m)	Cross Section (m^2)
r-channel	$5.18x10^{-2}$	$9.31x10^{-12}$
n-channel	$2.42x10^{-3}$	$2.53x10^{-11}$
s-channel	$3.60x10^{-3}$	$6.88x10^{-11}$
h-channel	$5.58x10^{-5}$	$1.29x10^{-11}$
m-channel	$3.28x10^{-3}$	$1.23x10^{-11}$
μ-channel	$2.83x10^{-6}$	$1.01x10^{-14}$

Component Numbers	
μ-channels per m-channel:	$1.07x10^{6}$
m-channels per equivalent gram:	$1.62x10^{6}$
m-channels per cell:	$2.59x10^{9}$

Further results for the aggregate model are not possible without the simultaneous involvement of the three elemental models. When these models are used together they constitute the VIAM model and the corresponding results are given as those for the VIAM model in section 7.3 below.

7.2.2 Aggregate Model Dimensions: a Discussion.

It is of interest to compare the aggregate model m-channel and μ-channel cross-sectional areas with the situation seen in the micrographs of figure 3.2. The model cross-sectional areas correspond to characteristic radii of 1.98×10^{-6} m and 0.0568×10^{-6} m for the m-channel and μ-channel respectively. When pores of these dimensions are superimposed on the micrographs it can be seen that the m-channel pores are typical of large voids between crystallite agglomerates. In addition, it can be seen that the μ-channel pores are typical of large voids within the agglomerate structure and very small voids between agglomerates. In both cases the dimensions are biased towards the larger voids in the structural features they represent. This bias can also be seen in the division of microstructure and macrostructure as suggested by Pavlov and Bashtavelova (1986) and as determined for the aggregate model here. The former sets the dividing radius at 0.20×10^{-6} m based on visual observations of the micrographs. The model sets the dividing radius at 0.35×10^{-6} m based on equating discharge volume changes to void volumes in the microstructure, in line with the elemental discharge capacity model. This reveals a slight shift in the definition of the μ-channel volume. Until now it has been taken to represent voids within the crystallite agglomerates only. As determined by the aggregate model parameters, however, it can be seen to include small pores between agglomerates in addition to the voids within the agglomerates.

The number of μ-channels per m-channel can be seen to be approximately 10^6. This shows grouping μ-channels to be a necessary technique to reduce the computational effort of a practical model.

The h, s, n and r-channel cross-sectional areas have values similar to the m-channel cross-sectional area from which they are derived. These channels also have lengths that reflect the dimensions of the components of the cell under test in which they are contained.

7.2.3 Functions for the Aggregate Model.

Before the aggregate model can used, several acid concentration dependent functions must be defined. These are the equilibrium potential of the PbO_2 electrode, the resistivity of H_2SO_4 solution, the diffusion coefficient of H_2SO_4 in solution and the anodic and cathodic exchange current density of the PbO_2 electrode. The first three functions were fitted to polynomials in concentration using well known experimental data (see appendix 3). The two exchange current density functions are far from certain (see section 3.3.2 and 3.3.3). The approach taken here was to adopt the reaction orders suggested by Hampson *et al* (1968) with likely values for the rate constants. This gave well defined, if rather uncertain, functions (see appendix 3). When used with the aggregate model, these functions were multiplied by a constant factor to allow adjustment of the rate constants. The reaction orders were not changed.

In practice the five functions described above were evaluated in advance for concentrations in the range 100 to 10000 $mol.m^{-3}$ using 100 $mol.m^{-3}$ steps. The results were placed into a look-up table within the aggregate model. Function evaluations for an arbitrary concentration were performed using a linear interpolation between adjacent table points. The look-up table approach was used to increase program execution speed.

7.3 THE VIAM MODEL.

The VIAM model is the combination of the three elemental models plus the aggregate model. Results for the VIAM model are obtained by operating the combination of models simultaneously. In practice the simultaneous operation was achieved by incorporating the simple elemental models directly into the aggregate model. The incorporation of the discharge capacity model was implicit since it is an assumption upon which the aggregate model was built. The incorporation of the discharge surface area model required the addition of a one line formulation. In principle, the incorporation of the simplified charge surface area model required the addition of two polynomial equations for the dependence on charge state and a linear interpolation equation for the dependence on current. In practice, the polynomial equations were evaluated for charge states in the range 0.01 to 1.00 using 0.01 steps and the results were placed in a look-up table within the aggregate model. Function evaluations for an arbitrary charge state were performed using a linear interpolation between adjacent table points. The linear interpolation for the current dependence was retained. Again the look-up table approach was used to increase program execution speed.

The VIAM model can be used with any discharge/charge cycle. For example, interrupted discharge, variable rest time and fast charge are cycle variations that can be examined. However, for the purposes of proving the model, the model operation has been limited to the few basic cycle variations that follow.

When considering the VIAM model results it is helpful to keep in mind the discrete nature of the model. The complete discharge or charge of AM associated with one m-channel segment, in some cases, results in a small step in the voltage/time characteristic. If desired, the number of

segments can be increased to minimise this effect with the cost of an increase in computing time.

7.3.1 VIAM Model Results for a Standard Case.

Figures 7.13 to 7.20 present comprehensive VIAM model results for the standard case of a medium 20 Ampere full discharge followed by a 0.5 hour rest and 20 Ampere charge.

The overall voltage/time characteristics predicted by the model are given in figures 7.13 and 7.14. The internal distributions † for AM state, voltage and concentration for the cell components represented by the model are given in figures 7.15 to 7.20. A description of important features for the medium discharge case and typical of other cases follows.

a) The discharge capacity.

The positive plate voltage reached the end of discharge value of approximately 1.450 volts in 4.0 hours (figure 7.13). That is, the cell had a discharge capacity of 80 Ampere hours at the 4 hour rate. This corresponds to an 89 Ampere hour capacity at the 5 hour rate of 17.8 Amperes (assuming typical de-rating curves see Linden (1984)).

b) Stages in the discharge.

The positive plate discharge voltage/time characteristic can be divided into initial, intermediate and final stages. These stages are considered in turn below.

† It should be noted when examining the figures for the internal distributions the solid, small dash and large dash line types are associated with the discharge, rest and charge portions of the discharge/charge cycle respectively

c) The initial discharge stage.

The initial stage is marked by an instantaneous then short but relatively rapid plate voltage drop.

Consider first the instantaneous voltage drop. This is a drop of 0.022 volts from the open-circuit value of 1.766 volts. Change in concentration cannot occur instantaneously and therefore change in electrode equilibrium potential is not a factor here. Figure 7.18 shows the contribution of the solution potential drop is between 0.001 and 0.010 volts depending on the position in the plate. By elimination, this means that the remaining (and largest) portion of the instantaneous voltage is due to the electrode overpotential.

Consider now the short but relatively rapid plate voltage drop. Figure 7.18 indicates that the solution potential drop is essentially constant here. However, observations of the model in operation show a relatively rapid drop in acid concentration in the plate. This concentration drop effects the electrode equilibrium potential and overpotential. The electrode equilibrium potential decreases with decreasing acid concentration in accordance with the Nernst equation (equation 3.5). The electrode overpotential increases with decreasing acid concentration because of the positive cathodic exchange current reaction order. Together these effects account for the drop in plate voltage seen here. The rapid drop in concentration is not sustained as concentration gradients develop and acid is supplied to the plate from the separator. For the case in point, the acid concentration changes at the plate surface were 89, 59, 50, 47, and 45 $mol.m^{-3}$ for the first five 0.05 hour intervals of the discharge.

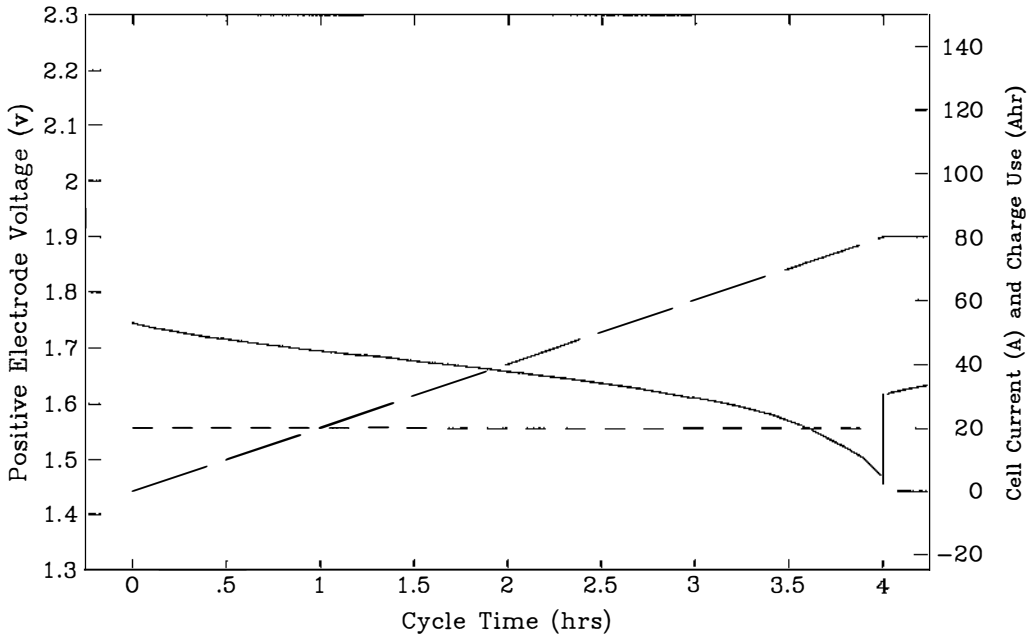

Solid: Positive electrode voltage (v). Small dash: Cell current (A).
Large dash: Charge usage (Ahrs).

Results for 20 A discharge, 0.5 hr rest and 20 A charge.

Figure 7.13: Discharge Voltage for 20 Ampere Full Discharge.

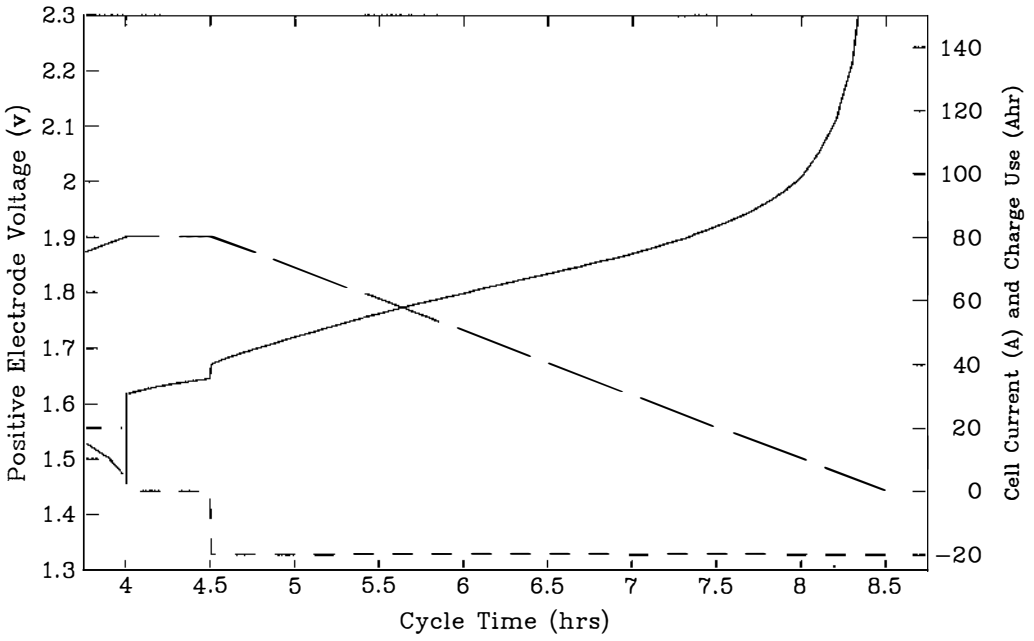

Solid: Positive electrode voltage (v). Small dash: Cell current (A).
Large dash: Charge usage (Ahrs).

Results for 20 A discharge, 0.5 hr rest and 20 A charge.

Figure 7.14: Rest and Charge Voltage for 20 Ampere Full Discharge.

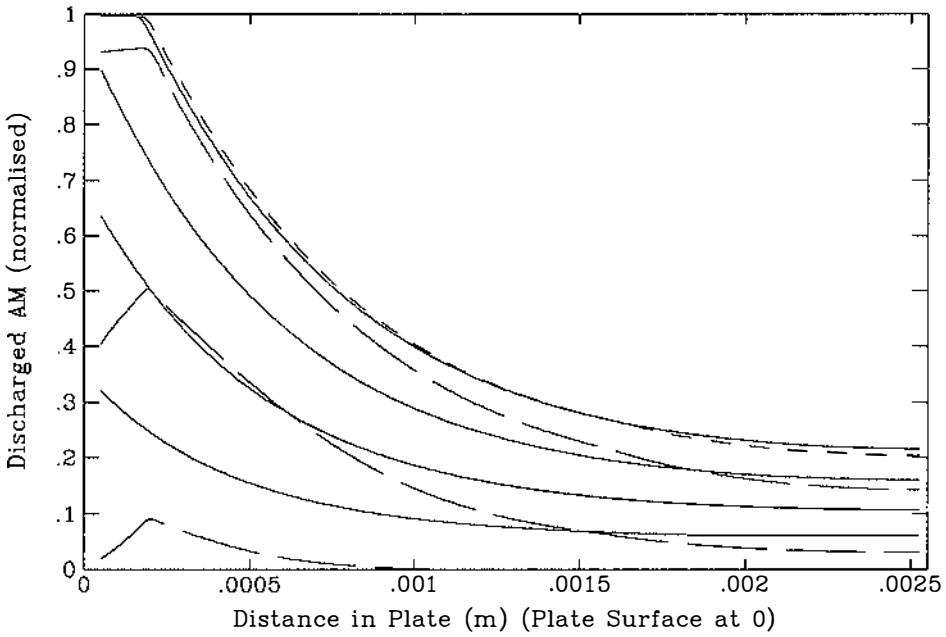

Solid: discharge profiles at 1.0, 2.0, 3.0 and 4.0 hrs bottom to top.
Small dash: rest profile at 4.3 hrs.
Large dash: charge profiles at 5.0, 7.0 and 8.4 hrs top to bottom.

Results for 20 A discharge, 0.5 hr rest and 20 A charge.
Discharged AM at each m−channel position defined as: $1-X_{AVERAGE}$.

Figure 7.15: Discharged Plate AM for 20 Ampere Full Discharge.

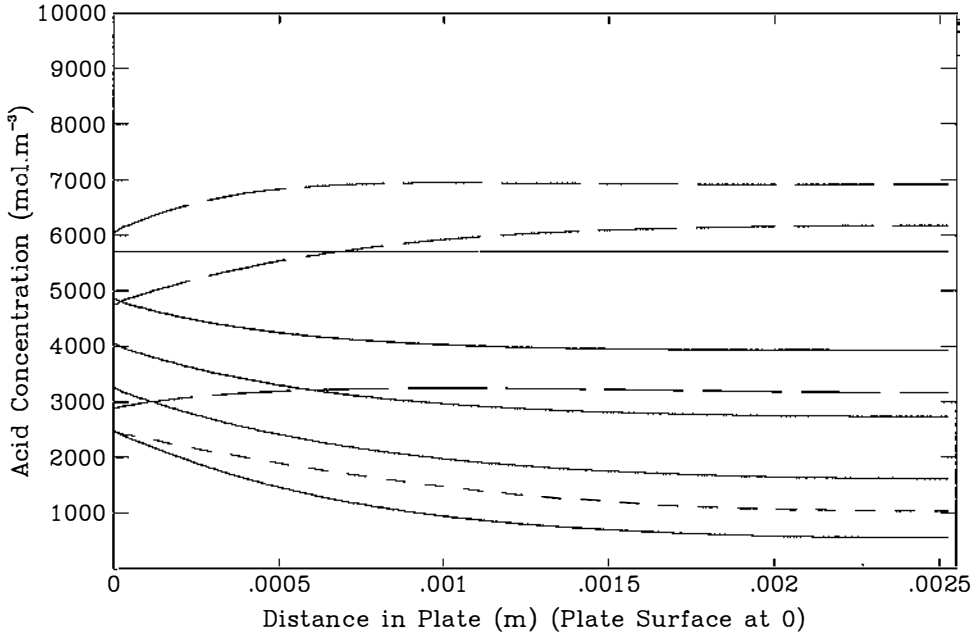

Solid: discharge profiles at 0.0, 1.0, 2.0, 3.0 and 4.0 hrs top to bottom.
Small dash: rest profile at 4.3 hrs.
Large dash: charge profiles at 5.0, 7.0 and 8.4 hrs bottom to top.

Results for 20 A discharge, 0.5 hr rest and 20 A charge.

Figure 7.16: Plate Acid for 20 Ampere Full Discharge.

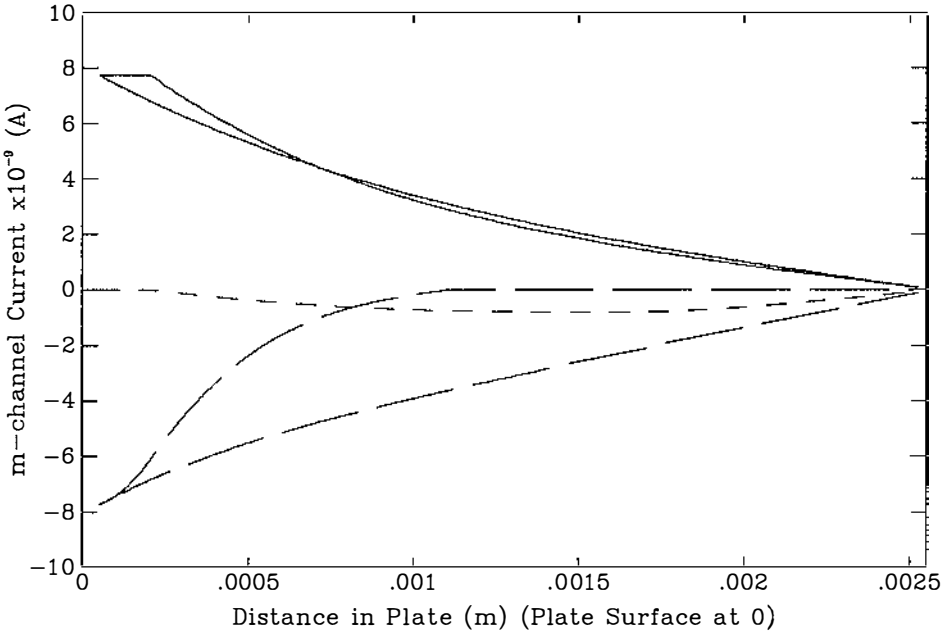

Solid: discharge profiles at 0.0 and 4.0 hrs left and right.
Small dash: rest profile at 4.3 hrs.
Large dash: charge profiles at 5.0 and 8.4 hrs right and left.
Results for 20 A discharge, 0.5 hr rest and 20 A charge.

Figure 7.17: Plate Current for 20 Ampere Full Discharge.

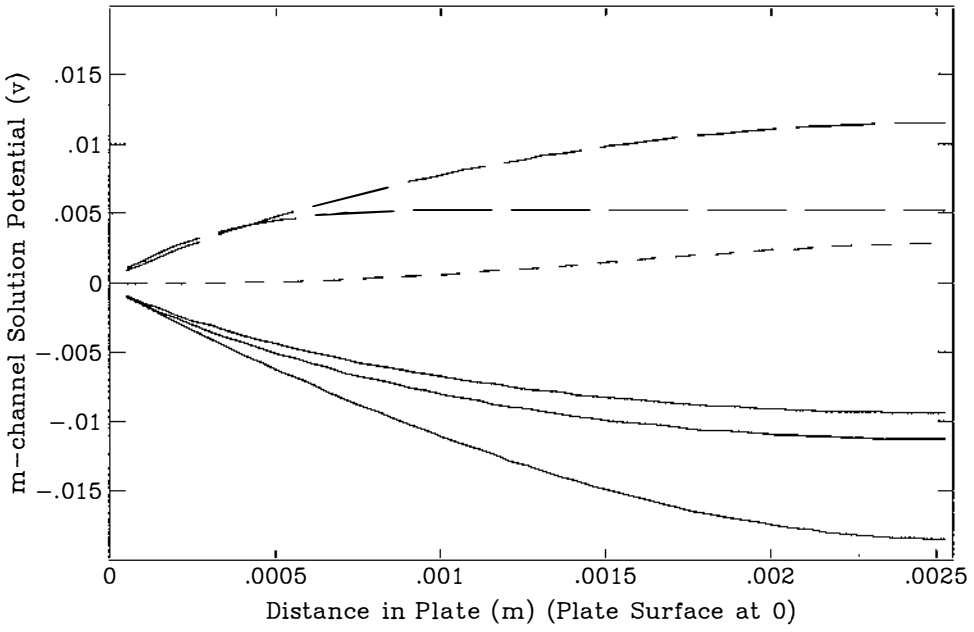

Solid: discharge profiles at 0.0, 2.0 and 4.0 hrs top to bottom.
Small dash: rest profile at 4.3 hrs.
Large dash: charge profiles at 5.0 and 8.4 hrs top and bottom.
Results for 20 A discharge, 0.5 hr rest and 20 A charge.

Figure 7.18: Plate Solution Potential for 20 Ampere Full Discharge.

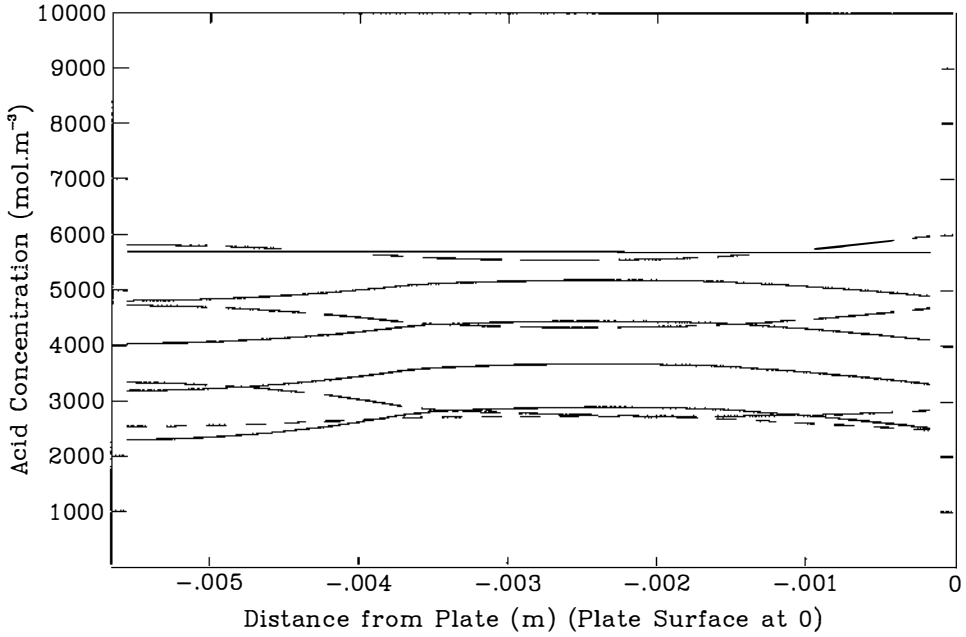

Solid: discharge profiles at 0.0, 1.0, 2.0, 3.0 and 4.0 hrs top to bottom.
Small dash: rest profile at 4.3 hrs.
Large dash: charge profiles at 5.0, 7.0 and 8.4 hrs bottom to top.

Results for 20 A discharge, 0.5 hr rest and 20 A charge.

Figure 7.19: Adjacent Acid for 20 Ampere Full Discharge.

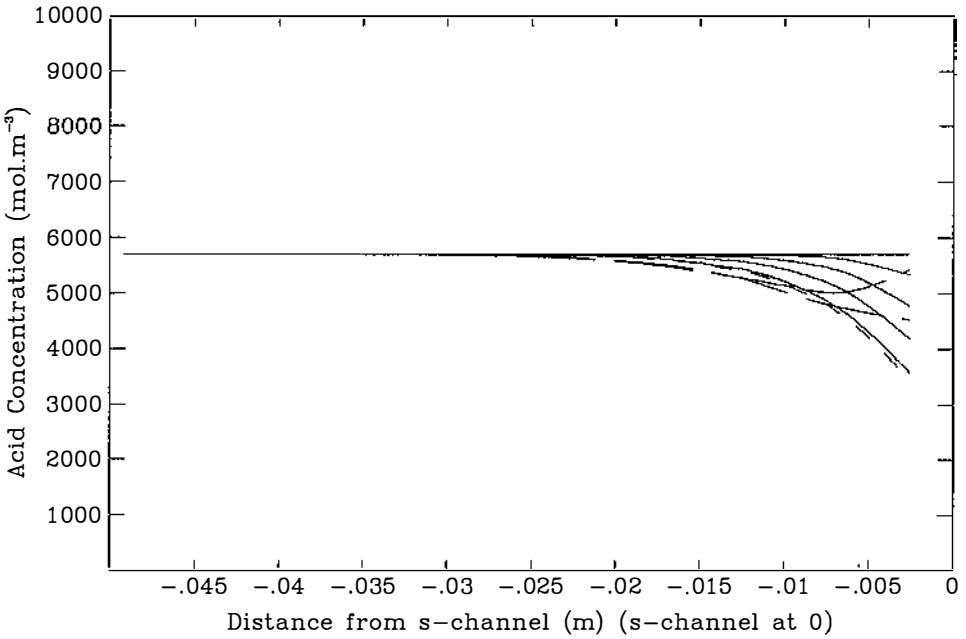

Solid: discharge profiles at 0.0, 1.0, 2.0, 3.0 and 4.0 hrs top to bottom.
Small dash: rest profile at 4.3 hrs.
Large dash: charge profiles at 7.0 and 8.4 hrs bottom to top.

Results for 20 A discharge, 0.5 hr rest and 20 A charge.

Figure 7.20: Reservoir Acid for 20 Ampere Full Discharge.

d) The intermediate discharge stage.

The majority of the discharge time is spent in the intermediate discharge stage. Here the plate voltage shows a gradual decline. Figure 7.18 shows that the potential drop due to solution resistance does not change significantly during this time. Reference to the internal acid concentration (figure 7.16) indicates that a decline in acid concentration and the effect that this has on the electrode equilibrium potential and overpotential, is again the main mechanism for voltage drop here. In this case, however, the decline in acid concentration is somewhat slower than before. It can be seen from figures 7.19 and 7.20 that the decline in acid concentration is not a consequence of massive depletion in the total cell acid. The decline is instead an effect of restricted transport within the cell components.

e) The final discharge stage.

In the final stage of the discharge, the plate voltage shows a rapid drop. Three factors contribute to this voltage drop.

Firstly, the solution potential drop increases at this stage of the discharge. This is due in part to the increase in acid resistivity as the acid concentration approaches zero. It is also due to the effect of the progression of the reaction region into the plate interior. The progression can be seen by the moving fronts for the discharged plate AM and plate current in figures 7.15 and 7.17 respectively. This requires the discharge current to pass through an acid solution component of increasing length before reaching the discharge reaction region. The increase in length is reflected in an increase in electrical resistance. The drop in solution potential that results is approximately 0.022 volts (figure 7.18).

Secondly, the effect of electrode equilibrium

potential discussed above rapidly increases in magnitude as the acid concentration in the plate approaches zero. The drop in this potential in the last hour of the discharge is approximately 0.100 volts. This is the same order as the total potential drop for the first three hours of the discharge (potentials estimated from the concentration change in figure 7.16).

Thirdly, the effect of the overpotential as discussed above rapidly increases in magnitude as the concentration approaches zero. By elimination this must be greater than 0.100 volts at the end of the discharge compared to 0.022 volts or less at the beginning of the discharge.

f) The open circuit rest stage.

The rest stage is between discharge and charge when there is no net cell current (that is, when the cell is open circuit). The voltage/time characteristic here is given in the early part of figure 7.14. It shows an instantaneous then gradual rise in plate voltage.

Consider first the instantaneous voltage rise. As with the initial discharge stage discussed above the electrode equilibrium potential cannot be a factor here. Figure 7.18 shows that some of the voltage rise is due to a reduction in solution potential drop as the cell current is discontinued. By elimination, a reduction in electrode overpotential must account for the remainder of the voltage rise seen here.

Consider now the gradual voltage rise. Figure 7.16 shows the acid concentration within the plate gradually rises during the rest period as acid is supplied from outside the plate. This rise in acid concentration dictates a gradual increase in equilibrium potential for the electrode. This accounts for the gradual rise in the voltage characteristic seen here.

A discharge/charge reaction occurs internally within the plate during the rest stage. This reaction is driven by variations in equilibrium potential due to the non-uniform concentration distribution (see figure 7.16). The non-uniform concentration is sustained by the supply of acid from the separator region. As a result AM near the plate surface continues to discharge and is balanced by an equal charge of AM in the plate interior. The current distribution in figure 7.17 and the redistribution of AM during the rest stage in figure 7.15 are evidence of this.

g) Stages in the charge.

As with the discharge, the charge can be divided into an initial, intermediate and final stage. These are discussed in turn below.

h) The initial charge stage.

The initial stage is marked by an instantaneous then relatively rapid rise in plate voltage. The reasons for this are similar to those given for the initial stage of the discharge. That is, the instantaneous voltage rise is due to solution potential rise and overpotential and the relatively rapid rise that follows is due to a rise in acid concentration and the effect this has on electrode equilibrium potential and overpotential. In this case the overpotential increases with increasing acid concentration because of the negative anodic reaction order of the exchange current density. Again the relatively rapid rise in acid concentration is unsustained.

i) The intermediate charge stage.

In the intermediate stage of the charge the voltage shows a gradual increase. This is a continuation of the initially rapid effects seen at the beginning of the charge and is controlled by a gradual increase in acid concentration (see figure 7.16). Again it compares directly

to the intermediate discharge stage. The one difference in the charge case is that the solution potential rise (compared to a fall in the discharge case) reduces with increasing acid concentration since the solution resistivity reduces. This can be seen in figure 7.18.

j) The final charge stage.

The final stage of the charge shows a rapid rise in plate voltage. Figure 7.16 shows that the acid concentration has no large increase at this stage. This means the electrode equilibrium potential and the solution potential rise do not contribute in a major way to the rapid voltage rise here. In fact, the contribution of the solution potential rise is less at the end than at the beginning of charge (see figure 7.18). By elimination, this leaves the electrode overpotential as the main contributor to the rapid voltage rise here. The high overpotential is to be expected since the current density increases rapidly as the charge current is concentrated onto a vanishing reaction surface area (the effective PbO_2 surface).

7.3.2 Other VIAM Model Results.

VIAM model results for five different cases follow. These include cases for slow and fast discharge rates, AM with increased tortuosity, AM with a significant non-participating portion and AM with an increased exchange current. In all cases the discharge is followed by a 0.5 hour rest and a 20 Ampere charge. Only the overall voltage/time characteristics and the internal distribution for AM state and plate acid concentration have been given for these cases.

a) VIAM model results for a slow discharge.

VIAM model results for a slow, 3.5 Ampere, full discharge case are presented in figures 7.21 to 7.23. The

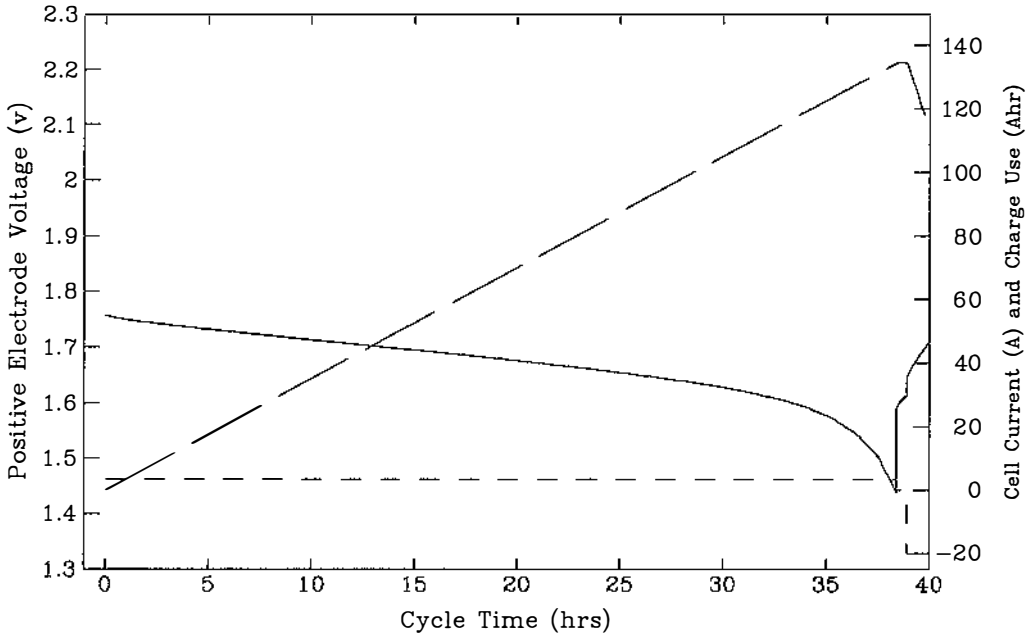

Solid: Positive electrode voltage (v). Small dash: Cell current (A).
Large dash: Charge usage (Ahrs).

Results for 3.5 A discharge, 0.5 hr rest and 20 A charge.

Figure 7.21: Discharge Voltage for 3.5 Ampere Full Discharge.

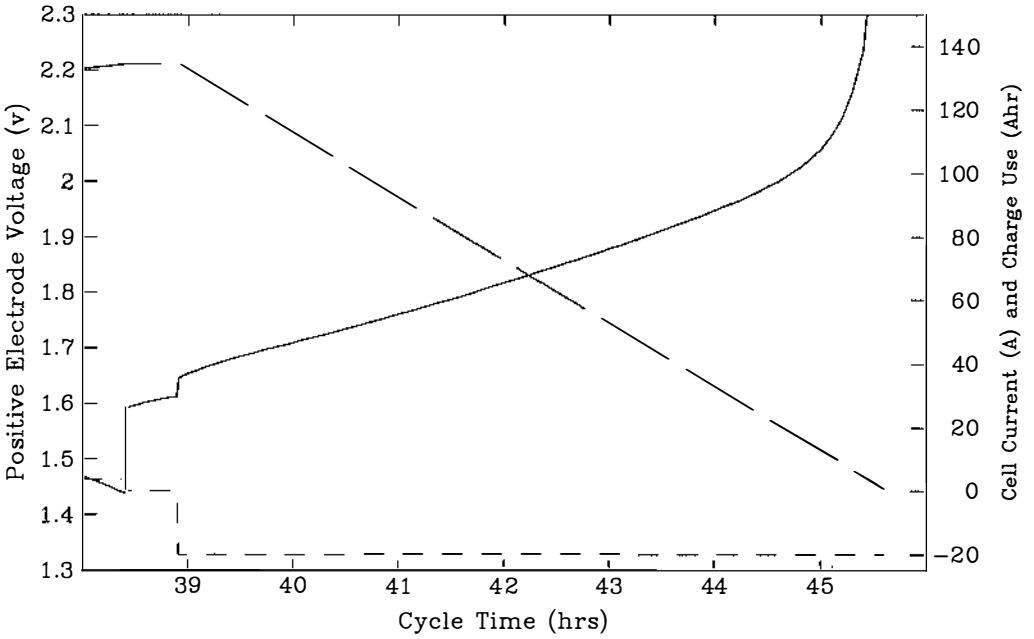

Solid: Positive electrode voltage (v). Small dash: Cell current (A).
Large dash: Charge usage (Ahrs).

Results for 3.5 A discharge, 0.5 hr rest and 20 A charge.

Figure 7.22: Rest and Charge Voltage for 3.5 Ampere Full Discharge.

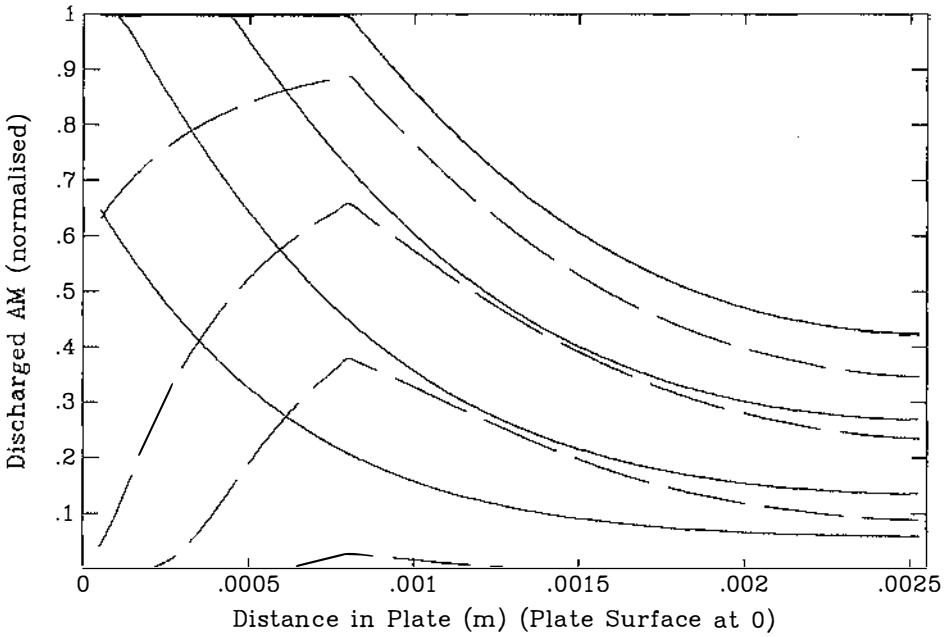

Solid: discharge profiles at 10.0, 20.0, 30.0 and 38.4 hrs bottom to top.
Small dash: rest profile at 38.7 hrs (same as discharge profile at 38.4 hrs).
Large dash: charge profiles at 40.0, 42.0, 44.0 and 45.6 hrs top to bottom.

Results for 3.5 A discharge, 0.5 hr rest and 20 A charge.
Discharged AM at each m-channel position defined as: $1-X_{AVERAGE}$

Figure 7.23: Discharged Plate AM for 3.5 Ampere Full Discharge.

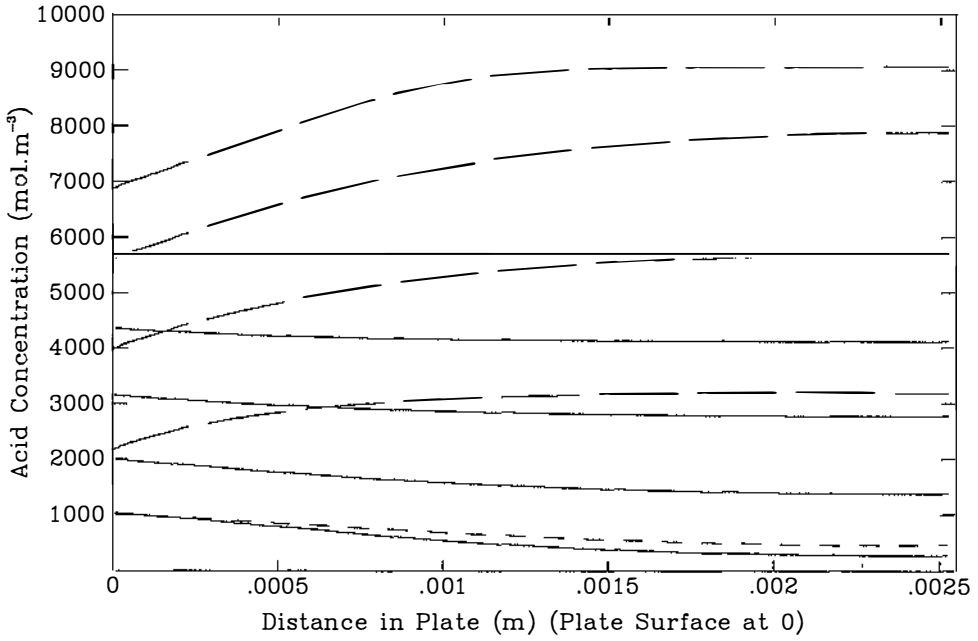

Solid: discharge profiles at 0.0, 10.0, 20.0, 30.0 and 38.4 hrs top to bottom.
Small dash: rest profile at 38.7 hrs.
Large dash: charge profiles at 40.0, 42.0, 44.0 and 45.6 hrs bottom to top.

Results for 3.5 A discharge, 0.5 hr rest and 20 A charge.

Figure 7.24: Plate Acid for 3.5 Ampere Full Discharge.

discharge capacity here of 134 Ampere hours is considerably higher than that for the standard case above. This comes about because of two polarisation reducing effects. Firstly, the lower discharge rate allows more time for acid to diffuse into the plates from elsewhere. As a result, the plate acid concentration is higher here than in the standard case given the same discharge depth. This gives a higher electrode equilibrium potential and a lower overpotential. Secondly, the lower current here gives a lower exchange current and therefore a lower overpotential than in the standard case.

The discharge voltage/time characteristic (figure 7.21) shows the dominant role of the electrode equilibrium potential. For example at the 30 hour mark the plate concentration (figure 7.24) corresponds to an equilibrium potential of 1.645 volts which is very near the plate voltage of 1.630 volts. It is only at the end of the discharge when the acid concentration is very low that the electrode overpotential becomes significant.

The rest stage involves only a small amount of AM redistribution (see figure 7.23). This is because the small concentration gradients involved in the slow discharge result in little electrode equilibrium potential difference within the plate. As a consequence the redistribution currents are small.

The charge voltage/time characteristic is given in figure 7.22. The voltage at the beginning of the charge is lower than in the standard case because of a lower plate acid concentration at this time (see figure 7.24). Later in the charge, the plate acid concentration becomes very high as the large amount of acid produced is, to some extent, contained in the plate. As a result the plate voltage towards the end of charge is higher than that for the standard case given the same amount of charge to restore.

b) VIAM model results for a fast discharge.

Initially the VIAM model was used to simulate a 140 Ampere discharge with the same model parameters as in the standard case. This gave a very rapid drop in plate voltage and a cell capacity of only 28 Ampere hours. Typical de-rating curves based on the five hour capacity from the standard case predict a capacity of 38 Ampere hours. At full discharge the lowest plate acid concentration was 2337 $mol.m^{-3}$. This is not a particularly low value and shows that electrode equilibrium potential and solution resistance do not contribute in a major way to the full discharge voltage. This means the rather low capacity predicted by this initial simulation is due to a high overpotential.

A low exchange current density could explain the performance obtained here. However, the exchange current density used was selected to give results (overpotentials) typical for the moderate and low current cases. Even a small increase in the exchange current reduces the overpotential contribution for these cases and gives unlikely results. A more likely explanation is that the single exchange current/overpotential relationship assumed in the VIAM model (actually in the underlying aggregate model) introduces significant errors when applied to situations spanning a large current range. Experimental studies have shown that different low and high overpotential reactions occur in both the cathodic and anodic directions (Hampson *et al* (1967,1968)). Ideally the model should represent the different reactions with different forms for the exchange current/overpotential relationship, rather than using a single compromise form. Although the model could be modified to incorporate different reactions this was not done. As an alternative, the exchange current for the single form was adjusted upwards to represent a high overpotential exchange reaction and the 140 Ampere simulation repeated. The results for the second case are given in figures 7.25 to 7.28.

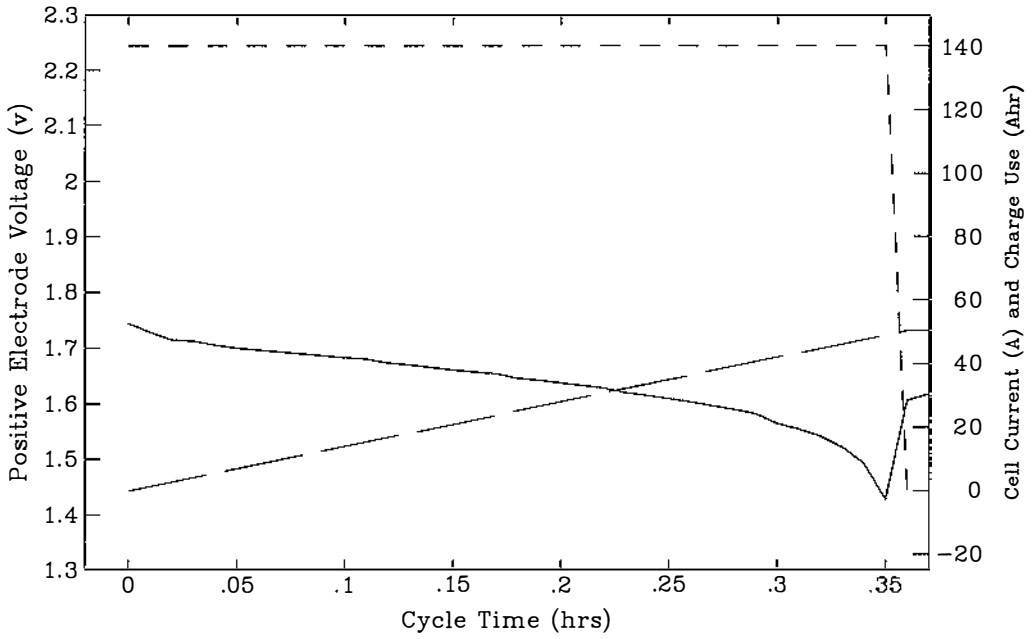

Solid: Positive electrode voltage (v). Small dash: Cell current (A).
Large dash: Charge usage (Ahrs).

Results for 140 A discharge, 0.5 hr rest and 20 A charge.

Figure 7.25: Discharge Voltage for 140 Ampere Full Discharge.

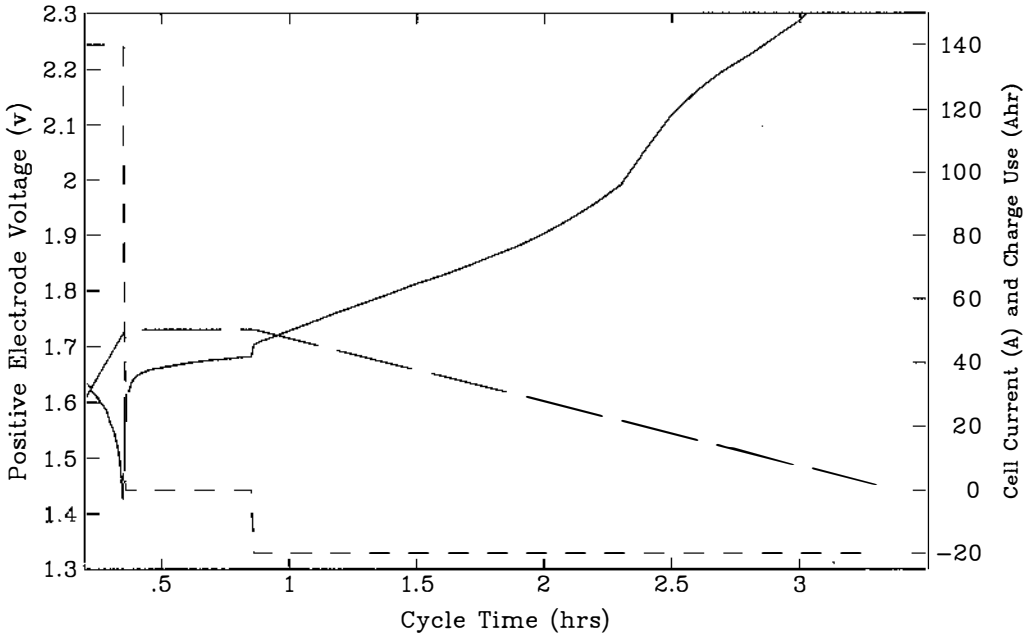

Solid: Positive electrode voltage (v). Small dash: Cell current (A).
Large dash: Charge usage (Ahrs).

Results for 140 A discharge, 0.5 hr rest and 20 A charge.

Figure 7.26: Rest and Charge Voltage for 140 Ampere Full Discharge.

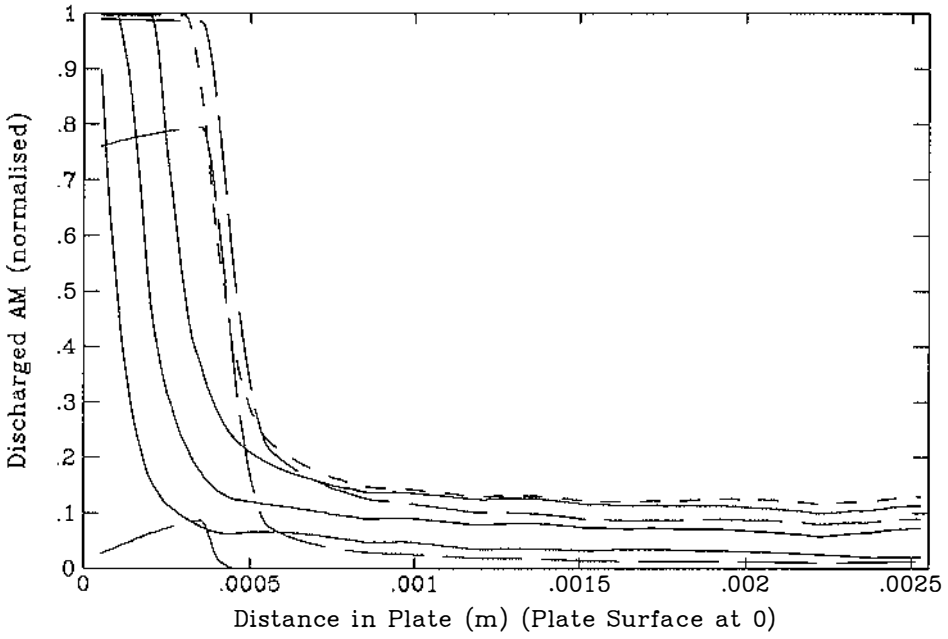

Solid: discharge profiles at 0.1, 0.2 and 0.3 hrs bottom to top.
Small dash: rest profile at 0.6 hrs.
Large dash: charge profiles at 1.0, 2.0 and 3.3 hrs top to bottom.

Results for 140 A discharge, 0.5 hr rest and 20 A charge.
Discharged AM at each m-channel position defined as: $1-X_{AVERAGE}$.

Figure 7.27: Discharged Plate AM for 140 Ampere Full Discharge.

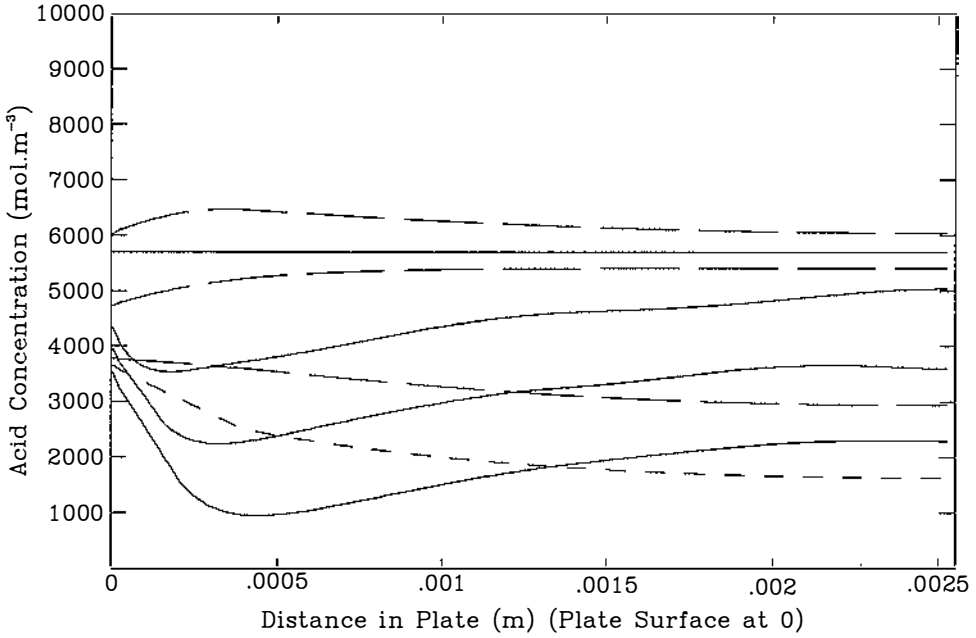

Solid: discharge profiles at 0.0, 0.1, 0.2 and 0.3 hrs top to bottom.
Small dash: rest profile at 0.6 hrs.
Large dash: charge profiles at 1.0, 2.0 and 3.3 hrs bottom to top.

Results for 140 A discharge, 0.5 hr rest and 20 A charge.

Figure 7.28: Plate Acid for 140 Ampere Full Discharge.

The cell capacity obtained in the second case was 49 Ampere hours. In fact this capacity was attained with the discharge continuing longer than it should. This is because the plate voltage as modelled did not have the additional voltage drop due to the low overpotential reaction. The capacity would be several Ampere hours less and close to the expected value of 38 Ampere hours had this been the case.

The discharge voltage/time characteristic has the same general features as in the standard case. The AM distribution (figure 7.27) shows that the discharge reaction is concentrated near the front of the plate in this case. This gives a very abrupt boundary between discharged and charged AM. It also means the effect of the solution potential drop (resistance) as the discharge proceeds into the plate interior is somewhat greater here. This can be seen by the sudden drops in the voltage characteristic as the discrete model segments are fully discharged (figure 7.25).

During the rest stage there is a considerable rearrangement of AM (figure 7.27). This due to the large concentration gradient near the surface of the plate (figure 7.28) and the resulting variation in electrode equilibrium potential which gives rise to a significant rearrangement current.

The charge voltage/time characteristic shows an unexpected rapid rise part way through the charge (figure 7.26). Reference to the AM distribution shows this is due to a rapid loss in charge surface area as the long portion of evenly discharged AM in the plate interior is recharged.

c) The VIAM model results with a more tortuous structure.

It is important to observe how the VIAM model results depend on structure. The dependence has implications for AM

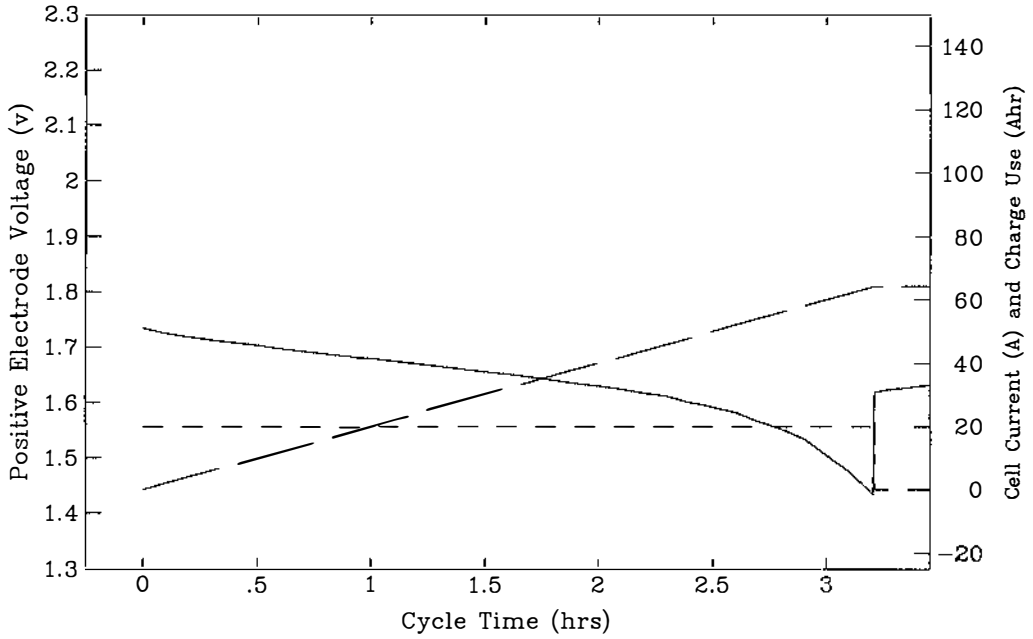

Solid: Positive electrode voltage (v). Small dash: Cell current (A).
Large dash: Charge usage (Ahrs).

Results for 20 A discharge, 0.5 hr rest and 20 A charge.
m and μ–channel tortuosity factor increased from 1.30 to 2.19.

Figure 7.29: Discharge Voltage for More Tortuous AM.

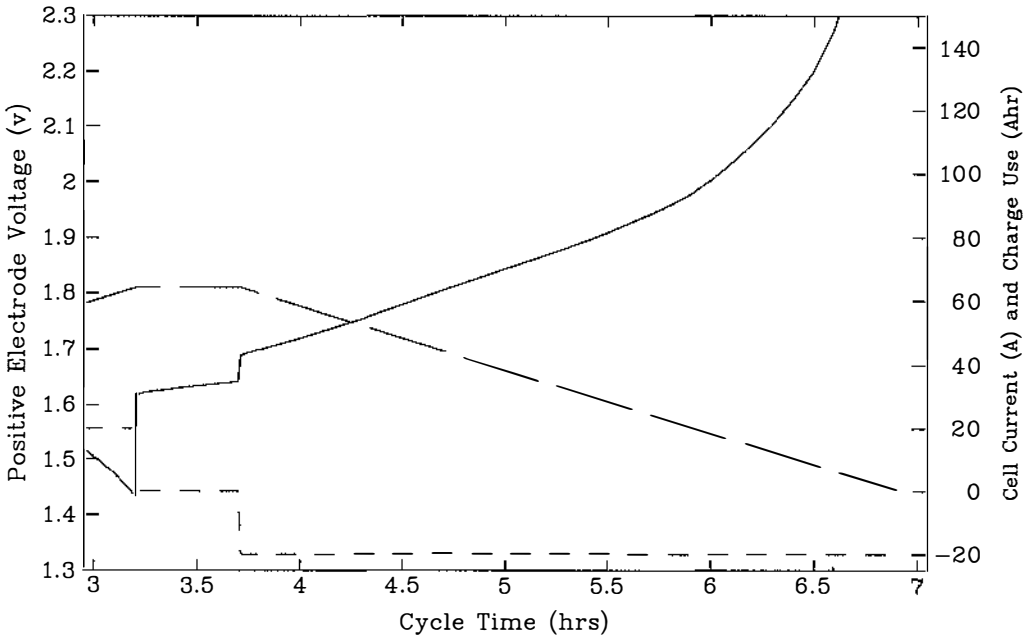

Solid: Positive electrode voltage (v). Small dash: Cell current (A).
Large dash: Charge usage (Ahrs).

Results for 20 A discharge, 0.5 hr rest and 20 A charge.
m and μ–channel tortuosity factor increased from 1.30 to 2.19.

Figure 7.30: Rest and Charge Voltage for More Tortuous AM.

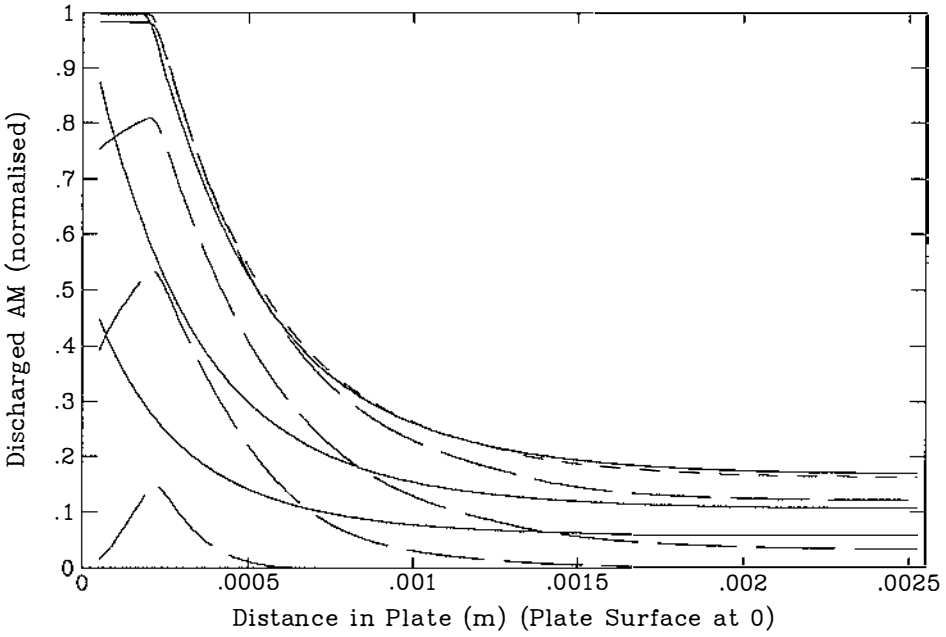

Solid: discharge profiles at 1.0, 2.0 and 3.2 hrs bottom to top.
Small dash: rest profile at 3.5 hrs.
Large dash: charge profiles at 4.0, 5.0, 6.0 and 6.8 hrs top to bottom.
Results for 20 A discharge, 0.5 hr rest and 20 A charge.
Discharged AM at each m−channel position defined as: $1-X_{AVERAGE}$.
m and μ−channel tortuosity factor increased from 1.30 to 2.19.

Figure 7.31: Discharged Plate AM for More Tortuous AM.

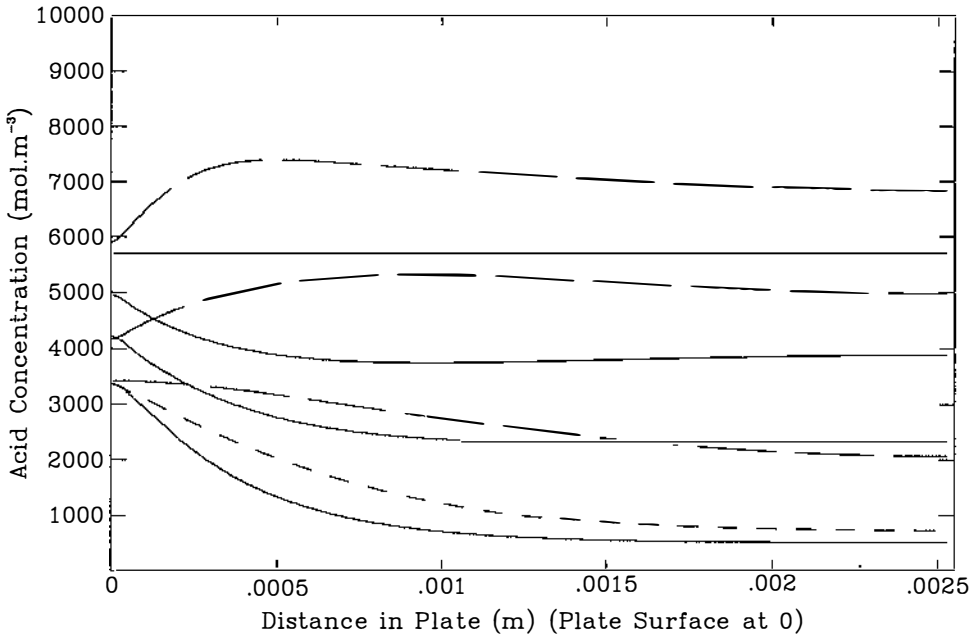

Solid: discharge profiles at 0.0, 1.0, 2.0 and 3.2 hrs top to bottom.
Small dash: rest profile at 3.5 hrs.
Large dash: charge profiles at 4.0, 5.0 and 6.8 hrs bottom to top.
Results for 20 A discharge, 0.5 hr rest and 20 A charge.
m and μ−channel tortuosity factor increased from 1.30 to 2.19.

Figure 7.32: Plate Acid for More Tortuous AM.

selection. To this end the model was operated with a more tortuous structure.

The results obtained for the more tortuous structure discharged at 20 Amperes are given in figures 7.29 to 7.32. The capacity of 64.2 Ampere hours obtained here is considerably less than that of the standard case. Figure 7.32 shows this is due to a more rapid drop in plate acid concentration particularly in the plate interior. This has the usual adverse effects on electrode equilibrium potential and overpotential. The drop in acid concentration is to be expected with the increased acid transport difficulties of the more tortuous structure. The acid transport difficulties also have the effect of concentrating the discharge reaction near the plate surface where the supply of acid is greatest. This is reflected in a sharper boundary between the discharged AM in this case (figure 7.31) compared to the standard case. In other respects the characteristics seen here are similar to those of the standard case.

d) VIAM model results with Non-participating AM.

The dependence of the VIAM model result on non-participating AM has important implications for service life (see Chang (1984) for example).

The plate parameters were adjusted to incorporate 20% of non-participating AM at the plate surface. The results obtained for a 20 Ampere discharge using this structure are given in figures 7.33 to 7.36. A low capacity of 56.6 Ampere hours is obtained in this case. As with the more tortuous structure, the result is a rapid drop in acid concentration in the plate interior. In this case the acid must diffuse through the tortuous non-participating AM to reach the reacting AM in the plate interior. A considerable concentration gradient forms in the non-participating AM reducing the acid concentration at the reacting region (figure 7.36). The reduced concentration gives a low

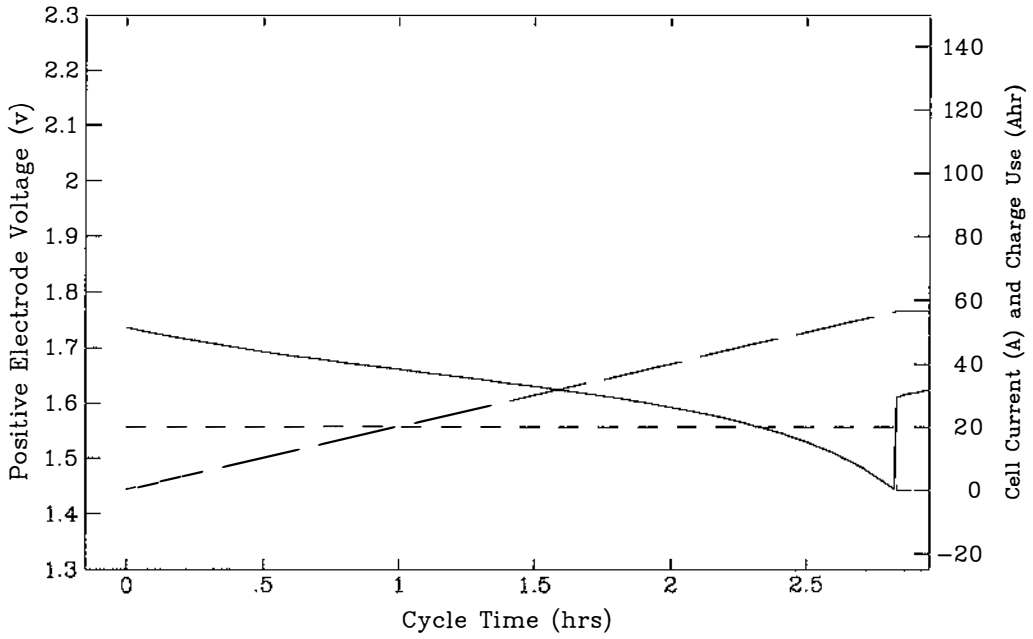

Solid: Positive electrode voltage (v). Small dash: Cell current (A).
Large dash: Charge usage (Ahrs).

Results for 20 A discharge, 0.5 hr rest and 20 A charge.
Non−participating AM increased from 1% to 20% of plate thickness.

Figure 7.33: Discharge Voltage with Non−participating AM.

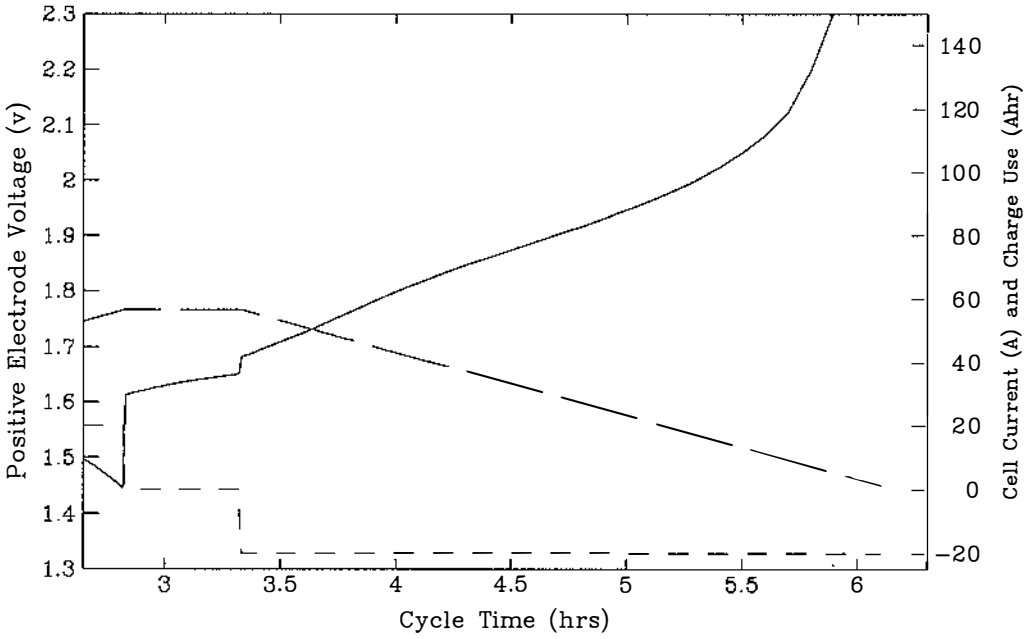

Solid: Positive electrode voltage (v). Small dash: Cell current (A).
Large dash: Charge usage (Ahrs).

Results for 20 A discharge, 0.5 hr rest and 20 A charge.
Non−participating AM increased from 1% to 20% of plate thickness.

Figure 7.34: Rest and Charge Voltage with Non−participating AM.

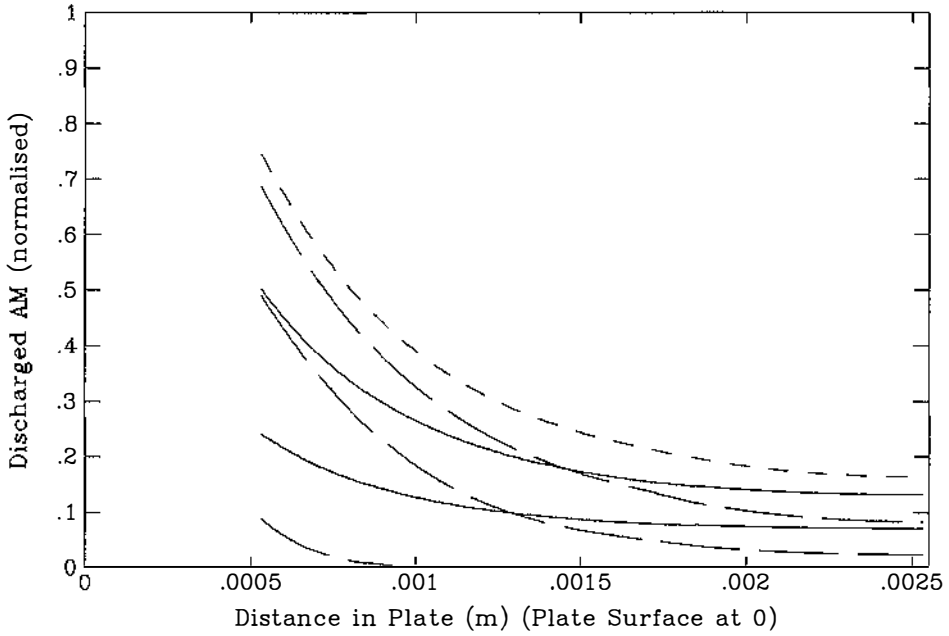

Solid: discharge profiles at 1.0 and 2.0 hrs bottom to top.
Small dash: rest profile at 3.1 hrs.
Large dash: charge profiles at 4.0, 5.0 and 6.1 hrs top to bottom.
Results for 20 A discharge, 0.5 hr rest and 20 A charge.
Discharged AM at each m-channel position defined as: $1-X_{AVERAGE}$.
Non-participating AM increased from 1% to 20% of plate thickness.

Figure 7.35: Discharged Plate AM with Non-participating AM.

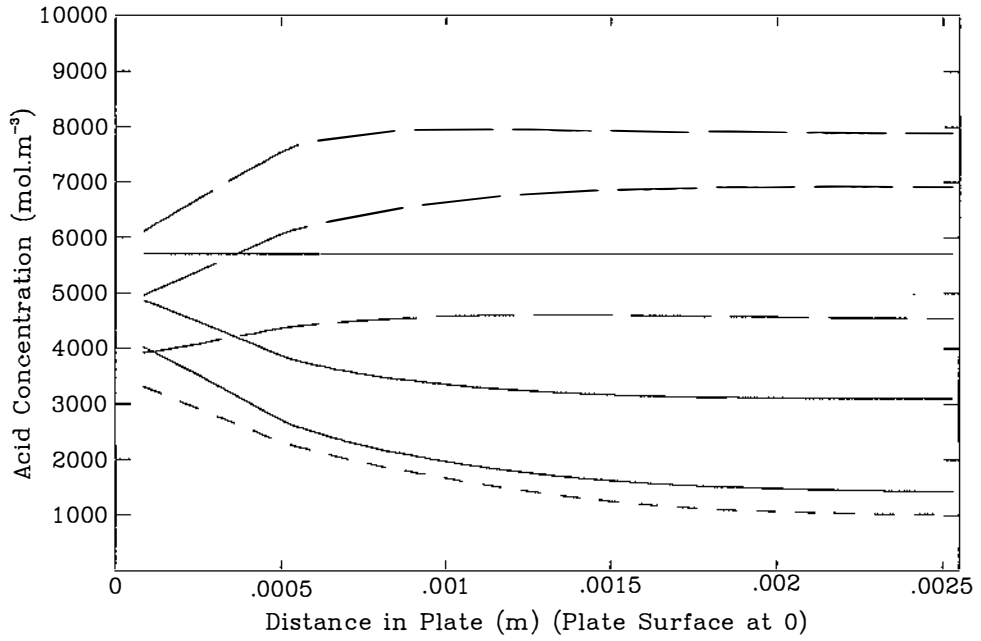

Solid: discharge profiles at 0.0, 1.0 and 2.0 hrs top to bottom.
Small dash: rest profile at 3.1 hrs.
Large dash: charge profiles at 4.0, 5.0 and 6.1 hrs bottom to top.

Results for 20 A discharge, 0.5 hr rest and 20 A charge.
Non-participating AM increased from 1% to 20% of plate thickness.

Figure 7.36: Plate Acid with Non-participating AM.

electrode equilibrium potential and a high overpotential. The high overpotential conditions are compounded by an increase in exchange current density due to the reduced proportion (area) of reacting AM (figure 7.35). The non-participating AM also adds to the solution potential drop since discharge or charge currents must pass through the resistive solution which the non-participating AM surrounds. In other respects the characteristics obtained here are similar to those for the standard case.

e) VIAM model results and uncertain exchange currents.

It is of interest to assess the sensitivity of the VIAM model results to changes in parameters which are most likely to differ from the assumed values. The model parameters for the single cathodic and anodic exchange current/overpotential relationships certainly fall into this category (see the discussion for the fast discharge above and sections 3.3.2 and 3.3.3). Also, to a lesser extent, the incorporated elemental model results for discharge surface area and effective charge surface area are somewhat uncertain (see sections 7.1.2 and 7.1.3).

In practice, assessing the sensitivity of the model to changes in the exchange current density amounts to doing the same for the surface area. This is because when used for calculations within the model, the exchange current density and surface area terms are always multiplied to give an exchange current term. Therefore, the model was operated with this standard exchange current term multiplied by the constant factor 10 to assess the sensitivity for both parameters. The results obtained are given in figures 7.37 to 7.40.

The discharge voltage/time characteristic (figure 3.37) shows less voltage drop than in the standard case. This is because with the increased exchange current the overpotential is much smaller. It is only at the end of the discharge, when the acid in the plates is almost completely

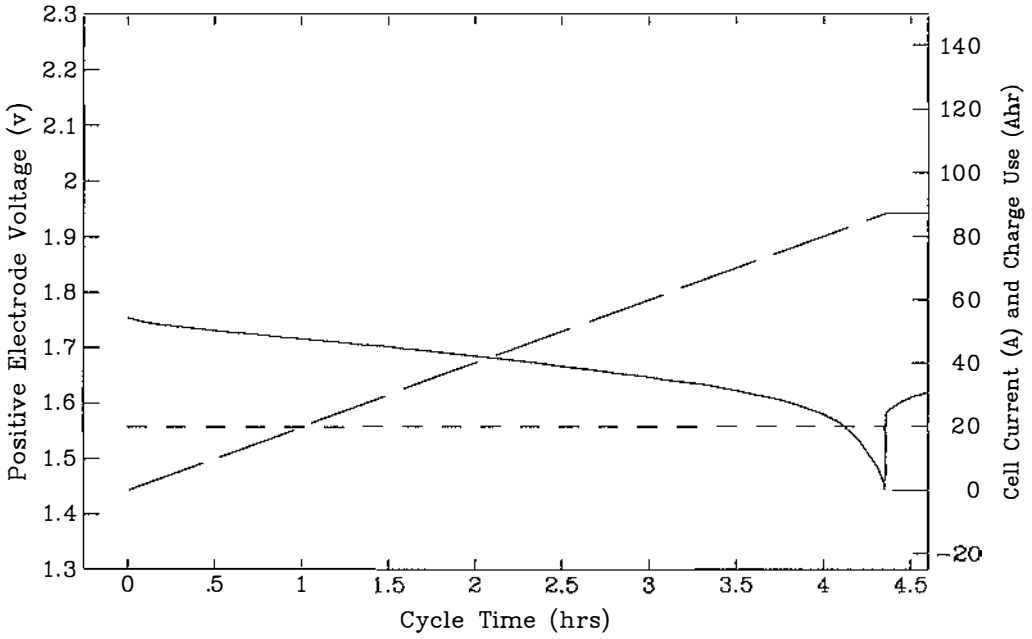

Solid: Positive electrode voltage (v). Small dash: Cell current (A).
Large dash: Charge usage (Ahrs).

Results for 20 A discharge, 0.5 hr rest and 20 A charge.
Exchange current increased by a factor of 10.

Figure 7.37: Discharge Voltage for Increased Exchange Current.

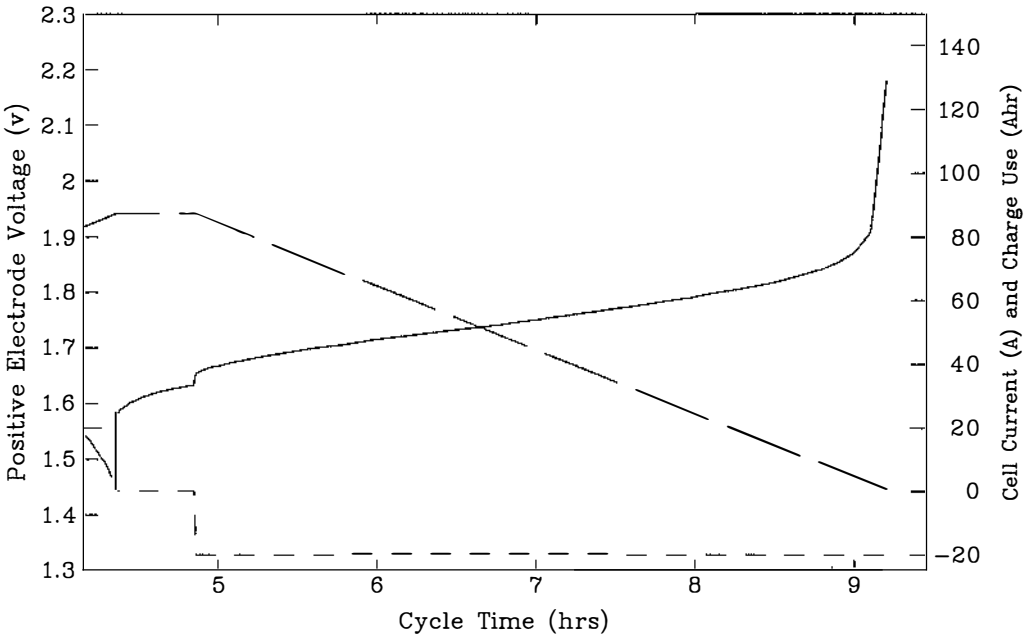

Solid: Positive electrode voltage (v). Small dash: Cell current (A).
Large dash: Charge usage (Ahrs).

Results for 20 A discharge, 0.5 hr rest and 20 A charge.
Exchange current increased by a factor of 10.

Figure 7.38: Rest and Charge Voltage for Increased Exchange Current.

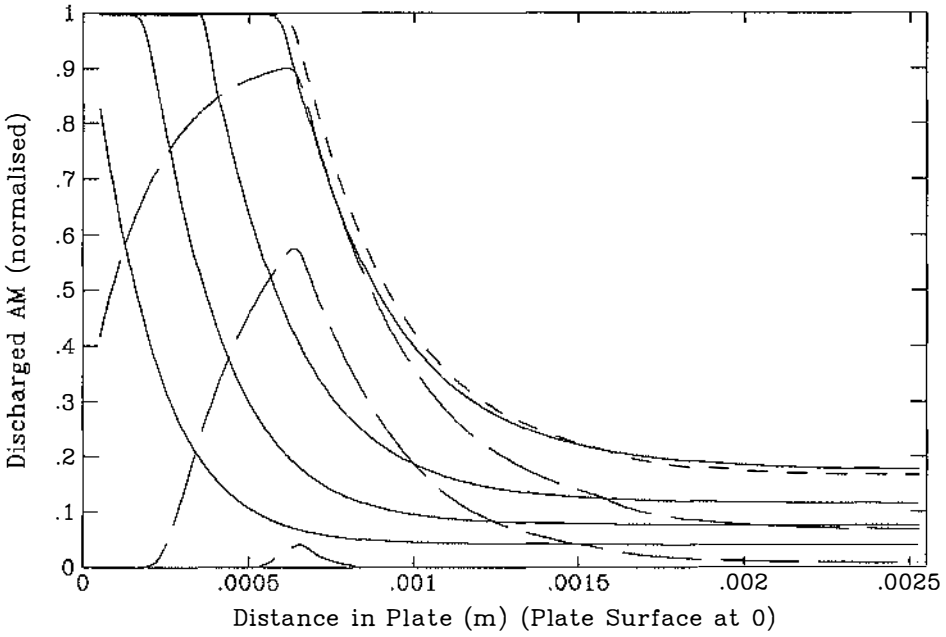

Solid: discharge profiles at 1.0, 2.0, 3.0 and 4.3 hrs bottom to top.
Small dash: rest profile at 4.6 hrs.
Large dash: charge profiles at 6.0, 8.0 and 9.2 hrs top to bottom.
Results for 20 A discharge, 0.5 hr rest and 20 A charge.
Discharged AM at each m-channel position defined as: $1-X_{AVERAGE}$.
Exchange current increased by a factor of 10.

Figure 7.39: Discharged Plate AM for Increased Exchange Current.

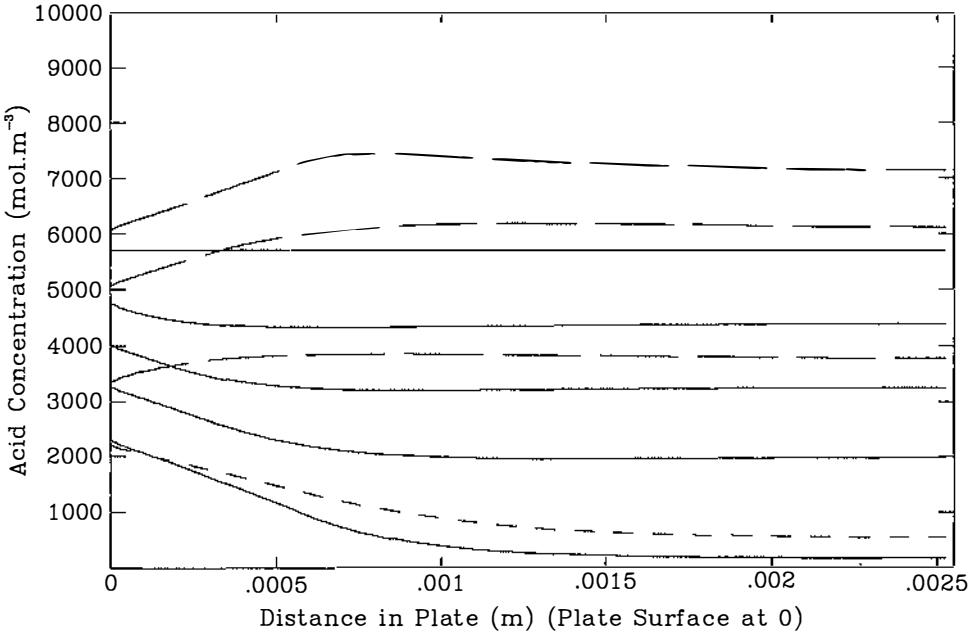

Solid: discharge profiles at 0.0, 1.0, 2.0, 3.0 and 4.3 hrs top to bottom.
Small dash: rest profile at 4.6 hrs.
Large dash: charge profiles at 6.0, 8.0 and 9.2 hrs bottom to top.
Results for 20 A discharge, 0.5 hr rest and 20 A charge.
Exchange current increased by a factor of 10.

Figure 7.40: Plate Acid for Increased Exchange Current.

exhausted (figure 7.40), that the plate voltage rapidly drops. The three effects of low equilibrium potential, high overpotential and high solution potential drop are all present at this time. The AM distribution (figure 7.39) shows the high cathodic exchange current gives a more distinct division between the discharge and charged AM than is seen in the standard case.

The charge voltage/time characteristic shows less voltage rise than in the standard case. This again is because with the increased exchange current the overpotential is much smaller. It is only when the charge is almost complete that the plate voltage shows a rapid rise. At this stage the rise is due to the overpotential that results from concentrating the current onto the vanishing effective charge surface.

7.3.3 The VIAM Model μ-channel Component.

Observation of the VIAM model in operation shows little variation of any result value with μ-channel length. For example, during the standard discharge/charge cycle, the μ-channel at the plate surface gave a maximum difference in open and closed end charge state (X_{open}-X_{close}) and concentration ((c_{open}-c_{closed})/$c_{initial}$) of only $4.3x10^{-5}$ and $3.8x10^{-4}$ respectively. The small variations seen here are indicative of the small μ-channel length and a low ratio of solution resistance to interface impedance within the μ-channel. It suggests that the VIAM model can be simplified by treating the complete μ-channel as a single segment for both the electrical and transport analysis.

7.3.4 The VIAM Model: a Discussion.

Some discussion has already taken place in the context of reporting and explaining the VIAM model results. Here

the discussion is concerned with evaluating the validity of the model by comparing the results obtained with other known or expected results.

a) The cell capacity.

The VIAM model parameters were set for a cell having a nominal capacity of 100 Ampere hours at the 5 hour rate. In the standard case the model gave a very similar capacity of 89 Ampere hours at this rate.

The model showed that the capacity was limited by a combination of factors that result from acid depletion. Close examination of the acid concentration in the discharged cell shows only a small proportion of the reservoir acid is used (figure 7.20). This suggests the poor transfer of acid from the reservoir into the separator and positive plate is a cause for the premature acid depletion. A likely reason for the poor transport results is the inappropriate use of the acid diffusion coefficient when considering the bulk solution of the reservoir.

During discharge, acid of a low density is produced within the plates and gradually moves through the separator region into the reservoir region. This low density acid rises to the top of the cell both in the separator and reservoir regions and, in doing so, sets up convection currents. These convection currents will greatly assist the diffusion process that controls the transfer of acid from the reservoir into the separator and positive plate. This is not taken into account in the standard model. It can be seen that a case exists for using an effective diffusion coefficient in the reservoir region which is considerably higher than that for the standard case of non-circulating bulk solution. This would move the model capacity even closer to the expected value of 100 Ampere hours. This was done for the results produced for comparison with the experimental results in section 7.5.

Using the VIAM model results for the slow, medium and fast discharge cases (figures 7.21, 7.13 and 7.25 respectively) the fit of the predicted cell capacity to Peuket's equation can be tested. Peuket's equation can be written as

$$I_n T = c \qquad (7.6)$$

where I (A) is the constant discharge current ,
T (hrs) is the full capacity discharge time and
n and c are constants for a particular cell.

The full capacity discharge time was calculated as discharge capacity divided by discharge rate. The constant "n" was found to be in the range 1.25 to 1.30 depending on which two discharge cases were used to calculate it. This is self-consistent and close to values expected in practice (see Asher *et al* (1980)).

b) The discharge voltage/time curve.

The discharge voltage/time curve has the normal form of a slow decline for most of the discharge which rapidly increases towards the end of charge (see for example Pavlov (1984)). The macrohomogeneous model does not predict such a rapid decline at the end of the discharge (Simonsson (1973)).

The experimental voltage/time data of Sunu and Burrows (1981) and data produced by the VIAM model are well suited for direct and detailed comparison. The situations are comparable in the following respects.

i) Sunu and Burrows used realistic electric vehicle cell components. The VIAM model is set up for similar traction cell components.

ii) Sunu and Burrows (1981) directly measured the positive plate voltage drop. This parameter is obtained directly from the VIAM model.

iii) The discharge rate used by Sunu and Burrows (1981) is very close to the rate used for the VIAM model. The discharge rates correspond to 0.19 and 0.23 of the five hour capacity in Amperes for the case of Sunu and Borrows (1981) and the standard model respectively.

Figure 7.41 gives the discharge results of the VIAM model together with the results of Sunu and Burrows (1981). The discharge capacity of all results has been scaled to 100 Ampere hours. For the results of Sunu and Burrows (1981) the initial voltage, which is a function of initial acid concentration, has been made equal to that for the VIAM model.

It can be seen that the model results agree closely with the experimental results. The only significant difference is seen at the beginning of the discharge. This could well be eliminated if the VIAM model was modified to account for the low and high exchange current/overpotential

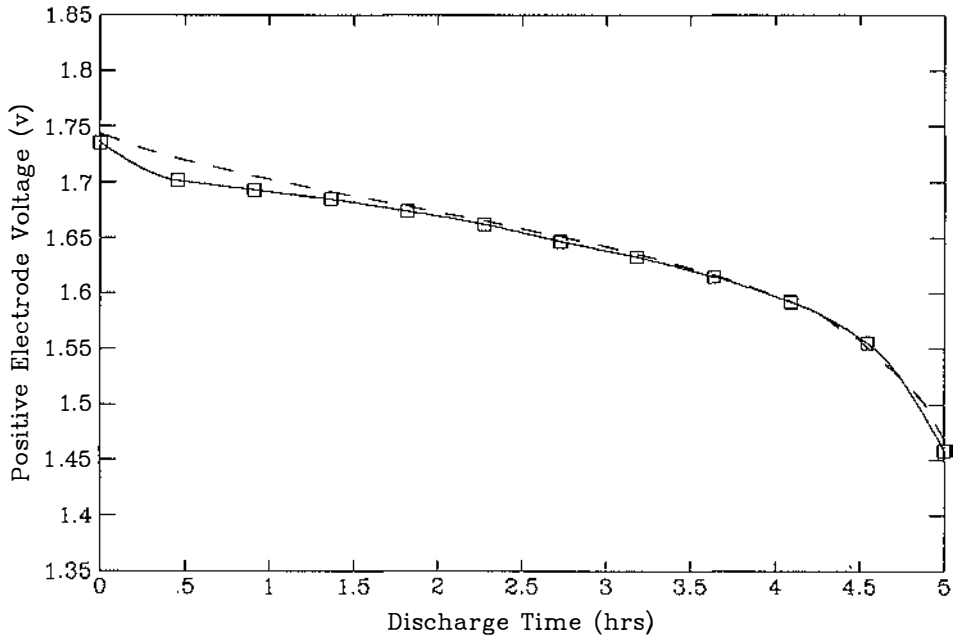

□/Solid: Experimental results of Sunu and Burrows (1981).
Small dash: VIAM model results for standard discharge case.
Standard case: 20 A full discharge, 0.5 hr rest and 20 A charge.

Capacity scaled to 100 Ahr, 5 hr discharge.

Figure 7.41: Experimental and Model Discharge Voltage.

relationships. This has already been discussed in the context of the high current discharge case in section 7.3.2

c) The charge voltage/time curve.

The charge voltage/time curve has the normal form of a slow rise for most of the charge which rapidly increases towards the end of charge (see Pavlov (1984)). However, two features are missing. Firstly, a voltage peak at the beginning of charge is sometimes observed (see Ekdunge and Simonsson (1985)). This may well be due to PbO_2 encapsulation during deep discharge, an effect noted but not accounted for in the charge surface area model (see section 7.1.3). Secondly, the increasing potential at the end of charge eventually levels out. This occurs when the charge current is diverted into the gassing reaction. The VIAM model does not account for the gassing reaction.

As before, the experimental voltage/time data of Sunu and Burrows (1981) and data produced by the VIAM model are

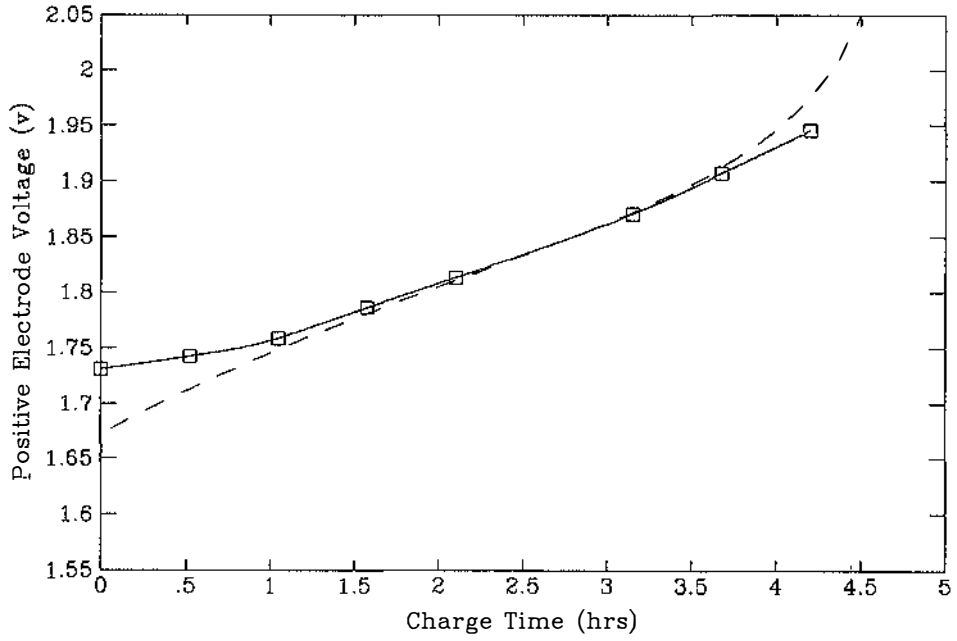

□/Solid: Experimental results of Sunu and Burrows (1981).
Small dash: VIAM model results for standard charge case.
Standard case: 20 A full discharge, 0.5 hr rest and 20 A charge.

Capacity scaled to 100 Ahr, 5 hr rate.

Figure 7.42: Experimental and Model Charge Voltage.

well suited for direct and detailed comparison. In the charge case, Sunu and Burrows (1981) use a slightly higher current than in the discharge which makes the actual charge rate virtually the same as that used for the VIAM model. Unfortunately the data can only be compared for the first 84% of the charge since at this stage the experimental current was necessarily reduced because of gassing. Figure 7.42 gives the charge results of the VIAM model together with the results of Sunu and Burrows. Again the capacity of all results have been scaled to 100 Ampere hours and the initial voltage for the experimental case has been made equal to that for the VIAM model (here the rest voltage at the start of charge). Also the initial voltage rise in the experimental case has been adjusted for the same reason as in the charge case.

It can be seen that the model results give reasonable agreement with the experimental results. Differences at the beginning of charge have already been discussed above. Differences throughout the charge may be due to a different acid concentration distribution when the charge started. This is likely since Sunu and Burrows (1981) do not specify the rest time before the charge began. A more satisfactory comparison of experimental and model results can be made using the experimental charge data collected for this work. This is done in section 7.5.

d) The internal AM distribution.

The VIAM model predicts a sharply defined boundary between the discharged and charged AM at high discharge currents (figure 7.27). At lower discharge currents the boundary is more graded (figure 7.23). This is in good agreement with the experimental observations (see Simonsson (1973) and Chang (1984)).

The VIAM model results for the 140 ampere discharge and the experimental results of Simonsson (1973) for a similar discharge current density are given in figure 7.43.

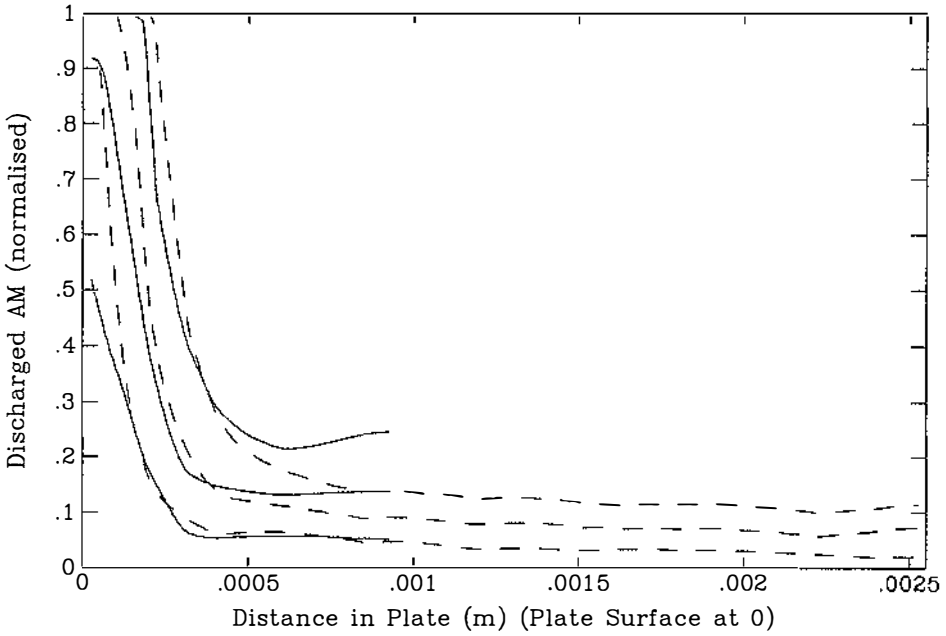

Solid: Experimental profiles Simonsson (1973) at 25, 50 and 100% full discharge capacity bottom to top.
Small dash: VIAM model profiles at 28.5, 57.1 and 85.7% full discharge capacity bottom to top.
Discharge current density approximately 1000 Am^{-2}.

Figure 7.43: Experimental and Model Discharged Plate AM.

In both cases the maximum discharged AM has been used to normalise the results. Also the start position for the discharged AM in the experimental case has been brought inside the plate to coincide with the start of the m-channel (inside the non-participating AM). The close agreement of the model and experimental results can be seen here. It is of interest to note that the macrohomogeneous model gave a more graded boundary at high discharge rates (see Simonsson (1973)).

e) The role of acid transportation.

For the parameters used in the VIAM model, the transport of acid has been seen to be the key factor in limiting the cell capacity. This is consistent with recent studies of cells with different AM (see Pavlov and Bashtavelova (1986)). This result serves to illustrate that both high internal surface area and effective internal transport are necessary features of effective cell plates.

f) The effects of cycling.

One case where non-participating AM was used to represent cycled AM has been given in section 7.3.2. The VIAM model was also operated with different quantities of non-participating AM and the effect on cell capacity noted. These results are given with experimental results from Chang (1984) in figure 7.44. The experimental results here are for a similar discharge rate to that for the VIAM model but the AM is different. The 15% non-participating AM case for the VIAM model and the 110 cycle point for the experimental results have been scaled to coincide since they both give a similar capacity drop.

It is difficult to draw any conclusions by comparing the effects of cycling as modelled and observed experimentally. This is because experimental results show a wide variation in effects (see Pavlov and Bashtavelova (1984) and Chang (1984) for example). Most commonly, after the initial few discharge/charge cycles where the capacity

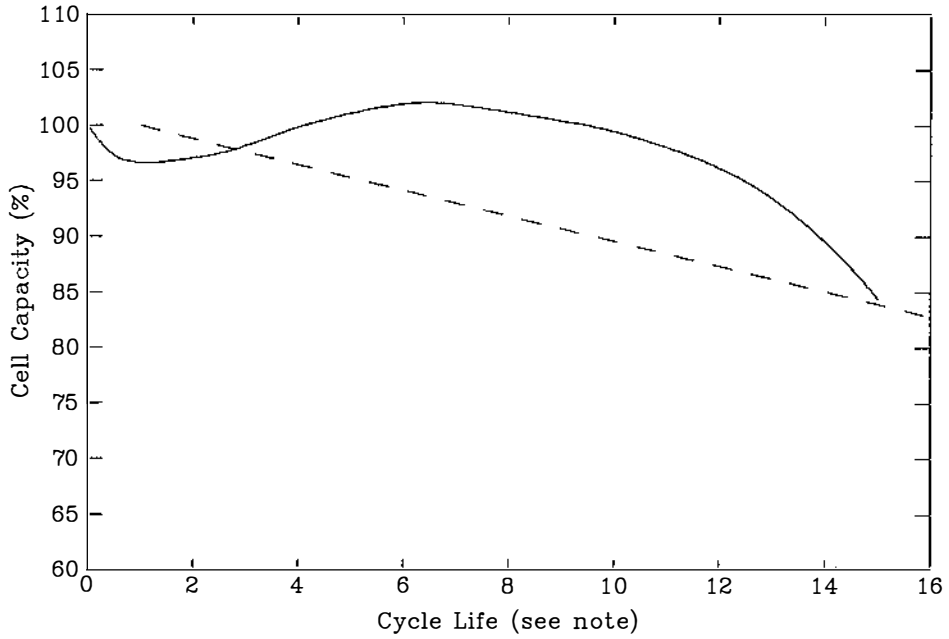

Solid: Experimental results of Chang (1984) for 5 hr full discharge.
Small dash: VIAM model results for 4.4 hr full discharge.

Note: Cycle life represented as the proportion (%) of non-participating AM in plate thickness. 110 cycles scaled to equal 15% non-participating AM.

Figure 7.44: Experimental and Model Cell Life.

may increase, there is a gradual decreasing in capacity (see Kordesch (1977)). The initial increase in capacity, when it occurs, is in effect the completion of unfinished plate forming. The VIAM model does not allow for any initial capacity increase of this kind.

g) Additional model evaluation.

The experimental results presented in the next section provide more data with which to evaluate the VIAM model. This is discussed in section 7.5.

7.4 EXPERIMENTAL RESULTS.

7.4.1 Calculations Performed on the Raw Data

The raw data collected experimentally has been described in chapter 6. Various calculations were performed on this data to give forms suitable for results here. These are described below.

a) Reconstruction of concentration values.

Calculations were performed on electrolyte specific gravity measurements to give an equally spaced data set in units of moles per cubic metre. The manually collected specific gravity measurements were taken at various time intervals ranging between 0.25 and 0.5 hours. These measurements were used for the interpolation of data at 0.1 hour spacings. The reconstructed values were then converted into concentration in moles per cubic metre.

b) Generation of reference potential values.

The equilibrium potential of the positive reference electrode and that of a hypothetical negative electrode are required for estimating the positive plate portion of the

total cell voltage. These were obtained for each of the reconstructed concentration values mentioned above using the equilibrium potential formulation given in appendix 3.

c) Data compression.

The data set collected by the automatic data acquisition system was compressed by eliminating nine out of every ten time steps to give data at 0.1 hour intervals.

d) Reconstruction of gassing values.

When the cell was opened for specific gravity measurements the gassing rate was incorrectly recorded as zero. These zero values were replaced with values interpolated from correct adjacent points in the compressed data set.

e) Positive electrode voltage estimation: procedure one.

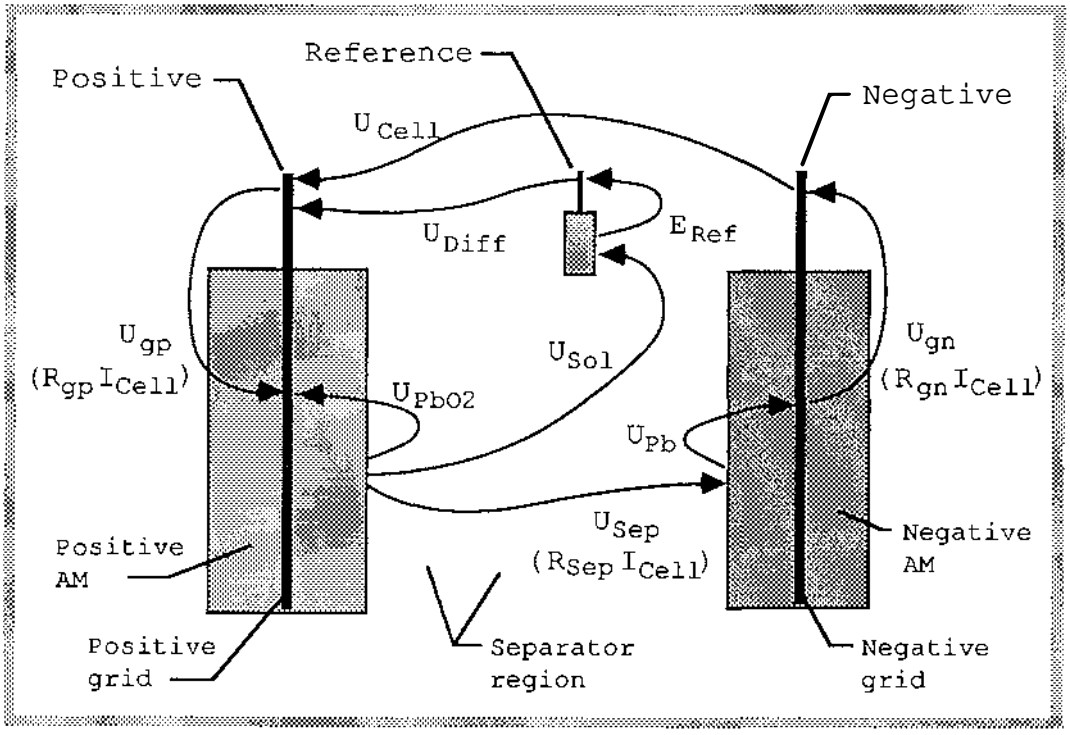

Figure 7.45: Potential Differences in Cell Under Test.

The positive electrode voltage is required for comparison with VIAM model results. Unfortunately this was not measured directly and must be estimated by relating various potential differences within the cell. The potential differences involved are shown in figure 7.45. For procedure one the relationship used is defined by

$$U_{PbO2} = U_{cell} + U_{Pb} + I_{cell}(R_{sep}+R_{gp}+R_{gn}) \qquad (7.7)$$

where

U_{PbO2} (v) is the required positive electrode voltage,
U_{cell} (v) is the potential at the positive post less the potential at the negative post,
U_{Pb} (v) is the potential at the negative grid less the potential in the solution at the negative plate surface,
I_{cell} (A) is the cell current,
R_{sep} (Ω) is the separator resistance,
R_{gp} (Ω) is the positive grid and post resistance and
R_{gn} (Ω) is the negative grid and post resistance.

U_{cell} and U_{Pb} were collected by the data acquisition system. The remaining terms on the right hand side are determined indirectly as described below.

U_{neg} is estimated from the negative electrode equilibrium voltage given the reconstructed concentration data for measurements made at the top of the cell. This is a valid approximation provided three qualifying conditions are met.

Firstly, the solution potential drop in the negative plate must be small. This is the case since the acid concentration variations from the charged value are limited and therefore the solution resistivity is low. The acid concentration variations are limited because only about 20% of the acid is consumed here compared with 80% at the positive (as determined by the hydrogen ion transportation number).

Secondly, the negative electrode overpotential must be small. This is the case except when the negative plate is nearing complete charge (see Sunu and Burrows (1981) for example).

Thirdly, the difference between the acid concentration at the negative electrode and the acid concentration at the top of the cell must be small. This is to limit the difference in equilibrium voltage calculated for the acid at the top of the cell but assumed to represent acid in the negative electrode. The acid concentration at the top of the cell is the low density acid most recently released from the separator region. This means the concentration measured here is close to the separator concentration during discharge and for the early part of the charge. Also the acid concentration gradient in the separator to the negative plate is relatively small because of the moderate acid consumption in the negative electrode (as mentioned above). As a result the concentration in the separator is close to the concentration in the negative electrode. The combination of the effects here means that the acid concentration at the top of the cell is a reasonable representation of the acid concentration at the negative electrode for the discharge and early part of the charge. Reviewing the three qualifying conditions above, the estimation used for U_{Pb} is seen to be valid for the discharge and early part of the charge only.

R_{sep}, R_{gp} and R_{gn} make up the internal resistance of the cell. R_{gp} and R_{gn} are determined by the resistivity of the lead grid and post members in the cell and can be taken as constant. R_{sep} is determined by the resistivity of the acid solution in the separator region. This can be assumed to be approximately constant since, as with the acid in the negative plate, the concentration variation here is limited and has a small effect on the solution resistivity. The combined effect gives an approximately constant cell resistance.

The cell resistance cannot be estimated from the initial voltage drop at the beginning of the discharge since this is made up of large contributions from the cell resistance and the positive electrode over-potential. In the cell tested by Sunu and Burrows (1981) these contributions were 0.045 and 0.049 volts respectively at about the 5 hour current rate. The approach taken here to obtain the required value made use of the similarity between the cell used by Sunu and Burrows (1981) and the cell under test. A first value was obtained by discounting the cell resistance reported by these authors to account for the difference in grid thickness between the two cells. This gave a cell resistance of 0.0017 Ω. This value was then applied in conjunction with equation 7.7 to the experimental data. It was found that the cell resistance contribution was too large for U_{PbO2} estimates at high currents and gave voltages higher than the corresponding lower current results. The cell resistance was subsequently reduced until the results obtained for different currents gave a spread with the same proportions as that for the total cell voltage. The value obtained in this way was 0.001 Ω.

The final equation used to estimate U_{PbO2} by procedure one was

$$U_{PbO2} = U_{cell} + E_{Pb} + I_{cell}(R_{sep}+R_{gp}+R_{gn}) \qquad (7.8)$$

where

E_{Pb} (v) is the negative electrode equilibrium potential described above.

In the results that follow, the estimation of U_{PbO2} by this procedure is used during the discharge, rest and for approximately the first 10% of the charge. The discussion above has shown that beyond this time the results obtained decrease in accuracy. As a consequence a second estimation procedure is required for the rest of the charge. This is presented below.

f) Positive electrode voltage estimation: procedure two.

The second estimation procedure required for most of the charge makes use of an alternative potential difference relationship. Again the potential differences involved are shown in figure 7.45. The alternative relationship is defined by

$$U_{PbO2} = E_{ref} + U_{diff} + U_{sol} + R_{gp} I_{cell} \qquad (7.9)$$

where

E_{ref} (v) is the reference electrode equilibrium voltage,

U_{diff} (v) is the potential at the positive post less the potential at the reference post,

U_{sol} (v) s the potential in solution at the reference electrode less the potential in the solution at the positive plate surface and

other quantities are as before.

U_{diff} was collected by the data acquisition system. E_{ref} is generated from the reconstructed concentration data for the measurements from the top of the cell. The potential drop effects of U_{sol} and R_{gp} are estimated as described below.

The difference in solution potential from part way down to the top of the plate plus that from the top of the plate to the reference electrode make up U_{sol}. The first contribution is due to polarisation effects with plate height. The second contribution is due to currents flowing in solution directly above the plates. The approach taken here assumes the first contribution is negligible. The second contribution is assumed to be determined by the potential in the solution at the surface of the positive and negative plates as averaged by the solution resistance above the plate. That is, it is taken as half the potential drop due to separator solution resistance. This means U_{sol} can be written as

$$U_{sol} = I_{cell} R_{sep}/2 \qquad (7.10)$$

The positive grid and post resistance R_{gp} is assumed to be equal to the negative grid and post resistance. This is reasonable given that the combined thickness of the three positive plates is almost equal to that of the four negative plates. As a result R_{gp} can be written as

$$R_{gp} = (R_{gp}+R_{gn})/2 \qquad (7.11)$$

Substituting equations 7.10 and 7.11 into equation 7.9 gives

$$U_{PbO2} = E_{ref} + U_{diff} + I_{cell}(R_{sep}+R_{gp}+R_{gn})/2. \qquad (7.12)$$

It can be seen that the combined resistance term in equation 7.12 is the cell resistance already discussed above. Equation 7.12 was the final form used to estimate U_{PbO2} by procedure two.

While the estimation procedures outlined above are not as precise as could be desired they are satisfactory for a qualitative comparison of the VIAM model results.

7.4.2 Presentation of the Experimental Results

The experimental results that follow generally agree with known results for cell discharging and charging (see Bode (1977) and Linden (1984) for example). The presentation given below emphasises only features that depart from expected results or are of particular interest in relation to the VIAM model results.

The graphical data given here is plotted at 0.1 hour intervals. This has the effect of making rapid changes in voltage appear rather slow. The one exception to this is the cell rest and charge voltage data given for the 10 Ampere hour discharge depth (figure 7.59). This is plotted at 0.01 hour intervals showing the rapidity of some changes in cell voltage.

7.4.3 Experimental Results for a Standard Case.

Complete experimental results for a 100 Ampere hour 20 Ampere discharge case are given in figures 7.46 to 7.48.

a) Cell voltage.

Figure 7.46 gives the variation of cell voltage with time. This shows a departure from the expected form where the rate of decline in cell voltage is reduced part way through the discharge. Reference to the gassing rate curve of figure 7.47 shows this is associated with gassing during discharge which presumably improves acid supply to the plate. During the rest stage, the voltage rapidly rises to an open circuit value controlled by the acid concentration in the plates. During charge, the cell follows the expected form until the constant voltage limit is reached. This occurs when the cell has had approximately 90% of its charge returned.

b) Estimated positive electrode voltage.

The estimated positive electrode voltage is given in figure 7.47. During discharge and rest, this follows the form of the total cell voltage but with the cell resistance and negative electrode potentials removed. During charge this also follows the form of the cell voltage until the onset of gassing at about 8 hours. From this time the plate voltage tends towards a constant value. The cell voltage, on the other hand, rapidly increases until it reaches the voltage limit. The difference in form here is due to the rapid polarisation of the negative electrode (Sunu and Burrows (1981)). It is of interest to note the range over which the positive electrode voltage estimated by procedure one is valid. The limit is determined by the onset of gassing (see figure 7.47).

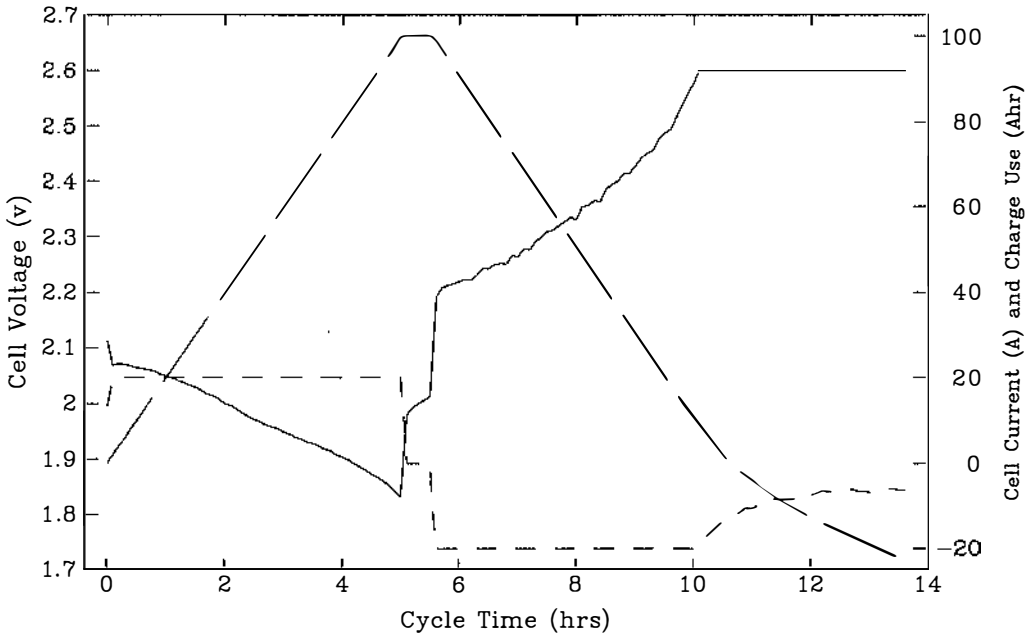

Solid: Total cell voltage (v). Small dash: Cell current (A).
Large dash: Charge usage (Ahrs).

Experiment AD100R20: 100 Ahr/20 A discharge, 0.5 hr rest and 20 A charge.

Figure 7.46: AD100R20 Cell Voltage.

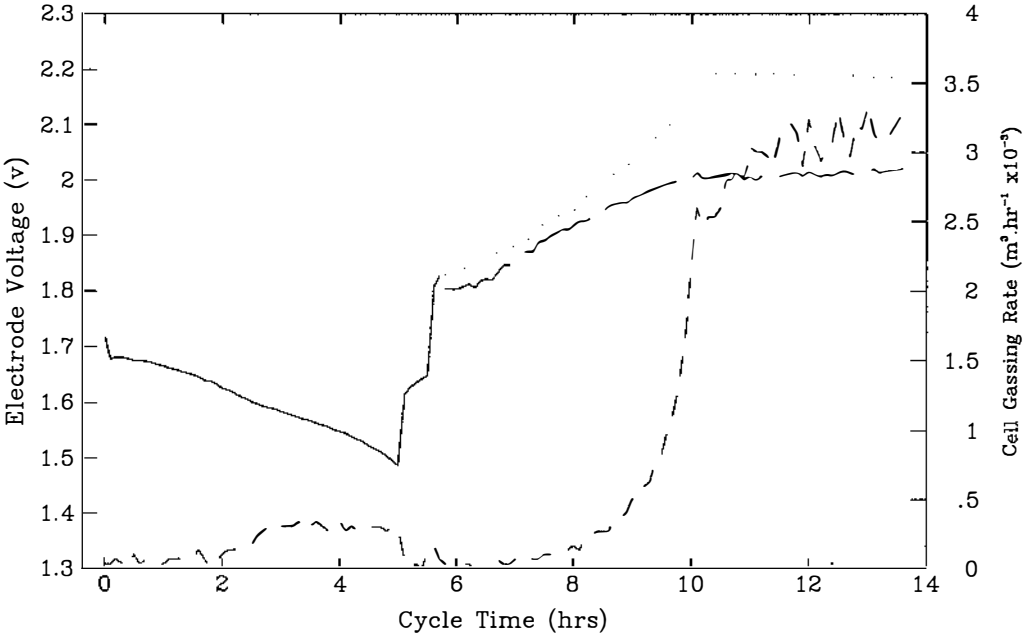

Solid: Electrode voltage (U_{PbO2}) (v) estimated by procedure one.
Dot: Extension of electrode voltage (v) estimated by procedure one.
Large dash: Electrode voltage (v) estimated by procedure two.
Small dash: Cell gassing rate ($m^3.hr^{-1}$ $x10^{-3}$).
Experiment AD100R20: 100 Ahr/20 A discharge, 0.5 hr rest and 20 A charge.

Figure 7.47: AD100R20 Electrode Voltage Estimate.

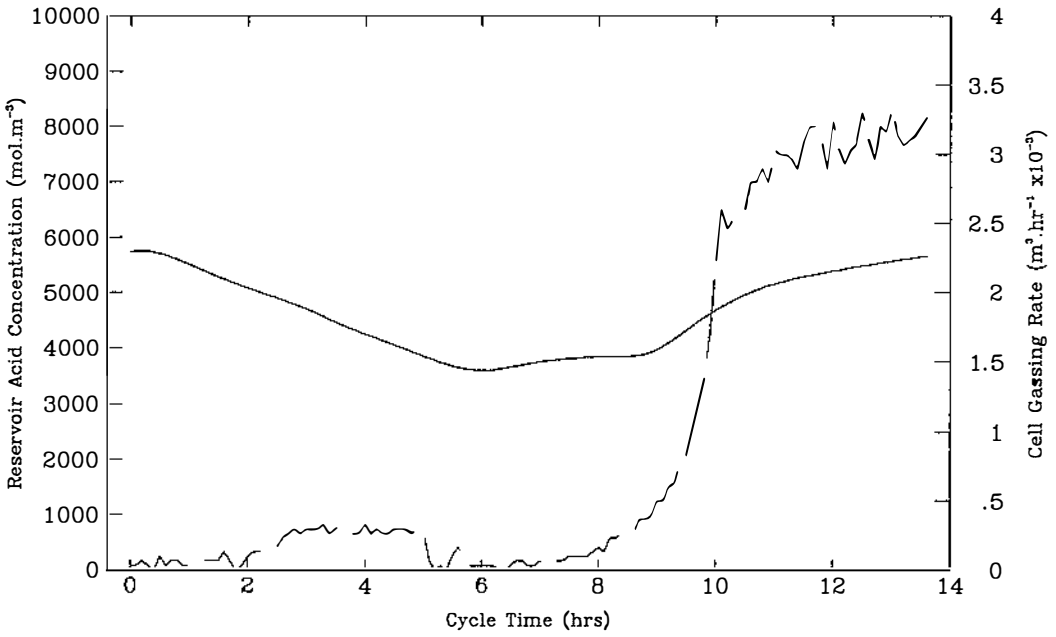

Solid: Reservoir acid concentration ($mol.m^{-3}$).
Large dash: Cell gassing rate ($m^3.hr^{-1}$ $x10^{-3}$).

Experiment AD100R20: 100 Ahr/20 A discharge, 0.5 hr rest and 20 A charge.

Figure 7.48: AD100R20 Reservoir Acid Concentration.

c) Reservoir acid concentration.

The reservoir acid concentration measured at the top of the cell is shown in figure 7.48. During the discharge and rest stage, acid concentration changes follow the acid consumption in the plates (indicated by the cell current) although the time response is slow. During initial charge the acid concentration changes are more gradual since the high density acid produced does not readily reach the top of the cell. The onset of gassing, however, causes mixing of acid and a rapid increase in the concentration measurement. Further concentration variations will not be given in the context of the other cases that follow. All gave the same form as seen in the standard case but the magnitude of the variations seen was dependent on the discharge depth.

d) Cell gassing.

The cell gassing rate is given in figures 7.47 and 7.48. The somewhat surprising feature here is the gassing during the latter part of the discharge. This helps maintain a high cell voltage as observed above. The onset of gassing during the charge is caused by hydrogen evolution at the polarised negative plate. Later in the charge when both positive and negative plates are charged, both contribute to the gassing. Further gassing results will not be given in the context of the other cases below. It should be pointed out, however, that gassing during discharge occurred for all the discharges with rates 20 Amperes or greater.

7.4.4 Other Experimental Results.

a) Discharge cell voltage.

The discharge cell voltage and estimated positive electrode voltage are given in figures 7.49 to 7.54. These are arranged in pairs giving cell and positive electrode voltage for each of the three discharge depths 100, 50 and 10 Ampere hours.

It is of interest to compare the cell voltage results for the same discharge rates but different discharge depths. It would be expected that, at a given discharge time, the voltage drops involved would be the same for the same current. In practice significant differences can be seen. For example a difference of approximately 0.050 volts can be seen for the AD100R20 and AD050R20 cases (figures 7.49 and 7.51 respectively). These differences can be attributed to differences in the past discharge/charge history of the cases concerned. For the example above, experiment AD100R20 was performed the day after the preceding experiment while AD050R20 was performed after a two week break from experimentation with only a short

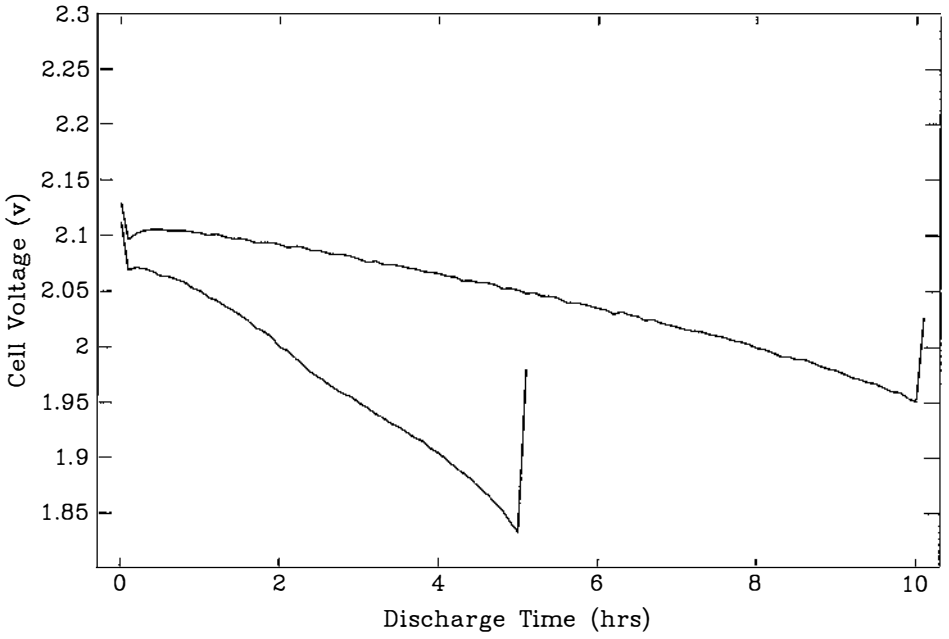

Discharge rates: 10 and 20 (A) top and bottom.

Experiments AD100R10 and AD100R20: 10 and 20 A discharge rate.
Both 100 Ahr depth followed by 0.5 hr rest and 20 A charge.

Figure 7.49: AD100R10–R20 Cell Discharge Voltage.

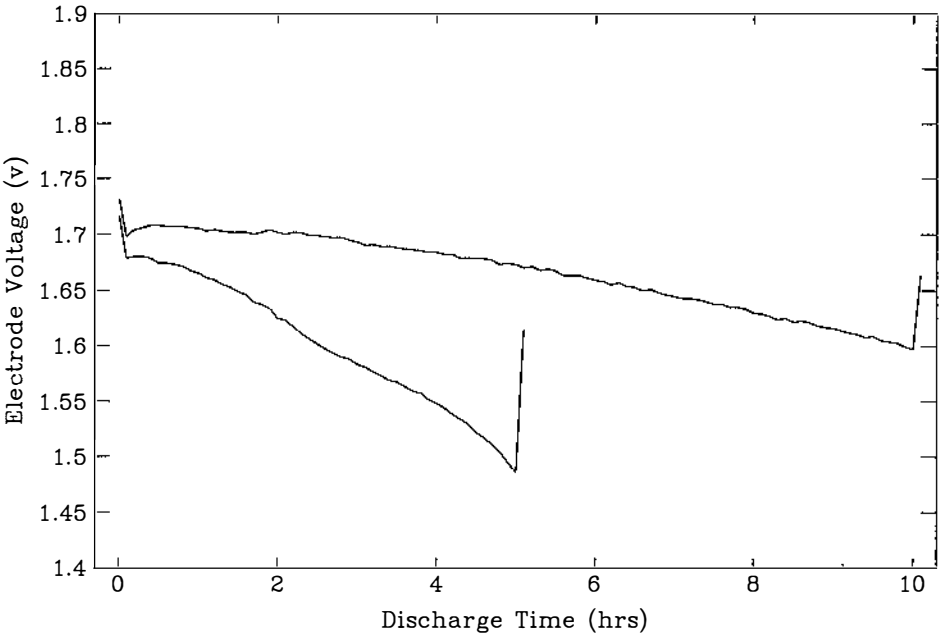

Discharge rates: 10 and 20 (A) top and bottom.

Experiments AD100R10 and AD100R20: 10 and 20 A discharge rate.
Both 100 Ahr depth followed by 0.5 hr rest and 20 A charge.

Figure 7.50: AD100R10–R20 Electrode Discharge Voltage.

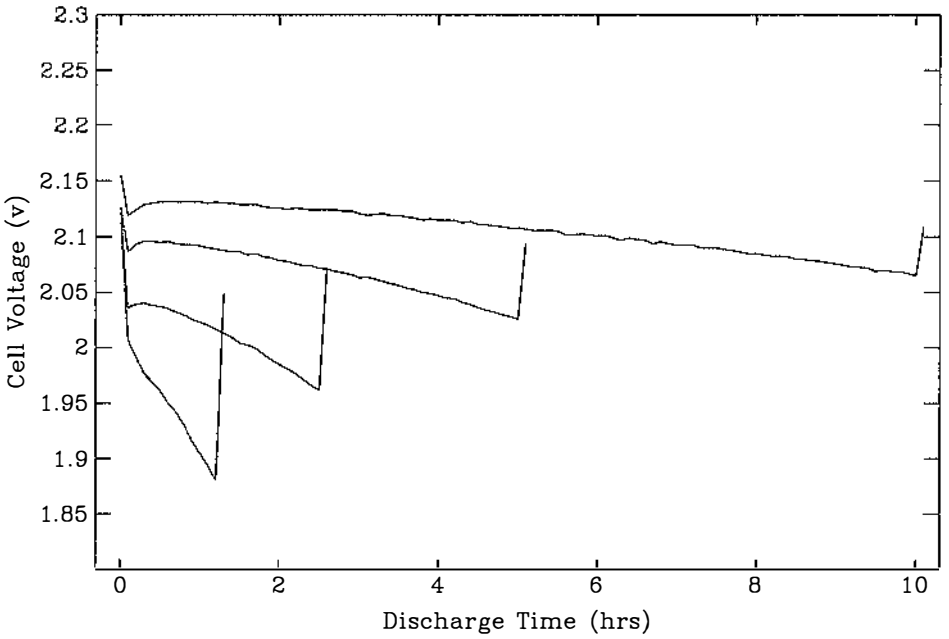

Discharge rates: 5 to 40 (A) top to bottom.

Experiments AD050R05, AD050R10, AD050R20 and AD050R40: 5, 10, 20 and 40 A discharge rate. All 50 Ahr depth followed by 0.5 hr rest and 20 A charge.

Figure 7.51: AD050R05–R40 Cell Discharge Voltage.

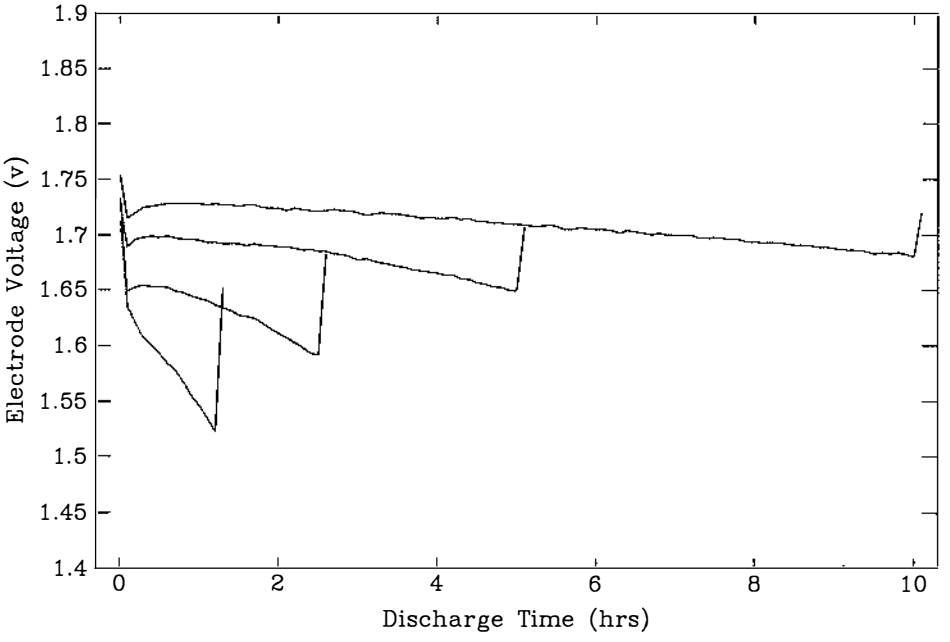

Discharge rates: 5 to 40 (A) top to bottom.

Experiments AD050R05, AD050R10, AD050R20 and AD050R40: 5, 10, 20 and 40 A discharge rate. All 50 Ahr depth followed by 0.5 hr rest and 20 A charge.

Figure 7.52: AD050R05–R40 Electrode Discharge Voltage.

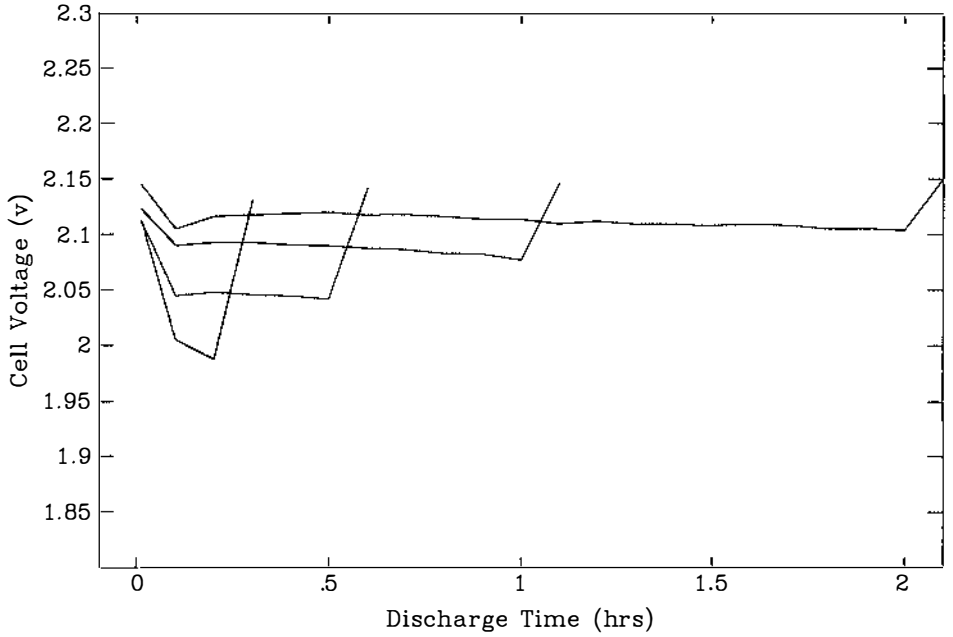

Discharge rates: 5 to 40 (A) top to bottom.

Experiments AD010R05, AD010R10, AD010R20 and AD010R40: 5, 10, 20 and 40 A discharge rate. All 10 Ahr depth followed by 0.5 hr rest and 20 A charge.

Figure 7.53: AD010R05–R40 Cell Discharge Voltage.

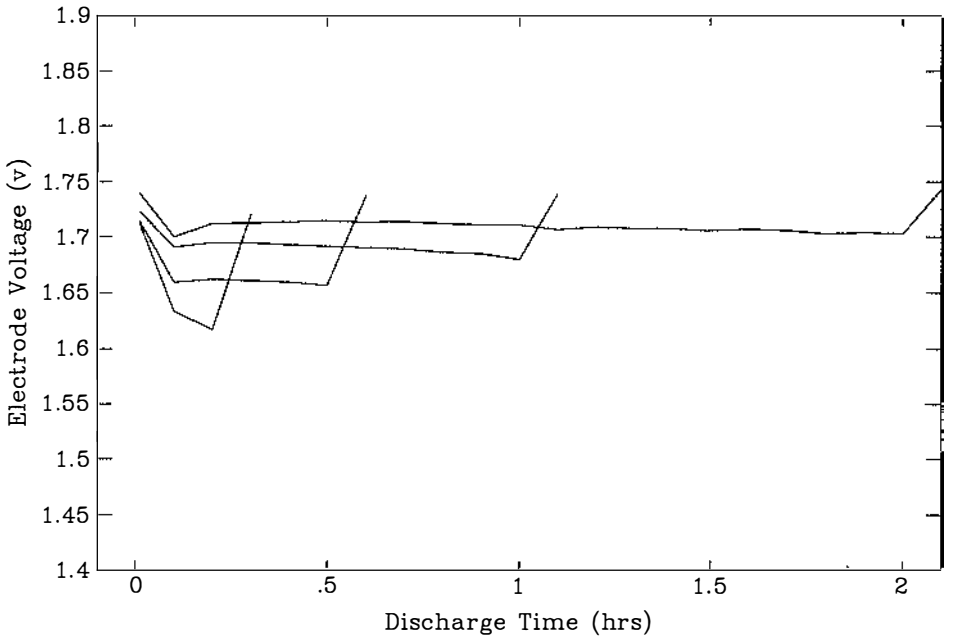

Discharge rates: 5 to 40 (A) top to bottom.

Experiments AD010R05, AD010R10, AD010R20 and AD010R40: 5, 10, 20 and 40 A discharge rate. All 10 Ahr depth followed by 0.5 hr rest and 20 A charge.

Figure 7.54: AD010R05–R40 Electrode Discharge Voltage.

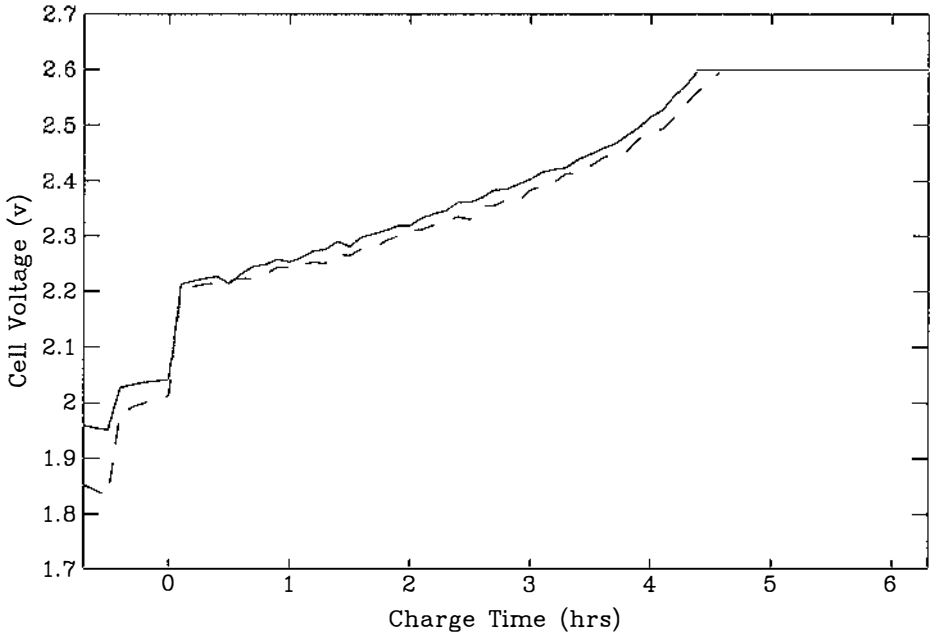

Solid: 10 A discharge rate (AD100R10).
Dash: 20 A discharge rate (AD100R20).

Both cases 100 Ahr depth followed by 0.5 hr rest and 20 A charge.

Figure 7.55: AD100R10–R20 Cell Rest and Charge Voltage.

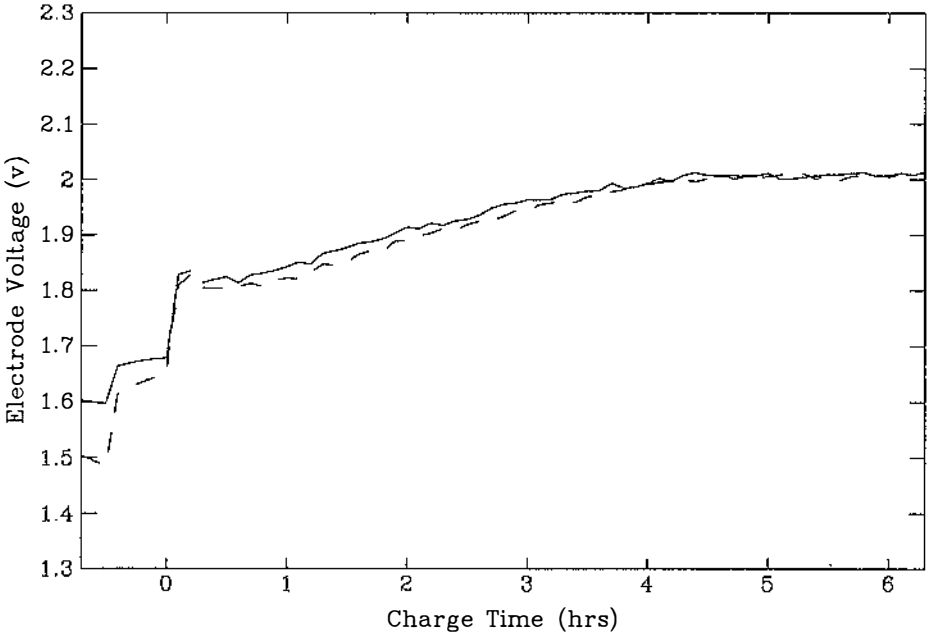

Solid: 10 A discharge rate (AD100R10).
Dash: 20 A discharge rate (AD100R20).

Both cases 100 Ahr depth followed by 0.5 hr rest and 20 A charge.

Figure 7.56: AD100R10–R20 Electrode Rest and Charge Voltage.

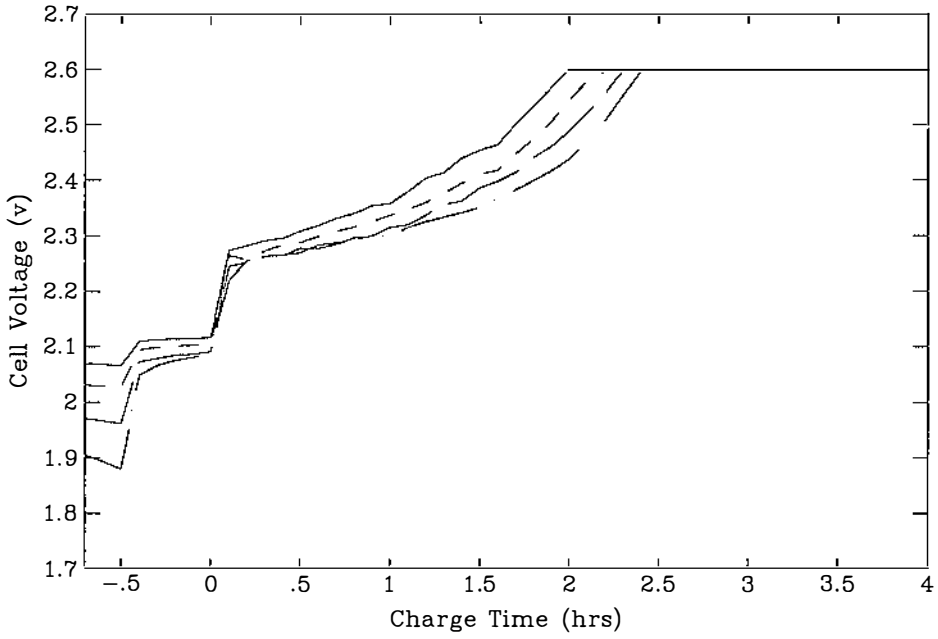

Solid: 5 A discharge rate (AD050R05).
Small dash: 10 A discharge rate (AD050R10).
Large dash: 20 A discharge rate (AD050R20).
Dash dot: 40 A discharge rate (AD050R40).

All cases 50 Ahr depth followed by 0.5 hr rest and 20 A charge.

Figure 7.57: AD050R05–R40 Cell Rest and Charge Voltage.

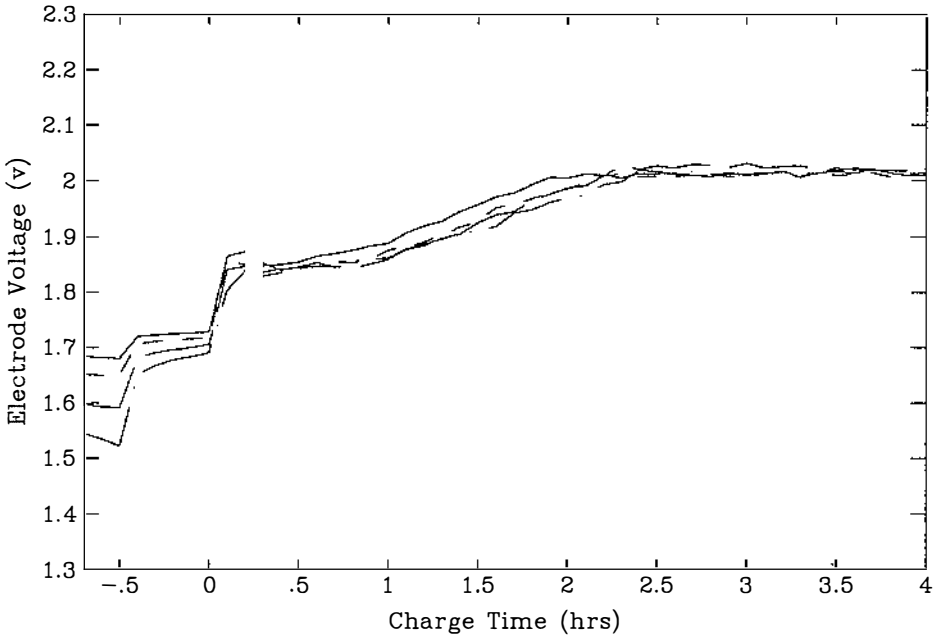

Solid: 5 A discharge rate (AD050R05).
Small dash: 10 A discharge rate (AD050R10).
Large dash: 20 A discharge rate (AD050R20).
Dash dot: 40 A discharge rate (AD050R40).

All cases 50 Ahr depth followed by 0.5 hr rest and 20 A charge.

Figure 7.58: AD050R05–R40 Electrode Rest and Charge Voltage.

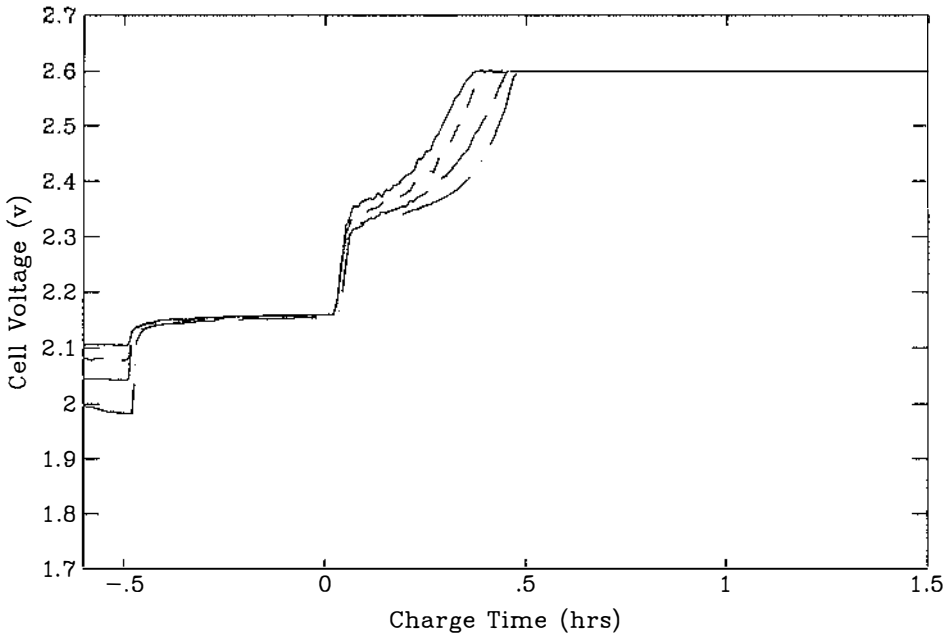

Solid: 5 A discharge rate (AD010R05).
Small dash: 10 A discharge rate (AD010R10).
Large dash: 20 A discharge rate (AD010R20).
Dash dot: 40 A discharge rate (AD010R40).

All cases 10 Ahr depth followed by 0.5 hr rest and 20 A charge.

Figure 7.59: AD010R05–R40 Cell Rest and Charge Voltage.

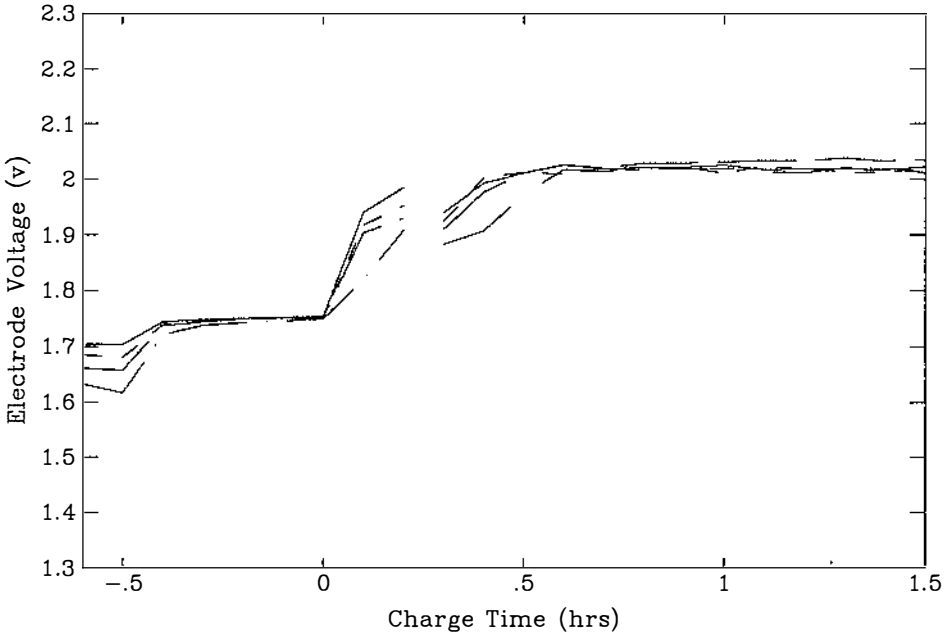

Solid: 5 A discharge rate (AD010R05).
Small dash: 10 A discharge rate (AD010R10).
Large dash: 20 A discharge rate (AD010R20).
Dash dot: 40 A discharge rate (AD010R40).

All cases 10 Ahr depth followed by 0.5 hr rest and 20 A charge.

Figure 7.60: AD010R05–R40 Electrode Rest and Charge Voltage.

preparatory charge. The history of the experiments reported here can be obtained from the experiment order given in table 6.2.

b) Charge cell voltage.

The charge cell voltage and estimated positive plate voltage are given in figures 7.55 to 7.60. These are arranged as for the discharge results above. In addition, the results have been aligned to have a charge start time of zero and the long constant voltage charge portion has been truncated. This allows differences in charge characteristics for each discharge depth to be readily seen.

The different discharge depths are naturally the main charge time determining factors. The discharge rates do, however, play a significant role in the time taken to reach the constant voltage limit. Differences of approximately half an hour can be seen in the case of the 50 Ampere hour discharge (figure 7.57). Greater time variations could be anticipated for the 100 Ampere hour discharge case had it been tested over the same range of discharge rates.

c) Estimated positive electrode voltage.

The estimated positive electrode voltage follows the corresponding cell voltage in the same way as for the standard case above.

7.4.5 Experimental Results: a Discussion.

As already mentioned, the experimental results generally agree with known forms. However, several features deserve further comment.

The variations in discharge voltage drop with past discharge/charge history are not likely to be a

consequence of solution potential drop or electrode equilibrium potential. These effects are controlled by the acid concentration which is at a known constant value at the beginning of the discharge. By elimination this means the variations are due to changes in cathodic exchange currents. This may be the result of a change in surface structure or reactivity. This effect adds to the uncertainty of the exchange current/overpotential relationship.

Results showing variations of charge characteristics for charge depths and rates are significant. They illustrate the difficulties involved in determining charge time from instantaneous voltage and current values. For example, if a voltage operated time-out termination scheme is used for the 50 Ampere hour case, unnecessary over or under charge of up to half an hour is possible. This points to the need for suitable models and model results to provide a basis for improved charge performance.

The gassing that occurred during moderate or higher discharge rates is of interest. This performance enhancing effect warrants further study. Such studies are lacking in the literature.

The generation of data for the positive electrode voltage estimates is an important result in the context of this work. This is used to test the VIAM model results in the following section.

7.5 COMPARING VIAM MODEL AND EXPERIMENTAL RESULTS.

7.5.1 Acid Diffusion and Exchange Currents for the VIAM Model.

a) Effective acid diffusion coefficients.

In section 7.3 it was noted that solution convection in the reservoir would give an effective acid diffusion coefficient considerably higher than the value for immobile electrolyte. This would be increased even further by the presence of gassing during discharge (let alone the gassing during charge) as observed in some of the experimental cases in section 7.4. In fact the gassing would aid acid transport within the plates themselves. This provides an argument for a high effective diffusion coefficient for these parts also. In the VIAM model implementation used for comparison with the experimental results, only the reservoir diffusion coefficient was altered. The value used was chosen to give a discharge capacity at the 5 hour rate of 110 Ampere hours. This is approximately the same as the capacity of the cell under test. The model attained the 110 Ampere hour capacity when the ratio of the effective to immobile diffusion coefficient was forty.

b) Exchange currents.

The inaccuracy introduced through the VIAM model using a single exchange current/overpotential relationship for both the cathodic and anodic reactions has been discussed in section 7.3.2. One approach to reduce the errors involved was to define new parameters for high current cases. The uncertainty of the anodic and cathodic current densities has already been discussed in section 7.3. In addition the experimental results suggest that the cathodic exchange current in particular is sensitive to such things as idle time and nature of the previous cycle. Together these factors indicate that the exchange current parameters

should be determined for each different discharge cycle. In the model results that follow, this was not done. Rather the same reaction orders were used as before (Hampson *et al* (1967)) and the reaction rate constants adjusted to give model results that compared well with the 100 Ampere hour/ 20 Ampere discharge case of the experimental results. The adjustment was performed by trial and error. The reaction rate constants found in this way were used for all other discharge cases. These are given in appendix 3.

7.5.2 The VIAM Model and Experimental Results.

The VIAM model results for the ten experimental cases are given in figures 7.61 to 7.70. Superimposed on these same figures are the corresponding experimental estimations for the positive electrode voltage. The trends seen when comparing the model and experimental results are similar in all ten cases. These are described for the various stages of the discharge/charge cycle below. The discharge/charge cycle stages are the same as in section 7.3.

a) The initial discharge voltage.

In the initial discharge stage the model predicts a voltage which is somewhat higher than the experimental voltage. The difference is in the order of 0.050 volts and is seen in all cases. This same trend was noted when comparing the VIAM model results with experimental results of Sunu and Burrows (1981) in section 7.3.4. As in that instance, the difference can be attributed to the inaccuracies introduced by the VIAM model using a single exchange current/overpotential relationship for the discharge.

b) The intermediate discharge voltage.

The discharge time for the 100 and 50 Ampere hour cases (figures 7.61 to 7.66) are long enough to exhibit an

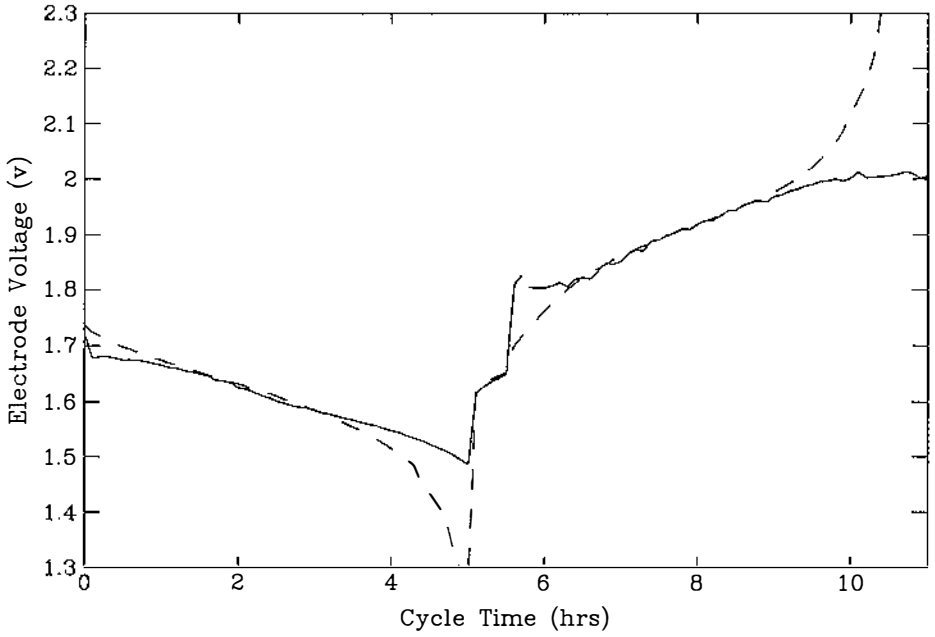

Solid: Experimental results.
Dash: VIAM model results.

Cycle: 100 Ahr/20 A discharge, 0.5 hr rest and 20 A charge.

Figure 7.61: VIAM Model and AD100R20 Electrode Voltage.

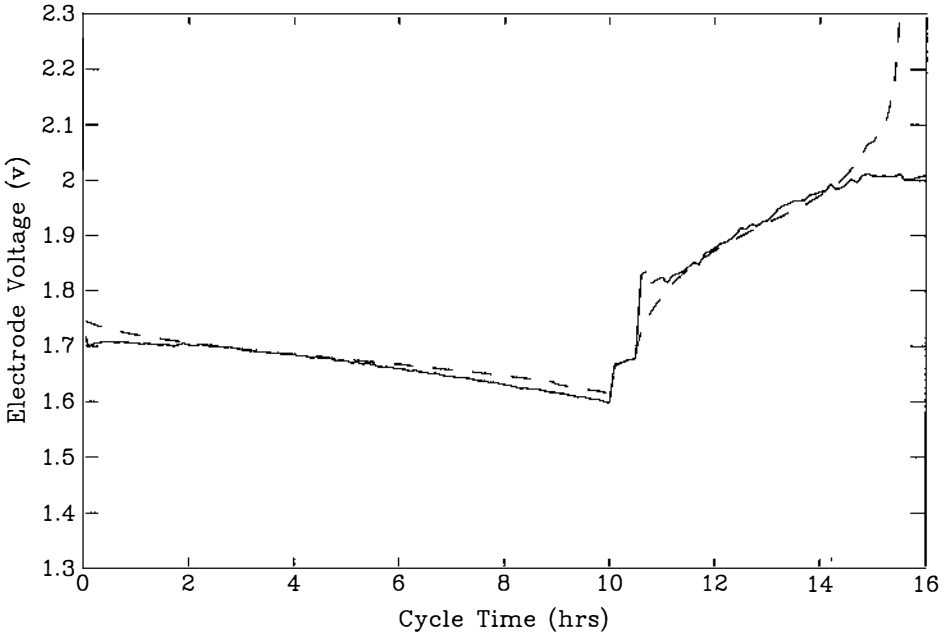

Solid: Experimental results.
Dash: VIAM model results.

Cycle: 100 Ahr/10 A discharge, 0.5 hr rest and 20 A charge.

Figure 7.62: VIAM Model and AD100R10 Electrode Voltage.

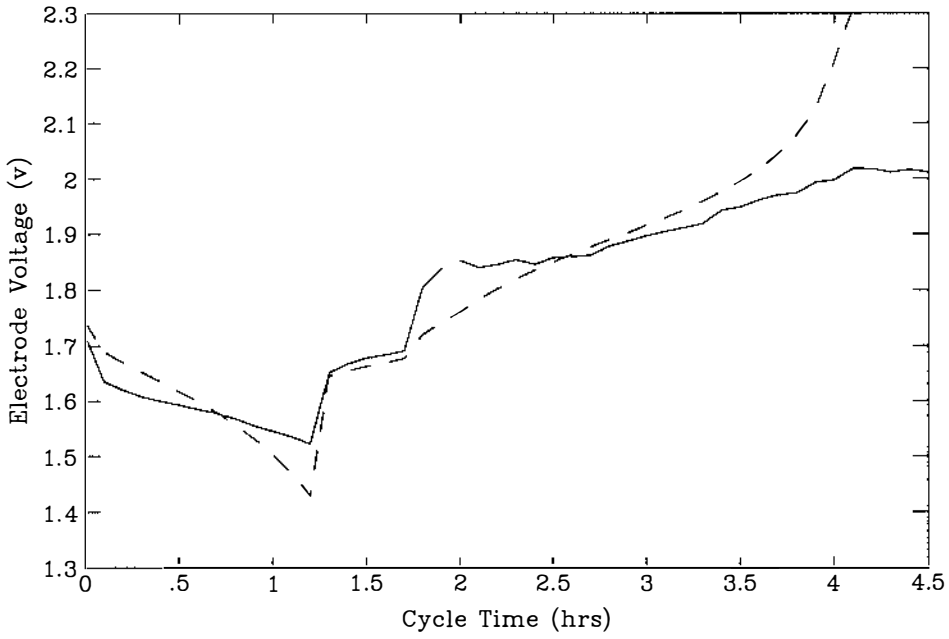

Solid: Experimental results.
Dash: VIAM model results.

Cycle: 50 Ahr/40 A discharge, 0.5 hr rest and 20 A charge.

Figure 7.63: VIAM Model and AD050R40 Electrode Voltage.

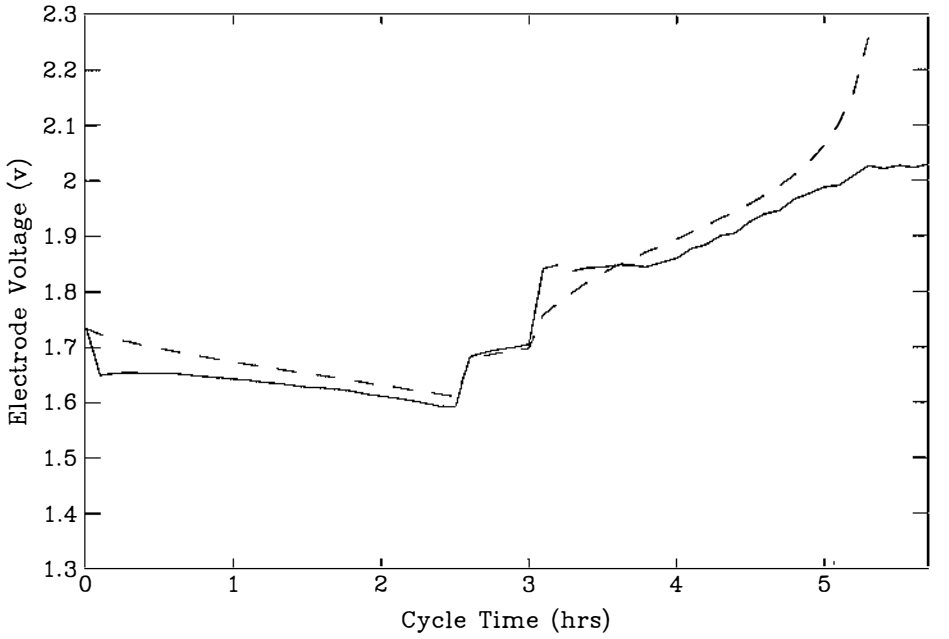

Solid: Experimental results.
Dash: VIAM model results.

Cycle: 50 Ahr/20 A discharge, 0.5 hr rest and 20 A charge.

Figure 7.64: VIAM Model and AD050R20 Electrode Voltage.

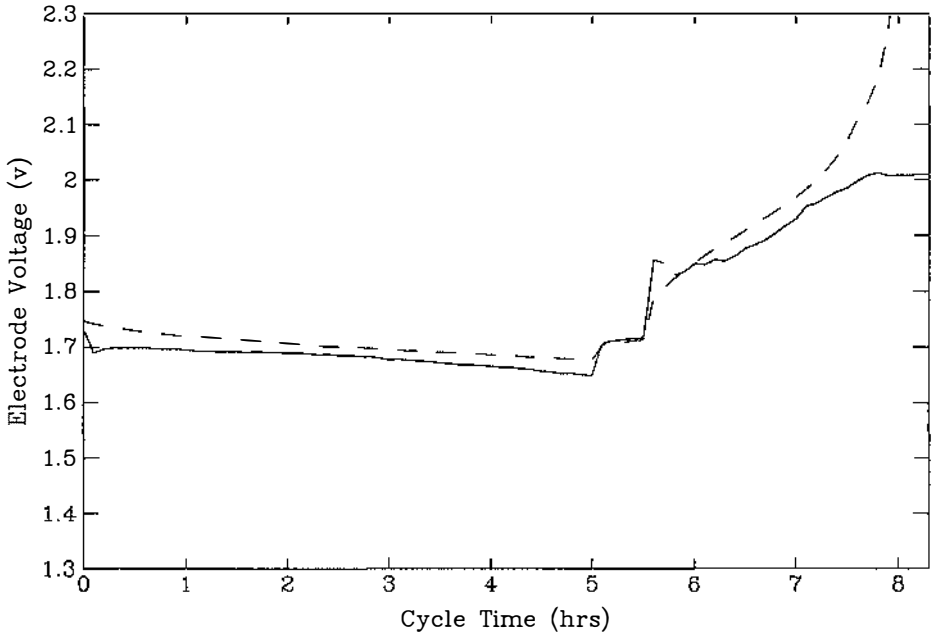

Solid: Experimental results.
Dash: VIAM model results.

Cycle: 50 Ahr/10 A discharge, 0.5 hr rest and 20 A charge.

Figure 7.65: VIAM Model and AD050R10 Electrode Voltage.

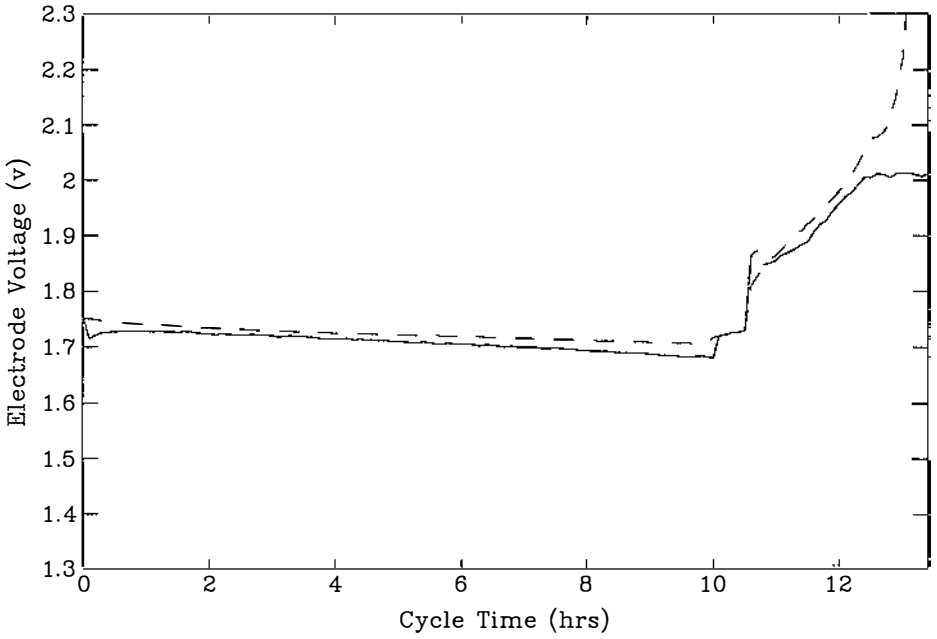

Solid: Experimental results.
Dash: VIAM model results.

Cycle: 50 Ahr/5 A discharge, 0.5 hr rest and 20 A charge.

Figure 7.66: VIAM Model and AD050R05 Electrode Voltage.

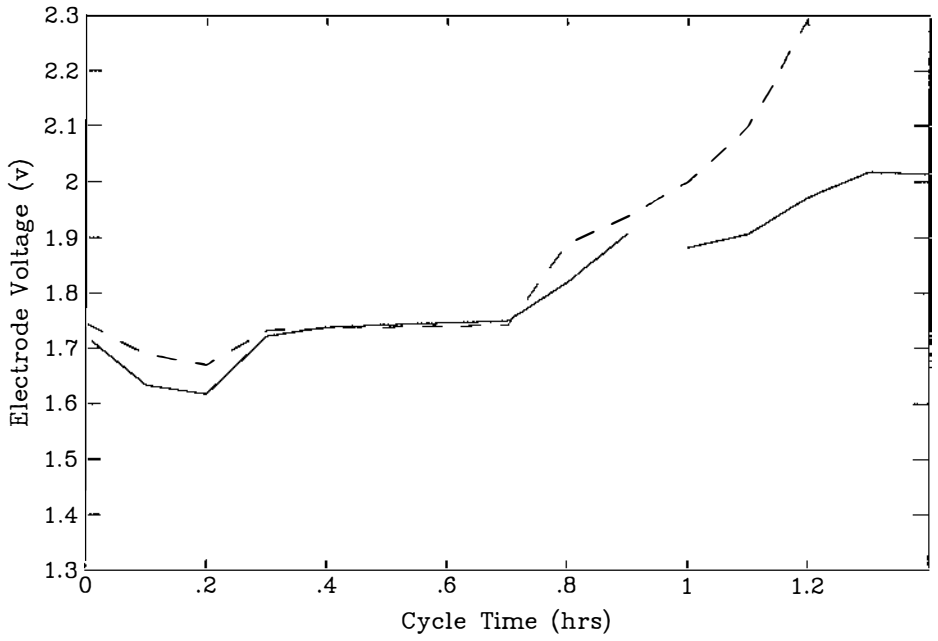

Solid: Experimental results.
Dash: VIAM model results.

Cycle: 10 Ahr/40 A discharge, 0.5 hr rest and 20 A charge.

Figure 7.67: VIAM Model and AD010R40 Electrode Voltage.

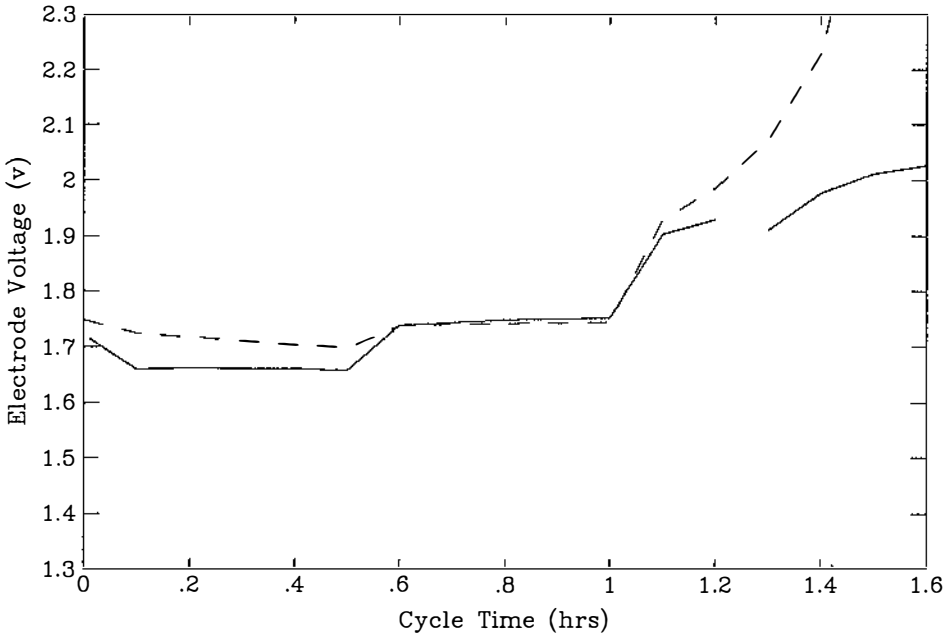

Solid: Experimental results.
Dash: VIAM model results.

Cycle: 10 Ahr/20 A discharge, 0.5 hr rest and 20 A charge.

Figure 7.68: VIAM Model and AD010R20 Electrode Voltage.

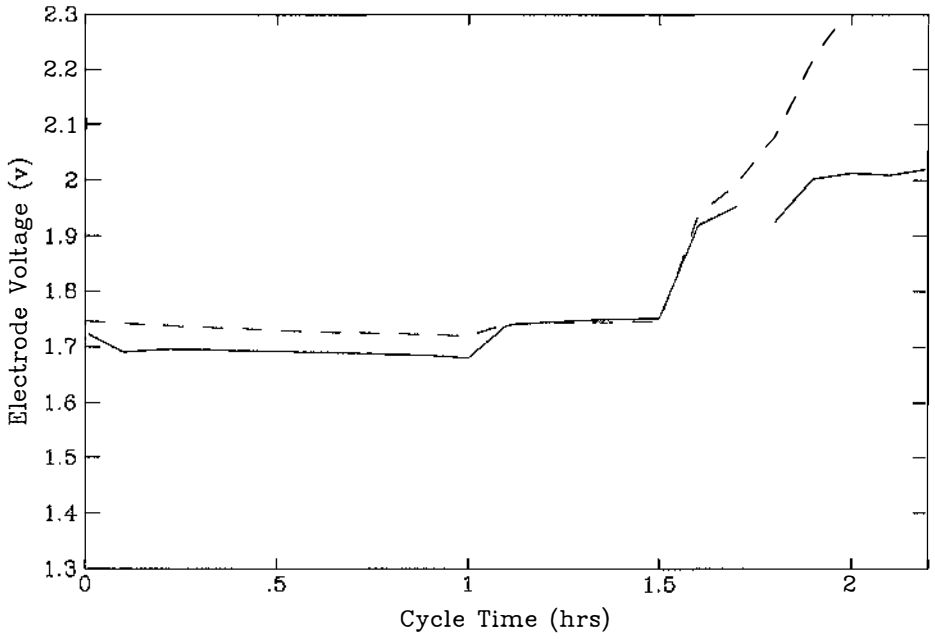

Solid: Experimental results.
Dash: VIAM model results.

Cycle: 10 Ahr/10 A discharge, 0.5 hr rest and 20 A charge.

Figure 7.69: VIAM Model and AD010R10 Electrode Voltage.

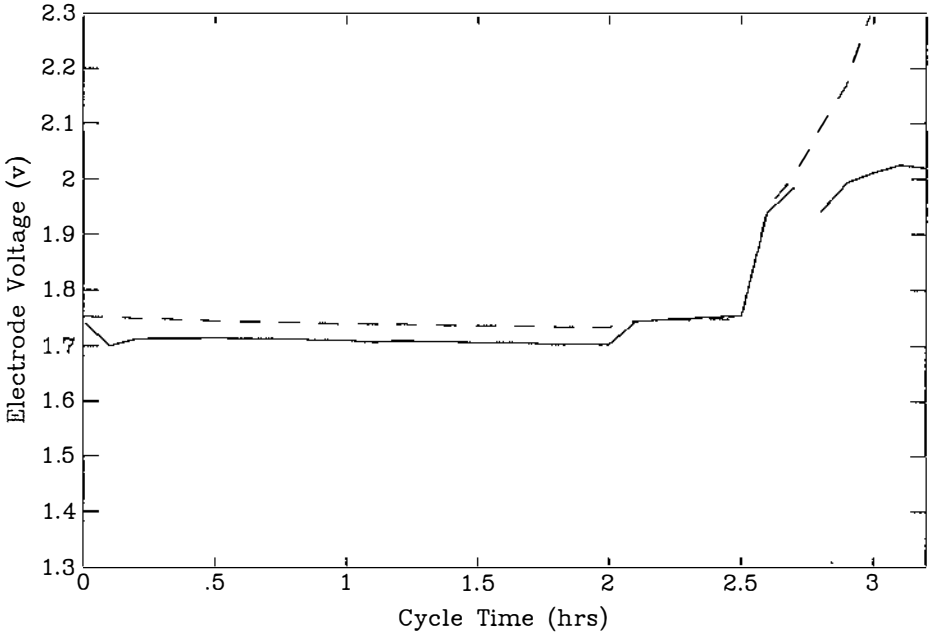

Solid: Experimental results.
Dash: VIAM model results.

Cycle: 10 Ahr/5 A discharge, 0.5 hr rest and 20 A charge.

Figure 7.70: VIAM Model and AD010R05 Electrode Voltage.

intermediate discharge stage. The model and experimental results generally have the same form and close to the same value for this stage of the discharge. The exceptions are the 50 Ampere hour/40 Ampere and 50 Ampere hour/20 Ampere discharge cases (figure 7.63 and 7.64). Again the single exchange current form of the VIAM model does not properly represent the high current discharge of the 50 Ampere hour/40 Ampere case. The 50 Ampere hour/20 Ampere case involves depressed experimental voltage values. This situation has been discussed in section 7.4.4.

c) The final discharge voltage.

Only the 100 Ampere hour/20 Ampere case (figure 7.61) reaches the final discharge stage. The predicted value is far lower than the experimental value. The high experimental value has been attributed to the effect of gassing during discharge (section 7.4.3). The model does not account for gassing effects.

d) The open circuit rest voltage.

In all cases the model and experimental results show excellent agreement for the rest stage. It is of interest that during the rest stage overpotential effects that have been a major factor in the differences in the model and experimental results are negligible.

e) The initial charge voltage.

Following a 100 or 50 Ampere hour discharge (figures 7.61 to 7.66) the model predicts a voltage that is considerably lower than the experimental estimate. This may in part be attributed to an elevated experimental estimate. The errors associated with the solution resistance and negative plate and reference electrode equilibrium potentials used for the experimental estimate (see section 7.4.1) are all greatest at this stage of a medium to deep discharge/charge cycle. It is unlikely that the large

difference in voltage is due to the experimental estimate alone. Two other effects that relate to the VIAM model are also likely to be significant contributors. The first effect is again the result of the VIAM model using a single form for the exchange current/overpotential relationship. If both a low and a high overpotential form were used the large initial overpotential could be modelled more accurately. The second effect is that of PbO_2 encapsulation (see section 7.1.6 and 7.3.4). This effect would be more marked in the medium and deep discharge cases. The model in its present form does not account for PbO_2 encapsulation. The VIAM model and experimental results are in better agreement in the initial stage of the 10 Ampere hour discharge cases. With the shallow discharge, the experimental estimation errors and PbO_2 encapsulation effects are less significant.

f) The intermediate charge voltage.

The charge time for the 100 and 50 Ampere hour cases are long enough to exhibit an intermediate charge stage. The model and experimental results have close to the same form and value for this stage of the charge.

g) The final charge voltage.

For the final stage of the charge the voltages predicted by the model rise rapidly while those obtained experimentally level out. The reason for the difference here is that the model does not account for gassing. The model assumes the full constant current charge until the voltage reaches the constant voltage limit. In fact an increasing proportion of the current is diverted into the gassing reaction at this stage of the charge. If the current used for the model was discounted for gassing, the voltage would not exhibit the same rapid rise as seen here.

Chapter 8
Conclusion

8.1. THE CONTRIBUTION OF THIS WORK.

8.1.1. A New Positive Electrode Model.

A detailed model for the positive electrode of the lead-acid cell has been developed in this thesis. This is the VIAM model which connects voltage, current and AM distributions within the electrode. The model represents a practical cell under likely discharge and charge conditions. The VIAM model is, itself, made up of four underlying models. These are the elemental discharge capacity model, the elemental discharge surface area model, the elemental charge surface area model and the aggregate model. The underlying models were developed from detailed experimental descriptions of cell components. This approach was taken to obtain an accurate electrode description useful in analysing and improving practical lead-acid cells and systems.

The VIAM model differs from previous porous electrode models (discussed in section 3.6) in the following respects.

i) The model is based on recent experimental studies showing microstructure and macrostructure in the positive AM (section 3.2 and chapter 5).

ii) The model accounts for non-participating AM that has recently been shown to extend from the plate surface inward and increase with cell cycling (section 3.2 and chapter 5).

iii) Discharge capacity, discharge surface area and charge surface area are defined from descriptions of the AM using elemental models (section 3.2 and chapter 4).

iv) The model incorporates the effect of acid transport in all cell components (chapter 5).

v) The model can be applied to discharge, rest and charge situations (chapter 7).

vi) The model can be applied over a wide range of discharge and charge currents (chapter 7).

8.1.2. Model Performance.

The results and performance obtained for the underlying models and the VIAM model are summarised below.

a) The elemental models.

Results for the elemental discharge capacity model were evaluated against typical cell capacity and AM distribution data. The results obtained were realistic (see section 7.1.2).

The elemental discharge surface area model was not fully developed. The formulations for the present implementation give a first approximation to the surface

area variation with discharge (see section 7.1.4).

The results for the elemental charge surface area model showed little variation with acid concentration or geometric parameters and were accurately represented as a function of charge state and current only. The results were in agreement with experimental studies at all but very deep discharge conditions. At deep discharge the effect of surface area masking due to PbO_2 encapsulation by $PbSO_4$ may be a factor. The model in its present form does not account for this (see section 7.1.6).

b) The aggregate model.

The dimensions of the aggregate model were compared with experimental studies of the AM structure. The dimensions were realistic although biased towards the larger AM features they represent (see section 7.2).

c) The VIAM model.

The VIAM model was used to simulate several different deep discharge/charge cycles. The results obtained agreed closely with experimental observations (see section 7.3). The results included electrode capacity, electrode voltage/time characteristics and AM distribution within the electrode. Additional results including potential, current and acid concentration distributions within the electrode could not be substantiated since suitable experimental data is not available.

The critical role of the exchange current/ overpotential relationship was identified. The use of a low and high overpotential relationship was discussed as an alternative to the single relationship used in the present implementation of the VIAM model. The need to account for gassing as it influences acid transport and charge current was identified.

d) The experimental results.

Experimental results for cell voltage were given for ten different discharge/charge cycles. In addition, gassing and cell concentration results were given for a standard case. In general, results were consistent with well known forms (see section 7.4). Minor exceptions were attributed to gassing during discharge and the effect the discharge/charge history of the cell. Estimates for the positive plate voltage were given to use in evaluating the VIAM model results.

e) The VIAM model and experimental results.

The VIAM model results and experimental estimates gave the same form and similar quantitative values over the wide range of conditions involved (see section 7.5). Agreement for the intermediate stage of the discharge and charge was close. Differences at other stages of the discharge/charge cycle were most likely due to two effects not accounted for in the model. These are the low and high overpotential exchange reactions for both the discharge and charge directions and the cell gassing. Both these effects could be incorporated into a future implementation of the VIAM model.

In the main, the model and experimental results were in close agreement. The exceptions noted above highlight areas for further development. These are discussed in section 8.2 below.

8.1.3. Model Application.

In presenting the background for this thesis (chapter 2) a case was made for the use of models to accurately determine the state of the cell and suitable charging schemes. The model developed here can be used for this purpose. For example the model can be used to simulate the

effect of different discharge conditions on the charge characteristics. Similarly, it can be used to simulate the effect of different charge schemes on charge time.

The model also has important applications in the area of cell development. For example the effect of different AM structures and cell construction can be studied.

8.2. EXTENSIONS TO THE MODEL.

8.2.1. Exchange Reaction Representation.

The incorporation of low and high exchange current/overpotential relationships into the VIAM model (actually the underlying aggregate model) for both the cathodic and anodic directions is desirable (see section 7.3). This is a relatively minor change that could be achieved by replacing the single interface impedance component with two components in parallel (see figure 5.6). The component for the low overpotential could have a linear current/voltage relationship (constant resistance) and the component for the high overpotential an exponential current/overpotential relationship (Tafel relationship see section 3.3). This is in accord with experimental observations (see Hampson *et al* (1967,1968) for example).

8.2.2. Cell Gassing.

Cell gassing was responsible for the difference between the model and experimental results during the latter stages of charging. (see section 7.3 and 7.5). Accounting for this in the VIAM model is not a simple matter. Gas evolving electrodes have been studied to a limited extent (see section 3.5). However, a considerable amount of work remains to be done before the most

significant effects for a practical lead-acid cell are identified. These should include a local gassing rate model to account for current diverted into the gassing reaction, and a model for determining the effect of gas evolution on transport parameters in the various cell components.

8.2.3. A Two Dimensional Plate.

The VIAM model treats the cell plate as a one dimensional structure, that is, as having thickness only. This assumes that the plate characteristics are independent of plate height and width. Experimental studies have shown this to be an approximation (see Sunu and Burrows (1981) for example). The VIAM model could be modified to represent the cell (and plate) as a cylindrical symmetric system with axis of symmetry through the centre of a circular plate. The cell has already been considered in this way to define the reservoir component. Such a modification would improve the representation of acid distribution to the plates. The cost is additional computational effort since a complete radial segment would need to be represented. The computational effort could be offset by assuming the micropores have uniform current and acid distribution over their length (see section 7.3.3).

8.2.4. Cell Temperature.

The model and experimental work reported here all assume the cell is at constant temperature. In practice cell temperature may vary tens of degrees over a normal working cycle (see Tomantschger (1984) for example). This effects acid transport, equilibrium potentials and overpotentials. It would be desirable for the model to take account of this. A comprehensive model for temperature changes in a cell has been developed by Lee *et al* (1986). It would be possible to incorporate a model of this type into the VIAM model.

Appendix 1

The Elemental Charge Surface Area Model Program Listing

The elemental charge surface area model is set out in detail in section 4.3. A Pascal computer program was written to solve the formulations that define the model. A flow diagram of the program is given in figure 4.8. As far as is practicable, the variable names used in the program correspond to the names used in the text (see section 4.3). The complete program listing is given below.

```
program Elemental_Charge_Surface_Area_Model(input,output);


   const
{primary physical constants}
   Pi=3.1415927; F=9.648E4;
   VmPbO2=25.86E-6; VmPbSO4=48.92E-6; MmPbO2=239.19; k=VmPbO2/VmPbSO4;
{parameters for adopted AM}
   Mcell=1645;  {g mass of PbO2 in charged cell}
   Vu=0.050E-6;   {m3.g-1 equivalent volume of microstructure solution}
   SdPbO2=1.57;   {m2.g-1 equivalent full discharge PbO2 surface}
{derived AM parameters}
   VuTot=Vu+VmPbO2/MmPbO2;   {m3.g-1 total microstructure volume}
   qd=2*F*Vu/(VmPbSO4-VmPbO2);   {A.s.g-1 full discharge capacity}
   VdPbO2=VmPbO2/MmPbO2-qd*VmPbO2/(2*F);   {m3.g-1 full discharge PbO2 volume}
   VdPbSO4=VuTot-VdPbO2; {m3.g-1 full discharge PbSO4 volume}
{system discretisation constants}
   nR=500;   {number of steps in radius for charge}


   var
{system parameters}
   Icell,   {A cell current}
   nvo,   {initial number of lobes}
   fo,   {surface factor for discharged PbO2 particles}
   fv,   {lobe circumference factor}
   D0,   {m2.s-1 Pb2+ diffusion coeff}
   c0,   {mol.m-3 Pb2+ concentration}
{model dimensions and constants}
   Ro,   {radius for box width; initial radius for PbSO4/sphere}
   Nx,   {number of boxes per gram}
   Rx,   {radius for box height}
   R_Lim1,   {PbSO4 radius limit for top/bottom spherical cap}
   R_Lim2,   {PbSO4 radius limit for spherical cap segment on top/bottom edges}
   R_Lim3,   {PbSO4 radius limit for spherical cap segment on side edges}
   Vx0,   {initial volume of PbO2 in box}
   sSdPbO2,   {surface of PbO2 in box at full discharge}
   sSdPbSO4,   {surface of PbSO4 in box at full discharge}
   dR,   {increment in PbSO4 radius}
{model variables}
   R,   {PbSO4 radius in box}
   Vx,   {volume enclosed by PbSO4 in box}
   Ix,   {total current in box}
   sSPbSO4, sS1PbSO4,   {present and past PbSO4 surface area within box}
   sSPbO2,  {present total PbO2 surface area in box}
   sScPbO2, sSg1PbO2,   {completed and past growing PbO2 surface area in box}
   SPbSO4,   {equivalent PbSO2 surface area}
   SPbO2,   {equivalent PbO2 surface area}
   SEffct,   {effective PbO2 surface area}
```

```
   t, dt,   {time and time interval}
   Ke,   {reaction rate constant}
   q,   {equivalent charge}
   rv_Max,   {maximum lobe radius}
   svo   {initial lobe surface}
      : double;
   rv, sv, cv : array[0..nR] of double;
      {lobe radius, surface area and Pb2+ ion concentration}
   Mv : array[0..nR] of integer; {lobe max size switch}
   jR, jR1, jR2, Col1 : integer;
   key : char;


procedure Initialise;
   const Esc=chr(27);
   type String=varying[40] of char;
{get function}
   function Get_para(Prompt:String;Nominal:double):double;
   var
      Val : double;
      Strval : string;
   begin
   write(Prompt,' (nominal value =',Nominal:8:3,') > ');
   readln(Strval);
   if Strval='' then Val:=Nominal
         else ReadV(Strval,Val);
   writeln(Esc,'[1F',Prompt,' (nominal value =',Nominal:8:3,') >',Val:8:3);
   Get_Para:=Val;
   end;
{procedure initialise}
   begin
   writeln(Esc,'[H',Esc,'[J','CHARGE SURFACE AREA MODEL');
   writeln;
{get parameters}
   Icell:=Get_para('Cell current',100);
   fo:=Get_para('Sphere surface factor',1.2);
   nvo:=Get_para('Initial number of lobes',4);
   fv:=Get_para('Lobe surface factor',2);
   D0:=1.0E-9*Get_para('Pb2+ diffusion coeff (x10^-9)',0.216);
   c0:=1.0E-2*Get_para('Pb2+ concentration (x10^-2)',0.428);
{set model dimensions and constants}
   Ro:=3*fo*VdPbO2/SdPbO2; Nx:=3*VdPbO2/(4*pi*Ro**3); Rx:=VuTot/(8*Nx*sqr(Ro));
   R_Lim1:=Rx; R_Lim2:=sqrt(sqr(Rx)+sqr(Ro)); R_Lim3:=sqrt(2)*Ro;
   Vx0:=VdPbO2/Nx; sSdPbO2:=SdPbO2/Nx; sSdPbSO4:=sSdPbO2;
   dR:=(sqrt(2*sqr(Ro)+sqr(Rx))-Ro)/nR;
   rv_Max:=0.999*sqrt(sSdPbSO4/(Pi*nvo)); svo:=sSdPbSO4/nvo;
   Ix:=Icell/(Mcell*Nx);
   sSg1PbO2:=sSdPbO2; sS1PbSO4:=sSdPbO2; sScPbO2:=0;
   rv[0]:=rv_Max; sv[0]:=0; Mv[0]:=1;
   jR1:=0; jR2:=0; Col1:=0;
   qPt:=0; lPic:=1;
   Ke:=1; q:=0; t:=0;
   writeln;
   writeln('Ro = ',Ro:10);
   writeln('Rx = ',Rx:10);
   writeln('Nx = ',Nx:10);
   writeln;
   write('Press return to continue >');
   readln;
   end;


procedure Update_PbSO4_Structure;
   const
       ff=0.08501; fff=0.08650;
   var
      Aa1, Bb1, Alpha1, Aa2, Bb2, Alpha2, Sx : double;
{procedure Update_PbSO4_Structure}
   begin
   R:=Ro+jR2*dR;
{calculate volume enclosed by retreating PbSO4, Vx}
   Vx:=(4/3)*Pi*R*R*R;   {complete spherical volume}
   Vx:=Vx-4*(Pi/3)*sqr(R-Ro)*(2*R+Ro);  {less 4 side caps}
   if R>R_Lim1 then
      Vx:=Vx-2*(Pi/3)*sqr(R-Rx)*(2*R+Rx);   {less 2 top/bottom caps}
```

```
   if R>R_Lim2 then
      begin   {plus 8 cap segments at top and bottom edges}
      Aa1:=sqrt(sqr(R)-sqr(R_Lim2)); Bb1:=R-R_Lim2; Alpha1:=arctan(Aa1/R_Lim2);
      Vx:=Vx+8*(1-Alpha1*ff)*
         (2/3)*(Aa1*(3*sqr(R)-sqr(Aa1))+3*sqr(R)*Alpha1*(Bb1-R));
      end; {if R>R_Lim2}
   if R>R_Lim3 then
      begin   {plus 4 cap segments at side edges}
      Aa2:=sqrt(sqr(R)-sqr(R_Lim3)); Bb2:=R-R_Lim3; Alpha2:=arctan(Aa2/R_Lim3);
      Vx:=Vx+4*(1-Alpha2*ff)*
         (2/3)*(Aa2*(3*sqr(R)-sqr(Aa2))+3*sqr(R)*Alpha2*(Bb2-R));
      end; {if R>R_Lim3}
{calculate the PbSO4 surface area}
   Sx:=4*Pi*sqr(R);   {complete spherical surface area}
   Sx:=Sx-4*(2*Pi)*R*(R-Ro);   {less 4 side caps}
   if R>R_Lim1 then Sx:=Sx-2*(2*Pi)*R*(R-Rx);   {less 2 top/bottom caps}
   if R>R_Lim2 then Sx:=Sx+8*(1-Alpha1*fff)*
      4*R*(Alpha1*(Bb1-R)+Aa1);   {plus 8 cap segments at top and bottom edges}
   if R>R_Lim3 then Sx:=Sx+4*(1-Alpha2*fff)*
      4*R*(Alpha2*(Bb2-R)+Aa2);   {plus 4 cap segments at side edges}
{multiply by surface factor to get PbSO4 surface}
   sSPbSO4:=fo*Sx;
{gram equivalent PbSO4 surface}
   SPbSO4:=Nx*sSPbSO4;
end;


procedure Update_Time_and_Charge;
   var q1 : double;
   begin
{Calculate state of charge}
   q1:=q;
   q:=2*F*Nx*(Vx-Vx0)/VmPbSO4;
{calculate time}
   dt:=(q-q1)/(ICell/MCell); if dt<0 then dt:=0;
   t:=t+dt;
   end;


procedure Update_PbO2_Structure;
   var
   overX, overX1, SumCS, dCdR, dCdR1, ErrFac, rv1 : double;
   sv_Sum, sv_Carry, sSgPbO2, dsSPbSO4 : double;
   YOverX, ZOverX : array[0..nR] of double;
{procedure Update_PbO2_Structure}
   begin
{setup for lobe growth at new boundary R2}
   cv[jR2]:=1;
   sv[jR2]:=Pi*sqr(rv[jR2-1]);
   rv[jR2]:=0;
   Mv[jR2]:=1;
{setup for concentration distribution solution}
   {define constant factors}
   overX1:=svo-Pi*sqr(rv[jR2-1]);
   for jR:=jR2-1 downto jR1+1 do
      begin
      overX:=svo-Pi*sqr(rv[jR-1]); {if overX=0 then overX:=1.0E-6*svo;}
      YoverX[jR]:=(overX1-overX)/(dR*overX);
      ZoverX[jR]:=Mv[jR]*(Ke/(2*F*D0))*
        (fv*2*Pi*rv[jR]-Pi*(sqr(rv[jR])-sqr(rv[jR-1]))/dR)/overX;
      overX1:=overX;
      end; {for jR:=jR2-1..}
{iterate for concentration distribution with constant Ke}
   repeat
      {solve for concentration distribution with estimated Ke}
      {parameters at R2 boundary}
      dCdR1:=Ix/(2*F*D0*sSPbSO4*c0);
      SumCS:=sv[jR2]*Mv[jR2];
      {parameters inside the R2 to the R1 boundary}
      jR:=jR2-1;
      while jR>=jR1 do
         begin
         cv[jR]:=cv[jR+1]-dR*dCdR1;
         if cv[jR]<=0 then
            begin
            for jR:=jR downto jR1 do cv[jR]:=0;
            jR:=jR1-1;
```

```
            end
            else
               begin
               dCdR:=dCdR1+dR*(YoverX[jR]*dCdR1+ZoverX[jR]*cv[jR]);
               if dCdR<0 then dCdR:=0;
               SumCS:=SumCS+cv[jR]*sv[jR]*Mv[jR];
               dCdR1:=dCdR; jR:=jR-1;
               end; {if cv[jR]<=0}
         end; {while jR>=jR1..}
      {adjust Ke (potential) so PbSO4 dissolved equals PbO2 deposited}
      ErrFac:=(Ix-Ke*SumCS*sSPbSO4*c0/svo)/Ix;
      Ke:=Ke*(1+ErrFac);
      if Ke<1.0E-3 then Ke:=1.0E-3; if Ke>1.0E36 then Ke:=1.0E36;
   until (abs(ErrFac)<0.001)or(Ke=1.0E36);
{calculate surface of a single growing PbO2 lobe}
   sv_Sum:=jR1*fv*2*Pi*rv_Max*dR;   {max size part}
   for jR:=jR2 downto jR1 do sv_Sum:=sv_Sum+sv[jR];   {remaining part}
{multiply to get total surface for all growing PbO2 lobes}
   sSgPbO2:=sv_Sum*sSPbSO4/svo;
{calculate surface of PbO2 lobes passing out of the growing zone}
   dsSPbSO4:=sS1PbSO4-sSPbSO4;   {change in growing zone}
   if dsSPbSO4<0 then dsSPbSO4:=0;
   sScPbO2:=sScPbO2+dsSPbSO4*sSg1PbO2/sS1PbSO4;   {surface passing out}
   sS1PbSO4:=sSPbSO4; sSg1PbO2:=sSgPbO2;
{calculate total PbO2 surface in box}
   sSPbO2:=sScPbO2+sSgPbO2;
{equivalent PbO2 surface}
   SPbO2:=Nx*sSPbO2;
{effective PbO2 surface}
   SEffct:=(Icell/Mcell)/(Ke*c0);
{update PbO2 lobe structure}
   sv_Carry:=0;
   for jR:=jR1 to jR2 do
      begin
      rv[jR]:=sqrt(sv_Carry+(Mv[jR]*Ke*VmPbO2*c0*cv[jR]*sv[jR]*dt/(2*Pi*F*dR))
         +sqr(rv[jR]));
      if rv[jR]>rv_Max then
         begin
         sv_Carry:=sqr(rv[jR])-sqr(rv_Max);
         rv[jR]:=rv_Max; Mv[jR]:=0;
         end
         else sv_Carry:=0; {if rv[jR]>rv_Max}
      end; {for jR:=jR1 to jR2}
{move R1 boundary}
   while rv[jR1]>=rv_Max do jR1:=jR1+1;
{lobe surface area between R2 and R1}
   if jR1=0 then rv1:=sqrt(svo/Pi)
      else rv1:=rv[jR1-1];
   for jR:=jR2 downto jR1 do
      if jR=0 then sv[jR]:=fv*2*Pi*rv[jR]*dR+abs(Pi*sqr(rv[jR])-svo)
         else sv[jR]:=fv*2*Pi*rv[jR]*dR+Pi*abs(sqr(rv[jR])-sqr(rv[jR-1]));
   end;


procedure Display_Results;
   const Esc=chr(27); nCol=80; nRow=15;
   var Col, Row, Row1, jRow : integer;
{gotoxy}
   procedure GotoXY(X,Y:integer);
   begin
   write(Esc,'[',Y:1,';',X:1,'H');
   end;
{procedure Display_Results}
   begin
   if jR2=1 then {first calculation display headings}
      begin
      writeln(Esc,'[H',Esc,'[J','CHARGE SURFACE AREA MODEL');
      writeln;
      writeln('  State ','  SPbO2 ',' SPbSO4 ',' STotal ',' SEffct ');
      end;
   {status line}
   GotoXY(1,4);
   writeln(' ',q/qd:6:4,'  ',SPbO2:6:4,'  ',SPbSO4:6:4,'  ',
      (SPbO2+SPbSO4):6:4,'  ',SEffct:6:4);
   {lobe profile}
   if ((jR2-1) rem 10)=0 then
      begin
```

```
      jR:=1; Row1:=1; Col:=1;
      GotoXY(1,7); writeln(Esc,'[J');
      repeat
         Row:=round(nRow*rv[jR]/rv_Max);
         for jRow:=Row1 downto Row+1 do
            begin
            GotoXY(Col-1,jRow+7); writeln('*');
            end;
         GotoXY(Col,Row+7); writeln('*');
         Row1:=Row; Col:=Col+1;
         jR:=round((Col-1)*nR/nCol)+1;
      until jR>=jR2;
         for Col1:=Col1+1 to Col do
           begin
           gotoXY(Col1,6);
           if (Col1 Rem 4)=0 then write('+')
              else write('-');
           end;
        writeln; Col1:=Col;
      end;
   end;


begin
Initialise;
repeat
  jR2:=jR2+1;
  Update_PbSO4_Structure;
  Update_Time_and_Charge;
  UpDate_PbO2_Structure;
  Display_Results;
until (jR2>=round(0.95*nR))or(q/qd+0.0001>=1);
end.
```

Appendix 2

The Aggregate Model Program Listing

The aggregate model is set out in detail in chapter 5. A Pascal computer program was written to solve the formulations that define the model. A flow diagram of the complete program is given in figure 5.11. Flow diagrams of the electrical and transport solution parts of the program are given in Figures 5.7 and 5.10 respectively. As far as is practicable, the variable names used in the program correspond to the names used in the text (see chapter 5). The complete program listing is given below.

```
[inherit('sys$library:starlet')]
program Aggregate_model(input,output);


   const
{primary physical constants}
   pi=3.1415927; F=9.648E4; R=8.3143; T=298;
   VmPbSO4=48.92E-6; VmPbO2=25.86E-6; VmPb=18.27E-6; MmPbO2=239.19;
{measurements from N7 cell}
   Np=6; Sp=2.55E-3; Hp=218E-3; Wp=136E-3; Hg=21E-3; Wg=17E-3;  {positive plate}
   Ss=3.6E-3;   {separator}
   Sn=2.05E-3;   {negative plate}
   Sc=62E-3; Hc0=300E-3; Wc=152E-3;   {reservoir}
{Aggregate model parameters}
   rho_p=0.518;   {positive AM}
   Vm=0.066E-6; Sm=0.08; fm=1.2; theta_m={2.19}1.3; chi_m=0.99;   {m-channel}
   Vu=0.050E-6; Su=3.52; fu=2; theta_u={2.19}1.3;   {u-channel}
   theta_h=2.19;   {h-channel}
   theta_n=1.18;   {negative AM}
   rho_n=0.548;    {n-channel}
   c0=5.7E3; {initial acid concentration}
{system discretisation constants}
   jlu=5; jlm=20; jlh=3; jls=10; jln=10; jlr=10;
   jli=jlm+jlh+jls+jln; jlsrs=round((jls+1)/2);
   dt=36;
{aggregate model dimensions}
   am=4*pi*sqr(fm*Vm/Sm); llm=theta_m*chi_m*Sp;
      dxm=llm/jlm;   {m-channel dimensions}
   Nme=Vm/(am*theta_m*Sp);   {m-ch's/equivalent gram}
   Vutot=Vu+VmPbO2/MmPbO2;   {total u-structure volume/equivalent gram}
   Vmu=chi_m*Vu/Nme;   {u-channel volume/m-channel}
   ac=am*theta_m*(1+Vutot/Vm);   {core sample area}
   au0=4*pi*sqr(fu*Vu/Su); llu=theta_u*(sqrt(ac)-sqrt(am))/sqrt(pi);
      dxu=llu/jlu;   {u-channel dimensions}
   Num=Vmu/(au0*llu);   {u-ch's/m-ch'}
   Nug=Num*dxm/llm;   {u-ch's/group or u-ch's/m-ch' segment}
   Nma=(Hp-Hg)*(Wp-Wg)/(ac*Hp*Wp);   {m-ch's/plate area}
   ah=rho_p*ac/theta_h; llh=theta_h*(1-chi_m)*Sp;
      dxh=llh/jlh;   {h-channel dimensions}
   lls=Ss; dxs=lls/jls; as=1/Nma;   {s-channel dimensions}
   an0=rho_n*ac/theta_n; lln=theta_n*Sn;
```

```
      dxn=lln/jln;   {n-channel dimensions}
   Nmc=Np*Hp*Wp*Nma;   {m-ch's/cell}
   Vmr0=(Hc0*Wc*Sc-Hp*Wp*(6*Sp+6*Ss+8*Sn))/Nmc;   {r-channel volume}
   Rp=sqrt(Hp*Wp/pi); Rc=sqrt(Hc0*Wc/pi);   {plate and cell radii}
   llr=Rc-Rp/sqrt(2); dxr=llr/jlr; ar0=Vmr0/llr;   {r-channel dimensions}
   Ndue=Nme*Num*jlu;   {u-channel du segments/equivalent gram}
   q0=2*F*Vu/(VmPbSO4-VmPbO2);   {specific discharge capacity}
   Acid_Tot=c0*(6*rho_p*Sp*(Hp-Hg)*(Wp-Wg)+8*rho_n*Sn*Hp*Wp+
        6*Ss*Hp*Wp+Vmr0*Nmc);   {total acid volume in cell}
 {numerical limits}
   dUPbO2=5.0E-2;   {initial step used for tuning UPbO2}
   Im_jlm_Limit=0.01/Nmc;   {precision for tuning Im[jlm] (A)}
   Iu_jlu_Limit=0.0001/(Nmc*Num);  {precision for tuning Iu[jlu] (A)}
   X_Limit=1.0E-3;    {minimum value for AM (discharge) state}
   uReset_Cnt=30; uBest_Cnt=130; mBest_Cnt=150;  {count limits for tuning}
   R_Key=1; E_Key=2; D_Key=3; i0c_Key=4; i0a_Key=5; SLo_Key=6; SHi_Key=7;
      {keys for identifying lookup tables}
   i0a_Fact=30; i0c_Fact=0.0050;
      {factors for adjusting exchange current reaction constants}
   Dr_Mult=30;  {factor for adjusting the reservoir diffusion coefficient}
   Esc=chr(27);

   type $uword = [word] 0..65535;
        $quword = array[1..4] of $uword;
   var
{look-up tables}
   R_Tbl, E_Tbl, D_Tbl, i0c_Tbl, i0a_Tbl,
      SLo_Tbl, SHi_Tbl : array[1..100] of real;
{model variables}
   cr : array[0..jlr] of real;
   ar, vr_jlr : real;
   Lr, Mr : array[1..jlr-1] of real;
   cn : array[0..jln] of real;
   Lnn, Mn : array[1..jln-1] of real;
   On, an, vn_jln : real;
   cs : array[1..jls] of real;
   Ls, Ms : array[2..jls-1] of real;
   Ns, Os : real; {only non-zero at position jlsrs}
   ch : array[1..jlh] of real;
   Lh, Mh : array[2..jlh-1] of real;
   Rh, vh : real;
   Uh, Ih, Ih1 : double;
   cm : array[1..jlm+1] of real;
   Lm, Mm, Nm, Om : array[2..jlm] of real;
   Rm, axvmu : array[1..jlm] of real;
   Im, Um : array[0..jlm] of double; {0 position n-channel values}
   cu : array[1..jlu+1,1..jlm] of real;
   X : array[1..jlu,1..jlm] of real;
   dIu, dIu1 : array[1..jlu,1..jlm] of double;
   Lu, Mu, Ou : array[2..jlu,1..jlm] of real;
   k : integer;
   UPbO2 : double;
   Icell : real;
{misc variables}
   Data_Source, mTune_Cnt : integer;
   Ahrs, Acid_I_Sum : real;
   SwitchOff : boolean;
   mBest_Tot, uBest_Tot : integer;
   Data_File : text; Data_File_Name : varying[20] of char;
   Key_Mask, Key_Chn : $uword;
   Key_This_k : unsigned;




procedure Display_Dimensions;
   const
   qT=2*F/MmPbO2;
   qc=q0*(1-rho_p)*Np*(Hp-Hg)*(Wp-Wg)*Sp*MmPbO2/VmPbO2;
{procedure Display_Dimensions}
   begin
   writeln(Esc,'[H',Esc,'[J','AGGREGATE MODEL DIMENSIONS');
   writeln;
   writeln('Model geometry:');
   writeln('Channel':10,'Length':15,'Area':15);
```

```
   writeln('r-channel':10,' ':5,llr:10,' ':5,ar0:10,' (initial value)');
   writeln('n-channel':10,' ':5,lln:10,' ':5,an0:10,' (initial value)');
   writeln('s-channel':10,' ':5,lls:10,' ':5,as:10);
   writeln('h-channel':10,' ':5,llh:10,' ':5,ah:10);
   writeln('m-channel':10,' ':5,llm:10,' ':5,am:10);
   writeln('u-channel':10,' ':5,llu:10,' ':5,au0:10,' (initial value)');
   writeln;
   writeln('m-channels per gram: ',Nme:10);
   writeln('m-channels per cell: ',Nmc:10);
   writeln('u-channels per m-channel: ',Num:10);
   writeln('u-channels per m-channel segment: ',Nug:10);
   writeln;
   writeln('Specific capacity: ',q0:10,' (A.s/g)');
   writeln('Cell capacity: ',(qc/3600):10,' (Ahrs)');
   writeln('AM utilisation: ',(q0/qT):10);
   writeln;
   write('Press Return to continue > '); readln;
   end;



procedure Set_Operating_Mode;
   begin
   writeln(Esc,'[H',Esc,'[J','SET OPERATING MODE');
   writeln;
   writeln('Data source options: 0 - key board entry');
   writeln('                     1 - data file');
   write('Select data source > '); readln(Data_Source);
   if Data_Source=1 then
      begin
      writeln;
      write('Enter data file name >'); readln(Data_File_Name);
      open(Data_File,File_Name:=Data_File_Name,History:=readonly);
      reset(Data_File);
      end;
   writeln;
   writeln;
   write('Enter Initial Current to Start Simulation> '); readln(ICell);
   writeln(Esc,'[H',Esc,'[J','          MODEL OPERATING');
   end;



procedure Init_Operate;
   const
   Lr_K=dt/(2*sqr(dxr)); Ln_K=dt/(2*sqr(dxn)); Ls_K=dt/(2*sqr(dxs));
   Lh_K=dt/(2*sqr(dxh)); Lm_K=dt/(2*sqr(dxm)); Lu_K=dt/(2*sqr(dxu));
   var
   KeyS : unsigned;
   R_File, E_File, D_File, i0c_File, i0a_File, SLo_File, SHi_File : text;
   D0 : real;
   jr, jn, js, jh, jjm, ju, Tbl_Ptr : integer;
{procedure Init_Operate}
   begin
{initialise terminal channel for interactive keyboard operation}
   KeyS:=$assign('tt',Key_Chn);
   Key_Mask:=io$_readlblk+io$m_timed+io$m_nofiltr+io$m_noecho;
{read in lookup tables inherent functions}
   open(R_File,'[ross.lead_acid_tables]R_H2SO4_H2O.dat',readonly);
   open(E_File,'[ross.lead_acid_tables]E_PBO2_H2SO4.dat',readonly);
   open(D_File,'[ross.lead_acid_tables]D_H2SO4_H2O.dat',readonly);
   open(i0c_File,'[ross.lead_acid_tables]i0c_H2SO4_H2O.dat',readonly);
   open(i0a_File,'[ross.lead_acid_tables]i0a_H2SO4_H2O.dat',readonly);
   open(SLo_File,'[ross.elementry_models]I1C5_FIT.dat',readonly);
   open(SHi_File,'[ross.elementry_models]I10C5_FIT.dat',readonly);
   reset(R_File); reset(E_File); reset(D_File); reset(i0c_File);
      reset(i0a_File); reset(SLo_File); reset(SHi_File);
   for Tbl_Ptr:=1 to 100 do
      begin
      readln(R_File,R_Tbl[Tbl_Ptr]); readln(E_File,E_Tbl[Tbl_Ptr]);
      readln(D_File,D_Tbl[Tbl_Ptr]);
      readln(i0c_File,i0c_Tbl[Tbl_Ptr]); readln(i0a_File,i0a_Tbl[Tbl_Ptr]);
      i0c_Tbl[Tbl_Ptr]:=i0c_Fact*i0c_Tbl[Tbl_Ptr];
      i0a_Tbl[Tbl_Ptr]:=i0a_Fact*i0a_Tbl[Tbl_Ptr];
      readln(SLo_File,SLo_Tbl[Tbl_Ptr]); readln(SHi_File,SHi_Tbl[Tbl_Ptr]);
```

```
      end;
   close(R_File); close(E_File); close(D_File); close(i0c_File);
      close(i0a_File); close(SLo_File); close(SHi_File);
{initialise concentration and past effects}
   D0:=D_Tbl[round(c0/100)];
   cr[0]:=c0; cr[jlr]:=c0;
   for jr:=1 to jlr-1 do
      begin
      cr[jr]:=c0; Lr[jr]:=Lr_K*D0; Mr[jr]:=0;
      end;
   cn[0]:=c0; cn[jln]:=c0; On:=0;
   for jn:=1 to jln-1 do
      begin
      cn[jn]:=c0; Lnn[jn]:=Ln_K*D0; Mn[jn]:=0;
      end;
   cs[1]:=c0; cs[jls]:=c0; Ns:=0; Os:=0;
   for js:=2 to jls-1 do
      begin
      cs[js]:=c0; Ls[js]:=Ls_K*D0; Ms[js]:=0;
      end;
   ch[1]:=c0; ch[jlh]:=c0;
   for jh:=2 to jlh-1 do
      begin
      ch[jh]:=c0; Lh[jh]:=Lh_K*D0; Mh[jh]:=0;
      end;
   cm[1]:=c0; cm[jlm+1]:=c0;
   for jjm:=2 to jlm do
      begin
      cm[jjm]:=c0; Lm[jjm]:=Lm_K*D0; Mm[jjm]:=0; Nm[jjm]:=0; Om[jjm]:=0;
      end;
   for jjm:=1 to jlm do
      begin
      cu[1,jjm]:=c0; dIu1[1,jjm]:=0; X[1,jjm]:=1; cu[jlu+1,jjm]:=c0;
      for ju:=2 to jlu do
         begin
         cu[ju,jjm]:=c0; dIu1[ju,jjm]:=0; X[ju,jjm]:=1;
         Lu[ju,jjm]:=Lu_K*D0; Mu[ju,jjm]:=0; Ou[ju,jjm]:=0;
         end;
      end;
   ar:=ar0; an:=an0;
{initialise misc variables}
   Acid_I_Sum:=0; Ih1:=0;
   Ahrs:=0;
   k:=0;
   SwitchOff:=false;
   mBest_Tot:=0; uBest_Tot:=0;
   end;




function Get_Key:unsigned;
{used to interrupt program to enter new variable value from keyboard}
var
   Key_Val : unsigned;
   Status : $quword;
   KeyS : unsigned;
begin
Key_Val:=0;
KeyS:=$qiow(,Key_Chn,Key_Mask,Status,,,%Ref Key_Val,1,0);
Get_Key:=Key_Val;
end;




function LookUp(Tbl_Key:integer;Index:real):real;
   var
      Base : real;
      Ptr1, Ptr2 : integer;
   begin
   if Tbl_Key<=5 then Base:=Index/100 {concentration dependent table}
      else Base:=Index*100; {charge state dependent table}
   if Base<1 then Base:=1; if Base>100 then Base:=100;
   Ptr1:=trunc(Base+0.01); Ptr2:=trunc(Base+1-0.01);
   case Tbl_Key of
```

```
      R_Key: LookUp:=R_Tbl[Ptr1]+(R_Tbl[Ptr2]-R_Tbl[Ptr1])*(Base-Ptr1);
      E_Key: LookUp:=E_Tbl[Ptr1]+(E_Tbl[Ptr2]-E_Tbl[Ptr1])*(Base-Ptr1);
      D_Key: LookUp:=D_Tbl[Ptr1]+(D_Tbl[Ptr2]-D_Tbl[Ptr1])*(Base-Ptr1);
      i0c_Key: LooKUp:=i0c_Tbl[Ptr1]+(i0c_Tbl[Ptr2]-i0c_Tbl[Ptr1])*(Base-Ptr1);
      i0a_Key: LookUp:=i0a_Tbl[Ptr1]+(i0a_Tbl[Ptr2]-i0a_Tbl[Ptr1])*(Base-Ptr1);
      SLo_Key: LookUp:=SLo_Tbl[Ptr1]+(SLo_Tbl[Ptr2]-SLo_Tbl[Ptr1])*(Base-Ptr1);
      SHi_Key: LookUp:=SHi_Tbl[Ptr1]+(SHi_Tbl[Ptr2]-SHi_Tbl[Ptr1])*(Base-Ptr1);
      end;
   end;



procedure Solve_mElectric;
{solve for the electrical characteristics of a m-channel/u-cnannel set}
   const
      alpha_c=9.0E-1; alpha_a=2.2E-1;
   var
      Eu, dRu, i0c, i0a, Sdis, SZr, SHi : array[1..jlu,1..jlm] of real;
      mTune_Sign, mTune_Sign1, jm, uBest_Acc : integer;
      mTune_Frac, Iu_0, UPbO2_Best, Im_Best  : double;
      dIu0 : array[1..jlu] of double;
      mStraddled, dE_Limit : boolean;


procedure Start_mElectric;
   begin
   writeln(Esc,'[H','E',Esc,'[H');
   mTune_Cnt:=0; mTune_Frac:=1;
   mStraddled:=false;
   dE_Limit:=false;
   Im_Best:=2; uBest_Acc:=0;
   end;


procedure Get_Icell;
   begin
   if Data_Source=1 then readln(Data_File,Icell);
   Ih:=dble(Icell/Nmc);
   end;


procedure Ri_dRu_Eu_i0c_i0a_Sdis_SZr_SHi;
   var
      Fact : real;
      jh, jjm, ju : integer;
{discharge surface area function}
   function Sdis_Fun(X:real):real;
   {discharge surface area at dxu; based on elemental model}
   const
      SfPbO2=3.60; SdPbO2=1.57; {m2.g-1}
      Sfdis=SfPbO2/Ndue; Sddis=SdPbO2/Ndue;
   begin
   Sdis_Fun:=Sfdis-(1-X)*(Sfdis-Sddis);
   end;
{procedure Ri_dRu_i0c_i0a_Sdis_SZr_SHi}
   begin
{h_channel resistance}
   Rh:=0;
   for jh:=1 to jlh do Rh:=Rh+LookUp(R_Key,ch[jh]);
   Rh:=llh*Rh/(ah*jlh);
{m_channel resistances}
   Fact:=llm/(am*jlm);
   for jjm:=1 to jlm do Rm[jjm]:=Fact*LookUp(R_Key,cm[jjm]);
{u_channel resistances}
   Fact:=llu/(jlu*au0);
   for jjm:=1 to jlm do
      for ju:=1 to jlu do
         begin
         dRu[ju,jjm]:=Fact*LookUp(R_Key,cu[ju,jjm])/X[ju,jjm];
         Eu[ju,jjm]:=LookUp(E_Key,cu[ju,jjm]);
         i0c[ju,jjm]:=LookUp(i0c_Key,cu[ju,jjm]);
         i0a[ju,jjm]:=LookUp(i0a_Key,cu[ju,jjm]);
         Sdis[ju,jjm]:=Sdis_Fun(X[ju,jjm]);
         SHi[ju,jjm]:=LookUp(SHi_Key,X[ju,jjm])/Ndue;
         SZr[ju,jjm]:=(10/9)*LookUp(SLo_Key,X[ju,jjm])/Ndue-(1/9)*SHi[ju,jjm];
         end;
   end;
```

```
procedure Calc_Uh;
   var jjm : integer;
   begin
   Uh:=-Ih*dble(Rh);
   Um[0]:=Uh; Im[0]:=Ih;
   jjm:=1;
   while (dIu[1,jjm]=0)and(jjm<jlm) do jjm:=jjm+1;
   if (jjm=jlm)and(dIu[1,jlm]=0) then jjm:=1;
   UPbO2:=dble(Eu[1,jjm])+Uh-(jjm+4)*Ih*dble(Rm[1]);
   end;

procedure Calc_Um;
   begin
   Um[jm]:=Um[jm-1]-Im[jm-1]*dble(Rm[jm]);
   end;


procedure Solve_uElectric;
{solve for the electrical characteristics of one u-channel}
   const
      Ecoeff_c=Alpha_c*F/(R*T); Ecoeff_a=Alpha_a*F/(R*T);
      dZu_Fact_c=R*T/(Alpha_c*F); dZu_Fact_a=R*T/(Alpha_a*F);
   var
      Uu, Iu : array[0..jlu] of double;
      jju, ju, Off_Cnt : integer;
      Iu_00, Iu_01, Iu_10, Iu_11, uTune_Frac, Iu_Step, Iu_Best,
         Iu_0_Best : double;
      uTune_Sign, uTune_Sign1, uTune_Cnt, uStrad_Cnt : integer;
      uStraddled : boolean;

{Charge surface area function}
   function Schg(ju,jm:integer;dIu:double):double;
   {charge surface area elemental model, fitted results}
   const dIu_Fact=1600*Ndue/1000;   {1/dIu_Hi=Mcell*Ndue/Icell_Hi}
   var Ratio, Chg_Temp : double;
   begin
   Ratio:=dIu_Fact*dIu;
   if Ratio>1 then Ratio:=1;
   if Ratio<0 then Ratio:=0;
   Chg_Temp:=Ratio*dble(SHi[ju,jm])+(1-Ratio)*dble(SZr[ju,jm]);
   if Chg_Temp<0 then Chg_Temp:=0;
   SChg:=Chg_Temp;
   end;

   procedure Sub_Start_uElectric;
   const Prop=0.5/jlu;
   var dEu, dZu : double;
   begin
   uTune_Frac:=1; uStraddled:=false;
   dEu:=-(dble(Eu[1,jm])+Um[jm]-UPbO2);
   if dEu<=0 then dZu:=dZu_Fact_c/dble(Sdis[1,jm]*i0c[1,jm])   {discharge}
      else dZu:=dZu_Fact_a/dble(SZr[1,jm]*i0a[1,jm]);   {charge}
   Iu_0:=(dble(Eu[1,jm])+Um[jm]-UPbO2)/(dble(dRu[1,jm])+Prop*dZu);
   end;

   procedure Start_uElectric;
   begin
   Sub_Start_uElectric;
   Iu_Step:=abs(Iu_0)/2;
   Iu[0]:=Iu_0;  Uu[0]:=Um[jm]; Iu_Best:=1;
   uTune_Cnt:=0; uStrad_Cnt:=0; Off_Cnt:=0;
   end;

   procedure Calc_Uu;
   begin
   Uu[ju]:=Uu[ju-1]-Iu[ju-1]*dble(dRu[ju,jm]);
   end;

   procedure Calc_dIu;
   var
      dEu, dIu_Fact, dIu00 : double;
   begin
   dEu:=-(dble(Eu[ju,jm])+Uu[ju]-UPbO2);
   if dEu<=0 then
      {discharge}
      if X[ju,jm]=X_Limit then
```

```
      begin {discharge state limit}
      Off_Cnt:=Off_Cnt+1;
      dIu0[ju]:=0;
      end
      else
         begin
         dEu:=-dEu;
         if dEu>1 then
            begin
            dEu:=1; dE_limit:=true;
            end;
         dIu_Fact:=dble(Sdis[ju,jm]*i0c[ju,jm]);
         if dEu>Ecoeff_c then dIu0[ju]:=dIu_Fact*exp(Ecoeff_c*dEu)
            else dIu0[ju]:=dIu_Fact*exp(1)*Ecoeff_c*dEu;
         end
   else
      {charge}
      if X[ju,jm]=1 then
         begin {charge state limit}
         Off_Cnt:=Off_Cnt+1;
         dIu0[ju]:=0;
         end
         else
            begin
            if dEu>1 then
               begin
               dEu:=1; dE_Limit:=true;
               end;
            dIu_Fact:=SChg(ju,jm,0)*dble(i0a[ju,jm]);
            if dEu>Ecoeff_a then
               begin
               dIu00:=dIu_Fact*exp(Ecoeff_a*dEu);
               dIu_Fact:=SChg(ju,jm,dIu00)*dble(i0a[ju,jm]);
               dIu0[ju]:=-dIu_Fact*exp(Ecoeff_a*dEu);
               end
               else
                  begin
                  dIu00:=dIu_Fact*exp(1)*Ecoeff_a*dEu;
                  dIu_Fact:=SChg(ju,jm,dIu00)*dble(i0a[ju,jm]);
                  dIu0[ju]:=-dIu_Fact*exp(1)*Ecoeff_a*dEu;
                  end;
            end;
end;

procedure Calc_Iu;
begin
Iu[ju]:=Iu[ju-1]-dIu0[ju];
end;

function uTuned:boolean;
var Key : char;

procedure uBisect;
begin
if uStraddled then
   begin
   uTune_Frac:=0.501*uTune_Frac; uStrad_Cnt:=uStrad_Cnt+1;
   end;
Iu_0:=Iu_0+uTune_Frac*uTune_Sign*Iu_Step;
end;

procedure uNewton;
var dIu_1 : double;
begin
dIu_1:=Iu_10-Iu_11;
if dIu_1=0 then Iu_0:=Iu_00
   else Iu_0:=Iu_00-(Iu_00-Iu_01)*Iu_10/dIu_1;
uStrad_Cnt:=uStrad_Cnt+1;
end;

procedure uReset;
begin
Sub_Start_uElectric;
uStrad_Cnt:=uReset_Cnt+1;
end;

procedure uBest;
```

```
   begin
   Iu_0:=Iu_0_Best;
   uStrad_Cnt:=uStrad_Cnt+1;
   uBest_Acc:=uBest_Acc+1;
   end;

   begin
   uTuned:=false;
   {writeln(' Iu_0',Iu_0,' Iu_jlu',Iu[jlu]);}
{setup controls for adjusting parameters}
   if Iu[jlu]<=0 then uTune_Sign:=1; {Iu_0 too small}
   if Iu[jlu]>0 then uTune_Sign:=-1; {Iu_0 too large}
   if abs(Iu[jlu])<abs(Iu_Best) then
      begin
      Iu_Best:=Iu[jlu]; Iu_0_Best:=Iu_0;
      end;
   if (uTune_Cnt=0)or(uStrad_Cnt=uReset_Cnt) then uTune_Sign1:=uTune_Sign;
   if (not uStraddled)and(uTune_Sign1<>uTune_Sign) then uStraddled:=true;
   if Iu[jlu]*Iu_l0<0 then
      begin
      Iu_01:=Iu_00; Iu_l1:=Iu_l0;
      end;
   Iu_00:=Iu_0; Iu_l0:=Iu[jlu];
{test for tuned to precision limit}
   if ((abs(Iu[jlu])<Iu_jlu_Limit)or(Off_Cnt=jlu))or
         (uStrad_Cnt>uBest_Cnt) then uTuned:=true
      else
         case uStrad_Cnt of
            0..2:                     uBisect;
            3..(uReset_Cnt-1):        uNewton;
            uReset_Cnt:               uReset;
            uReset_Cnt+1..uBest_Cnt-1: uBisect;
            otherwise                 uBest;
            end;
{save tune controls for next time}
   uTune_Sign1:=uTune_Sign;
   Iu[0]:=Iu_0;
   uTune_Cnt:=uTune_Cnt+1;
   if Off_Cnt=jlu then Iu_0:=0;
   end;
{procedure solve_uElectric}
   begin
   Start_uElectric;
   repeat
      ju:=1; Off_Cnt:=0;
      repeat
         Calc_Uu;
         Calc_dIu;
         Calc_Iu;
         ju:=ju+1;
      until ju>jlu;
   until uTuned;
   end;


procedure Calc_Im;
   var ju : integer;
   begin
   for ju:=1 to jlu do dIu[ju,jm]:=dIu0[ju];
   Im[jm]:=Im[jm-1]-Nug*Iu_0;
   end;


function mTuned:boolean;

   Procedure mBisect;
   begin
   if mStraddled then mTune_Frac:=0.501*mTune_Frac;
   UPbO2:=UPbO2+mTune_Frac*mTune_Sign*dUPbO2;
   end;

   procedure mBest;
   begin
   UPbO2:=UPbO2_Best;
   mBest_Tot:=mBest_Tot+1;
   writeln(Esc,'[2;40H','Sub-optimum m-channel solution');
   end;
```

```
   begin
   mTuned:=false;
   {writeln(mTune_Cnt:3,' UPbO2',UPbO2,' Im_jlm',Im[jlm]);}
{setup controls for adjusting parameters}
   if Im[jlm]<=0 then mTune_Sign:=1; {UPbO2 too small}
   if Im[jlm]>0 then mTune_Sign:=-1; {UPbO2 too large}
   if (abs(Im[jlm])<abs(Im_Best))and(not dE_Limit) then
      begin
      Im_Best:=Im[jlm]; UPbO2_Best:=UPbO2;
      end;
    if mTune_Cnt=0 then mTune_Sign1:=mTune_Sign;
   if (not mStraddled)and(mTune_Sign1<>mTune_Sign) then mStraddled:=true;
{test for tuned to precision limit}
   if ((abs(Im[jlm])<Im_jlm_Limit)and(not dE_Limit))or
         (mTune_Cnt>mBest_Cnt) then mTuned:=true
      else
         case mTune_Cnt of
            0..(mBest_Cnt-1): mBiSect;
            otherwise mBest;
            end;
{save tune controls for next time}
   if mTune_Cnt>mBest_Cnt then uBest_Tot:=uBest_Tot+uBest_Acc;
   dE_Limit:=false; uBest_Acc:=0;
   mTune_Sign1:=mTune_Sign;
   mTune_Cnt:=mTune_Cnt+1;
   end;


{Solve_mElectric}
begin
Start_mElectric;
Get_Icell;
Ri_dRu_Eu_i0c_i0a_Sdis_SZr_SHi;
Calc_Uh;
repeat
   jm:=1;
   repeat
      Calc_Um;
      Solve_uElectric;
      Calc_Im;
      jm:=jm+1;
   until jm>jlm;
until mTuned;
end;




procedure Ex_Results;
   var
   Skip_Pos, jjm : integer;

   function cPer(ci:real):integer;
   begin
   cPer:=round(100*ci/c0);
   end;

   function XPer(Xi:real):integer;
   begin
   XPer:=round(100*Xi);
   end;

   function IPer(Ii:double):integer;
   begin
   IPer:=round(Nmc*100*Ii/20);
   end;

   function AcPer(Aci:real):integer;
   begin
   AcPer:=round(100*Aci/Acid_Tot);
   end;

   procedure Write_Ln;
   begin
```

```
   writeln(jjm:3,'  [ ',cPer(cm[jjm]):3,' I .. ',cPer(cu[jlu,jjm]):3,
      ' ]        I',XPer(X[1,jjm]):3,' .. ',XPer(X[jlu,jjm]):3,' ]   (Im: ',
      IPer(Im[jjm-1]-Im[jjm]):3,')');
   end;

{procedure Ex_Results}
   begin
   writeln(Esc,'[H','R'); writeln(Esc,'[J');
   Skip_Pos:=1;
   while (Im[Skip_Pos]=Ih)and(Skip_Pos<jlm-9) do Skip_Pos:=Skip_Pos+1;
   if (k rem 1)=0 then writeln(Esc,'[H',(k*dt/3600):6:2);
   if (k rem 1)=0 then
      begin
      writeln;
      write(' jn  +-----+'); writeln('      voltage: ',UPbO2:10:8);
      write('1':3,'  [ ',cPer(cn[1]):3,' ]');
         writeln('         Ahrs: ',Ahrs:3:1);
      write(jln:3,'  [ ',cPer(cn[jln]):3,' ]');
         writeln('         Acid: ',AcPer(Acid_Tot+Acid_I_Sum):1);
      writeln(' js  +-----+');
      writeln('1':3,'  [ ',cPer(cs[1]):3,' ] ',jlr:3,' .. ','1':3,' jr ');
      writeln(jlsrs:3,'  [ ',cPer(cs[jlsrs]):3,' I ',cPer(cr[jlr]):3,' .. ',
         cPer(cr[1]):3,' ]');
      writeln(jls:3,'  [ ',cPer(cs[jls]):3,' ]');
      writeln(' jh  +-----+');
      writeln('1':3,'  [ ',cPer(ch[1]):3,' ]');
      writeln(jlh:3,'  [ ',cPer(ch[jlh]):3,' ]');
      writeln(' jm  +-----+ .. ',jlu:3,' ju ');
      if (Skip_Pos>1)and(Skip_Pos<=jlm-9) then
         begin
         jjm:=1; Write_Ln;
         for jjm:=Skip_Pos to Skip_Pos+5 do Write_Ln;
         jjm:=jlm; Write_Ln;
         end;
      if (Skip_Pos=1) then
         begin
         for jjm:=Skip_Pos to Skip_Pos+5 do Write_Ln;
         jjm:=jlm; Write_Ln;
         end;
      if (Skip_Pos>jlm-7) then
         begin
         jjm:=1; Write_Ln;
         for jjm:=Skip_Pos to jlm do Write_Ln;
         end;
      writeln('     +-----+');
      writeln(uBest_Tot:1,'/',mBest_Tot:1,' ',mTune_Cnt:3,' ',(Im[jlm]/Ih):10);
      writeln(Esc,'[H');
      end;
   end;



procedure Solve_Transport;
   const t_plus=0.8;
   var
   rUP : array[0..jlr-1] of double;
   rDI, rKK : array[0..jlr] of double;
   rLO : array[1..jlr] of double;
   Grs : real; {boundary parameter at jlsrs}
   sCC : double; {solution at position jlsrs}
   uUP : array[1..jlu,1..jlm] of double;
   uDI, uKK : array[1..jlu+1,1..jlm] of double;
   uLO : array[2..jlu+1,1..jlm] of double;
   Gmu : array[1..jlm] of real;
   mCC : array[1..jlm] of double;
   jm : integer;


procedure Start_cr;
   const
   dxsrs=2*(1-1/sqrt(2))*sqrt(as/Pi);
      asrs=2*Pi*sqrt(as/Pi)*(1/sqrt(2))*lls; {rs boundary parameters}
   Lr_K=dt/(2*sqr(dxr)); Mr_K1=dt/(4*dxr); Mr_K2=1/(2*dxr);
   var
   jr : integer;
   vr_sum, grllb, grlb, gsrsb, Grl : real;
```

```
   vr, Dr : array[0..jlr] of real;
   Fact : double;

   begin
   writeln(Esc,'[H','T',Esc,'[H');
{calculate present Dr and vr}
   vr_Sum:=-(sngl(Ih1)/(2*F))*(2*VmPBSO4-VmPbO2-VmPb)/ar; vr_jlr:=vr_sum;
   for jr:=jlr downto 1 do
      begin
      vr[jr]:=vr_Sum*jr/jlr; Dr[jr]:=Dr_Mult*LookUp(D_Key,cr[jr]);
      end;
{dummy boundary position values}
   cr[0]:=cr[1]; Dr[0]:=Dr[1]; vr[0]:=-vr[1];
{load constant vector with past effects}
   for jr:=1 to jlr-1 do
      rKK[jr]:=dble(Lr[jr]-Mr[jr])*dble(cr[jr-1])
         +(1+dble(-2*Lr[jr]))*dble(cr[jr])
         +dble(Lr[jr]+Mr[jr])*dble(cr[jr+1]);
{calculate present Lr and Mr}
   for jr:=1 to jlr-1 do
      begin
      Lr[jr]:=Lr_K*Dr[jr]; Mr[jr]:=Mr_K1*(Mr_K2*(Dr[jr+1]-Dr[jr-1])-vr[jr]);
      end;
{calculate s/r boundary equation parameters}
      gsrsb:=2*asrs*LookUp(D_Key,cs[jlsrs])/dxsrs; grlb:=2*ar*Dr[jlr]/dxr;
      grllb:=2*ar*Dr[jlr-1]/dxr;
   Grl:=grllb*grlb/(grllb+grlb); Grs:=grlb*gsrsb/(grlb+gsrsb);
{load tri-diagonal matrix and constant vector}
   rDI[0]:=1; rUP[0]:=-1; rKK[0]:=0; {closed end boundary equation}
   for jr:=1 to jlr-1 do {general equations}
      begin
      rLO[jr]:=dble(-Lr[jr]+Mr[jr]);
      rDI[jr]:=1+dble(2*Lr[jr]);
      rUP[jr]:=dble(-Lr[jr]-Mr[jr]);
      end;
   rLO[jlr]:=dble(Grl/Grs); rDI[jlr]:=-1+dble(-Grl/Grs);
      rKK[jlr]:=0; {s/r boundary equation}
{perform forward elimination}
   for jr:=1 to jlr do
      begin
      Fact:=rLO[jr]/rDI[jr-1];
      rDI[jr]:=rDI[jr]-Fact*rUP[jr-1];
      rKK[jr]:=rKK[jr]-Fact*rKK[jr-1];
      end;
   end;


procedure Start_cu;
   const
   dxmu=2*(1-1/sqrt(2))*sqrt(am/Pi);
      amu=2*Pi*sqrt(am/Pi)*(1/sqrt(2))*llm/Num; {mu boundary paramaters}
   Lu_K=dt/(2*sqr(dxu)); Mu_K1=dt/(4*dxu); Mu_K2=1/(2*dxu);
    Ou_K=-dt*(3-2*t_plus)/(4*F*dxu*au0); vu_K=-(VmPbSO4-VmPbO2)/(2*F*au0);
   var
   ju : integer;
   vu_sum, gu1b, gu2b, gmmub, Gu1 : real;
   vu, Du, X0 : array[1..jlu+1] of real;
   Fact : double;

   begin
   for jm:=1 to jlm do
      begin
   {calculate present Du and vu}
      vu_Sum:=0;
      for ju:=jlu downto 1 do
         begin
         X0[ju]:=X[ju,jm]; Du[ju]:=LookUp(D_Key,cu[ju,jm]);
         vu_Sum:=vu_Sum+vu_K*sngl(dIu1[ju,jm]); vu[ju]:=vu_Sum/X0[ju];
         end;
   {dummy boundary values}
      X0[jlu+1]:=X0[jlu]; cu[jlu+1,jm]:=cu[jlu,jm];
      Du[jlu+1]:=Du[jlu]; vu[jlu+1]:=-vu[jlu];
   {calculate volume moving across m/u boundary}
      axvmu[jm]:=au0*X0[1]*vu[1];
   {load constant vector with past effects}
      for ju:=2 to jlu do
         begin
```

```
          uKK[ju,jm]:=dble(Lu[ju,jm]-Mu[ju,jm])*dble(cu[ju-1,jm])
             +(1+dble(-2*Lu[ju,jm]))*dble(cu[ju,jm])
             +dble(Lu[ju,jm]+Mu[ju,jm])*dble(cu[ju+1,jm])
             +dble(Ou[ju,jm]);
          end;
    {calculate present Lu, Mu and Ou}
       for ju:=2 to jlu do
          begin
          Lu[ju,jm]:=Lu_K*Du[ju];
          Mu[ju,jm]:=Mu_K1*
             (Mu_K2*(X0[ju+1]*Du[ju+1]-X0[ju-1]*Du[ju-1])/X0[ju]-vu[ju]);
          Ou[ju,jm]:=Ou_K*sngl(dIu[ju,jm])/X0[ju];
          end;
    {calculate m/u boundary equation parameters}
          gmmub:=2*amu*LookUp(D_Key,cm[jm])/dxmu; gu1b:=2*au0*X0[1]*Du[1]/dxu;
          gu2b:=2*au0*X0[2]*Du[2]/dxu;
       Gu1:=gu1b*gu2b/(gu1b+gu2b); Gmu[jm]:=gmmub*gu1b/(gmmub+gu1b);
    {load tri-diagonal matrix and constant vector}
       uDI[1,jm]:=-1+dble(-Gu1/Gmu[jm]); uUP[1,jm]:=dble(Gu1/Gmu[jm]);
     uKK[1,jm]:=dble((3-2*t_plus)*sngl(dIu[1,jm])/(4*F*Gmu[jm])); {m/u boundary}
       for ju:=2 to jlu do {general equations}
          begin
          uLO[ju,jm]:=dble(-Lu[ju,jm]+Mu[ju,jm]);
          uDI[ju,jm]:=1+dble(2*Lu[ju,jm]);
          uUP[ju,jm]:=dble(-Lu[ju,jm]-Mu[ju,jm]);
          uKK[ju,jm]:=uKK[ju,jm]+dble(Ou[ju,jm]);
          end;
       uLO[jlu+1,jm]:=-1; uDI[jlu+1,jm]:=1; uKK[jlu+1,jm]:=0; {closed boundary}
    {perform forward elimination}
       for ju:=jlu downto 1 do
          begin
          Fact:=uUP[ju,jm]/uDI[ju+1,jm];
          uDI[ju,jm]:=uDI[ju,jm]-Fact*uLO[ju+1,jm];
          uKK[ju,jm]:=uKK[ju,jm]-Fact*uKK[ju+1,jm];
          end;
       end;
    end;


procedure Calc_cn_cs_ch_cm;
    const
    Ln_K=dt/(2*sqr(dxn)); Mn_K1=dt/(4*dxn); Mn_K2=1/(2*dxn);
       On_K=-dt*(2*t_plus-1)/(4*F*dxn*jln);
    Ls_K=dt/(2*sqr(dxs)); Ms_K1=dt/(4*dxs); Ms_K2=1/(2*dxs);
       Ns_K1=dt/2; Ns_K2=-1/(2*dxs);
    Lh_K=dt/(2*sqr(dxh)); Mh_K1=dt/(4*dxh); Mh_K2=1/(2*dxh);
    Lm_K=dt/(2*sqr(dxm)); Mm_K1=dt/(4*dxm); Mm_K2=1/(2*dxm);
       Nm_K1=dt/2; Nm_K2=-1/(2*dxm); vm_K=Nug/am;
    var
    jn, js, jh, jm, ji, b1, b2 : integer;
    ci0 : array[0..jli+1] of real;
    vm, Dm : array[1..jlm+1] of real;
    vm_sum, gm1b, gm2b, Gm1 : real;
    Dh : array[1..jlh] of real;
    gh1b, gh2b, ghllb, ghlb, Ghl, Ghl, Ghm : real;
    vs, Ds : array[1..jls] of real;
    gs1b, gs2b, gsllb, gslb, Gsl, Gsl, Gsh : real;
    vn, Dn : array[0..jln] of real;
    vn_sum, gnllb, gnlb, Gnl, Gns : real;
    Fact : double;
    iUP : array[0..jli] of double;
    iDI, iKK, iCC : array[0..jli+1] of double;
    iLO : array[1..jli+1] of double;

    begin
{calculate present Di and vi and move cm}
{m-channel}
    vm_Sum:=0;
    for jm:=jlm downto 1 do
       begin
       vm_Sum:=vm_Sum+axvmu[jm]; vm[jm]:=vm_K*vm_Sum;
       Dm[jm]:=LookUp(D_Key,cm[jm]);
       end;
    vm[jlm+1]:=-vm[jlm]; Dm[jlm+1]:=Dm[jlm]; cm[jlm+1]:=cm[jlm]; {dummy pos}
{h-channel}
    vh:=vm[1]*am/ah;
    for jh:=jlh downto 1 do Dh[jh]:=LookUp(D_Key,ch[jh]);
```

```
{n-channel}
   vn_sum:=sngl(Ih1)*(VmPbSO4-VmPb)/(2*F*an); vn_jln:=vn_sum;
   for jn:=jln downto 1 do
      begin
      vn[jn]:=vn_sum*jn/jln; Dn[jn]:=LookUp(D_Key,cn[jn]);
      end;
   vn[0]:=-vn[1]; Dn[0]:=Dn[1]; cn[0]:=cn[1]; {dummy pos}
{s-channel}
   for js:=jls downto jlsrs+1 do
      begin
      vs[js]:=vh*ah/as; Ds[js]:=LookUp(D_Key,cs[js]);
      end;
   for js:=1 to jlsrs-1 do
      begin
      vs[js]:=vn[jln]*an/as; Ds[js]:=LookUp(D_Key,cs[js]);
      end;
   vs[jlsrs]:=0; Ds[jlsrs]:=LookUp(D_Key,cs[jlsrs]); {r-channel entry pos}
{load constant vector with past effects}
{n-channel}
   b1:=0; {boundary eqn position}
   for jn:=1 to jln-1 do
      iKK[jn]:=dble(Lnn[jn]-Mn[jn])*dble(cn[jn-1])
         +(1+dble(-2*Lnn[jn]))*dble(cn[jn])
         +dble(Lnn[jn]+Mn[jn])*dble(cn[jn+1])
         +dble(On);
{s-channel}
   b1:=b1+jln+1;
   for js:=2 to jls-1 do
      iKK[b1+js-1]:=dble(Ls[js]-Ms[js])*dble(cs[js-1])
         +(1+dble(-2*Ls[js]))*dble(cs[js])
         +dble(Ls[js]+Ms[js])*dble(cs[js+1]);
   {adjust equation at the r-channel entry position}
   iKK[b1+jlsrs-1]:=iKK[b1+jlsrs-1]+dble(Ns*cs[jlsrs])+dble(Os);
{h-channel}
   b1:=b1+jls;
   for jh:=2 to jlh-1 do
      iKK[b1+jh-1]:=dble(Lh[jh]-Mh[jh])*dble(ch[jh-1])
         +(1+dble(-2*Lh[jh]))*dble(ch[jh])
         +dble(Lh[jh]+Mh[jh])*dble(ch[jh+1]);
{m-channel}
   b1:=b1+jlh;
   for jm:=2 to jlm do
      iKK[b1+jm-1]:=dble(Lm[jm]-Mm[jm])*dble(cm[jm-1])
         +(1+dble(-2*Lm[jm]+Nm[jm]))*dble(cm[jm])
         +dble(Lm[jm]+Mm[jm])*dble(cm[jm+1])
         +dble(Om[jm]);
{calculate present Li, Mi and Ni}
{n-channel}
   for jn:=1 to jln-1 do
      begin
      Lnn[jn]:=Ln_K*Dn[jn]; Mn[jn]:=Mn_K1*(Mn_K2*(Dn[jn+1]-Dn[jn-1])-vn[jn]);
      end;
{s-channel}
   for js:=2 to jls-1 do
      begin
      Ls[js]:=Ls_K*Ds[js]; Ms[js]:=Ms_K1*(Ms_K2*(Ds[js+1]-Ds[js-1])-vs[js]);
      end;
   Ns:=Ns_K1*Ns_K2*(vs[jlsrs+1]-vs[jlsrs-1]); {r-channel entry pos}
{h-channel}
   for jh:=2 to jlh-1 do
      begin
      Lh[jh]:=Lh_K*Dh[jh]; Mh[jh]:=Mh_K1*(Mh_K2*(Dh[jh+1]-Dh[jh-1])-vh);
      end;
{m-channel}
   for jm:=2 to jlm do
      begin
      Lm[jm]:=Lm_K*Dm[jm]; Mm[jm]:=Mm_K1*(Mm_K2*(Dm[jm+1]-Dm[jm-1])-vm[jm]);
      Nm[jm]:=Nm_K1*Nm_K2*(vm[jm+1]-vm[jm-1]);
      end;
{calculate boundary equation parameters}
      gnllb:=2*Dn[jln-1]*an/dxn; gnlb:=2*Dn[jln]*an/dxn; gs1b:=2*Ds[1]*as/dxs;
      gs2b:=2*Ds[2]*as/dxs; gsllb:=2*Ds[jls-1]*as/dxs; gslb:=2*Ds[jls]*as/dxs;
      gh1b:=2*Dh[1]*ah/dxh; gh2b:=2*Dh[2]*ah/dxh; ghllb:=2*Dh[jlh-1]*ah/dxh;
      ghlb:=2*Dh[jlh]*ah/dxh; gm1b:=2*Dm[1]*am/dxm; gm2b:=2*Dm[2]*am/dxm;
   Gnl:=gnllb*gnlb/(gnllb+gnlb); Gns:=gnlb*gs1b/(gnlb+gs1b);
   Gs1:=gs1b*gs2b/(gs1b+gs2b); Gsl:=gsllb*gslb/(gsllb+gslb);
   Gsh:=gslb*gh1b/(gslb+gh1b); Gh1:=gh1b*gh2b/(gh1b+gh2b);
```

```
   Ghl:=ghllb*ghlb/(ghllb+ghlb); Ghm:=ghlb*gm1b/(ghlb+gm1b);
   Gml:=gm1b*gm2b/(gm1b+gm2b);
{n-channel source term}
   On:=On_K*sngl(Ih)/an;
{load tri-diagonal matrix and constant vector}
{n-channel}
   b1:=0; b2:=jln; {boundary eqn positions}
   iDI[b1]:=1; iUP[b1]:=-1; iKK[b1]:=0;
   for jn:=1 to jln-1 do
      begin
      ji:=jn;
      iLO[ji]:=dble(-Lnn[jn]+Mn[jn]);
      iDI[ji]:=1+dble(2*Lnn[jn]);
      iUP[ji]:=dble(-Lnn[jn]-Mn[jn]);
      iKK[ji]:=iKK[ji]+dble(On);
      end;
   iLO[b2]:=dble(Gnl/Gns); iDI[b2]:=-1+dble(-Gnl/Gns); iUP[b2]:=1;
      iKK[b2]:=dble((2*t_plus-1)*Ih/(4*F*jln*Gns));
{s-channel}
   b1:=b1+jln+1; b2:=b2+jls;
   iLO[b1]:=1; iDI[b1]:=-1+dble(-Gs1/Gns); iUP[b1]:=dble(Gs1/Gns); iKK[b1]:=0;
   for js:=2 to jls-1 do
      begin
      ji:=b1+js-1;
      iLO[ji]:=dble(-Ls[js]+Ms[js]);
      iDI[ji]:=1+dble(2*Ls[js]);
      iUP[ji]:=dble(-Ls[js]-Ms[js]);
      end;
   {adjust equation at the r-channel entry position}
   ji:=b1+jlsrs-1;
   iDI[ji]:=iDI[ji]+dble(-Ns)+dble(dt*Grs/(2*as*dxs))*(1+1/rDI[jlr]);
   iKK[ji]:=iKK[ji]+dble(dt*Grs/(2*as*dxs))*(rKK[jlr]/rDI[jlr]);
   iLO[b2]:=dble(Gsl/Gsh); iDI[b2]:=-1+dble(-Gsl/Gsh); iUP[b2]:=1; iKK[b2]:=0;
{h-channel}
   b1:=b1+jls; b2:=b2+jlh;
   iLO[b1]:=1; iDI[b1]:=-1+dble(-Gh1/Gsh); iUP[b1]:=dble(Gh1/Gsh); iKK[b1]:=0;
   for jh:=2 to jlh-1 do
      begin
      ji:=b1+jh-1;
      iLO[ji]:=dble(-Lh[jh]+Mh[jh]);
      iDI[ji]:=1+dble(2*Lh[jh]);
      iUP[ji]:=dble(-Lh[jh]-Mh[jh]);
      end;
   iLO[b2]:=dble(Ghl/Ghm); iDI[b2]:=-1+dble(-Ghl/Ghm); iUP[b2]:=1; iKK[b2]:=0;
{m-channel}
   b1:=b1+jlh; b2:=b2+jlm+1;
   iLO[b1]:=dble(Ghm/(Ghm+Gm1));
      iDI[b1]:=-1+dble(-Nug*Gmu[1]/(Ghm+Gm1))*(1+1/uDI[1,1]);
      iUP[b1]:=dble(Gm1/(Ghm+Gm1));
      iKK[b1]:=dble(-Nug*Gmu[1]/(Ghm+Gm1))*(uKK[1,1]/uDI[1,1]);
   for jm:=2 to jlm do
      begin
      ji:=b1+jm-1;
      iLO[ji]:=dble(-Lm[jm]+Mm[jm]);
      iDI[ji]:=1+dble(2*Lm[jm]-Nm[jm])
         +dble(dt*Nug*Gmu[jm]/(2*am*dxm))*(1-(-1/uDI[1,jm]));
      iUP[ji]:=dble(-Lm[jm]-Mm[jm]);
      iKK[ji]:=iKK[ji]+dble(dt*Nug*Gmu[jm]/(2*am*dxm))*(uKK[1,jm]/uDI[1,jm]);
      end;
   iLO[b2]:=1; iDI[b2]:=-1; iKK[b2]:=0;
   {ji:=0; writeln(iDI[ji]:10,iUP[ji]:10,iKK[ji]:10);
   for ji:=1 to jli do writeln(iLO[ji]:10,iDI[ji]:10,iUP[ji]:10,iKK[ji]:10);
   ji:=jli+1; writeln(iLO[ji]:10,iDI[ji]:10,iKK[ji]:10);}
{perform elimination}
   for ji:=1 to jli+1 do
      begin
      Fact:=iLO[ji]/iDI[ji-1];
      iDI[ji]:=iDI[ji]-Fact*iUP[ji-1];
      iKK[ji]:=iKK[ji]-Fact*iKK[ji-1];
      end;
{perform back-substitution}
   iCC[jli+1]:=iKK[jli+1]/iDI[jli+1];
   for ji:=jli downto 0 do iCC[ji]:=(iKK[ji]-iCC[ji+1]*iUP[ji])/iDI[ji];
{change precision}
   for ji:=0 to jli+1 do ci0[ji]:=sngl(iCC[ji]);
{save concentration}
{n-channel}
```

```
   b1:=0;  {offset positions}
   for jn:=1 to jln do cn[jn]:=ci0[jn];
{s-channel}
   b1:=b1+jln;
   for js:=1 to jls do cs[js]:=ci0[js+b1];
   sCC:=iCC[jlsrs+b1];
{h-channel}
   b1:=b1+jls;
   for jh:=1 to jlh do ch[jh]:=ci0[jh+b1];
{m-channel}
   b1:=b1+jlh;
   for jm:=1 to jlm do
      begin
      cm[jm]:=ci0[jm+b1];
      mCC[jm]:=iCC[jm+b1];
      end;
   end;


procedure Finish_cr;
   var
   rCC : array[1..jlr] of double;
   jr : integer;

   begin
{perform back-substitution}
   rCC[jlr]:=(rKK[jlr]-sCC)/rDI[jlr];
   for jr:=jlr-1 downto 1 do rCC[jr]:=(rKK[jr]-rCC[jr+1]*rUP[jr])/rDI[jr];
{change precision and save concentration}
   for jr:=1 to jlr do  cr[jr]:=sngl(rCC[jr]);
{calculate the past source term for s-channel}
   Os:=-(dt*Grs/(2*as*dxs))*sngl(sCC-rCC[jlr]);
   end;


procedure Finish_cu;
   var
   uCC : array[1..jlu] of double;
   jm, ju : integer;

   begin
      for jm:=1 to jlm do
      begin
   {perform back-substitution}
      uCC[1]:=(uKK[1,jm]-mCC[jm])/uDI[1,jm];
      for ju:=2 to jlu do uCC[ju]:=(uKK[ju,jm]-uCC[ju-1]*uLO[ju,jm])/uDI[ju,jm];
   {change precision and save concentration}
      for ju:=1 to jlu do  cu[ju,jm]:=sngl(uCC[ju]);
   {calculate the past source term for the m-channel}
      if jm>1 then Om[jm]:=(dt*Nug*Gmu[jm]/(2*am*dxm))*sngl(uCC[1]-mCC[jm]);
      end;
   end;


{Solve_Transport}
begin
   Start_cr;
   Start_cu;
   Calc_cn_cs_ch_cm;
   Finish_cr;
   Finish_cu;
end;




procedure Up_Structure;
   const
   X_K=Nme*Num*llu*dt/(q0*dxu);
   var
   X_Carry : array[1..jlu] of real;
   jm, ju : integer;
{procedure Up_Structure}
   begin
{update state of charge}
   Acid_I_Sum:=Acid_I_Sum-dt*Icell/(2*F);
   Ahrs:=Ahrs+Icell*dt/3600;
```

```
   for ju:=1 to jlu do X_Carry[ju]:=0;
   for jm:=1 to jlm do
      for ju:=1 to jlu do
         begin
         X[ju,jm]:=X[ju,jm]-X_K*sngl(dIu[ju,jm])+X_Carry[ju];
         X_Carry[ju]:=0;
         if X[ju,jm]<X_Limit then
            begin
            X_Carry[ju]:=X[ju,jm]-X_Limit;
            X[ju,jm]:=X_Limit;
            end;
         if X[ju,jm]>1 then
            begin
            X_Carry[ju]:=X[ju,jm]-1;
            X[ju,jm]:=1;
            end;
      end;
{update n-channel and r-channel}
   an:=an-vn_jln*an*dt/(jln*dxn);
   ar:=ar-vr_jlr*ar*dt/(jlr*dxr);
{increment time}
   k:=k+1;
   Ih1:=Ih;
   dIu1:=dIu; {array assign}
   end;



procedure Menu;
{used to enter variable values and commands during program operation}
  var Key : char;
      KeyStr : varying[5] of char;
  begin
  Key_This_k:=Get_Key;
  if Key_This_k<>0 then
     begin
     write(Esc,'[8;40H','Switch off simulation (Y/N) >');  readln(KeyStr);
     if KeyStr='' then
        begin
        write(Esc,'[9;40H','Enter cell current (A) >'); readln(KeyStr);
        if KeyStr<>'' then readv(KeyStr,ICell);
        end
        else
          if (KeyStr='Y')or(KeyStr='y') then SwitchOff:=true;
     end;
  end;



function Test_Time:boolean;
   var   Key : char;
   begin
   Test_Time:=false;
   if (Data_Source=1)and(eof(Data_File)) then Test_Time:=true;
   if (Ahrs<(-5*Icell*dt/3600))and(Icell<0) then Test_Time:=true;
   if SwitchOff then Test_Time:=true;
   end;




begin
Display_Dimensions;
Set_Operating_Mode;
Init_Operate;
repeat
   Solve_mElectric;
   Ex_Results;
   Solve_Transport;
   Up_Structure;
   Menu;
until Test_Time;
end.
```

Appendix 3

Functions for Various Models

A3.1 EFFECTIVE CHARGE SURFACE AREA FUNCTIONS.

The elemental charge surface area model was used to generate effective PbO_2 surface area versus charge state data for a 100 and 1000 Ampere charge in 5000 $mol.m^{-3}$ acid. This data was fitted to polynomial functions of charge state to enable the surface area to be estimated without recourse to the general model (see the end of section 7.1.5). The polynomial functions obtained for the 100 and 1000 Ampere cases are

$$S_E = 1.5777 + 1.2525X - 8.2498X^2 + 31.2122X^3 - 73.2036X^4 + 86.6819X^5 - 39.1789X^6$$

and

$$S_E = 1.6006 - 0.1262X + 5.1294X^2 - 27.1896X^3 + 45.3814X^4 - 25.6633X^5 + 0.8066X^6$$

respectively, where

S_E ($m^2.g^{-1}$) is the equivalent gram effective PbO_2 surface area and

X is the charge state.

A3.2 THE LEAD DIOXIDE ELECTRODE EQUILIBRIUM POTENTIAL.

The lead dioxide equilibrium potential is required by the aggregate model to determine the electrical properties of the positive electrode (see section 7.2.3). This was defined by the polynomial function given by Bode (1977) and repeated below.

$$E_{PbO2} = 1628.194 + 73.924x + 33.120x^2 + 43.220x^3 + 21.567x^4$$

where

E_{PbO2} is in millivolts and

x is the logarithm (base ten) of acid concentration in molality ($mol.kg^{-1}$).

When used for the aggregate model the potential was converted to volts and the concentration converted to moles per cubic metre.

A3.3 THE ELECTROLYTE RESISTIVITY.

The H_2SO_4 electrolyte solution resistivity is also required by the aggregate model to determine the electrical properties of the positive electrode (see section 7.2.3). This was defined by fitting a polynomial function of concentration to conductivity data given by Bode (1977). The polynomial function obtained is given below.

$$1/R = - 3.6101 + 54.7615c - 11.5017c^2 + 0.8976c^3 - 0.0255c^4$$

where

R (Ω.m) is the solution resistivity and

c ($x10^{-3}$ $mol.m^{-3}$) is the acid concentration.

A3.4 THE ACID DIFFUSION COEFFICIENT.

The acid diffusion coefficient is required by the aggregate model to determine the acid transport properties of the positive electrode system (see section 7.2.3). This was defined by the polynomial function of concentration given by Micka and Rousar (1973) and repeated below.

$$D = 1.48\text{x}10^{-9} + 0.125\text{x}10^{-9}\ c$$

where

D ($m^2.s^{-1}$) is the acid diffusion coefficient and

c ($\text{x}10^{-3}$ $mol.m^{-3}$) is the acid concentration.

A3.5 THE LEAD DIOXIDE ELECTRODE EXCHANGE CURRENT.

The cathodic and anodic exchange current densities at the PbO_2/solution interface are required by the aggregate model to determine the electrical characteristics of the positive electrode. The reaction order for these current densities was taken from Hampson *et al* (1967) and is shown in the general forms below.

$$i_a = i_{0a}\ c_{Pb2+}{}^{1}\ c_{H+}{}^{-0.4}$$

$$i_c = i_{0c}\ c_{H+}{}^{1.5}$$

where

i_a ($A.m^{-2}$) is the concentration dependent anodic exchange current density,

i_c ($A.m^{-2}$) is the concentration dependent cathodic exchange current density,

i_{0a} ($A.m^{-2}$) is the anodic exchange current density representing the reaction rate constant,

i_{0c} ($A.m^{-2}$) is the cathodic exchange current density representing the reaction rate constant

c_{Pb2+} ($mol.m^{-3}$) is the lead ion concentration and

c_{H+} ($mol.m^{-3}$) is the acid concentration.

Different values for i_{0a} and i_{0c} were used for the various result sets given in chapter 7. These are specified below.

The values of i_{0a} and i_{0c} used in section 7.3 for all cases with discharge rates less than or equal to 20 Amperes

were 4.099×10^{1} $A.m^{-2}$ and 1.217×10^{-8} $A.m^{-2}$ respectively.

The values of i_{0a} and i_{0c} used in section 7.3 for the 140 Ampere discharge case were 4.099×10^{1} $A.m^{-2}$ and 1.217×10^{-6} $A.m^{-2}$ respectively.

The value of i_{0a} and i_{0c} used for all cases in section 7.5 were 2.733×10^{1} $A.m^{-2}$ and 5.356×10^{-9} $A.m^{-2}$ respectively.

An example of the concentration dependent exchange current densities determined by these values can be obtained by substitution in the general forms above. Using $i_{0a} = 4.099 \times 10^{1}$ $A.m^{-2}$, $i_{0c} = 1.217 \times 10^{-8}$ $A.m^{-2}$ and $c_{H+} = 5000$ $mol.m^{-3}$ gives $i_a = 5.816 \times 10^{-3}$ $A.m^{-2}$ and $i_c = 4.303 \times 10^{-3}$ $A.m^{-2}$. Here the Pb^{2+} ion concentration was taken as 0.428×10^{-3} $mol.m^{-3}$ as determined by the solubility of $PbSO_4$ in 5000 $mol.m^{-3}$ acid.

References

Alzieu,J., Koechlin,N. and Robert,J., "Internal Stress Variations in Lead-Acid Batteries During Cycling", **Journal of the Electrochemical Society** 134:1881-1884, (1987).

Asher,M., Hampson,N.A., Kelly,S. and Holmes,G.S., "The Discharge (Reduction) of Porous Lead Dioxide In Sulphuric Acid", **Surface Technology**, 10:371-377, (1980).

Asher,M., Hampson,N.A. and Holmes,G.S., "Modelling of Lead-Acid Batteries I:Parameters for the Macrohomogeneous Model" **Surface Technology**, 11:17-26, (1980).

Atlung,S. and Fastrup,B., "Limitations in the Design of Lead-Acid Cells with Immobilised Electrolyte", **Journal of Power Sources**, 13:39-54, (1984).

Barak,M. in Barak,M. (ed.), **Electrochemical Power Sources. Primary and Secondary Batteries**, Peregrins, (1980).

Bjornbom,P., "Modeling the Recharge Kinetics of the Positive Electrode Active Mass of a Lead-Acid Battery", **Journal of the Electrochemical Society**, 134:1600-1603, (1987).

Bockris,J.O. and Reddy,A.N.K., **Modern Elecrochemistry Volume 1**, Plenum Press, (1977).

Bockris,J.O. and Reddy,A.N.K., **Modern Elecrochemistry Volume 2**, Plenum Press, (1977).

Bode,H., **Lead-Acid Batteries**, Wiley, (1977).

Bode,H., Panesar,H. and Voss.E., "Mass Uitilisation and Current Distribution in Porous Lead Dioxide Electrodes", **Chemie-Ingenieur-Technik**, 41:878-879, (1969).

Broshtein,I.N and Semendyayev,K.A., **A Guide Book to Mathematics**, Springer-Verlay, (1973).

Bullock,K.R. and Butler,M.A., "Corrosion in Lead in Sulfuric Acid at High Potentials", **Journal of the Electrochemical Society**, 133:1085-1090, (1986).

Bullock,K.R. and Tiedemann,W.H., "The Corrosion of a Strontium-Lead Alloy in Sulfuric Acid", **Journal of the Electrochemical Society**, 127:2112-2118, (1980).

Bullock,K.R., Trischan,G.M. and Burrow,R.G., "Photo-electrochemical and Microprobe Laser Raman Studies of Lead Corrosion in Sulfuric Acid", **Journal of the Electrochemical Society**, 130:1283-1289, (1983).

Carr,J.P. and Hampson,N.A., "The Lead Dioxide Electrode", **Chemical Reviews**, 72:679-703, (1972).

Chang,T.G., "Structual Changes of Positive Active Material in Lead-Acid Batteries in Deep-Discharge Cycling", **Journal of the Electrochemical Society**, 131:1755-1762, (1984).

Chiswell,B. and Grigg,E.C.M., **SI Units**, Wiley, (1971).

Cussler,E.L., **Diffusion. Mass Transfer in Fluid Systems**, Cambridge University Press, (1984).

Dacres,C.M., Sutula,R.A. and Larrick,B.F., "A Comparison of Procedures Used in Assessing the Anodic Corrosion of Metal Matrix Composites and Lead Alloys for Use in Lead-Acid Batteries", **Journal of the Electrochemical Society**, 130:981-985, (1983).

Danel,V. and Plichon,V., "Study of Pb(II) in Various H_2O-H_2SO_4 Mixtures by Differential Pulse Polarography: Solubility of Lead Sulphate, Diffusion Coefficient of Pb(II) and Half-Wave Potential of Pb(Hg)/Pb(II)", **Electrochimica Acta**, 27:771-774, (1982).

Dasoyan,M.A. and Aguf,I.A., **Current Theory of Lead-Acid Batteries**, Technicopy, (1979).

Dawson,J.L., Rana,M.E., Munasiri,B. and McWhinnie,J. in Thompson,J. (ed.), "Morphological and Kinetic Studies on Lead Dioxide Electrodes", **Power Sources 7**, Academic Press, (1978).

Dees,D.W. and Tobias,C.W., "Mass Transfer at Gas Evolving Surfaces", **Journal of the Electrochemical Society**, 134:1702-1713, (1987).

Delahay,P., **Double Layer and Electrode Kinetics**, Interscience, (1965).

de Levie,R., "Electrochemical Response of Porous and Rough Electrodes", **Advances In Electrochemistry And Electrochemical Engineering** 6:329-397, (1967).

Dukovic,J. and Tobias,C.W., "The Influence of Attached Bubbles on Potential Drop and Current Distribution at Gas-Evolving Electrodes", **Journal of the Electrochemical Society**, 134:331-343, (1987).

Ekdunge,P. and Simonsson,D., "Recharge Kinetics of the Porous Lead Dioxide Electrode. I. The Effect of Structural Changes", **Journal of the Electrochemical Society**, 132:2521-2529, (1985).

Ekdunge,P. and Simonsson,D., "Recharge Kinetics of the Porous Lead Dioxide Electrode. II. The Effect of Sulfuric Acid Concentration", **Journal of the Electrochemical Society**, 132:2529-2533, (1985).

Flood,E.A. (ed.), **The Sold Gas Interface Volume 1**, Marcel Dekker, (1967).

Gibson,I.K. and Peters,K., "Sulphation in Discharged Lead-Acid Batteries", **Journal of Power Sources**, 8:143-157, (1982).

Hampson,N.A., Jones,P.C. and Phillips,R.F., "Electrochemical Reactions at PbO2 Electrodes. Part I. The Passivation of β-PbO_2 in Perchloric Acid", **Canadian Journal of Chemistry**, 45:2039-2044, (1967).

Hampson,N.A., Jones,P.C. and Phillips,R.F., "Electrochemical Reactions at PbO_2 Electrodes. Part II. The Exchange Reaction at β-PbO_2 Electrodes", **Canadian Journal of Chemistry**, 45:2045-2049, (1967).

Hampson,N.A., Jones,P.C. and Phillips,R.F., "Electrochemical Reactions at PbO_2 Electrodes. Part III. β-PbO_2 Electrodes in Acid Perchlorate Electrolytes at High Overpotential", **Canadian Journal of Chemistry**, 46:1325-1335, (1968).

Hampson,N.A., Jones,P.C. and Phillips,R.F., "Electrochemical Reactions at PbO_2 Electrodes. Part IV. Electrochemical Behavior of α-PbO_2 in Acid Perchlorate Electrolytes", **Canadian Journal of Chemistry**, 47:2171-217, (1969).

Hattori,S., Yamaura,M., Kohno,M., Ohtani,Y., Yamane,M. and Nakashima,H. in Collins,D.H. (ed.), "Perodic Observation of the Same Pin-point of Battery Plate with the Scanning Electron Microscope", **Power Sources 5**, Academic Press, (1975).

Hill,R.J., "Application of Diffraction Techniques in Studies of Lead-acid Battery Performance", **Journal of Power Sources**, 11:19-32, (1984).

Hill,R.J. and Madsen,I.C., "Structural Parameters of β-PbO_2 and Their Relationship to the Hydrogen-Loss Concept of Lead-Acid Battery Failure", **Journal of the Electrochemical Society**, 131:1486-1491,(1984).

Hine,F. and Murakami,K., "Bubble Effects on the Solution IR Drop in a Vertical Electrolyser Under Free and Forced Convection", **Journal of the Electrochemical Society**, 127:292-297, (1980).

Hurd,R.M., "Polarisation Curves of Radox Systems Involving Consecutive Electron-Transfers: Some Theoretical Aspects", **Journal of the Electrochemical Society**, 109:327-332, (1962).

Jordan,P.C., **Chemical Kinetics and Transport**, Plenum Press, (1979).

Kappus,W. and Bohmann,J., "The Influence of Acid Diffusion on the Performance of Lead-Acid Cells", **Journal of Power Sources**, 10:355-376, (1983).

Kordesch,K.V. (ed.), **Batteries. Volume 2 Lead-Acid Batteries and Electric Vehicles**, Marcel Dekker, (1977).

Kramer,M. and Tomkiewicz,M., "Porous Electrodes. I. Numerical Simulation Using Random Network and Single Pore Models", **Journal of the Electrochemical Society**, 131:1283-1288, (1984).

Kreysa,G. and Kulps,H.J., "Experimental Study of the Gas Bubble Effects on the IR Drop at Inclined Electrodes", **Journal of the Electrochemical Society**, 128:979-984, (1981).

Lee,J., Choi,K.W., Yao,N.P. and Christianson,C.C., "Three-Dimensional Thermal Modeling of Electric Vehicle Batteries", **Journal of the Electrochemical Society**, 133:1286-1291, (1986).

Lehning,H., "Contribution to the Mathmatical Description of the Electrochemical Events in the Lead Accumulator", **Zeitschrift fuer Elektrotechemie.**, 93:62-66, (1972).

Mahato,B.K., Strebe,J.L., Wilkinson,D.F. and Bullock,K.R., "Effect of Antimony on Lead-Acid Battery Negitive", **Journal of the Electrochemical Society**, 132:19-23, (1985).

Micka,K., "Mass Transfer In Concentrated Binary Electrolytes", **Berichte der Bunsengesellschaft**, 72:60-63, (1968).

Micka,K. and Rousar,I., "Theory of Porous Electrodes. XI. The Positive Plate of the Lead-Acid Battery", **Electrochimica Acta**, 18:629-633, (1973).

Micka,K. and Rousar,I., "Theory of Porous Electrodes. XIV. The Lead-Acid Cell", **Electrochimica Acta**, 21:599-603, (1976).

Micka,K. and Svata,M., "Study of Structural Factors of Lead-Acid Battery Electrodes", **Journal of Power Sources**, 4:43-51, (1979).

Miller,D.G., "Application of Irreversible Thermodynamics to Electrolyte Solutions. I. Determination of Ionic Transport Coefficients l_{ij} for Isothermal Vector Transport Processes in Binary Electrolyte Systems", **Journal of Physical Chemistry**, 70:2639-2659, (1966).

Moseley,P.T., Hutchison,J.L., Wright,C.J., Bourke,M.A.M., Hill,R.I. and Rainey,V.S., "Inelastic Neutron Scattering and Transmission Electron Microscope Studies of Lead Dioxide", **Journal of the Electrochemical Society**, 130:829-834, (1983).

Nagy,Z., "Calculations on the Effect of Gas Evolution on the Current-Overpotential Relation and Current Distribution in Electrolytic Cells", **Journal of Applied Electrochemistry**, 6:171-181, (1976).

Newman,J., Bennion,D. and Tobias,C.W., "Mass Transport in Concentrated Binary Electrolytes", **Beriche der Bunsengesellschaft**, 69:608-612, (1965).

Newman,J. and Tiedeman,W., "Porous-Electrode Theory with Battery Applications", **Journal of the American Institute of Chemical Engineers**, 21:25-41, (1975).

Papazov,G., Rogatchev,T. and Pavlov,D., "Influence of the Lead Dioxide Active Mass on the Corrosion Rate of the Spines of the Positive Lead-Acid Battery Plates", **Journal of Power Sources**, 6:15-24, (1981).

Pavlov,D. in McNicol,B.D. and Rand,D.A.I. (ed.), **Power Sources For Electrical Vehicles**, Elsevier, (1984).

Pavlov,D. and Bashtavelova,E., "A Model of the Structure of the Positive Lead-Acid Battery Active Mass", **Journal of the Electrochemical Society**, 131:1468-1476, (1984).

Pavlov,D. and Bashtavelova,E., "Structural Properties of the PbO_2 Active Mass Determining its Capacity and the 'Breathing' of the Positive Plate During Cycling", **Journal of the Electrochemical Society**, 133:241-248, (1986).

Pavlov,D. and Dinev,Z., "Mechanism of the Electrochemical Oxidation of Lead to Lead Dioxide in H_2SO_4 Solution", **Journal of the Electrochemical Society** , 127:855-863, (1980).

Pavlov,D. and Rogachiev,T., "Dependence of the Phase Composition of the Anodic Layer on Oxygen Evolution and Anodic Corrosion of Lead Electrode in Lead Dioxide Potential Region", **Electrochimica Acta**, 23:1237-1242, (1978).

Pohl,J.P. and Schendler,W., "Electrochemical Investigations on the Kinetics of the Growth of PbO_2 Layers on Lead", **Journal of Power Sources**, 13:101-113, (1984).

Ruetschi,P., "Review on the Lead-Acid Battery Science and Technology", **Journal of Power Sources**, 2:3-24, (1977).

Runge,W., "Comparison of Calculated with Measured Behaviour of Lead Storage Batteries and Causes of the Deviations", **Elektrotechnishe Zeitschrift ETZ-A.**, 93:67-72, (1972).

Santoro,A., D'Antonio,P. and Caulder,S.M., "A Neutron Power Diffraction Study of α- and β-PbO_2 in the Positive Electrode Material of Lead-Acid Batteries", **Journal of the Electrochemical Society**, 130:1451-1459, (1983).

Shepherd,C.M., "Design of Primary and Secondary Cells. I. Effect of Polarisation and Resistance on Cell Characteristics", **Journal of the Electrochemical Society**, 112:252-257, (1965).

Sides,P.J. and Tobias,C.W., "Primary Potential and Current Distribution Around a Bubble on an Electrode", **Journal of the Electrochemical Society**, 127:288-291, (1980).

Sides,P.J. and Tobias,C.W., "A Close View of Gas Evolution from the Back Side of a Transparent Electrode", **Journal of the Electrochemical Society**, 132:583-587, (1985).

Simon,A.C., "Stress Corrosion in Grids of the Lead-Acid Storage Battery", **Journal of the Electrochemical Society**, 114:1-8, (1967).

Simon,A.C. and Caulder,S.M. in Collins,D.H. (ed.), "Recent developments in the NRL-ILZRO investigation of the Porous $PbO_2/PbSO_4$ Electrode", **Power Sources 8**, Academic Press, (1975).

Simon,A.C. and Caulder,S.M. and Stemmle,J.T., "Structrual Transformations of the PbO_2 Active Material during Cycling", **Journal of the Electrochemical Society**, 122:461-466, (1975).

Simon,A.C., Wales,C.P. and Caulder,S.M., "Morphological Changes in the Lead Dioxide Electrode During its Reduction and Reoxidation", **Journal of the Electrochemical Society**, 117:987-992, (1970).

Simonsson,D., "A Mathematical Model for the Porous Lead Dioxide Electrode", **Journal of Applied Electrochemistry**, 3:261-270, (1973).

Simonsson,D., "Current Distribution in the Porous Lead Dioxide Electrode", **Journal of the Electrochemical Society**, 120:151-157, (1973).

Simonsson,D., "A Mathematical Model for the Porous Lead Dioxide Electrode. II. The Pseudo-steady State Approach for Low Rates of Discharge", **Journal of Applied Electrochemistry**, 4:109-115, (1974).

Siwek,E.G., "A System Evaluation of Lead-Acid Battery Chargers: Part II. Cells with Cast Lead-Calcium Grids", **Journal Of Power Sources**, 2:317-336, (1977).

Smith,G., **Storage Batteries Including Operation, Charging, Maintenance and Repair**, Pitman, (1980).

Smith G.D., **Numerical Solution of Partial Differential Equations**, Oxford University Press, (1969).

Sunu,W.G. and Burrows,B.W., "Current Density and Electrolyte Distrubution in Motive Power Lead-Acid Cells", **Journal of the Electrochemical Society**, 128:1405-1411, (1981).

Takahashi,K., Tsubota,M., Yonezu,K. and Ando,K., "Physical Changes in Positive Active Mass during Deep Discharge-Charge Cycles of Lead-Acid Cell", **Journal of the Electrochemical Society**, 130:2144-2149, (1983).

Tomantschger,K., "Effects of Electrolyte Agitation on the Performance of Lead-Acid Traction Batteries at Various Temperatures", **Journal of Power Sources**, 13:137-149, (1984).

Turner,A.D. and Moseley,P.T., "The Influence of Mass Transport Processes on the Performance of the Lead-Acid Cell", **Journal of Power Sources** 9:19-40, (1983).

Turner,A.D. and Moseley,P.T., "The Influence of Mass Transport Processes on the Performance of the Lead-Acid Cell on Pulsed Discharge", **Journal of Power Sources**, 10:53-61 (1983).

Twizell,E.H., **Computational Methods for Partial Differential Equations**, Ellis Horwood, (1984).

Valeriote,E.M.L. and Gallop,L.D., "The Kinetics of the Potentiostatic Oxidation of Lead Sulphate Films on Lead in Sulfuric Acid Solution", **Journal of the Electrochemical Society**, 124:370-380, (1977).

Vetter,K.J., **Electrochemical Kinetics Theoretical and Experimental Aspects**, Academic Press, (1967).

Vinal,G.W., **Storage Batteries 4th Ed.**, Wiley, (1955),

Vogt,H., "A Hydrodynamic Model for the Ohmic Interelectrode Resistance of Cells with Vertical Gas Evolving Electrodes", **Electrochima Acta**, 26:1311-1317, (1981).

Wales,C.P. and Simon,A.C., "Effects of Deep Cycling on Lead Positive Plates", **Journal of the Electrochemical Society**, 128:2512-2517, (1981).

Weininger,J.L. and Siwek,E.G., "A System Evaluation of Lead-Acid Battery Chargers: Part I. Cells with Antimonial Positive Grids", **Journal Of Power Sources**, 2:301-316, (1977).

Whyatt,P.R. and Hampson,N.A., "Discharge Profiles in the Porous PbO2 Electrode", **Surface Technology**, 9:351-358, (1979).

Winsel,A., "Contribution to the Understanding of Current Distribution in Porous Electrodes", **Zleifschrift fuer Elektrochemie**, 66:287-304, (1962).